Anisotropic thermocouples article

A. A. Snarskiĭ

Ukrainian National Technical University, 252056 Kiev, Ukraine

A. M. Pal'ti

Institute of Metal Physics, Ukrainian National Academy of Sciences, 252680 Kiev, Ukraine

A. A. Ashcheulov

Chernovtsy State University, 274003 Chernovtsy, Ukraine
(Submitted April 17 1996; accepted February 24 1997)
Fiz. Tekh. Poluprovodn. **31**, 1281–1298 (November 1997)

IN MEMORY OF ANATOLIĬ GRIGOR'EVICH SAMOĬLOVICH

Theoretical and experimental investigations of the generation of transverse thermoelectric power in anisotropic media and methods of direct conversion of heat, which are based on this generation, are described. Converters based on both semiconductors and high-T_c superconductor films are examined. © *1997 American Institute of Physics.* [S1063-7826(97)00111-7]

INTRODUCTION

In a homogeneous isotropic material, a temperature difference produces a irrotational (potential) electric field. The condition for an emf to appear in an isotropic material as a result of a temperature difference is that the material must be inhomogeneous. The inhomogeneity is ordinarily produced by creating a junction of two materials with different properties. For this reason, a thermoelement is ordinarily a thermocouple.

In general, a temperature difference in a material exhibiting a thermoelectric power anisotropy produces a transverse (perpendicular to the temperature gradient) thermoelectric field[1–3]

$$\mathbf{E}^T = -\hat{\alpha}\nabla T. \tag{1}$$

Here $\hat{\alpha}$ is the thermoelectric power tensor, and $\mathbf{E}^T$ is the so-called thermoelectric field. In general, the existence of both $\mathbf{E}^T_{\parallel} \| \nabla T$ and $\mathbf{E}^T_{\perp} \perp \nabla T$ follows from Eq. (1). This transverse thermoelectric field $\mathbf{E}^T_{\perp}$, in contrast to the longitudinal field $\mathbf{E}^T_{\parallel}$ employed in ordinary thermocouples, can lead to the appearance of an electric current even in a homogeneous closed circuit.[3,4] For this reason, even a homogeneous, thermoelectrically anisotropic medium can serve as a thermoelectric power generator, i.e., a thermoelement.[5]

Investigations of the anisotropy of α for the purpose of thermoelectric power generation were initiated in 1964 by A. G. Samoĭlovich and continued in the Department of Anisotropic Semiconductors at Chernovtsy State University under his guidance. Great progress was made in both the theory and practical applications.

CdSb single crystals served as the standard material for anisotropic thermoelements (ATs). Anomalously large, transverse-type, thermoelectric responses in single-crystal films of high-T_c superconductors in the normal state were discovered very recently. The appearance of new, possibly much more efficient, materials for ATs is rekindling interest, it would appear, in the transverse thermoelectric effect and makes the present review article timely.

The review article consists of the following sections:

1. Theoretical investigations.
   - 1.1. Elementary theory of anisotropic thermoelements.[6,7]
   - 1.2. Anisotropic thermoelements with end contacts (rigorous approach)
   - 1.3. Anisotropic thermoelements with allowance for end contacts
     - 1.3.1. Rectangular anisotropic thermoelements
     - 1.3.2. Anisotropic thermoelements with allowance for thermal conductivity anisotropy
     - 1.3.3. Allowance for electrical conductivity anisotropy
     - 1.3.4. Ring-shaped anisotropic thermoelements
     - 1.3.5. Anisotropic thermoelements with quasicrystallographic axes
   - 1.4. Anisotropic thermoelements with point contacts.
     - 1.4.1. EMF of anisotropic thermoelements with allowance for thermal conductivity anisotropy (Fig. 6a).
     - 1.4.2. EMF of anisotropic thermoelements with allowance for thermal conductivity anisotropy (Fig. 6b).
   - 1.5. Efficiency of anisotropic thermoelements
   - 1.6. Anisotropic thermoelements in a magnetic field
   - 1.7. Artificially anisotropic media
     - 1.7.1. Effective properties of layered media
2. Experimental investigations
   - 2.1. Semiconductor anisotropic thermoelements and devices
   - 2.2. Anisotropic thermoelements based on single-crystal high-T_c superconductor films

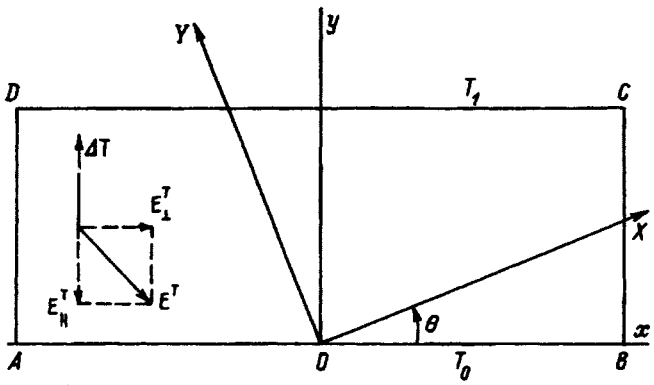

FIG. 1. Thermoelectrically anisotropic plate. X,Y — crystallographic axes, T_1, T_0 — temperatures of the top and bottom faces, θ — angle of inclination of the crystallographic axes X,Y with respect to the laboratory axes x,y.

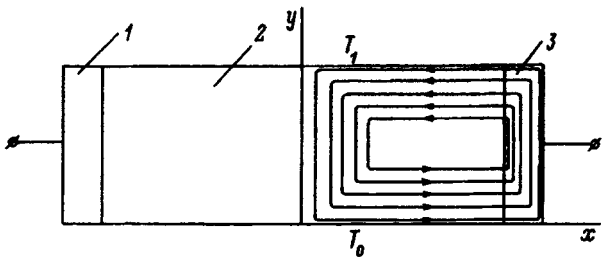

FIG. 2. Anisotropic thermoelement. Regions *1* and *3* — end contacts for extracting the thermoelectric signal, region *2* — thermoelectrically anisotropic plate. The lines of the thermoelectric eddy currents are shown on the right-hand side of the figure.

1. THEORETICAL INVESTIGATIONS

1.1. Elementary theory of anisotropic thermoelements[6,7]

Let us consider a thermoelectrically anisotropic medium whose thermoelectric power tensor in the crystallographic axes has the form

$$\hat{\alpha}=\begin{pmatrix}\alpha_\parallel & 0\\ 0 & \alpha_\perp\end{pmatrix}. \tag{2}$$

For simplicity, we shall consider the two-dimensional case. We cut from this medium a plate in a manner so that the crystallographic X axis makes an angle θ with the edge AB (Fig. 1). The thermoelectric power tensor in the laboratory coordinate system has the form

$$\hat{\alpha}=\begin{pmatrix}\alpha_\parallel \cos^2\theta+\alpha_\perp \sin^2\theta & (\alpha_\parallel-\alpha_\perp)\sin\theta\cos\theta\\ (\alpha_\parallel-\alpha_\perp)\sin\theta\cos\theta & \alpha_\parallel \sin^2\theta+\alpha_\perp \cos^2\theta\end{pmatrix}. \tag{3}$$

If the temperatures at the top and bottom boundaries (AB and CD) are maintained equal to T_1 and T_0, respectively, then (ignoring lateral heat transfer) a one-dimensional temperature distribution with a constant gradient

$$\frac{\partial T}{\partial y}=\frac{T_1-T_0}{b}\equiv\frac{\Delta T}{b},\quad \frac{\partial T}{\partial x}=0 \tag{4}$$

will be produced inside the plate.

According to Eqs. (1), (3), and (4), the transverse (with respect to ∇T) thermoelectric field arising in the process will have the form

$$E_x^T=\alpha_{12}\frac{\Delta T}{b}, \tag{5}$$

where $\alpha_{12}=(\alpha_\parallel-\alpha_\perp)\sin\theta\cos\theta$ is the off-diagonal component of the tensor (3). In what follows, for convenience, we shall often employ the notation for the indices $1,\ 2=x,\ y$.

According to Eq. (5), the thermoelectric power arising between the ends AD and BC has the form

$$\varepsilon=\int_{-a/2}^{a/2}E_x^T dx=\alpha_{12}\Delta T\frac{a}{b}. \tag{6}$$

The fundamental difference of AT from ordinary thermocouples is seen immediately from this expression, since the emf of an AT contains the geometric factor a/b. At the same time, the emf of an ordinary thermocouple does not depend on the geometric dimensions of these thermocouples. In the case of an AT, the emf is proportional to the length and inversely proportional to the thickness. Therefore, for example, the emf can be increased by increasing the length of the AT.

The expression (6) for the emf of an AT is qualitatively correct, but it has a number of important drawbacks. We shall list some of them.

1) On the one hand, the derivation of the expression (6) assumed that the plate is finite ($-a/2\leqslant x\leqslant a/2$). On the other hand, the expression (5) was written for a plate which is infinite along the x axis; i.e., the possible boundary conditions at $x=\pm a/2$ were neglected. Since any real AT has current collecting contacts, allowance must be made for their presence in the corresponding boundary conditions.

2) The temperature distribution in an AT can be strongly nonuniform. For this reason, Eq. (6) must be extended to the case $\nabla T\neq\text{const}$.

3) The temperature dependence of the electric and thermal conductivities and the thermoelectric power of real materials can alter Eq. (6) substantially.

4) The expression (6) disregards the possibility that the electric and thermal conductivity can be of a tensor character. As a rule, a medium exhibiting anisotropy of $\hat{\alpha}$ also exhibits anisotropy of $\hat{\sigma}$.

1.2. Anisotropic thermoelement with end contacts (rigorous approach)

In any real AT, metallic current-collecting contacts (CCs) must be soldered to the lateral faces (Fig. 2). Two boundary-value problems of mathematical physics must be solved in order to allow for the effect of the CCs on the emf of an AT. These problems make it possible to establish the effect of a CC on the temperature distribution and electrochemical potential distribution inside the AT.

Ignoring the effect of thermoelectric eddy currents on the temperature distribution (we shall estimate it below), the equation for the latter follows from the condition $\nabla\cdot\mathbf{q}=0$ and for isotropic thermal conductivity

$$\frac{\partial^2 T}{\partial x^2}+\frac{\partial^2 T}{\partial y^2}=0. \tag{7}$$

The boundary conditions are: 1) continuity of the temperatures and heat fluxes at a boundary between the CCs (regions *1* and *3*) and an anisotropic plate (region *2*); 2) the values of the temperatures T_1 and T_0 on the top and bottom faces of the plate and the CCs; and 3) heat transfer on the lateral faces of the CCs:

$$-\kappa\frac{\partial T^{(3,1)}}{\partial x}=\beta(T^{(3,1)}-T_0)$$

at $x=\pm(a/2+l)$. The superscripts denote the regions of the AT and CCs, and β is the heat-transfer coefficient; the temperature of the surrounding medium is assumed to be T_0. It is obvious that the isotherms is horizontal if $\beta=0$ (the condition of adiabaticity on the outer ends of the contacts). For $\beta\neq 0$, the solution of the boundary-value problem is rather complicated:[6]

$$T=T_0+\frac{\Delta T}{b}y+2\frac{\beta b\Delta T}{\kappa''}\sum_{k=1}^{\infty}(-1)^k\delta_k\cosh\frac{k\pi x}{b}\sin\frac{k\pi y}{b},$$

$$\frac{1}{\delta_k}=\left(k\pi+\frac{\beta b}{\kappa''}\right)\left(\cosh\frac{k\pi a}{2b}+\frac{\kappa}{\kappa''}\sinh\frac{k\pi a}{2b}\right)\times\exp\frac{k\pi d}{b}$$
$$-\left(k\pi-\frac{\beta b}{\kappa''}\right)\left(\cosh\frac{k\pi a}{2b}-\frac{\kappa}{\kappa''}\sinh\frac{k\pi a}{2b}\right)\times\exp\left(-\frac{k\pi d}{b}\right), \tag{8}$$

where κ and κ'' are the thermal conductivities of the AT and CCs, respectively. Taking into account the real value of β ($\beta\approx 0.4$–4.2 W/m$^2\cdot$K) shows that the deviation of the temperature distribution from a linear distribution is small.

In contrast to the effect on the temperature distribution, the effect on the distribution of the electrochemical potential ζ is fundamental. We assume that the electrical conductivity of the AT and CCs are equal, respectively, to σ and σ'', that both of them are isotropic, and that the thermoelectric power of the CCs can be ignored since they are metallic. The distribution $\zeta(\mathbf{r})$ in the stationary case is determined by the continuity equation for the current density $\nabla\cdot\mathbf{j}=0$, where

$$\mathbf{j}=-\hat{\sigma}\nabla\zeta-\hat{\sigma}\hat{\alpha}\nabla T, \tag{9}$$

which reduces to the equation

$$\frac{\partial^2\zeta}{\partial x^2}+\frac{\partial^2\zeta}{\partial y^2}=-2\alpha_{12}\frac{\partial^2 T}{\partial x\partial y}. \tag{10}$$

We assume that the thermoelement is insulated. The following conditions are satisfied at the boundaries between the anisotropic plate and the CC (ζ is continuous and the current density is perpendicular to the boundary):

$$\zeta(-a/2,y)=\zeta^{(1)}(-a/2,y),\quad \zeta(a/2,y)=\zeta^{(3)}(a/2,y),$$
$$j_x(-a/2,y)=j_x^{(1)}(-a/2,y),\quad j_x(a/2,y)=j_x^{(3)}(a/2,y). \tag{11}$$

The solution of the boundary-value problem by the method of separation of variables gives the expression

$$\Delta\zeta=\zeta^{(1)}(-a/2,y)-\zeta^{(3)}(a/2,y),$$
$$\Delta\zeta=\alpha_{12}\Delta T\frac{a}{b}+2\frac{\alpha_{12}\Delta T\beta b}{\kappa''}\frac{a}{b}\sum_{k=1}^{\infty}(-1)^k\gamma_k\cos\frac{k\pi}{b}y, \tag{12}$$

$$\gamma_k=\frac{\delta_k}{\sinh\frac{k\pi}{b}\sinh\frac{k\pi}{b}\frac{a}{2}+\frac{\sigma}{\sigma''}\cosh\frac{k\pi}{b}\cosh\frac{k\pi}{b}\frac{a}{2}},$$

where δ_k is determined in Eq. (8).

We note that in the case of a linear temperature distribution the right side of Eq. (10) vanishes and only the first term remains in the expression for $\Delta\zeta$. However, even in the case of a nonlinear temperature distribution, if $\sigma/\sigma''\to 0$, for finite l the second term in Eq. (12) approaches zero. Thus, $\Delta\zeta$ ceases to depend on y, and since the thermoelectric power of the CCs $\alpha''=0$, the value obtained for $\Delta\zeta$ can be taken as the thermoelectric power. A detailed investigation of the expression for $\zeta=\zeta(x,y)$ in the the limit $\sigma/\sigma''\to 0$ showed that the function ζ vanishes at the boundaries $x=\pm(a/2+l)$ for arbitrary l. The latter can be assumed to be much smaller than $a/2$.

The main conclusion to be drawn from the investigation of the effect of the CCs on the emf of an AT is that this effect can be taken into account by simplified boundary conditions

$$\zeta(a/2,y)=\varphi_1,\quad \zeta(-a/2,y)=\varphi_2, \tag{13}$$

where φ_1 and φ_2 are the potentials on the ends ΔT and are constants[1] independent of y. Under the boundary conditions (13) the boundary-value problem (10) and (11) simplifies substantially and in many cases it is possible to obtain an analytical expression for the emf in much more complicated cases than in the one studied above, for example, for arbitrary $T=T(x,y)$.

We also note that in determining $T=T(x,y)$ in the heat-conduction equation the terms describing the release or absorption of heat by eddy currents were dropped. An estimate made of these currents in Refs. 7 and 8 shows that in this case they can be ignored.

1.3. Anisotropic thermoelements with allowance for end contacts

It is assumed that $\sigma_{at}\ll\sigma_{ec}$, where σ_{at} and σ_{ec} are the conductivities of the thermoelement and end contact, respectively.

1.3.1. Rectangular anisotropic thermoelements

The equations and boundary conditions which describe the distributions of the fields and currents in an AT now has the form

$$\nabla \cdot \mathbf{j} = 0, \tag{14}$$

$$j_y(x, y=0, b) = 0, \tag{15}$$

$$\zeta(a/2, y) = \varphi(a/2), \quad \zeta(-a/2, y) = \varphi(-a/2), \tag{16}$$

where the boundary condition (16) takes into account the presence of the CCs.

As shown in Ref. 9, in this case a general expression suitable for an arbitrary temperature distribution and an arbitrary temperature dependence $\alpha_{ik} = \alpha_{ik}(T)$ (α_{ik} can also depend on r) can be obtained for the emf:

$$\varepsilon = -\frac{1}{b}\int_0^b dy \int_{-a/2}^{a/2} E_x^T dx,$$
$$E_x^T = -\alpha_{11}\frac{\partial T}{\partial x} - \alpha_{12}\frac{\partial T}{\partial y}. \tag{17}$$

where E_x^T is a component of the thermoelectric field.

The expression obtained for the emf of an AT can be easily extended to the three-dimensional case and includes many previously known particular cases, starting with the standard thermocouple.

Rewriting Eq. (17) in dimensionless coordinates ($X = x/a$, $Y = y/b$) and substituting the explicit form of E_x^T, we obtain

$$\varepsilon = \int_0^1 dY \int_{-1/2}^{1/2} \alpha_{11}\frac{\partial T}{\partial X} dX + \frac{a}{b}\int_0^1 dY \int_{-1/2}^{1/2} \alpha_{12}\frac{\partial T}{\partial Y} dX. \tag{18}$$

The main conclusion for the entire question of generation of emf by anisotropic media follows immediately from Eq. (18) — the part of the emf that is associated with the thermoelectric power anisotropy always appears in the geometric factor a/b. The expression (17) can be extended to the case where $\sigma = \sigma(y)$. Then

$$\varepsilon = -\frac{1}{b}\int_0^b dy \int_{-a/2}^{a/2} E_x^T dx \Bigg/ \frac{1}{b}\int_0^b \sigma(y) dy. \tag{19}$$

An expression for the emf without the boundary condition (16) was obtained in Ref. 10. It was assumed that $a \gg b$ and the indicated condition is thereby unimportant. Furthermore, and this is very important, the temperature distribution was assumed to be one-dimensional ($\partial T/\partial x = 0$), which made it possible to replace, to a high degree of accuracy, $\partial T/\partial y$ by $\Delta T/b$. These assumptions made it possible to take into account the anisotropy of the electrical conductivity

$$\varepsilon = \frac{a\int_0^b \frac{\alpha_{12}}{\rho_{11}}\frac{\partial T}{\partial y} dy}{\int_0^b \frac{dy}{\rho_{11}}} \simeq \frac{a}{b}\Delta T \frac{a\int_{T_0}^{T_1} \frac{\alpha_{12}}{\rho_{11}} dT}{\int_0^b \frac{dy}{\rho_{11}}}, \tag{20}$$

where $\rho_{11} = \sigma_{22}/(\sigma_{11}\sigma_{22} - \sigma_{12}^2)$.

The dependence on y $\rho_{11} = \rho_{11}(y)$, but not on x, can also be taken into account. For isotropic electrical conductivity the expression (20) is a particular case of Eq. (19).

In some cases taking into account $\partial T/\partial x$ is fundamental. One such case is an AT with thermal conductivity anisotropy.

1.3.2. Anisotropic thermoelement with allowance for thermal conductivity anisotropy

To determine the emf of an AT it is first necessary to find the temperature distribution. The heat-conduction equation, in contrast to Eq. (7), now includes components of the thermal conductivity tensor. Its form is similar to that of the thermoelectric power tensor (3)

$$\kappa_{11}\frac{\partial^2 T}{\partial x^2} + 2\kappa_{12}\frac{\partial^2 T}{\partial x \partial y} + \kappa_{22}\frac{\partial^2 T}{\partial y^2} = 0. \tag{21}$$

We choose the previous boundary conditions — the temperature is constant at the top and bottom boundaries and equals $T(0,x) = T_0$, $T(b,x) = T_1$, and we ignore heat transfer from the lateral faces.

This boundary-value problem can be solved analytically only in the presence of a small parameter, which, for example, can be $\kappa_{12}/\sqrt{\kappa_{11}\kappa_{22}}$ and has the form[11]

$$T(x,y) = T_0 + \Delta T\left(\frac{y}{b} - \frac{4\kappa_{12}}{\sqrt{\kappa_{11}\kappa_{22}}} \times \sum_{k=1,3,\ldots}^{\infty} \frac{\sinh(k\pi x/b)\sin(k\pi y/b)}{(k\pi)^3 \cosh(k\pi a/2b)}\right). \tag{22}$$

Numerical simulation confirms this solution.[11] Substituting the expression (22) into the general expression for the emf (17) of an AT gives[9] (see also Ref. 11)

$$\varepsilon = \alpha_{12}\Delta T\frac{a}{b} - \alpha_{11}\Delta T\frac{16\kappa_{12}}{\pi^3\sqrt{\kappa_{11}\kappa_{22}}} \times \sum_{k=1,3,\ldots}^{\infty} k^{-3} \tan\frac{k\pi}{2}\sqrt{\frac{\kappa_{22}}{\kappa_{11}}}. \tag{23}$$

The first term in Eq. (23) is the standard emf of an AT, and the second term is the part of the emf that is produced by the temperature gradient appearing along the x axis as a result of the thermal conductivity anisotropy ($\kappa_{12} \neq 0$). It is important that this term remains finite as $a/b \to \infty$. If $\sqrt{\kappa_2/\kappa_{11}} \approx 1$, then even at $a/b \approx 3$ the sum in Eq. (23) equals 1.05, to a high degree of accuracy, and therefore

$$\varepsilon(a/b \gg 1) \approx \alpha_{12}\Delta T\frac{a}{b} - 1.7\frac{\kappa_{12}}{\sqrt{\kappa_{11}\kappa_{22}}}\alpha_{11}\Delta T. \tag{24}$$

We note that the second term does not include the geometric factor a/b.

Questions concerning the generation of an emf in the case of an anisotropic thermal conductivity were also studied in Ref. 12, but the expression obtained there for the temperature distribution does not satisfy the boundary conditions. This work was criticized in Ref. 13. Besides the valid criticism, the following assertion was made in Ref. 13: ''Thermal conductivity anisotropy can to some degree distort the temperature, potential, and current distributions in a thermal electric medium but it cannot itself serve as a source of emf.'' We cannot concur with this assertion. Indeed, any source of emf contains CCs, which unavoidably make the AT as a whole inhomogeneous. In this case, as one can see,

for example, from Eq. (22), even under conditions of an isotropic thermoemf ($\alpha_{12}=0$, $\alpha_{11}=\alpha$) the emf is not zero and equals $\varepsilon\sim\alpha\kappa_{12}$. In reality, this is a standard ''thermocouple'' emf with an unusual method of creating a temperature difference at the junctions (CCs) — by thermal conductivity anisotropy. The thermoelectric power of the second branch does not appear in Eq. (23), since it was assumed in advance that the thermoelectric power of the CCs equals zero.

1.3.3. Allowance for electrical conductivity anisotropy

By analogy with thermal conductivity anisotropy, allowing for electrical conductivity anisotropy does not make it possible to obtain a solution of the boundary-value problem and therefore the emf in an analytic form for anisotropy of arbitrary magnitude. In the presence of the small parameter $\sigma_{12}/\sqrt{\sigma_{11}\sigma_{22}}$, allowing for the CCs in boundary conditions of the type (16) makes it possible to obtain the emf in an analytical form[14]

$$\varepsilon=\alpha_{12}\Delta T\frac{a}{b}+\alpha_{22}\Delta T\frac{a}{b}\frac{\sigma_{12}}{\sigma_{11}}\left(1-\frac{16}{\pi^3}\sum_{k=1,3,\ldots}^{\infty}k^{-3}\tanh\frac{k\pi a}{2b}\right). \tag{25}$$

For $a/b>4$ and $\sigma_{11}/\sigma_{22}\approx 1$ the sum in Eq. (25) equals 1.052, to a high degree of accuracy, and for $a/b\geqslant 5$ the 1 in parentheses can be ignored in contrast with the second term:

$$\varepsilon\approx\alpha_{12}\Delta T\frac{a}{b}-\frac{1}{2}\alpha_{12}\Delta T\left(\frac{a}{b}\right)^2\sigma_{12}\sqrt{\sigma_{22}/\sigma_{11}^3}. \tag{26}$$

It follows from Eq. (26) that, besides the standard term ($\alpha_{12}\Delta T(a/b)$), the emf of an AT also contains a term that is proportional to the off-diagonal component of the electrical conductivity and a geometric factor a/b. We note that the term that takes into account the thermal conductivity anisotropy in Eq. (24) does not include a geometric factor. We also note that the expression (26), obtained for the emf of an AT taking into account the CCs, also differs from the emf (20) of an AT neglecting the CCs. The latter does not include the term with σ_{12}.

1.3.4. Ring-shaped anisotropic thermoelements

In some cases a nonrectangular, more complicated shape of an AT, for example, a ring (Fig. 3), is advantageous. The boundary conditions (16) make it possible to obtain for the emf of an AT an expression similar to Eq. (17):[15]

$$\varepsilon=-\frac{1}{\ln(R_1/R_0)}\int_{R_0}^{R_1}d\rho\int_0^{\theta}E_\theta^T d\theta, \tag{27}$$

where $E_\theta^T=-E_x^T\sin\theta+E_y^T\cos\theta$ is a component of the thermoelectric field.

It is easily shown that Eq. (27) also describes diverse cases of so-called eddy thermoelements.[16] According to Ref. 16, if thermoelectric eddy currents (TECs) circulate in an uncut ring made of an anisotropic thermoelectric material with a fixed temperature distribution, then in a cut ring they are extracted into an external circuit; i.e., the generation of an emf is attributed to the presence of a TEC. The generation principle is assumed to be fundamentally different from that in an AT. Although the idea of extraction of TECs into an external circuit made it possible in a number of cases to obtain satisfactory temperature distributions, from our standpoint, the emf in an AT of arbitrary shape is not associated with extraction of TECs. Specifically, we mention as an example Ref. 15 , where there are no TECs before the ring is cut and an emf is generated after the ring is cut.

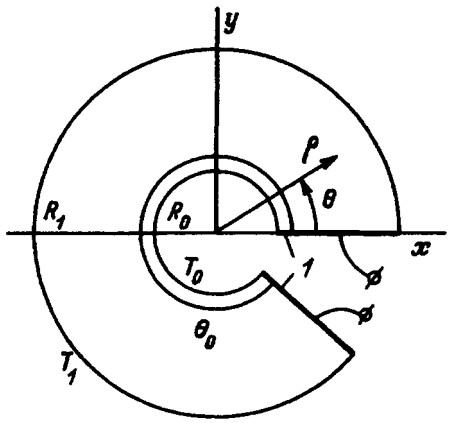

FIG. 3. Ring-shaped anisotropic thermoelement: *1* — Metallic end of the contact, T_1, T_0 — temperatures of the outer and inner parts of the ring, R_1, R_2 — outer and inner radii.

1.3.5. Anisotropic thermoelements with quasicrystalline axes

It is well known that in a number of cases a medium consisting of alternating layers with different properties (κ_1, α_1, σ_1, κ_2, α_2, σ_2) can be represented as homogeneous but anisotropic. Such materials and their applications in rectangular ATs will be examined in greater detail in Sec. 1.6. If the layers of such a material are curved, then the averages described will depend on the coordinates: The properties of such a medium are tensors $\hat{\sigma}$, $\hat{\alpha}$, and $\hat{\kappa}$. For clarity, we can introduce quasicrystallographic axes — the tangent to them will be directed along one of the principal axes of the indicated tensors. Such media — with curved quasicrystalline axes — can be used to produce ATs.

As an example, let us consider a ring-shaped AT with spiral axes[17] with a radial temperature distribution (Fig. 4). The direction of the axes is fixed by the unit vector **n**, tangent to this axis. The components of the tensor α_{ik} are expressed in terms of **n** as

$$\alpha_{ik}=\alpha_\perp\delta_{ik}+\Delta\alpha n_i n_k,\quad \Delta\alpha=\alpha_\parallel-\alpha_\perp. \tag{28}$$

The temperature distribution has the form

$$T=T_0+\frac{\Delta T}{\ln(R_1/R_0)}\ln\frac{\rho}{R_0}. \tag{29}$$

The emf is calculated from Eq. (27), where

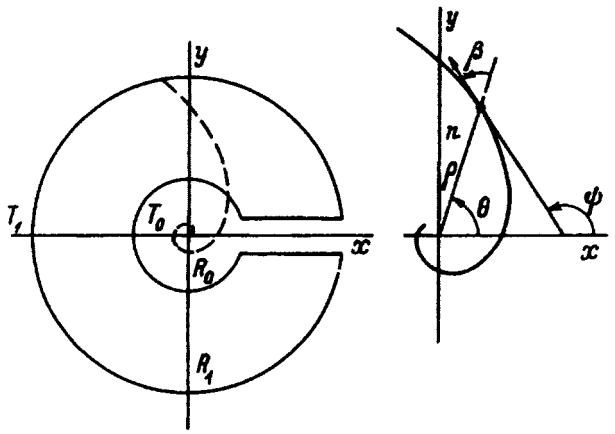

FIG. 4. Ring-shaped anisotropic thermoelement with quasicrystallographic axes. The dashed line indicates the direction of the crystallographic axes; θ,ρ,β,ψ,n — parameters determining the form of the quasicrystallographic axes.

$$E_\theta^T = -\alpha_{\theta\theta}\frac{\partial T}{r\,\partial\theta} - \alpha_{\theta r}\frac{\partial T}{\partial \rho}, \tag{30}$$

and since $\partial T/\partial\theta = 0$, it is necessary to know only the component $\alpha_{\theta r}$ of the thermoelectric power tensor

$$\alpha_{\theta r} = \alpha_{xx}\sin^2\theta - \alpha_{xy}\sin 2\theta + \alpha_{yy}\cos^2\theta, \tag{31}$$

where

$$\alpha_{xx} = \alpha_\perp + \Delta\alpha\cos^2(\varphi+\beta), \quad \alpha_{xy} = \frac{1}{2}\Delta\alpha\sin 2(\varphi+\beta),$$
$$\alpha_{yy} = \alpha_\perp + \Delta\alpha\sin^2(\varphi+\beta). \tag{32}$$

Substituting Eqs. (29)–(32) into Eq. (27), we obtain

$$\varepsilon = \frac{\Delta\alpha\Delta T}{\pi\ln(R_1/R_0)}\sin 2\beta. \tag{33}$$

In the two extreme cases $\beta = 0$ and $\beta = \pi/4$ the emf of the AT equals zero. The axes degenerate into radii in the first case and concentric circles in the second case. The maximum emf is reached for $\beta = \pi/4$. The ring-shaped AT studied is a continuous analog of the four-branch, closed AT studied in Ref. 5 .

1.4. Anisotropic thermoelements with point contacts

In some cases current is extracted into an external circuit by point contacts placed on the surface of the AT (see Fig. 5). Such an arrangement of the contacts is possible when the boundary conditions at the edges of the AT can be ignored, i.e. the AT can be regarded as infinitely long.

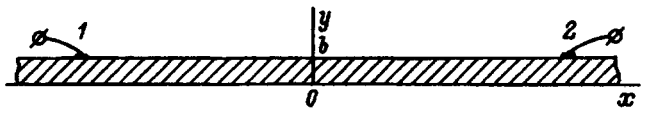

FIG. 5. Arrangement of an anisotropic thermoelement with flat contacts *1, 2*.

Let us examine two possible cases of boundary conditions in the thermal problem for which a simple analytical solution can be obtained for the emf allowing for thermal and electrical conductivity anisotropies (Fig. 6).

1.4.1. EMF of anisotropic thermoelements with allowance for thermal conductivity anisotropy

Let us consider the case in which there is a constant heat flux at the outer boundary and we have an isotherm at the bottom boundary (Fig. 6a)

$$q_y|_{y=b} = -\kappa_{12}\frac{\partial T}{\partial x} - \kappa_{22}\frac{\partial T}{\partial y}\bigg|_{y=b} = -q_0, T(x) = T_0. \tag{34}$$

According to Eqs. (34) and (21), the temperature distribution has the simple form

$$T(x,y) = T_0 + \frac{q_0}{\kappa_{22}}y. \tag{35}$$

We set the boundary conditions of the problem on the basis of the electrical insulation condition $j_n|_s = 0$. Now, we can take into account the fact that a real thermal element has a finite size along the x axis and therefore

$$\zeta(x,y) = -\frac{\Delta T}{b}(\alpha_{12}x + \alpha_{22}y). \tag{36}$$

An expression for the emf follows immediately from Eq. (36) (in Fig. 6, a is the distance between the points *1* and *2*)

$$\varepsilon = \alpha_{12}\Delta T(a/b), \tag{37}$$

which is identical to Eq. (6).

We note that for such boundary conditions of the thermal problem neither thermal conductivity anisotropy nor electrical conductivity anisotropy appears in the expression for the emf of the AT.

1.4.2. EMF of an anisotropic thermoelement with allowance for thermal conductivity anisotropy

Let us now examine the case where a constant heat flux $q_y|_{y=0,b} = -q_0$ is fixed on the top and bottom boundaries of the AT (Fig. 6b). Then the solution of the thermal conductivity equation has the form

$$T_1 = T_0 + q_0(k_{12}x + k_{22}y), \tag{38}$$

where $\hat{k} = \hat{\kappa}^{-1}$ is the thermal-resistance tensor, and the solution of the electrical problem, with the same electrical insulation boundary conditions as before, is

$$\zeta(x,y) = q_0[(\alpha_{12}\kappa_{22} + \alpha_{11}\kappa_{12})x + (\alpha_{12}\kappa_{12} + \alpha_{22}\kappa_{22})y]. \tag{39}$$

The expression for the emf

$$\varepsilon = q_0 a(\alpha_{12}\kappa_{22} + \alpha_{11}\kappa_{12}), \tag{40}$$

which includes the components of the thermal conductivity tensor, follows immediately from Eq. (39).

In both cases it was assumed that the conductivity of the point contacts is much higher than the conductivity σ_{ik} of the thermoelement, and therefore the thermoelectric power of the point contacts can be neglected. This means that the differ-

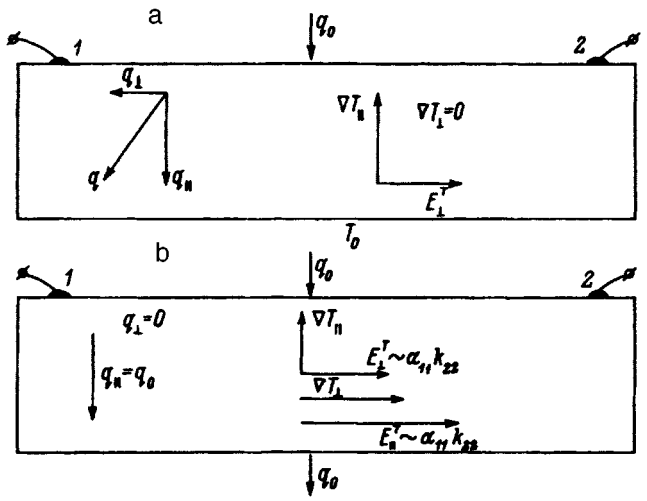

FIG. 6. Anisotropic thermoelement with the givens: a — heat flux on the top face, b — heat fluxes on the top and bottom faces. Insets: Directions of the fields, fluxes, and gradients.

ence $\Delta\zeta$ the electrochemical potentials can be replaced by the difference $\Delta\varphi = -\varepsilon$ in the electrical potentials.

Both expressions (37) and (40) for the emf of the AT are physically transparent. In the first case $\nabla T \| Y$ generates a field $\mathbf{E}^T \| X$, which generates $\varepsilon \sim \alpha_{12}$. In the second case the flux $\mathbf{q} \| Y$ (in connection with the fact that the thermal conductivity is anisotropic) produces not only $\nabla T_\perp \| Y$ but also $\nabla T_\parallel \| X$. The component $\nabla T_\perp$ generates a transverse field $E_\perp^T$ and α_{12}, and the gradient $\nabla T_\parallel$ generates a field $E_\parallel^T \sim \alpha_{11}\kappa_{12}$ parallel to it. The emf produced by the field $E_\parallel^T$ is the ''standard'' thermocouple emf, since in this case a temperature gradient exists not only along Y but also along X. This temperature gradient produces the temperature difference at the junctions $\Delta T_\parallel = T_2 - T_1 = q_0 a k_{12}$ at the points *1* and *2* (Fig. 6b). The ''anisotropy'' obtained with this emf is related with k_{12}.

We note that the longitudinal temperature difference $\Delta T_\parallel$ can, at first glance, make it possible to obtain for a finite value of q_0 an arbitrarily large temperature differential (as is pointed out in Ref. 13). In reality, this is impossible, since it is impossible to achieve ''thermal'' boundary conditions (creating $q = \text{const}$) for which $\Delta T_\parallel$ is arbitrarily large.

As an example of ATs examined above, we turn to Ref. 18, where detailed calculations of an AT employing thermal conductivity anisotropy were performed by a method analogous to that studied in Sec. 1.4.2. An anistropic heat conductor, which consists of the same material as the AT, with a lower boundary beveled at an angle ψ and which is in thermal contact with a thermostat (Fig. 7), is used to produce a uniform heat flux in a medium with an anisotropic thermal conductivity. The AT itself and the heat conductor are separated by a thin, electrically insulating and thermally conducting interlayer. Disregarding the effect of the interlayer on the temperature distribution and assuming that the lateral faces are thermally insulated, it is easy to determine from Eq. (38) the angle ψ, for which $q = \text{const}$ and the isotherms are inclined at an angle ψ with respect to X. One of the isotherms is also the lower boundary of the heat conductor and

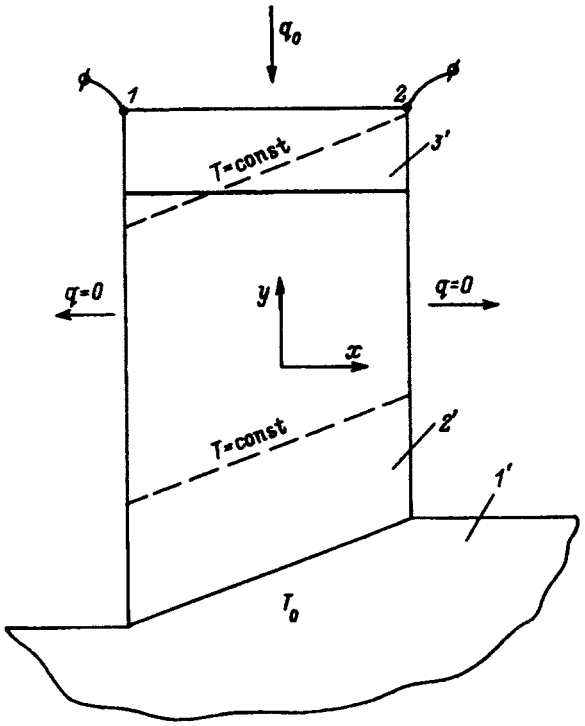

FIG. 7. Arrangement of an anisotropic thermoelement with a heat conductor of a special form. *1′* — thermostat, *2′* — heat conductor, *3′* — anisotropic thermoelement.

$$\tan\psi = \frac{\kappa_{12}}{\kappa_{11}}. \tag{41}$$

The temperature differential $\Delta T_\parallel$ between the contacts *1* and *2* increases with increasing length a of the heat conductor with anisotropic thermal conductivity. It is obvious that $\Delta T_\parallel$ cannot become arbitrarily large — this requires that all boundary conditions are satisfied ideally. However, for example, for very high T_2 or very low T_1, it is impossible to achieve thermal insulation of the lateral boundaries and have $q = \text{const}$ at the top and bottom boundaries.

1.5. Efficiency of anisotropic thermoelements

We shall examine very briefly the question of the efficiency η of an AT in connection with the fact that the efficiency of all real ATs employed in practice is low. This is why ATs are ordinarily used not as a generator of an emf but rather as transducers in measuring devices. In Refs. 7 and 19 the efficiency of an AT is studied in the case of a low thermoelectric figure of merit ($ZT \ll 1$), and in Ref. 20 a similar calculation was performed for arbitrary values of ZT. For this reason, we shall first consider Ref. 20, after which we shall study $ZT \ll 1$ as a special case.

To calculate the efficiency η of an anisotropic thermoelement, just as the efficiency of any heat machine, it is necessary to find the heat $\dot{Q}_1$ obtained from a heater and the heat $\dot{Q}_0$ given up to a refrigerator per unit time. The result for the efficiency is

$$\eta=\frac{\dot{Q}_1-\dot{Q}_0}{\dot{Q}_0}. \tag{42}$$

To determine $\dot{Q}_1$ and $\dot{Q}_0$ it is necessary to know the temperature and current distributions in the AT. The calculation in Ref. 20 was performed for $a/b\gg 1$, with allowance for the effect of the end contacts (ECs). In this case the temperature is a function only of y and the heat-conduction equation, which, in general, has the form

$$\frac{\partial}{\partial x_i}\kappa_{ik}\frac{\partial T}{\partial x_k}+\rho_{ik}j_i j_k-\tau_{ik}j_k\frac{\partial T}{\partial x_i}-\Pi_{ik}\frac{\partial j_k}{\partial x_i}=0, \tag{43}$$

acquires the much simpler form

$$\kappa_{22}\frac{d^2T}{dy^2}+\rho_{11}j_1^2-T\alpha_{12}\frac{dj_1}{dy}=0, \tag{44}$$

where $\tau_{ik}=T\dfrac{\partial\alpha_{ik}}{\partial T}$ is the Thompson tensor and $\Pi_{ki}=\alpha_{ik}T$ is the Peltier tensor. In the same approximation $(a/b\gg 1)$, $j_2=0$,

$$j_1=E_1/\rho_{11}-(\alpha_{12}/\rho_{11})dT/dy$$

and Eq. (44) can be written as

$$(1+ZT)\frac{d^2T}{dy^2}-Z\frac{2E}{\alpha_{12}}\frac{dT}{dy}+Z\left(\frac{dT}{dy}\right)^2+Z\left(\frac{E}{\alpha_{12}}\right)^2=0, \tag{45}$$

where $Z=\alpha_{12}^2/\kappa_{22}\rho_{11}$ is the thermoelectric figure of merit in the anisotropic case. In the isotropic case $Z=\sigma\alpha^2/\kappa$, and Z is also called the Ioffe number. The quantity $Z=\alpha_{12}^2/\kappa_{22}\rho_{11}$ determines the efficiency of an AT. The solution of the nonlinear equation (44) is sought in the form

$$\frac{dy}{dT}=\frac{b}{\Delta T}[1+\varphi(T)], \tag{46}$$

assuming y is the dependent variable and T is the independent variable,

$$\varphi=(1-b/\Delta T)^2\ \ln(1+ZT)+C,$$

$$C=-\frac{(1+b/\Delta T)^2}{Z\Delta T}[(1+ZT_1)\ln(1+ZT_1)$$

$$-(1+ZT_0)\ln(1+ZT_0)-Z\Delta T]. \tag{47}$$

We recall the ''long AT'' approximation and that the ECs are disregarded: $E_x=\text{const}$. The constant C is determined from the equation

$$\int_{T_0}^{T}\varphi(T)dT=0, \tag{48}$$

which follows from Eq. (46).

In solving the heat-conduction equation, it was assumed that $\varphi(T)\ll 1$ for arbitrary ZT. A detailed analysis[20] (see also Refs. 21–23) confirms the fact that $\varphi(T)$ is small. The quantities $\dot{Q}_1$ and $\dot{Q}_0$ can be determined from Eqs. (46)–(48):

$$\dot{Q}_1=s\kappa_{22}\frac{\Delta T}{b}[1-\varphi(T_1)]+s\Pi_{21}(T_1)j_x(T_1),$$

$$\dot{Q}_0=s\kappa_{22}\frac{\Delta T}{b}[1-\varphi(T_0)]+s\Pi_{21}(T_0)j_x(T_0), \tag{49}$$

where s is the area of the top and bottom faces of the AT. Substituting the expression (49) into Eq. (42), we obtain an expression for the efficiency of the AT.

The efficiency of an AT is obtained by optimization. There are two possibilities — optimization with respect to the field E_k and optimization with respect to the current flowing along the AT. Optimization with respect to the field gives

$$\eta^{\text{opt}}=\eta_k\left[1+\frac{2(1+M)}{zT_1}\right]^{-2}, \tag{50}$$

where $\eta_k=(1-T_0/T_1)$ is the efficiency of the Carnot cycle, and

$$M=\left\{\frac{[1+Z(\overline{T}+\Delta T/2)][1+Z(\overline{T}-\Delta T/2)]}{Z\Delta T}\right.$$

$$\left.\times\ln\frac{1+Z(\overline{T}+\Delta T/2)}{1+Z(T-\Delta T/2)}\right\}^{1/2},$$

$$\Delta T=T_1-T_0,\quad \overline{T}=(T_1+T_0)/2. \tag{51}$$

We note that it is impossible to optimize the efficiency if the small correction $\varphi(T)$ to the linear temperature distribution is ignored. When the efficiency of the AT is optimized with respect to current, it is necessary to substitute for M into the expression (50) the expression from Eq. (51)

$$M=\sqrt{1+Z\overline{T}}. \tag{52}$$

For large ZT the thermoelectric eddy currents (TECs) arising in the AT, in general, should substantially distort the temperatures. The product ZT is the dimensionless parameter that determines the feedback — the heat flow produces ∇T, ∇T produces TECs, the eddy currents release and absorb Joule, Peltier, and Bridgman heats, and the heats distort the temperature distribution. However, the concrete calculations examined above show that the effect of the TECs on the temperature distribution is small.[20,22] The effect of the TEC j_{curl} on $T=T(y)$ can be investigated:

$$j_{\text{curl}}=j_x-\frac{1}{b}\int_0^b j(y)dy.$$

As shown in Ref. 23, for $Z=10^{-2}$ K^{-1}, $\Delta T=1400$ K $(Z\overline{T}\gg 1)$. The efficiency of ATs equals 0.608 if the TECs are ignored and 0.641 if the TECs are taken into account, i.e., the two values are almost identical. The apparent discrepancy is explained by the fact that Bridgman heat [the last term in Eq. (43)], which is negligible for small $Z\overline{T}$, becomes substantial in the AT for $Z\overline{T}\gg 1$. It can be shown[20] that the Bridgman heat is canceled exactly by the change in the Peltier heat, due to the TECs. For this reason $\dot{Q}_1-\dot{Q}_0$ equals exactly its value in the absence of TECs. The heat $\dot{Q}_1$ itself is virtually independent of the presence of TECs, since $\varphi(T)\ll 1$. Despite the smallness of $\varphi(T)$, its value is funda-

mental — the distortion of the temperature gradient is of paramount importance in the calculation of the efficiency of ATs.

Optimization of the efficiency of converters built on the basis of artificially anisotropic thermoelements was studied in Ref. 24. However, in the case of the approach employed in the present paper (layered isotropic medium is replaced by a homogeneous but anisotropic medium) the thermoelement under study is in no way different from a standard AT. The results obtained in Ref. 24 using approximate methods to solve the nonlinear heat-conduction equation (in Ref. 22 it was solved exactly) are close to the results obtained in Refs. 20 and 22.

A generalized thermoelectric figure of merit of the material was introduced in Ref. 25. The entropy production density

$$\dot{S}=\nabla\cdot\mathbf{j}_S, \tag{53}$$

where $\mathbf{j}_S=(j/T)(\hat{\Pi}\mathbf{j}-\hat{\kappa}\nabla T)$ is the entropy flux density per unit time, was determined for an element of volume of an anisotropic material with an arbitrary angle between the heat flux $\mathbf{k}$ and the current $\mathbf{j}$.

On the one hand $\mathbf{j}_S$ is determined in terms of $\hat{\kappa}$, $\hat{\Pi}$, and $\hat{\rho}$ and, on the other, it is possible to introduce the efficiency $\Delta\eta$ of an element of volume

$$\Delta\eta=\Delta\eta_k\left(1+\frac{d\ \ln j_S}{d\ \ln T}\right) \tag{54}$$

which can be optimized.

Therefore, according to Ref. 25 (''It is possible to obtain a general expression for the maximum efficiency of a material, which is determined only by α, ρ, and κ, rather than by the geometric characteristics of the thermoelement'')

$$\Delta\eta=\frac{\Delta T}{T}-b\frac{\mathbf{j}\cdot\hat{\rho}\mathbf{j}+\nabla T\cdot\dfrac{\hat{\kappa}}{T}\nabla T}{-\boldsymbol{\tau}\cdot\hat{\Pi}\mathbf{j}+\boldsymbol{\tau}\cdot\hat{\kappa}\nabla T}, \tag{55}$$

where the unit vector $\boldsymbol{\tau}\|\nabla T$, and b is the height of the thermoelement.

It is evident immediately from Eq. (55) that this approach is possible only in the case where the current and temperature gradient are independent of one another. However, as shown in Refs. 8 and 19–23, the deviation of the temperature from a linear law is fundamental for calculating the efficiency of ATs.

1.6.. Anisotropic thermoelements in a magnetic field

In this review article we cannot investigate in any detail the efficiency and emf of ATs in a magnetic field. We present, with minimum commentary, only some references. A classification of thermogalvanomagnetic phenomena in anisotropic media is given in Refs. 26 and 27. Anisotropic thermoelements in a magnetic field were studied in Ref. 28. The figure of merit of an AT operating in both the emf generator mode and the refrigerator mode was investigated in Refs. 29–31.

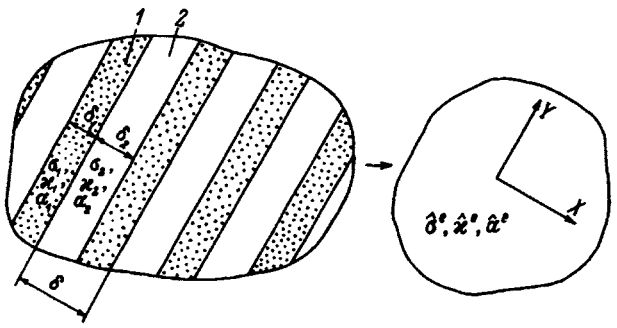

FIG. 8. Model of a layered medum. Layers with different physical properties: *1* — σ_1, κ_1, α_1; *2* — σ_2, κ_2, α_2. The equivalent average medium is indicated on the right — homogeneous, anisotropic with effective kinetic coefficients σ^e, κ^e, and α^e.

1.7.. Artificially anisotropic media

In Ref. 32 it was proposed that a layered-inhomogeneous medium consisting of alternating layers with different values of the local coefficients α, σ, and κ (Fig. 8) be used as the material for ATs. If the region under study in such a medium is much larger than the thicknesses of the layers, then such an inhomogeneous, locally isotropic medium can be described approximately, on the average, as homogeneous but anisotropic. The criterion for the applicability of this description is given in Ref. 33.

Anisotropic thermoelements based on such media are customarily called artificially anisotropic thermoelements (AATs). Such thermoelements have a number of advantages over single-crystalline ATs. The principal advantage is that their properties can be optimized by varying the materials and thicknesses of the layers. Optimization of the properties of AATs operating as emf generators and Peltier refrigerators, including in a magnetic field, is dealt with in Refs. 32 and 34–40. The large number of variable parameters made it possible to produce AATs for measuring nonstationary heat fluxes ranging from 0.1 up to 10^6 W/m^2 with a high figure of merit. However, as shown in Ref. 37, the figure of merit of AATs cannot exceed that of a longitudinal-type thermoelement composed of the components of the AAT.

The calculation of the emf and efficiency of an AAT, if its material is described in an average manner (it is assumed to be homogeneous and anisotropic), is identical to the analogous calculations for ATs based on single crystals. However, there do exist cases in which the behavior of the AAT is different from that of the AT. One such case is presented in Ref. 41, where the time constant of an AAT is studied for the example of a transverse Peltier effect. The time constant τ of a transient process (establishment of a stationary state) is of interest in connection with the fact that the power versus voltage sensitivity of an AT does not depend on the size of the element in the direction ∇T. Experiments performed with AATs based on the heterophase system $Bi_{0.5}Sb_{0.5}Tl_3$–Bi with thicknesses ranging from 2 to 10 mm confirm the theoretical results.

The transient process in an AAT includes establishment of a stationary state in an elementary two-layer packet τ_0 of thickness δ (Fig. 8) and in a thermoelement as a whole — τ.

TABLE I.

Materials	Spectral transparency range λ, μm	Thermoelectric power anisotropy $\Delta\alpha$, μV/K	Thermal conductivity $10^2\kappa$, W/cm·K	Electrical conductivity 10σ, $\Omega^{-1}\cdot$cm^{-1}	References
Bi	—	50	8.0	9×10^4	[45–47]
Bi_2Te_3	—	60	1.8	2.11×10^3	[49]
Te	3.5–20	140	2.9	40.0	[50]
$MnSi_{1.75}$	—	100	—	8.0×10^2	[51–55]
$CrSi_2$	—	45	—	6.0×10^3	[51–55]
CdS	0.5–12	130	20.0	0.2	[56,57]
$ZnAs_2$	1.3–18	350	6.0	0.5	[58,59]
CdAs	1.8–20	225	4.7	1.0	[58,59]
ZnSb	2.2–30	120	1.1	7.2	[54,58]
CdSb	2.6–30	300	1.2	4.0	[60,61]
CdSb-NiSb	—	270	2.5	2.0	[60,61]
CdSb-CoSb	—	295	2.3	2.0	[60,61]
CdSb-MnSb	—	280	2.8	1.8	[60,61]

It is obvious that for $\tau \geqslant \tau_0$ it is impossible to establish a stationary state in the entire AAT until it is established in the packet. Furthermore, the time τ increases with decreasing ratio δ/b. It was found that the time constant τ of an AAT (which is limited by τ_0) can be decreased by using composites consisting of materials with high thermal conductivity and decreasing the thickness δ of the two-layer packet.

1.7.1. Effective properties of layered media

It is virtually impossible to calculate the electrochemical potential distribution in AATs, allowing for the finiteness of the thickness of the consituent layers. Therefore, a standard method is used — the properties of the medium are averaged, after which the medium is assumed to be homogeneous. The effective kinetic coefficients give relations between the volume-averaged thermodynamic fields and fluxes. For example, for

$$\mathbf{j}=\sigma\mathbf{E}-\sigma\hat{\alpha}\nabla T$$

the effective values σ^e and α^e by definition relate $\langle\mathbf{j}\rangle$ with $\langle\mathbf{E}\rangle$ and $\langle\nabla T\rangle$, where $\langle\ \ldots\ \rangle$ is the volume average, and

$$\langle\mathbf{j}\rangle=\sigma^e\langle\mathbf{E}\rangle-\sigma^e\alpha^e\langle\nabla T\rangle. \tag{56}$$

The calculation of the effective kinetic coeffiicents assumes that the characteristic size of the inhomogeneity, in this case the thicknes δ of the packet, is much larger than the characteristic mean free path lengths. The problem of calculating the effective kinetic coeffiicents, in general, for an inhomogeneity of an arbitrary form (coordinate dependences of the local coefficients) has not been solved. However, an exact solution, suitable for an arbitrary ratio of the coefficients in different layers, is possible in the case of plane-layered media. Effective kinetic coefficients were obtained in Ref. 32 for the case where an elementary packet consists of two layers and the local coefficients are isotropic. In Ref. 33, these calculations were made on the basis of the methods of Ref. 42 for the general case of an arbitrary periodic dependence of σ and α on κ, and the term omitted in Ref. 32 was also added to the component κ^e_{zz}. The effective kinetic coefficients are

$$\begin{aligned}
&\rho^e_{xx}=\rho^e_{yy}=\frac{1}{\sigma^e_{xx}}=\frac{1}{\sigma^e_{yy}}\\
&\qquad=\frac{1}{\delta}\left(\frac{\delta_1}{\sigma_1}+\frac{\delta_2}{\sigma_2}+\frac{(\alpha_1-\alpha_2)^2\delta_1\delta_2 T}{\kappa_1\delta_1+\kappa_2\delta_2}\right),\\
&\sigma^e_{zz}=(\sigma_1\delta_1+\sigma_2\delta_2)/\delta,\\
&\alpha^e_{xx}=\alpha^e_{yy}=\frac{\alpha_1\delta_1/\kappa_1+\alpha_2\delta_2/\kappa_2}{\sigma_1\delta_1+\sigma_2\delta_2},\\
&\alpha^e_{zz}=\frac{\alpha_1\sigma_1/\delta_1+\alpha_2\sigma_2/\delta_2}{\sigma_1\delta_1+\sigma_2\delta_2},\\
&\kappa^e_{xx}=\kappa^e_{yy}=\delta/(\delta_1/\kappa_1+\delta_2/\kappa_2),\\
&k^e_{zz}=\frac{1}{\delta}\left(\kappa_1\delta_1+\kappa_2\delta_2+\frac{\sigma_1\sigma_2(\alpha_1-\alpha_2)^2\delta_1\delta_2 T}{\sigma_1\delta_1+\sigma_2\delta_2}\right).
\end{aligned} \tag{57}$$

These expressions are repeated in Ref. 43. The extension to the case of a nonzero magnetic field is given in Ref. 36 (see also Ref. 43). The general solution is given in a review article.[44].

2. EXPERIMENTAL INVESTIGATIONS

2.1. Semiconductor anisotropic thermoelements and devices

Interest in the investigation and practical application of thermoelectric phenomena in anisotropic media appeared after new semiconductor materials were synthesized. Their basic characteristics are given in Table I.

As indicated above, a thermoelectric field which is transverse with respect to the temperature gradient arises in thermoelectrically anisotropic media in a nonuniform temperature field. Correspondingly, when a current passes through such a medium, a transverse heat flux arises in it. These features made it possible to produce a thermal device of a new type called an anisotropic thermoelement (AT).

The first ATs were made of single-crystalline bismuth. The magnitude and character of the temperature dependence of the anisotropic thermoelectric power in Bi can be quite

easily controlled by doping and introducing double interlayers.[45,46] Bismuth has proven itself well in different radiation detectors and microelements. Bi–Sb alloys with a high thermoelectric figure of merit in the range 140–180 K are used in thermoelectric refrigerators operating in a transverse magnetic field.[47,48]

Single crystals such as Bi_2Te_3 and Te, which are technologically inefficient, are highly layered and ductile. This is due to instability of their thermoelectric and electric parameters. As a result, such materials are difficult to use for ATs.[49,50]

Single crystals of some silicon compounds with transition elements, for example, $MnSi_{1.75}$ and $CrSi_2$, are of interest.[51–56] The high thermoelectric power anisotropy ($\Delta\alpha \simeq 100$ μV/K at 300 K), which remains in a very wide temperature range (200–1000 K for $CrSi_2$), makes it possible to use them as high-sensitivity, low-noise anisotropic radiation detectors. These detectors possess a gigantic dynamic range and a high linearity of the output parameters. Furthermore, these compounds are promising for use as the basis for high-voltage, anisotropic, heat-to-electricity converters operating, for example, in combination with silicon solar cells.

Some single crystals of II–V semiconductors ($\Delta\alpha = 120-350$ μV/K[57–59]) possess a high thermoelectric power anisotropy at high temperatures combined with high optical transparency in the infrared range (IR). These materials are employed for optical ATs operating in optical transmission regimes and make it possible to control heat fluxes exceeding 1.0 MW/m^2.

The group of anisotropic thermoelectric and optical-thermoelectric materials based on CdSb single crystals and directionally crystallized eutectics CdSb–MeSb, where Me denotes a metal (Ni, Co, Mn), must be specially singled out.[60,61] The low anisotropic thermoelectric figure of merit of these materials makes it difficult to use them for direct conversion of heat into electricity. However, because of the weak temperature-dependence of the voltage–power sensitivity of the ATs in the range 210–310 K (the temperature coefficient is $\mu_s = 1.1\% \cdot \mathrm{K}^{-1}$ for CdSb and $\mu_s = 0.12-0.15\% \cdot \mathrm{K}^{-1}$ for CdSb–CoSb) and the high value of this sensitivity, as well as the temporal stability of the parameters[62] and large geometric size of the crystals, a number of devices and systems are serially produced. The kinetic characteristics and other parameters of ATs based on different classes of anisotropic materials can be compared using Table I.

When ATs are used as temperature or heat flux transducers, the following basic parameters are used: temperature and voltage–power sensitivity S_t and S_q, the time constant τ, the threshold sensitivity $P_{\min}$, and the detection power D.[63,64] The chief characteristic of ATs is the voltage–power sensitivity S_q. From the heat balance equation for a vacuum AT operating as a radiation sensor, we obtain[63]

$$S_q = 0.5(\alpha_\parallel \kappa_\perp - \alpha_\perp \kappa_\parallel)(\kappa_\parallel \kappa_\perp)^{-1} c^{-1}, \tag{58}$$

where c is the width of the AT. The temperature sensitivity of the AT is determined mainly by the thermoelectric power anisotropy coefficient of the material and the shape factor a/b

$$S_t = (\alpha_\parallel - \alpha_\perp) a/b. \tag{59}$$

If the Peltier effect is weak, the time constant of the AT is given by the expression[65]

$$\tau = 0.4 b^2/\xi, \tag{60}$$

where ξ is the thermal diffusivity of the AT material in the direction of heat flow.

The threshold sensitivity of the AT (the equivalent noise power) is limited only by the thermal noise

$$P_{\min} = \frac{8\kappa_\parallel \kappa_\perp (\sigma_0 \rho T a c b^{-1})^{0.5}}{(\alpha_\parallel \kappa_\perp - \alpha_\perp \kappa_\parallel)}, \tag{61}$$

where σ_0 is the Stefan–Boltzmann constant, T is the temperature of the AT, and ρ is the resistivity of the AT. Analysis of this expression shows that the equivalent noise power is determined by the geometry of the AT and the material parameters. Depending on the specific problem, the AT can be optimized with respect to one of the parameters listed above.[63,65]

Optimization of the physical properties of a highly perfect CdSb single crystal and the technology of treatment of the crystal made it possible to build and put into production a number of new optical devices and systems. For example, this material can be used to delimit the short-wavelength part of the IR region of the spectrum with a substantial transmission (98%) in the range 2.6–40 μm (Refs. 66 and 67). The high refractive index ($n = 4$) makes it possible to use this material for immersion IR filters–lenses and internal-absorption ATs.[68] Such devices reliably protect onboard and stationary apparatus of different kinds from background radiation as well as artificial and natural illuminations. An example of such an apparatus is the ''Fakel'' fire detector in a smoky atmosphere; ''Kvant,'' ''Kvant-RT,'' and RPI pyrometers; and sensors for prevention of explosions in coal mines and for other objects. The construction and fabrication technology of a unified thermoelectric module and AT piles have been developed (the characteristics of anisotropic thermoelectric modules are presented in Table II).

The characteristic features of anisotropic thermoelements — the presence of one branch, the heat flow is perpendicular to the electric field, the voltage–power sensitivity is independent of the geometric size in the direction of heat flow combined with optical transparency and possibility of producing a device with a short time constant — have opened up prospects for wide applications of such elements.

One of the first devices developed is a device for measuring the effective values of high-frequency currents and voltages (measurement range 1–500 mA with a nominal emf of the AT of 20–60 mV).[69,70] The transducer consisted of two ATs, connected electrically in series, together with an electrically insulated ohmic heater with a definite resistance between them. Different working faces of the ATs were equipped with radiators.

The weak temperature-dependence of AT-based modules made it possible to use them in systems for rapid,

TABLE II.

Type	Area of working faces, cm^2	Power-voltage sensitivity S_q, V/W	Internal resistance R, kΩ	Time constant τ, s
ATÉM	0.2×0.2	0.46	0.2	0.5
ATÉM	0.5×0.6	0.54	4.3	1.1
ATÉM	0.7×0.7	0.63	7.0	1.2
ATÉM	1.0×1.0	0.06	0.09	1.6
ATÉM	1.0×0.3	0.52	8.2	0.6
ATÉM	1.2×1.0	0.27	16.0	2.4
ATÉM	1.5×1.5	0.72	27.0	1.3

contact-free monitoring of the parameters of semiconductor transistors, integrated circuits, Peltier microrefrigerators, and other devices. The modules in such systems are used as nonselective radiation detectors (sensitivity~0.56 V/W and the time constant is of the order of 0.4 s). They are made of an optimized CdSb–NiSb eutectic. The setup makes it possible to monitor the parameters of the devices being checked in the controlled heat load regime in the temperature range 200–360 K within 0.1 K and to measure in a wide current interval the dynamical characteristics of the refrigeration and heating capacity.[71]

Anisotropic thermoelements are used in devices for measuring millimeter and submillimeter microwave power. The main part of a device is the absolute measuring transducer, which consists of a waveguide and a CdSb–CoSb AT. A thin-film heater is deposited under an absorbing layer on its top face. This makes it possible to determine the average microwave power by the substitution method. The minimum detectable power is 1 μW, the meaurement limits are 0.05–10 mW, the error equals 5%, and the time constant equals 0.6 s.[72] Through-type AT-based detectors have been made by the transparent-wall method. Such detectors make it possible to detect radiant fluxes of average and high power.[73,74]

Coordinate-sensitive, anisotropic, nonselective radiation detectors have been developed. They are used in the range 0.2–40 μm. They locate the coordinates of radiation focused in a spot in a 0.05–0.1 mm^2 region to within 20% on a receiving area of 1–1000 mm^2. Other detectors of an analogous type with a detecting area of 30×30 cm^2 and a resolution of 1×1 cm^2, $S_q=0.06$ V/W, $\tau=1.6$ s, and threshold power 1.5 W/cm^2 have also been developed.[75]

A heat-flux comparator for performing measurements in a wide temperature range has been developed on the basis of a CdSb AT module.[76] Depending on the purpose of the comparator, consisting of 8–20 ATs with a detecting area of 10^{-4}–10^{-3} mm^2 and a coating with a prescribed spectral characteristic, the construction of the transducer makes it possible to perform measurements by both contact and contact-free methods.

A series of devices for measuring heat fluxes of up to 40 kW/m^2 has been developed using CdSb ATs and artificially anisotropic thermoelements (the working coefficient is of the order of 100 $W/cm^2 \cdot mV$ and the time constant equals 0.1–3.0 s).[77] The devices are temperature controlled with thermoelectric Peltier modules. They possess several measurement limits and can operate both from a grid and autonomously. Heat meters operating in the optical transmission regime are especially efficient.

Meters for measuring the intensity of ultrasound in liquid organic media,[78] power in lasers,[18] and density of incoherent radiation from light-emitting diodes ($S_q=0.15$ V/W, detection area 1.4×1.4 cm^2, $\tau=2$ s), have been developed. The compensating radiator is a STV-1 incandescent lamp, whose current depends linearly on the temperature being measured (the pyrometer is especially effective at room temperatures).

In the dynamic operating regime, AT-based devices make it possible to detect thermal processes with a duration of the order of 1.0–0.01 ms.[79] The power substitution method is used in the microwave power meter in order to eliminate any effect due to the surrounding medium.[80] A constant current is passed through a standard heater placed on the top working face ($S_q=0.24$ V/W, $\tau=0.2$ s).

Calvet microcalorimeters, which employ an AT in the form of a spiral, possess a high threshold sensitivity 1.0–0.1 μW with a time constant three to four orders of magnitude lower than in the thermocouple analogs.[81] The temperature range of the measurements of a differential anisotropic microcalorimeter is 280–380 K.

2.2. Anisotropic thermoelements based on single-crystalline high-T_c superconductor films

In 1988, it was discovered that single-crystal high-T_c superconductor films in a normal state generate an anomalously high thermoelectric signal when irradiated with an IR laser. Such films are promising materials for primary transducers of measuring instruments employing thermoelectric power anisotropy. There is an extensive literature on the anisotropy of their physical properties. We present some references with no pretensions about being complete.

Most experimental data on thermoelectric power have been obtained on $YBa_2Cu_3O_{7-x}$ single crystals (YBCO).[82–85] The properties of the samples are usually measured in the ab plane, since they differ little in the a and b directions and along the c axis. Comparative investigations of the thermoelectric power in ceramic, epitaxial films, and single crystals have established a good correspondence between data for single crystals and films in the ab plane and data for ceramics.[86,87] The maximum values of the thermoelectric power are of the order of 70 μV/K in the ab plane and 10 μV/K along the c axis.[88,89] In compounds of other high-T_c superconductors, for example, $(La_{1-x}Sr_x)_2CuO_4$

(Refs. 89 and 90), $Bi_2Sr_2CaCu_2O_8$ (Refs. 91 and 92), and $EuBa_2Cu_3O_7$ (Ref. 93), a similar behavior of the thermoelectric power tensor components α_{ab} and α_c, differing mainly in the magnitude of the coefficient, is observed.

The greatest amount of data on the anisotropy of the resistivity is available for high-T_c superconductors of the type $MBa_2Cu_3O_{7-x}$, where M is ytterbium or different lanthanides.[94–98] Data on other compounds can be found in other works: $Bi_2Sr_{2.2}Ca_{0.8}Cu_2O_3$ (Refs. 99–101) and $La_{2-x}Sr_xCuO_4$ (Refs.102–104). We note that the thermoelectric power anisotropy in these materials is much weaker than the resistivity anisotropy ($\alpha_c/\alpha_{ab} \simeq 3-6$, $\rho_c/\rho_{ab} \simeq 30-50$).

The thermal conductivity of polycrystalline samples with the composition $RBa_2Cu_3O_x$, where R=Y, Eu, Gd, Dy, Er, Sm, and Ho (the so-called 123 system) has been studied extensively.[105–109] Another class of materials are samples of the type $La_{2-x}Sr_xCuO_4$ (214 system).[106,110,111] The thermal conductivity anisotropy of these materials has received less attention.[92,112]

The investigation of the responses of single crystal high-T_c superconductor samples for thermal and electromagnetic effects started immediately after these materials were synthesized.[113] The results obtained on single-crystal YBCO films with *c* axis inclined with respect to the surface at room temperatures are especially interesting. When such films are irradiated with IR laser radiation (in the cw or pulsed modes), gigantic voltaic signals are generated [according to some data, up to 100 V (Ref. 114)]. The mechanism leading to such a response is still being discussed by different groups of investigators. Analysis of the published data[115–121] shows that the dominant mechanism is anisotropy of the thermoelectric properties of these materials. Arguments in favor of this assertion are presented below.

In one of the first investigations, the transverse voltage under laser irradiation of YBCO films, both with and without a transport current, was measured.[116] Films ranging in thickness from 0.1 to 1.5 μm were irradiated with 10–20 ns pulses with wavelengths of 355, 532, and 1064 nm. The laser radiation energy density was equal to 10–300 J/m^2. $SrTiO_3$, Al_2O_3, and MgO wafers were used as substrates. The measured transverse voltage reached 0.2 mV (when a transport current is present, this voltage is approximately 30% lower). The amplitude of the laser pulse dropped practically to zero over 50 ns, while the measured signal dropped to 30% of its maximum value over 200 ns and then dropped more slowly. The signal changed very little when the contacts were screened from irradiation and dropped by 95% when only the region of each contact was irradiated. As the beam was scanned along the sample between the contacts, the signal exhibited a wide maximum. The polarity of the signal changed when the contacts were interchanged.

Similar results were obtained in Ref. 122. It was also established there that the polarity of the signal changes when the backside of the film is irradiated. This behavior clearly indicates that the signal depends on the temperature gradient in the film. In Ref. 123 these data are explained by a photoeffect with a tensorial photoconductivity. However, even in a medium with tensorial properties, the photoresponse should not change sign when the direction of irradiation is reversed. This change in polarity indicates that the signal depends on the temperature gradient in the film. The response does not depend on the polarization of the laser beam and exhibits a strong temperature-dependence, characterized by the presence of two temperature thresholds. The laser-induced voltage arises not only in the pulsed regime but also in the case of irradiation in the cw regime. A signal is present in the orthorhombic phase of YBCO and is absent in the tetragonal phase. Crystals with *c* axis making different angles with the substrate were investigated. Electrodes for measuring the voltage were placed along a circle every 22.5°. The signal was strongest when the line connecting the electrodes made an angle of 45° with the *c* axis (or coincided with the projection of this axis onto the surface of the film).

These results have been reproduced in many samples. In experiments where the *c* axis of the films was perpendicular to the MgO or $SrTO_3$ substrates, the signal strength depended strongly on the disorientation of the *c* axis (in the range of angles 1–3°). For example, films with an inclination of 1.0° gave 20 times stronger signals than films with an inclination of 0.3°. Films with a zero disorientation gave a negligible signal. Stable signals were also obtained with continuous irradiation of the film by a 20-mW He–Ne laser.[117] In the experiments, they reached a magnitude of 1 mW. Since the signal does not depend on the polarization of the laser beam, the tensorial photoeffect mechanism (occurring in the case of the piezoelectricity) cannot be used to describe the phenomenon. We note that under conditions of weak thermal actions and strong conductive coupling between the film and the substrate, the polarity of the signal can change. Other experimental results confirm the thermoelectrically anisotropic nature of the effect at temperatures above 240 K. Furthermore, the values obtained for the signals are much higher than the expected photoresponse (the authors even called the phenomenon an anomalous photoeffect). The dependence of the signal magnitude on the density of the energy incident on the film is confirmed by all known studies where such measurements were performed. This undoubtedly also confirms the thermoelectric nature of the phenomenon.

The photoresponse of a 0.5 μm thick $Bi_2Sr_2CaCu_2O_8$ film, carrying a current ranging from 2 to 200 mA, irradiated with IR laser pulses ($\lambda = 447$ μm, pulse repetition frequency 165 Hz, average pulse duration at half-height 65 ns) was investigated in Ref. 98. It was observed that the responses are nonbolometric (i.e., the film resistance did not change near the signal maximum). These data attest to a weak temperature dependence of the thermoelectric power.[124,88]

The nonbolometric nature of the responses was confirmed in Ref. 125. The maximum signal reached 2 V with beam energy density 30 mJ/cm^2. The magnitude of the signal was proportional to the irradiation energy but not the energy density. This stems from the fact that the signal remained constant when the region of illumination with the laser beam on the film between the contacts changed. An influence due to the Seebeck effect and the off-diagonal components of the thermoelectric power tensor was rejected on the basis of the symmetry of the YBCO structure (i.e., the

presence of thermoelectric power anisotropy was rejected). The signal was found to depend on the angle between the laser beam and the film. When the angle between the normal to the film and the beam changed from $-55°$ to $+55°$, the signal decreased linearly (from 110 to 55 mV), i.e., it changed antisymmetrically. It was also asserted that the generated signal does not depend on the wavelength and polarization of the radiation. In our opinion, it is incorrect to draw conclusions about the macroscopic kinetic coefficients of real high-T_c superconductor films on the basis of the symmetry properties of an ideal lattice. The experimental data presented in the paper mainly are in agreement with the mechanism due to the anisotropy of thermoelectricity. In order to describe some specific experiments on the basis of the indicated mechanism, it is necessary to construct a special mathematical model allowing for the concrete conditions of heat transfer between the film and the surrounding medium and the location of the electric contacts on the film.

The dependence of the response on the irradiation frequency on 16 laser lines with frequencies ranging from 10 to 1000 μm was investigated in Ref. 118. It was established that the sensitivity of the signal decays strongly with increasing frequency ($\sim\omega^{-2.3}$). A current ranging from 2 to 40 μA was passed through single-phase c-oriented films. The duration of the response was less than 4 ns and its maximum was proportional to the bias current passed through the sample. The authors believe that the mechanisms of electronic heating and the regions of heating proposed for very thin films (thickness less than 100 nm) are unsuitable for describing granular films exceeding 200 nm in thickness.

A thin (0.3 μm) $Bi_2Sr_2CaCu_2O_8$ film was investigated in Ref. 127. Laser pulses with a sharp leading edge with a duration of about 5 ms in the wavelength range from 80 to 200 μm were employed. A rapid response and a slow bolometric component were recorded. The energy density in the laser pulses irradiating the sample fell into the range 2–24 kW/cm^2. Only rapid responses with a time constant of the order of 1 ns were observed above a critical wavelength of 100 μm.

The preparation and investigation of 500-nm-thick and 10×10-mm^2 films with a small angle between the c axis and the normal to the substrate are described in Ref. 119. The films were investigated at room temperature. A signal appeared in the films heated with 100-ns laser pulses ($\lambda=1.06$ μm) with an energy of 1–10 mJ per pulse. The central region of the film was irradiated with a beam with a 2 mm in diameter region of illumination and energy density 10 mJ/cm^2. Under direct irradiation the signal from contacts separated by 6 mm was equal to about 1 V with a temperature difference of 50–100 K between the surface of the film and the substrate. The behavior of the signal in time corresponded to decay of the temperature gradient as a result of heat conduction. These experiments were compared with the results of numerical simulation (the modified Schmidt method was used[127]). When the backside of the film was irradiated (through the substrate), the sign of the signal was different from the case of direct irradiation of the film, but after termination of the heating the polarity of the signal changed once again. These data were attributed to the normalization of the temperature gradient with respect to the surface of the film. When the heat flux from the film to the substrate is higher than the flux from the free surface of the film into the surrounding air, the direction of the temperature gradient in the freely cooled film can change. The maximum signal was obtained when the spot was located between the contacts. The sign of the signal changed when the spot was moved beyond the limits of the contacts. When the film was rotated relative to the axis passing through its center, the signal maximum dropped sinusoidally. A model according to which the laser beam produces a dipole heat source in the film was proposed. The authors note that the recorded signal was several orders of magnitude stronger than expected in the ordinary Seebeck effect, and a model of ''atomic thermocouples'' was proposed. The essence of the model lies in the fact that the CuO_2 layers and the lower-conductivity layers separating them are treated as a thermopile. As a result of the fact that the signals from separate thermocouples are summed, the ratio of the diameter a of the region of illumination to the thickness b of the film appears in the expression for the thermoelectric power. The number of thermocouples is also related with the angle between the c axis and the substrate (see also Ref. 128). Thus the following expression was obtained:

$$U=(a/b)\Delta T(\alpha_{ab}-\alpha_c)\sin\theta. \tag{62}$$

Using the data from Ref. 84 on the Seebeck coefficient parallel and perpendicular to the c axis (15 and 5 μV/K, respectively) and the values $a=2$ mm, $\theta=10°$, and $\Delta T=100$ K, a thermoelectric power of the same order of magnitude as in the experiment was obtained: $U=0.7$ V. Furthermore, a correlation was found between the quality of the films and the magnitude of the thermoelectric signal. Granular films did not exhibit a thermoelectric response. The strongest signals were obtained from smooth films with a mirror surface.

The following objections can be made concerning the mechanism described by the formula presented above. Indeed, the formula predicts that the effect will be maximum at $\theta=90°$, while experimentally the strongest effect was recorded at $\theta=45°$.[117] Furthermore, when the laser spot is scanned in the region between the contacts, the number of ''atomic'' thermocouples does not change and therefore the signal magnitude should not change, which is at variance with the experimental data obtained by the authors.

Additional detailed investigations were performed in Ref. 120 for the purpose of clarifying the discrepancies between the results obtained by different experimental groups. Films with a different angle between the c axis and the substrate surface were studied. It was found that the signal strength depends on the angle between the line connecting the contacts and the projection of the c axis onto the film surface. The experimental samples consisted of 2-mm-long and 20 to1000-μm-wide bridges. A beam from a cw ion (As) laser illuminated, through a rectangular spectral filter, the entire width of the bridge. It was determined that the signal does not depend on the width of the bridge but is proportional to the length of the bridge. The result of Ref. 119 that the signal is generated along the c axis only was confirmed. For small angles of incilnation from the c axis the signal is

proportional to the angle θ. The increase in temperature was very small (2.2 mK) in the case where a laser with a low radiation density (1.4 W/cm^2) was used. Hence it was concluded that the use of pulsed lasers, which give an enormous temperature increase, only complicates the interpretation of the measurements. The signal strength remained virtually unchanged when the region between the electrodes was scanned (in contrast to Ref. 103 , where a peak was observed at the midpoint). This fact was attributed to large pulsed heat loads (greater than ΔT).

Different temperature dependences of the signal were observed in experiments with different films for films grown on substrates with different orientations of the crystallographic axes ($SrTiO_3$,[110] $SrTiO_3$,[100] and $SrTiO_3$[103]). Even for the same film, different measurements gave different results when a different pair of contacts was chosen (i.e., when the direction of the line connecting the contacts relative to the c axis was changed). The temperature dependence $R(T)$ remained unchanged. The mechanism producing the signal was attributed to the recently observed, long-period, time-dependent changes in the superconductivity.[129] More accurately, it is postulated that the changes indicated include oxygen-ordered charge transfer, which influences the thermoelectric power.

The last study virtually confirms the results of the preceding study and is consistent with the thermoelectric-anisotropy mechanism. The discrepancies are essentially due to the specific experimental conditions.

Analysis of the studies described above shows that the determining mechanism of the gigantic response of high-T_c superconductor films to thermal and electromagnetic perturbations is anisotropy of their thermoelectric properties.

The questions considered in this review were discussed, at different times, with P. I. Baranskiĭ, A. B. Belikov, L. P. Bulat, O. S. Gorya, T. S. Gudkin, V. I. Kaĭdanov, S. L. Korolyuk, G. N. Logvinov, V. M. Pan, I. M. Pilat, I. M. Rarenko, and E. E. Fiskind. We are deeply grateful to them all. We wish to acknowledge separately the contribution made by V. M. Slipchenko during his short life to the theory of anisotropic thermocouples.

[1)]The possibility of using such boundary conditions was pointed by A. D. Myshkis.

[1] A. G. Samoĭlovich and L. L. Korenblit, Usp. Fiz. Nauk **49**, 243 (1953).
[2] L. D. Landau and E. M. Lifshitz, *Electrodynamics of Continuous Media*, Pergamon Press, N. Y. [Russian original, Nauka, Moscow, 1989].
[3] W. Thomson, Math. Phys. Pap. **1**, 266 (1882).
[4] C. Herring, Phys. Rev. **59**, 889 (1941).
[5] A. G. Samoilovich and L. L. Korenblit, Patent UK N 1088764, October 25, 1964.
[6] S. L. Kopolyuk, I. M. Pilat, A. G. Samoĭlovich, V. I. Slipchenko, A. A. Snarskiĭ, and E. V. Tsar'kov, Fiz. Tekh. Poluprovodn. **7**, 725 (1973) [Sov. Phys. Semicond. **7**, 502 (1973)].
[7] A. G. Samoĭlovich in *Problems in Modern Physics* [in Russian], Nauka, Leningrad, 1980, p. 304.
[8] A. G. Samoĭlovich and A. A. Snarskiĭ, Fiz. Tekh. Poluprovodn. **13**, 1539 (1979) [Sov. Phys. Semicond. **13**, 1539 (1979)].
[9] A. A. Snarskiĭ, Fiz. Tekh. Poluprovodn. **11**, 2053 (1977) [Sov. Phys. Semicond. **11**, 1207 (1977)].
[10] A. G. Samoĭlovich and V. N. Slipchenko, Fiz. Tekh. Poluprovodn. **9**, 594 (1975) [Sov. Phys. Semicond. **9**, 397 (1975)].
[11] V. N. Slipchenko and A. A. Snarskiĭ, Fiz. Tekh. Poluprovodn. **8**, 2010 (1974) [Sov. Phys. Semicond. **8**, 1305 (1974)].
[12] I. M. Pilat, A. B. Belikov, L. L. Kazanskaya, and A. A. Ashcheulov, Fiz. Tekh. Poluprovodn. **10,** 1019 (1976) [Sov. Phys. Semicond. **10**, 604 (1976)].
[13] O. Ya. Luste and A. G. Samoĭlovich, Fiz. Tekh. Poluprovodn. **11**, 209 (1977) [Sov. Phys. Semicond. **11**, 121 (1977).
[14] A. A. Snarskiĭ and S. S. Trofimov, Fiz. Tekh. Poluprovodn. **17**, 953 (1983) [Sov. Phys. Semicond. **17**, 600 (1983)].
[15] A. A. Snarskiĭ, Fiz. Tekh. Poluprovodn. **12**, 815 (1978) [Sov. Phys. Semicond. **12**, 479 (1978)].
[16] L. I. Anatychuk, *Thermoelements and Thermoelectric Devices* [in Russian], Naukova. Dumka, Kiev, 1970.
[17] A. A. Snarskiĭ, Fiz. Tekh. Poluprovodn. **14**, 170 (1980) [Sov. Phys. Semicond. **14**, 99 (1980)].
[18] A. A. Ashcheulov, A. B. Belikov, and A. I. Rarenko, Ukr. Fiz. Zh. **8**, 825 (1993).
[19] A. G. Samoĭlovich and V. N. Slipchenko, Fiz. Tekh. Poluprovodn. **7**, 725 (1973) [Sov. Phys. Semicond. **7**, 502 (1973)].
[20] V. N. Slipchenko, Ukr. Fiz. Zh. **21**, 126 (1976).
[21] A. G. Samoĭlovich and V. N. Slipchenko, Fiz. Tekh. Poluprovodn. **15**, 427 (1981) [Sov. Phys. Semicond. **15**, 247 (1981)].
[22] A. G. Samoĭlovich and V. N. Slipchenko, Fiz. Tekh. Poluprovodn. **15**, 968 (1981) [Sov. Phys. Semicond. **15**, 554 (1981)].
[23] A. G. Samoĭlovich and V. I. Shevuk, Fiz. Tekh. Poluprovodn. **16**, 1951 (1982) [Sov. Phys. Semicond. **16**, 1260 (1982)].
[24] O. S. Gorya and E. F. Lupashko, Zh. Tekh. Fiz. **50**, 2602 (1980) [Sov. Phys. Tech. Phys. **25**, 1525 (1980)].
[25] O. S. Gryaznov, B. Ya. Moĭzhes, and V. A. Nemchinskiĭ, Zh. Tekh. Fiz. **48**, 1720 (1978) [Zh. Tekh. Fiz. **23**, 975 (1978)].
[26] P. I. Baranskii, I. S. Buda, I. V. Dakhovskii, and A. G. Samoilovich, Phys. Status Solidi B **67**, 201 (1975).
[27] P. I. Baranskii, I. S. Buda, and V. V. Savyak, Phys. Status Solidi B **112**, 111 (1989).
[28] A. G. Samoĭlovich and V. N. Slipchenko, Fiz. Tekh. Poluprovodn. **9**, 1897 (1975) [Sov. Phys. Semicond. **9**, 1249 (1975)].
[29] A. G. Samoĭlovich and V. N. Slipchenko, Fiz. Tekh. Poluprovodn. **15**, 965 (1981) [Sov. Phys. Semicond. **15**, 724 (1981)].
[30] E. F. Lupashko, Fiz. Tekh. Poluprovodn. **15**, 724 (1981) [Sov. Phys. Semicond. **15**, 411 (1981)].
[31] A. G. Samoĭlovich and V. N. Slipchenko, Fiz. Tekh. Poluprovodn. **16**, 736 (1982) [Sov. Phys. Semicond. **16**, 474 (1982)].
[32] V. P. Babin, T. S. Gudkin, Z. M. Dashevxkiĭ, L. D. Dudkin, E. K. Iordanishvili, V. I. Kaĭdanov, N. V. Kololmoets, O. M. Narva, and L. S. Stil'bans, Fiz. Tekh. Poluprovodn. **8**, 748 (1974) [Sov. Phys. Semicond. **8**, 478 (1974)].
[33] E. D. Belotskiĭ, A. A. Snarskiĭ, and S. S. Trofimov, Ukr. Fiz. Zh. **27**, 91 (1974).
[34] T. S. Gudkin, E. K. Iordanishvili, and E. É. Fiskind, Fiz. Tekh. Poluprovodn. **11**, 1790 (1977) [Sov. Phys. Semicond. **11**, 1048 (1977)].
[35] T. S. Gudkin, E. K. Iordanishvili, and E. É. Fiskind, Pis'ma Zh. Tekh. Fiz. **4**, 607 (1978) [Sov. Tech. Phys. Lett. **4**, 244 (1978)].
[36] T. S. Gudkin, E. K. Iordanishvili, V. A. Kudinov, and E. É. Fiskind, Fiz. Tekh. Poluprovodn. **16**, 1620 (1982) [Sov. Phys. Semicond. **16**, 1034 (1982)].
[37] T. S. Gudkin and E. É. Fiskind, Fiz. Tekh. Poluprovodn. **18**, 234 (1984) [Sov. Phys. Semicond. **18**, 145 (1984)].
[38] L. I. Bytenskiĭ, T. S. Gudkin, E. K. Iordanishvili, and E. É. Fiskind, Fiz. Tekh. Poluprovodn. **12**, 538 (1978) [Sov. Phys. Semicond. **12**, 310 (1978)].
[39] O. A. Gerashchenko, E. K. Iordanishvili, T. S. Gudkin, E. F. Fiskind, and Zh. L. Pogurskaya, Inzh. Fiz. Zh. **35**, 229 (1978).
[40] O. S. Gorya and E. F. Lupashko, Fiz. Tekh. Poluprovodn. **13**, 340 (1979) [Sov. Phys. Semicond. **13**, 196 (1979)].
[41] T. S. Gudkin nad E. É. Fiskind, Pis'ma Zh. Tekh. Fiz. **4**, 844 (1978) [Sov. Tech. Phys. Lett. **4**, 340 (1978)].
[42] V. A. Kudinov and B. Ya. Moĭzhes, Tekh. Fiz. **42**, 591 (1972) [Sov. Phys. Tech. Phys. **17**, 467 (1972)].
[43] B. Ya. Balagurov, Fiz. Tverd. Tela (Leningrad) **28**, 2068 (1986) [Sov. Phys. Solid State **28**, 1156 (1986)].
[44] A. A. Snarskiĭ and P. M. Tomchuk, Ukr. Fiz. Zh. **32**, 66 (1987).
[45] W. Lukosz, Z. Naturforsch. **19**, 1599 (1964).
[46] G. A. Ivanov and V. M. Grabov, Fiz. Tekh. Poluprovodn. **29**, 1040 (1995) [Semiconductors **29**, 538 (1995)].

[47] A. R. Regel', G. A. Ivanov, V. M. Grabov, L. I. Anatychuk, and O. Ya. Luste, Inventor's Certificate N 245859 (1969).
[48] V. M. Grabov and A. F. Panarin in *Abstracts of Reports at the 4th International Seminar on Materials for Thermoelectric Transducers* [in Russian], St. Petersburg, 1995, p. 66.
[49] B. M. Gol'tsman, V. A. Kudinov, and I. A. Smirnov, *Semiconductor Thermoelectric Materials Based on Bi_2Te_3* [in Russian], Nauka, Moscow, 1972.
[50] E. O. Movchan, *Tellurium* [in Russian], Tekhnika, Kiev, 1967.
[51] B. K. Voronov, L. D. Dudkin, and N. N. Trusov, Kristallografiya **12**, 519 (1967) [Sov. Phys. Crystallogr. **12**, 448 (1967)].
[52] V. I. Kaĭdanov, V. A. Tselishchev, A. P. Usov, L. D. Dudkin, B. K. Voronov, and N. N. Trusov, Fiz. Tekh. Poluprovodn. **4**, 1338 (1970) [Sov. Phys. Semicond. **4**, 1135 (1970)].
[53] V. K. Zaitsev, *Thermoelectric Properties of Anisotropic MNSI. CRC Handbook of Thermoelectrics*, N. Y., 1995, p. 299.
[54] A. T. Burkov, A. Heinrich, and M. V. Vedernikov in *Proceedings 13th International Conference on Thermoelectrics*, N. Y., 1995, p. 76–80.
[55] S. V. Ordin in *Proceedings 14th International Conference on Thermoelectrics*, June 27–30, 1995, St. Petersburg, Russia, p. 212.
[56] A. A. Ashcheulov, OMP **12**, 47 (1989).
[57] P. I. Baranskiĭ, V. P. Klochkov, and I. V. Potykevich, *Handbook of Semiconductor Electronics* [in Russian], Naukova Dumka, Kiev, 1971.
[58] V. B. Lazarev, V. Ya. Shevchenko, Ya. L. Grinberg, and V. V. Sobolev, *II–V Semiconductor Compounds* [in Russian], Nauka, Moscow, 1978.
[59] S. F. Marenkin, A. M. Raukhman, D. I. Pishchikov, and V. B. Lazarev, Neorg. Mater. **28**, 1813 (1992).
[60] A. A. Ashcheulov, N. K. Voronka, S. M. Kulikovskaya, and S. F. Marenkin, Izv. Akad. Nauk SSSR, Neorg. Mater. **25**, 1614 (1989).
[61] A. A. Ashcheulov, V. A. Grebenshchikov, V. A. Belotskiĭ, and S. M. Kulikovskaya, Izv. Akad. Nauk SSSR, UKhZh. **57**, 597 (1991).
[62] A. A. Ashcheulov, A. F. Semizorov, and I. M. Rarenko in *Thermal Radiation Detectors* [in Russian], GOI, Leningrad, 1980, p. 74.
[63] I. M. Pilat, V. S. Vetoshnikov, and O. A. Gorbatyuk in *Abstracts of Reports at the All-Union Conference on Thermoelectric Materials and Methods for Investigating Them* [in Russian], Kishinev, 1971, p. 123.
[64] L. I. Antychuk, V. T. Dmitrashchuk, O. Ya. Luste, and Yu. S. Tsyganok, Izv. Vyssh. Uchebn. Zaved. Fiz. **6**, 149 (1971).
[65] L. I. Anatychuk, L. I. Bogomolov, O. I. Kupchinksiĭ, and O. Ya. Luste, OMP **1**, 27 (1971).
[66] I. M. Rarenko, P. A. Bogomolov, and A. N. Borets, OMP **10**, 64 (1972).
[67] A. A. Ashcheulov, V. M. Kondratenko, and I. M. Rarenko, *Thermoelements* [in Russian], Voronezh State University, Voronezh, 1987, p. 94.
[68] A. A. Ashcheulov, N. V. Karpan, and I. M. Rarenko, Izv. Vyssh. Uchebn. Zaved., Élektromekh. **12**, 1336 (1980).
[69] I. M. Pilat, A. A. Ashcheulov, A. B. Belikov, K. D. Soliĭchuk, V. S. Vetoshnikov, É. A. Osipov, and N. I. Trishin, *Thermoelements. Prospectus of the Exposition of Achievements of the National Economy of the Soviet Union* [in Russian], Chernovtsy, 1975.
[70] I. M. Pilat, K. D. Soliĭchuk, B. G. Shabashkevich, V. S. Vetoshnikov, A. M. Skubak, and V. I. Deba in *Thermal Radiation Detectors* [in Russian], GOI, Leningrad, 1982, p. 65.
[71] A. A. Ashcheulov, N. N. Glemba, and L. I. Prostebi, Izv. Vyssh. Uchebn. Zaved., Élektromekh. **12**, 1333 (1980).
[72] V. Ya. Shevchenko, S. F. Marenkin, and A. A. Ashcheulov, *Materials Science of II–V Semiconductors Materials* [in Russian], Prospectus of the Exposition of Achievements of the National Economy of the Soviet Union, Moscow, 1975, p. 12.
[73] A. A. Ashcheulov, V. M. Kondratenko, N. K. Voronka, and I. M. Rarenko in *Direct Methods of Energy Conversion* [in Russian], Ashkhabad, 1986, p. 210.
[74] A. A. Ashchulov, I. M. Gutsul, and I. M. Rarenko, Ukr. Fiz. Zh. **38**, 923 (1993).
[75] A. A. Ashcheulov and S. F. Marenkin in *Abstracts of Reports at the 7th All-Union Conference on Materials Science of II-V Semiconductor Compounds* [in Russian], Chernovtsy, 1990, p. 111.
[76] I. M. Pilat, V. S. Vetoshnikov, and M. E. Belov in *Abstracts of Reports on Materials Science of II-V Semiconductor Compounds* [in Russian], Dushanbe, 1982, p. 124.
[77] I. M. Pilat, V. S. Vetoshnikov, and M. E. Belov in *Abstracts of Reports on Materials Science of II–V Semiconductor Compounds* [in Russian], Dushanbe, 1982, p. 125.
[78] A. G. Samoĭlovich, I. M. Pilat, V. S. Vetoshnikov, I. G. Mikhaĭlov, V. A. Shutilov, and V. G. Krivtsov, Inventor's Certificate N 259503 (1969).
[79] S. I. Pirozhenko, V. N. Slipchenko, amd B. G. Shabashkevich in *Abstracts of Reports on Materials Science of II-V Semiconductor Compounds* [in Russian], Kamenets-Podol'sk, 1984, p. 92.
[80] V. I. Trifonov, V. A. Stukan, V. B. Lazarev, V. Ya. Shevchenko, and S. F. Marenkin, Élektron. Tekh., No. 1, 119 (1977).
[81] Yu. F. Red'ko, *Author's Abstract of Candidate's Dissertation*, Chernovtsy, 1981.
[82] Z. Z. Wong and N. P. Ong, Phys. Rev. B **38**, 7160 (1988).
[83] Li Lu, Europhys. Lett. **7**, 555 (1988).
[84] M. F. Crommie, A. Zettl, T. W. Barbee, and M. L. Cohen, Phys. Rev. B **37**, 9734 (1988).
[85] K. A. Geĭm and S. V. Dubonos, SFKhT **2**, 7 (1989).
[86] V. É. Gosuyants, S. A. Kaz'min, V. I. Kaĭdanov, and V. A. Tselishchev SFKhT **6**, 1836 (1993).
[87] P. P. Konstantinov, V. N. Vasil'ev, A. T. Burkov, and V. B. Glushkova, SFKhT **4**, 295 (1991).
[88] J. L. Cohn, E. F. Skelton, S. A. Wolf, J. Z. Liu, and R. N. Shelton, Phys. Rev. B **45**, 13140 (1992).
[89] M. Sera, S. Shamoto, and M. Sato, Solid State Commun. **68**, 649 (1988).
[90] R. C. Yu, N. J. Naughton, and X. Yan, Phys. Rev. B **37**, 7962 (1988).
[91] I. M. Tsidil'kovskiĭ, V. L. Konstantinov, K. R. Krylov, A. I. Ponomarev, M. B. Kosmyna, A. B. Levin, and T. B. Chirikova, SFKhT **2**, 45 (1989).
[92] M. F. Crommie, A. Y. Liu, L. Marvin, M. L. Cohen, and A. Zettl, Phys. Rev. B **41**, 2526 (1990).
[93] V. F. Kraĭdenov and E. S. Itskevich, Fiz. Nizk. Temp. **18**, 1187 (1992) [Sov. J. Low Temp. Phys. **18**, 829 (1992)].
[94] P. G. Huggard, Gi. Schneider, T. O'Brien, P. Lemoine, and W. Blau, Appl. Phys. Lett. **58**, 2549 (1991).
[95] S. W. Tozer, A. W. Kleinsasser, and D. Penney, Phys. Rev. Lett. **59**, 1768 (1987).
[96] T. Penney, S. von Molnar, D. Kaiser, F. Holtzberg, and A. W. Kliensasser, Phys. Rev. B **38**, 2918 (1988).
[97] *Physical Properties of High-Temperature Superconductors* [Russian translation], Mir, Moscow, 1990.
[98] H. L. Stormer, A. F. J. Levi, K. W. Baldwin, M. Anzlowar, and G. S. Beebinger, Phys. Rev. B **38**, 2472 (1988).
[99] S. Martin, A. T. Fiory, R. M. Fleming, L. F. Schneemeyer, and I. V. Wasczak, Phys. Rev. Lett. **60**, 2194 (1988).
[100] V. L. Arbuzov, O. M. Bakunin, A. É. Davletshin, S. M. Klotsman, M. B. Kosmyna, A. B. Levin, and V. P. Seminozhenko, JETP Lett. **48**, 440 (1988).
[101] M. Brinkmann, H. Somnitz, H. Bach, and K. Westerholt, Physica C **217**, 418 (1993).
[102] M. Gurvitch and A. T. Fiory, Phys. Rev. Lett. **59**, 1337 (1987).
[103] S. A. Wolf and V. Z. Kresin [Eds.], *Novel Sperconductivity*, Plenum Press, N. Y., 1987.
[104] M. Gurvitch, A. T. Fiory, and L. S. Schneemeyer, Physica C **153–155**, 1369 (1988).
[105] Yu. A. Kirichenko, K. V. Rusanov, and E. G. Tyurina, SFKhT **3**, 1385 (1990).
[106] S. T. Hagen, Z. Z. Wang, and N. P. Ong, Phys. Rev. B **40**, 9398 (1989).
[107] M. A. Izbizky, M. R. Nunez, P. Esquinuri, and C. Fainstain, Phys. Rev. B **38**, 9220 (1988).
[108] M. R. Nunez, D. Castello, M. A. Izbizky, D. Esparza, and C. D. Ovidio, Phys. Rev. B **36**, 8813 (1987).
[109] D. T. Morelli, J. Heremans, and D. E. Swets, Phys. Rev. B **36**, 3917 (1987).
[110] D. T. Morelli, J. Heremans, G. Doll, P. I. Picone, H. P. Jenssen, and V. S. Dresselehaus, Phys. Rev. B **39**, 804 (1989).
[111] J. Heremans, D. T. Morelli, W. Smith, and S. C. Strite, Phys. Rev. B **37**, 1604 (1988).
[112] A. V. Inyushkin, A. N. Taldenkov, L. N. Dem'yanets, and T. G. Uvarova, SFKhT **6**, 985 (1993).
[113] M. Leung, P. R. Broussard, J. H. Claassen, M. Osofsky, S. A. Wolf, and U. Strom, Appl. Phys. Lett. **51**, 2046 (1987).
[114] H. Lengfellner, S. Zeuner, W. Prettl, and K. Renk, Europhys. Lett. **25**, 375 (994).
[115] J. C. Culbertson, U. Strom, S. A. Wolf, P. Skeath, E. J. West, and W. D. Burns, Phys. Rev. B **39**, 12359 (1989).
[116] C. L. Chang, A. Kleinhammes, W. G. Moulton, and L. R. Tetardi, Phys. Rev. B **41**, 11564 (1990).
[117] H. S. Kwok, J. P. Zheng, and S. Y. Dong, Phys. Rev. B **43**, 6270 (1991).
[118] A. Kleinhammes, C. L. Chang, W. G. Moulton, and L. R. Testardi, Phys. Rev. B **44**, 2313 (1991).

[119] H. Lengfellner, G. Kremb, A. Schnellbogl, J. Betz, K. Renk, and W. Prettl, Appl. Phys. Lett. **60**, 501 (1992).
[120] H. S. Kwok and J. P. Zheng, Phys. Rev. B **46**, 3692 (1992).
[121] A. Palti, V. Svetchnikov, V. Pan, and A. Snarskii, J. Appl. Phys. **77**, 2814 (1995).
[122] K. L. Tate, R. D. Johnson, C. L. Chang, and E. F. Hilinski, J. Appl. Phys. **67**, 375 (1990).
[123] J. F. Scott, Appl. Phys. Lett. **56**, 1914 (1990).
[124] H. Ma, G. Xiong, L. Wang, H. Zhang, L. Tong, S. Liang, and S. Yan, Phys. Rev. B **40**, 9374 (1989).
[125] G. Schneider, P. G. Huggard, T. O'Brien, P. Lemoine, and W. Blau, Appl. Phys. Lett. **60**, 648 (1992).
[126] W. Prettl, H. Lengfellner, G. P. Kaminnski, and G. Schneider, Int. J. Infrared Millim. Waves **13**, 1659 (1992).
[127] H. S. Carlslow and J. C. Jaeger, *Conduction of Heat in Solids*, Clarendon Press, Oxford, 1959.
[128] J. D. Budai, M. F. Chisholm, and R. Feenstra, Appl. Phys. Lett. **58**, 2174 (1991).
[129] V. I. Kudinov, A. I. Kiriluk, and N. M. Kreines, Phys. Lett. A **151**, 358 (1990).

Translated by M. E. Alferieff

Low-energy nonparabolicity and condenson states in In_4Se_3 crystals

D. M. Bercha, L. Yu. Kharkhalis, and A. I. Bercha

Uzhgorod State University 294000 Uzhgorod, Ukraine

M. Shnajder

Institute of Physics of the Pedagogical University Rzhesow, Poland

(Submitted August 30, 1996; accepted for publication December 16, 1996)
Fiz. Tekh. Poluprovodn. **31**, 1299–1303 (November 1997)

It is shown that a condenson state and instability of the electron–phonon system, which resolve into a nonuniform state, are possible in the three-dimensional case of an In_4Se_3 crystal because of low-energy nonparabolicity and the characteristic features of the density of states. © *1997 American Institute of Physics.* [S1063-7826(97)00211-1]

In_4Se_3 is a promising material for solar power applications. In recent years, it has been under intensive study in both the crystalline and film states (see, for example, Refs. 1–10). Since an In_4Se_3 crystal possesses a layered structure, some of its unique properties can probably be explained by these features of the structure and chemical bond. The question of current-carrier localization, which is due to the specific nature of defects[11,12] and the capability of forming large-scale fluctuations as a result of the existence of different polytypic states or as a result of the existence of metastable states of unknown nature in real samples is important for these crystals.

The simplest form of localization is electron localization near a deformation caused by the field of the electron itself, as first indicated by Landau.[13] An analysis in ionic[14] and homeopolar[15] dielectrics led to the concept of a polaron and condenson. As shown by Pekar and Deĭgen,[15] the condenson state is due to the interaction of an electron with acoustic phonons. This interaction was described in an adiabatic approximation and the effective-mass approximation with the aid of a deformation potential. The criterion obtained in Ref. 15 showed that in principle condensons with a rather large radius can exist only in the one-dimensional case.[16] For two- and three-dimensional systems, the criterion is essentially not satisfied for any known semiconductor material, if the formation of the condenson state is analyzed only for a quadratic current-carrier dispersion law. Kibis[17] showed that in two-dimensional layers of hole semiconductors a hole energy spectrum $E(\boldsymbol{k}) \sim k^4$ is realized under some conditions, and in this case a large-radius condenson state can form for an arbitrarily weak interaction of the charge carriers with acoustic phonons. We shall show that condenson states are also possible for three-dimensional systems, specifically, for In_4Se_3 crystals. According to Ref. 17, the dispersion law is of great significance for solving this problem. Therefore, we shall briefly discuss the characteristic features of the band spectrum of an In_4Se_3 crystal.

An In_4Se_3 crystal contains 14 atoms in a unit cell with the lattice parameters $a_1 = 15.297$ Å and is described by the space group *Pnnm*.[18] According to our calculations,[19–21] the valence band (VB) consists of 60 subbands, grouped into minimal band complexes with two subbands each.[20] The band structure at the valence band edge is very complicated, since a large number of subband crossings is characteristic for it. The smallest band gap is localized at the point Γ ($\mathbf{k}=0$, $E_g = 0.67$ eV). The VB and the conduction band (CB) contain additional extrema, localized at the points $(0,0,2\pi/a_2,0)$ and $(0,0,0{,}425\pi/a_3)$. The energy splitting between two minima of the CB is of the order of 0.06–0.08 eV and the splitting between two maxima of the VB is ~ 0.05 eV.

Detailed investigations of the dispersion curves near the extremal point Γ (Ref. 20) showed that they can be described by the analytical expression

$$E(k) = -\alpha_1 k_x^2 - \alpha_2 k_y^2 - \alpha_3 k_z^2 + \beta_1 k_x^4 + \beta_2 k_y^4 + \beta_3 k_z^4, \quad (1)$$

although it has not been ruled out, as follows from our analysis,[20] that the electron and hole dispersion relations are much more complicated.

For further analysis, we shall use the dispersion relation (1) with parameters obtained from a least-squares analysis of the computed data: $\alpha_1 = 1.348\times10^{-18}$ eV·m^2, $\alpha_2 = 1.996\times10^{-18}$ eV·m^2, $\alpha_3 = 5.245\times10^{-20}$ eV·m^2, $\beta_1 = 2.697\times10^{-35}$ eV·m^4, $\beta_2 = 2.092\times10^{-35}$ eV·m^4, $\beta_3 = 8.452\times10^{-37}$ eV·m^4, for the CB and $\alpha_1 = -5.445\times10^{-19}$ eV·m^2, $\alpha_2 = 6.911\times10^{-19}$ eV·m^2, $\alpha_3 = 5.680\times10^{-19}$ eV·m^2, $\beta_1 = -5.870\times10^{-36}$ eV·m^4, $\beta_2 = 7.106\times10^{-36}$ eV·m^4, $\beta_3 = 3.799\times10^{-37}$ eV·m^4 for the CB. Rewriting the expression (1) in terms of the dimensionless quantities, we find that the coefficients of the fourth powers of the variables $k_x a_1/\pi$, $k_y a_2/\pi$, and $k_z a_3/\pi$ are two orders of magnitude larger than the coefficients of the quadratic terms. It should be noted that the coefficients of the quadratic terms are negative, and that the dispersion relation (1) differs substantially, by its nonparabolicity, from the standard dispersion relation used for rather large values of k, as happens in III–V semiconductors.

It is evident from the expression (1) that the absolute extrema are localized not exactly at the center of the Brillouin zone ($\mathbf{k}=0$); rather, they are shifted into the points

$k_i = \pm(\alpha_i/2\beta_i)^{1/2}$ $(i=1,2,3)$. A region of negative curvature is present near the point Γ (see Fig. 2 from Ref. 21). The depth of the band minimum is determined from the relation $E_{0i}=\alpha_i^2/4\beta_i$; as numerical estimates for the CB showed, the largest depth is observed in the direction $\Gamma-Y$: $E_{02}=47.6$ meV, and the smallest depth lies in the $\Gamma-Z$ direction ($E_{03}=1.0$ meV).

In summary, the dispersion relation (1) is characterized by a many-valley nonparabolicity with negative curvature at the smallest wave numbers. The dispersion relations of the additional valleys have essentially no anomalies and are described quite well by a quadratic function.

To solve the problem of the formation of a condenson state we shall examine the interaction of charge carriers with acoustic phonons, taking into account the dispersion relation (1). Accordingly, we employ a variational procedure, as done in the classical work by Deĭgen and Pekar.[15] The problem consists of finding the extremals of the functional

$$E(\psi,u_{ij}) = -\int\left[\alpha_1\left(\frac{\partial\psi}{\partial x}\right)^2+\alpha_2\left(\frac{\partial\psi}{\partial y}\right)^2+\alpha_3\left(\frac{\partial\psi}{\partial z}\right)^2\right]d^3\mathbf{r} + \int\left[\beta_1\left(\frac{\partial^2\psi}{\partial x^2}\right)^2+\beta_2\left(\frac{\partial^2\psi}{\partial y^2}\right)^2 + \beta_3\left(\frac{\partial^2\psi}{\partial z^2}\right)^2\right]d^3\mathbf{r}+\int\sum_{ij} b_{ij}u_{ij}|\psi|^2 d^3\mathbf{r} + \frac{1}{2}\sum_{ijkl}\lambda_{ijkl}u_{ij}u_{kl}, \tag{2}$$

where b_{ij} ($b_{ii}\equiv b_{i'}$) are the components of the deformation potential tensor, and $\lambda_{ijkl}\equiv\lambda_{i'k'}$ are the components of the tensor of elastic moduli.

The extremal $\psi(\mathbf{r})$, which is a characteristic function of the Schrödinger equation, in the presence of an electron-phonon interaction term in the deformation potential approximation is determined with the additional condition

$$\int |\psi|^2 d^3\mathbf{r}=1. \tag{3}$$

For the interaction of an electron with longitudinal acoustic phonons, the diagonal terms of the deformation tensor are sufficient: $u_{ij}=u_{ii}$ $(i=1,2,3)$.

The absolute minimum of the functional can be sought by varying first the components of the deformation tensor with a fixed arbitrary function ψ and then varying ψ. We equate to zero the variation of the functional E with respect to u_{ij}. For the case of an orthorhombic crystal, we obtain the system of equations

$$\begin{aligned}&\lambda_{11}u_{11}+\lambda_{12}u_{22}+\lambda_{13}u_{33}+b_1\psi^2=0,\\ &\lambda_{22}u_{22}+\lambda_{12}u_{11}+\lambda_{23}u_{33}+b_2\psi^2=0,\\ &\lambda_{33}u_{33}+\lambda_{13}u_{11}+\lambda_{23}u_{22}+b_3\psi^2=0.\end{aligned} \tag{4}$$

It follows from the system (4) that

$$u_{11}=-\frac{B}{\Lambda}\psi^2;$$

$$u_{22}=\left[-\frac{\lambda_{21}\lambda_{33}-\lambda_{13}\lambda_{23}}{\lambda_{23}^2-\lambda_{22}\lambda_{33}}\frac{B}{\Lambda}+\frac{b_2\lambda_{33}-b_3\lambda_{23}}{\lambda_{23}^2-\lambda_{22}\lambda_{33}}\right]\psi^2;$$

$$u_{33}=\left[-\frac{\lambda_{22}\lambda_{13}-\lambda_{21}\lambda_{23}}{\lambda_{23}^2-\lambda_{22}\lambda_{33}}\frac{B}{\Lambda}+\frac{b_3\lambda_{22}-b_2\lambda_{23}}{\lambda_{23}^2-\lambda_{22}\lambda_{33}}\right]\psi^2, \tag{5}$$

where

$$B=\lambda_{12}\frac{b_2\lambda_{33}-b_3\lambda_{23}}{\lambda_{23}^2-\lambda_{22}\lambda_{33}}+\lambda_{13}\frac{b_3\lambda_{22}-b_2\lambda_{23}}{\lambda_{23}^2-\lambda_{22}\lambda_{33}},$$

$$\Lambda=\lambda_{11}+\lambda_{12}\frac{\lambda_{21}\lambda_{33}-\lambda_{13}\lambda_{23}}{\lambda_{23}^2-\lambda_{22}\lambda_{33}}+\lambda_{13}\frac{\lambda_{22}\lambda_{13}-\lambda_{21}\lambda_{23}}{\lambda_{23}^2-\lambda_{22}\lambda_{33}}.$$

Eliminating u_{ij} from Eqs. (2), we reduce the problem to finding the extremals of a new functional. The result is

$$E(\psi)=E_0(\psi)-\widetilde{A}\int|\psi|^4 d^3\mathbf{r}. \tag{6}$$

Here $E_0(\psi)$ is the part of the functional without the electron-phonon interaction, and

$$\widetilde{A}=b_1\frac{B}{\Lambda}+b_2\left[\frac{\lambda_{21}\lambda_{33}-\lambda_{13}\lambda_{23}}{\lambda_{23}^2-\lambda_{22}\lambda_{33}}\frac{B}{\Lambda}-\frac{b_2\lambda_{33}-b_3\lambda_{23}}{\lambda_{23}^2-\lambda_{22}\lambda_{33}}\right] + b_3\left[\frac{\lambda_{22}\lambda_{13}-\lambda_{21}\lambda_{23}}{\lambda_{23}^2-\lambda_{22}\lambda_{33}}\frac{B}{\Lambda}-\frac{b_3\lambda_{22}-b_2\lambda_{23}}{\lambda_{23}^2-\lambda_{22}\lambda_{33}}\right]. \tag{7}$$

We minimize the functional (5) with the aid of the trial function[23]

$$\psi(\mathbf{r})=\left(\frac{(\mu_1\mu_2\mu_3)^{1/3}\sqrt{2}}{(a_1a_2a_3)^{1/3}}\right)^{3/2}\exp\left[-\pi\left[\left(\frac{\mu_1}{a_1}\right)^2x^2+\left(\frac{\mu_2}{a_2}\right)^2y^2+\left(\frac{\mu_3}{a_3}\right)^2z^2\right]\right], \tag{8}$$

which satisfies the normalization condition; μ_1, μ_2, and μ_3 are dimensionless variational parameters, and a_1, a_2, and a_3 are lattice constants.

After integrating we obtain

$$E(\mu)=-\pi\left[\alpha_1\left(\frac{\mu_1}{a_1}\right)^2+\alpha_2\left(\frac{\mu_2}{a_2}\right)^2+\alpha_3\left(\frac{\mu_3}{a_3}\right)^2\right] + 3\pi^2\left[\beta_1\left(\frac{\mu_1}{a_1}\right)^4+\beta_2\left(\frac{\mu_2}{a_2}\right)^4+\beta_3\left(\frac{\mu_3}{a_3}\right)^4\right] - \widetilde{A}\frac{\mu_1\mu_2\mu_3}{a_1a_2a_3}. \tag{9}$$

In order for stable condenson states to form, the functional $E(\mu)$ must possess a minimum. The necessary condition for an extremum can be found from the system of equations

$$-\frac{2\pi\alpha_1}{a_i^2}\mu_i+\frac{12\pi^2\beta_i}{a_i^4}\mu_i^3-\widetilde{A}\frac{\mu_j\mu_k}{a_ia_ja_k}=0, \tag{10}$$

$i=1,2,3$; $j=2,3,1$; and, $k=3,2,1$. However, for the purpose of estimation, we restrict the discussion to the case where

μ_1, μ_2, and μ_3 are equal to one another, and the lattice parameters can be replaced by the reduced value $a_{av}=(a_1a_2a_3)^{1/3}$ and only one of the equations in (10) need be used.

Solving Eq. (10), we obtain the following expression for $\mu_{\min}$:

$$\mu_{\min}=\frac{\widetilde{A}a_{av}+a_{av}(\widetilde{A}^2+96\pi^3\alpha\beta)^{1/2}}{24\pi^2\beta}, \tag{11}$$

where α and β assume the values $\alpha_1,\alpha_2,\alpha_3$ and β_1,β_2,β_3, which are presented above.

We shall estimate $\widetilde{A}$ on the basis of the data on the deformation potentials[1)24] and elastic moduli[25] for an In_4Se_3 crystal: $\widetilde{A}=5.588\times10^{-29}$ eV·m^3. Then $\mu_{\min}\sim0.06$. As one can easily see from Eq. (11), the parameters α and β in the dispersion relation make the main contribution to $\mu_{\min}$. Since $E(\mu_{\min})<0$, a condenson state forms. The radius of this state is determined from the expression

$$a_0^2\sim\frac{1}{\pi}\frac{a_{av}^2}{\mu},$$

from which we find $a_0=9.4a_{av}\sim100$ Å$\gg a_{av}$.

The latter estimate shows that a condenson state is determined in the model with the parameters of In_4Se_3 in the continuum approximation, and its binding energy is $E_b\sim4\times10^{-2}$ eV.

The role of the electron-phonon interaction in the In_4Se_3 crystal actually reduces to scattering of current carriers inside a complicated valley, where an electron can occupy states with different ''effective masses'' (positive, negative, and infinite), which promotes mixing of the states described by the Bloch functions $\mu_{\mathbf{k}}$ and formation of a localized function of the form

$$\psi=\int C(k)\psi_{\mathbf{k}}d\mathbf{k}. \tag{12}$$

The condenson model corresponds to the situation in which each current carrier interacts with the lattice individually via a deformation potential. Such an analysis is justified for low, free-carrier densities. Since in insulators or semiconductors a lattice is formed in the absence of free carriers; in their presence the electron-phonon system can become unstable.[26–28] In Ref. 26 a critical parameter A for the appearance of such an instability at low temperatures was obtained for the isotropic case:

$$A=\frac{3b^2n}{2\lambda E(k_f(n))}=(a_0^3n)^{1/3},$$

where a_0 is the condenson radius. As indicated in Refs. 26 and 27 , the instability criterion $A>1$ corresponds to carrier densities for which the regions of the condenson states overlap, i.e., a case in which a multicondenson forms (condenson liquid). However, since a condenson state in the continuous approximation is not obtained in the quadratic dispersion relation approximation, in this approach finite multicondenson states could not be obtained. In our case, such obstacles apparently do not arise.

The conditions for forming ''drops'' of a multicondensate liquid, most often in the region of deformation random wells, which exist in the spatial relief of the CB or VB edge, are created by producing additional current carriers by doping, injection, or photogeneration.

Stable, nonuniform states are sure to be obtained if the decrease in the electronic energy, associated with the overflow of carriers into the region where the band bottom is lowered, exceeds the gain in the lattice deformation energy. The parameter A is then defined as[27]

$$A=\frac{b^2}{\lambda\,\partial E_f(N,T)/\partial N}. \tag{13}$$

Since the density of states (DS) as a function of density is directly proportional to the reciprocal of the rate of change of the Fermi energy E_f as a function of density, it follows from Eq. (13) that an instability arises for a high DS at the Fermi level. Substantial growth of the DS at the Fermi level is achieved by two avenues: by carrier redistribution in many-valley semiconductors from a lighter to a heavier valley or by ''explosive'' growth of the DS at the Fermi level as a result of the characteristic features of the topology of isoenergetic surfaces (ISs). We shall show that in our case the DS possesses features that ensure the criterion $A>1$ for the standard values of the constants b of the deformation potentials and elastic moduli λ.

Figure 1 shows the sequence of ISs for electrons in the main valley of an In_4Se_3 crystal. As one can see from Fig. 1, the topology of the IS changes abruptly, and this correspondingly results in a change of the DS as a function of energy.

Since the anisotropy is not very important for realization of a stable condenson state (only the presence of terms with fourth powers of the components of the wave numbers in the dispersion law (1) is important), to find the characteristic features in the DS we shall restrict the analysis to the isotropic case of the current-carrier dispersion relation (1).

Equation (1) in spherical coordinates is

$$E(k,\theta,\varphi)=-k^2+A(\theta,\varphi)k^4, \tag{14}$$

where

$$A(\theta,\varphi)=\frac{\beta}{\alpha^2}[(\sin^4\varphi+\cos^4\varphi)\cos^4\theta+\sin^4\theta].$$

We thus find

$$K^2(E,\theta,\varphi)=\frac{1\pm[1+4EA(\theta,\varphi)]^{1/2}}{2A(\theta,\varphi)}. \tag{15}$$

The surface of minima (Fig. 2a) depends on the directions and is determined by the expression

$$E_{\min}=-\frac{1}{4A(\theta,\varphi)};\quad k_{\min}^2=\frac{1}{2A(\theta,\varphi)}. \tag{16}$$

The absolute minima of the energy are concentrated at the vertices of a cube. Figure 2b shows the IS, which consists of two parts — internal and external. As one can see from Fig. 2b, the surface is an average between a torus with ''loops'' of minima and a three-dimensional torus with a surface of minima. As a result of the change in the topology of the IS,

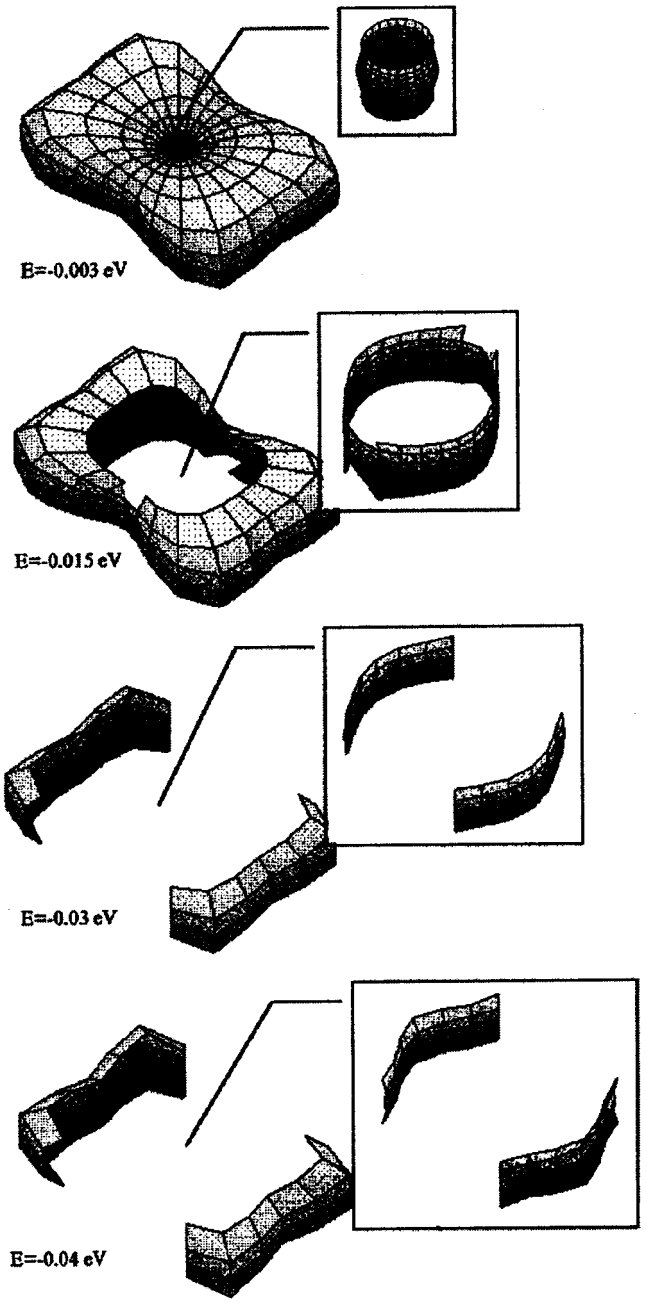

FIG. 1. Sequence of isoenergy surfaces for electrons in the main valley of an In_4Se_3 crystal.

the Euler characteristic[22] $\chi(E)$ changes from 8×2 to $+4$ with increasing energy. In the process, the DS increases in a peak-like manner with increasing density [P_0 is a singularity corresponding to $\chi(E)=4$, which is slightly ''smeared'' on the left side by a transition from another topology with characteristic $\chi(E)=2$]. The computed energy dependence of the DS for the dispersion relation (1) with the parameters of an In_4Se_3 crystal is shown in Fig. 3.

In summary, just as in the case of electrons in a quantizing magnetic field,[29] the concentration barrier, which is used for the realization of the critical state and which exists for the standard quadratic dispersion relation, can be eliminated. The instability that develops because of the appearance of carriers with infinitely large and negative masses is most likely resolved by a transition into a nonuniform state.

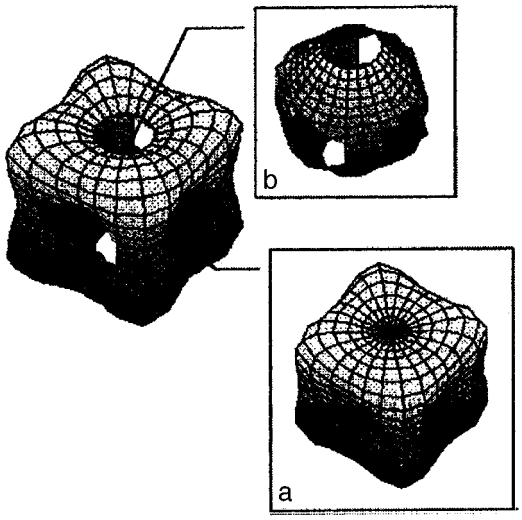

FIG. 2. Surface of minima (a) and parts of the isoenergy surface obtained with the MAPLE 4 program (b) for the dispersion relation (14).

Thus, we verify in different approaches that the dispersion relation (1) can be used to obtain a nonuniformity in the form of multicondenson drops, which apparently are responsible for the particular features of the physical properties of an In_4Se_3 crystal (realization of a temperature dependence of the electrical conductivity in the manner of the Mott law in a sufficiently wide temperature range,[30] frequency dependence of the electrical conductivity,[31] complex temperature dependence of the thermoelectric power,[32] and anisotropy parameter of the electrical conductivity, multiple inversion of the Hall coefficient,[32] anisotropic scattering of x rays,[2] and deviation from Hooke's law at low stresses[33]).

We thank A. N. Borts for assisting in the analysis of the relation between the topology of the isoenergetic surfaces

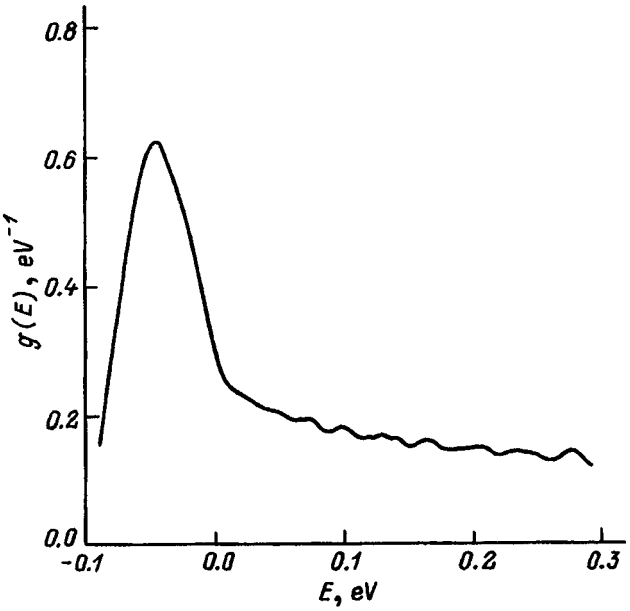

FIG. 3. Computed density of states for the dispersion relation (1) with the parameters for an In_4Se_3 crystal.

and the density of states. We also thank Al. L. Éfros for a discussion of the materials presented in this paper.

[1)]The magnitudes of the deformation potentials from Ref. 24 must be taken with the opposite sign, since they were estimated there for a compressive deformation.

[1] U. H. Schwarz, H. Hillebrecht, H. J. Deiseroth, and R. Walter, Z. Kristallografiya **210**, 342 (1995).
[2] O. I. Bodak, Yu. M. Orishchin, and V. P. Savchin, Kristallografiya **25**, 628 (1980).
[3] I. M. Stakhira and P. G. Ks'ondzik, Ukr. Fiz. Zh. **26**, 762 (1981).
[4] I. M. Stakhira and P. G. Ks'ondzik, Ukr. Fiz. Zh. **27**, 1196 (1982).
[5] A. B. Onyskiv, Yu. M. Orishchin, V. P. Savchin, I. M. Stakhira, and I. M. Fetsyukh, Fiz. Tekh. Poluprovodn. **24**, 423 (1990) [Sov. Phys. Semicond. **24**, 264 (1990)].
[6] V. P. Zakharko, V. P. Savchin, I. M. Stakhira, and G. P. Sheremet, Fiz. Tekh. Poluprovodn. **23**, 1881 (1981) [Sov. Phys. Semicond. **23**, 1101 (1981)].
[7] E. P. Zhad'ko, É. I. Rashba, V. A. Romanov, I. M. Stakhira, and K. D. Tovstyuk, Fiz. Tverd. Tela (Leningrad) **7**, 1777 (1965) [Sov. Phys. Solid State **7**, 1432 (1965)].
[8] C. Julien, A. Khelfa, and J. P. Guesdon, Mater. Sci. Eng. B **27**, 53 (1994).
[9] C. Julien, A. Khelfa, N. Benramdane, J. P. Guesdon, P. Dzwonkowski, I. Samaras, and M. Balkanski, Mater. Sci. Eng. B **23**, 105 (1994).
[10] N. Benramdane and R. H. Misho, Sol. Energy Mater. Sol. Cells **37**, 367 (1995).
[11] D. M. Bercha, V. T. Maslyuk, and M. P. Zayachkovskiĭ, Ukr. Fiz. Zh. **20**, 1417 (1975).
[12] F. V. Motsnyĭ, Author's Abstract of Doctoral Dissertation, Kiev (1993).
[13] L. D. Landau, *On the Motion of an Electron in a Crystal Lattice* [in Russian], Edited by E. M. Lifshitz, Nauka, Moscow, 1970.
[14] S. I. Pekar, *Investigations in the Theory of Crystal Lattices* [in Russian], Soviet Academy of Sciences Press, Moscow, 1951.
[15] M. F. Deĭgen and S. I. Pekar, Zh. Éksp. Teor. Fiz. **21**, 803 (1951).
[16] É. I. Rashba, Opt. Spektrosk. **2**, 88 (1957).
[17] O. V. Kibis, Fiz. Tekh. Poluprovodn. **29**, 125 (1995) [Semiconductors **29**, 66 (1995)].
[18] J. H. C. Hogg, H. H. Sutherland, and D. J. Willimas, Acta Crystallogr., Sect. B: Struct. Crystallogr. Cryst. Chem. **29**, 1590 (1973).
[19] D. M. Bercha, O. B. Mitin, and A. V. Rishko, in *Optoelectronics Materials* [in Russian], Tekhnika, Kiev, 1992, No. 1, p. 81.
[20] D. M. Bercha, O. B. Mitin, L. Yu. Kharkalis, and A. I. Bercha, Fiz. Tverd. Tela (St. Petersburg) **37**, 3233 (1995) [Phys. Solid State **37**, 1778 (1995)].
[21] D. M. Bercha, L. Yu. Kharkalis, and O. B. Mitin Ukr. Fiz. Zh. **40**, 729 (1995).
[22] A. N. Borets, VINITI N 2475-75, Uzhgorod, 1975.
[23] A. S. Davydov, *The Theory of Solids* [in Russian], Nauka, Moscow, 1976.
[24] D. M. Bercha, O. B. Mitin, I. M. Rarnko, L. Yu. Kharkhalis, and A. I. Bercha, Fiz. Tekh. Poluprovodn. **28**, 1249 (1994) [Semiconductors **28**, 711 (1994)].
[25] V. Ya. Kuryachiĭ, G. Yu. bogachev, V. P. Mikhal'chenko, and I. M. Stakhira, Izv. Akad. Nauk SSSR, Neorg. Mater. **22**, 855 (1986).
[26] S. I. Pekar, V. I. Pipa, and V. N. Piskovoĭ, JETP Lett. **12**, 230 (1970).
[27] V. A. Kochelap, V. N. Sokolov, and B. Yu. Vengalis, *Phase Transitions in Semiconductors with Deformation Electron-Phonon Interaction* [in Russian], Nauk. Dumka, Kiev, 1984.
[28] V. I. Pipa and V. N. Puskovoĭ, Fiz. Tverd. Tela (Leningrad) **14**, 2286 (1972) [Sov. Phys. Solid State **14**, 1979 (1972)].
[29] V. A. Kochelap and V. N. Sokolov, Zh. Éksp. Teor. Fiz. **65**, 823 (1973) [JETP **38**, 408 (1974)].
[30] I. M. Stakhira, V. P. Savchin, and G. M. Demkiv, Ukr. Fiz. Zh. **38**, 891 (1993).
[31] I. M. Stakhira, G. M. Demkiv, and O. E. Flyunt, Ukr. Fiz. Zh. **40**, 737 (1995).
[32] V. P. Savchin, Fiz. Tekh. Poluprovodn. **15**, 1430 (1981) [Sov. Phys. Semicond. **15**, 827 (1981)].
[33] A. A. Logvinenko, I. M. Spitkovskiĭ, and I. M. Stakhira, Fiz. Tverd. Tela (Leningrad) **16**, 2743 (1974) [Sov. Phys. Solid State **16**, 1774 (1974)].

Translated by M. E. Alferieff

Tunneling effects in light-emitting diodes based on InGaN/AlGaN/GaN heterostructures with quantum wells

V. E. Kudryashov, K. G. Zolin, A. N. Turkin, and A. É. Yunovich*

Department of Physics, M. V. Lomonosov Moscow State University, 119899 Moscow, Russia

A. N. Kovalev and F. I. Manyakhin

Moscow Institute of Steels and Alloys, 119235 Moscow, Russia
(Submitted January 28, 1997; accepted for publication March 18, 1997)
Fiz. Tekh. Poluprovodn. **31**, 1304–1309 (November 1997)

Tunneling effects in the luminescence spectra and the electrical properties of blue light-emitting diodes based on InGaN/AlGaN/GaN heterostructures have been investigated. The tunneling radiation in the energy range 2.1–2.4 eV predominates for weak currents (<0.2 mA), and its role increases as the peak of the main blue band shifts into the short-wavelength region. The position $\hbar\omega_{\max}$ of the maximum is approximately proportional to the voltage eU. The shape and intensity of the band are described by the theory of tunneling radiation. The current-voltage characteristics for low direct currents possess a tunneling component with exponent $E_J=130-140$ meV. The distribution of electrically active centers reveals extended, compensated layers in the n- and p-type regions, adjoining the active layer, and indicates the presence of charged walls at the boundaries of the heterojunctions. A strong electric field is present in the InGaN active region. The energy diagram of the structures is discussed.[1)] © *1997 American Institute of Physics.* [S1063-7826(97)00311-6]

1. INTRODUCTION

In Refs. 2–4 we discovered that tunneling radiation plays a large role in the luminescence spectra of ultrabright blue LEDs based on InGaN/AlGaN/GaN heterostructures (HSs) at low currents. A tunneling-current component was present in the current-voltage characteristic (IVC) of the diodes. The difference of the blue LEDs from green diodes based on similar HSs with a different In content in the InGaN active region was explained by the smaller thickness of the space-charge region and high electric field.[3] It was proposed[2,4] that tunneling-radiation models, developed for other III–V compounds,[5,6] be used for analysis.

In the present work we investigated in detail the tunneling-radiation spectra and electrical properties of blue LEDs, described in Refs. 2–4. Measurements of the dynamic capacitance and charge distribution in the structures were analyzed. It was shown that tunneling effects dominate when the field strength is sufficiently high in the active region—a quantum well. The energy diagram of the heterostructures was determined more accurately. The spectra were analyzed on the basis of the diagonal-tunneling theories. The role of fluctuations in the active layer is discussed.

2. EXPERIMENTAL PROCEDURE

Light-emitting diodes based on InGaN/AlGaN/GaN structures, grown by gas-phase epitaxy using organometallic compounds, which were provided by Dr. S. Nakamura,[7] were investigated. n-GaN:Si ($t\approx 5\ \mu$m) and a thin ($d=2.5-3.5$ nm) active $In_xGa_{1-x}N$ layer were grown on a sapphire substrate. This was followed by p-$Al_{0.1}Ga_{0.9}N$:Mg (≈ 100 nm) and p-GaN:Mg ($\approx 0.5\ \mu$m) layers. For compositions x varying in the range 0.2–0.43, the wavelength at the emission maximum varied in the range corresponding to the blue and green region of the spectrum (see Refs. 2–4 and 7 for a more detailed discussion).

The spectra were investigated in the current interval $J=0.02-30$ mA on a KSVU-12 system with a 486 IBM personal computer. The direct and reverse branches of the IVCs were measured in the interval $J=1\times 10^{-7}-30$ mA. Measurements of the dynamic capacitance of the space charge region by the method of Ref. 8 made it possible to determine the distribution of electrically active centers in the p-type layer.

3. EXPERIMENTAL RESULTS

3.1. Room-temperature spectra

The spectra of one of the blue LEDs at room temperature and with the current varying in the range $J=0.03-0.1$ mA are shown in Fig. 1. The spectral band, whose maximum shifts from $\hbar\omega_{\max}=2.20$ to 2.34 eV as a function of the voltage V on the diode, is related with tunneling radiative recombination. This band dominates for small J; for $V>2.30$ V, the blue band, which predominates at high currents, grows rapidly.

Figure 2 shows that the relative role of the tunneling band increases (with the same voltage as U on the $p-n$ junction) as the maximum of the blue band for different LEDs shifts into the short-wavelength region (the In fraction decreases).

Figure 3 shows $\hbar\omega_{\max}$ and the intensity $I_{\max}$ versus the voltage $eU=e(V-JR_s)$ (R_s is the serial resistance). The quantity $\hbar\omega_{\max}$ is related linearly with eU: $\hbar\omega_{\max}=eU-D$; $I_{\max}$ is related exponentially: $I_{\max}\sim\exp(eU/E_I)$, where $E_I=70-80$ meV.

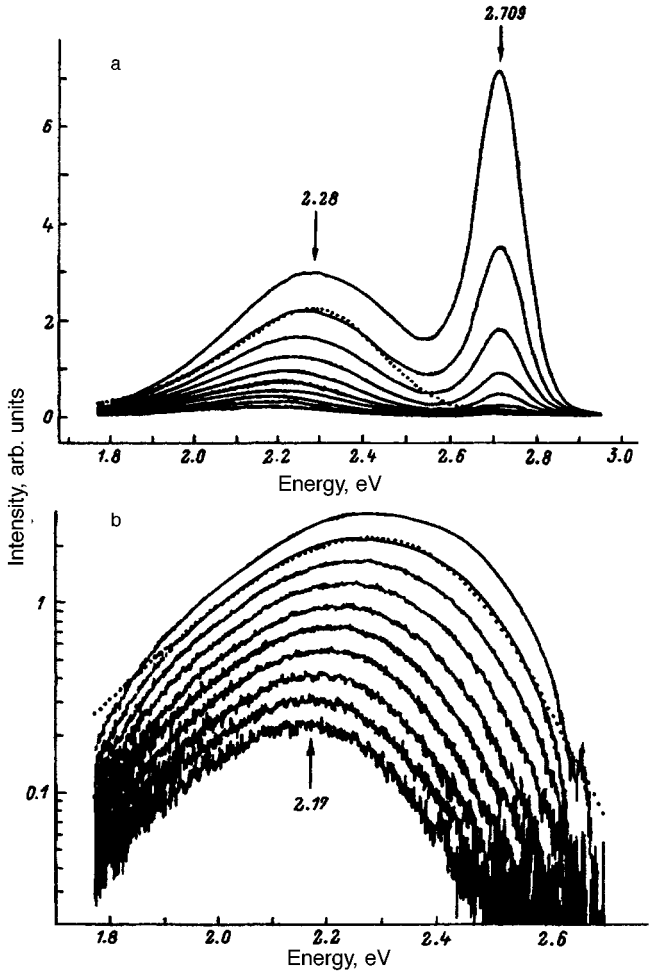

FIG. 1. Room-temperature tunneling radiation spectra of blue LED No. 3 with currents $J=35-100$ μA and voltages $V=2.16-2.34$ V. a—Linear scale; b—logarithmic scale, the blue line is subtracted out. The dots show the theoretical approximation at currents of 60 and 90 μA.

3.2. Current-voltage characteristics

Figure 4 shows the direct and reverse branches of the IVC at 300 and 77 K; the variation of the derivative $E_J=dV/d(\ln J)$ in the range $U=1.8-3.0$ V is also shown. In the exponential part $J\sim\exp(eU/E_J)$, the energy $E_J=130-140$ meV (with voltage $V=1.5-2.5$ V) at low direct currents; similar results were presented in Ref. 9. The quantity E_J is virtually independent of T (155–165 meV at 77 K). This part corresponds to the tunneling component of the current. In this interval, the intensity of the tunneling band is approximately a quadratic function of the current, $I_{\max}\sim J^2$. The injection component of the current dominates at high voltages $V>2.6-2.7$ V:

$$J\sim\exp(eU/mkT);\quad U=V-JR_s.$$

It should be noted that in the interval $1.8<V<3.0$ V the semilogarithmic derivative $E_J(V)=dV/d(\ln J)$ possesses a maximum near $V=2.3-2.5$ V and a minimum near $V=2.5-2.6$ V, i.e., in the region of the transition of the spectra from the tunneling band to the main band (Fig. 2). The shift of these extrema from one diode to another equals the shift of the maximum of the blue band. The minimum E_J and R_s decrease with increasing $\hbar\omega_{\max}$. This behavior is evidence of a change in the mechanisms of the current and radiation from tunneling to injection into the active region.

Figure 4 also shows the IVCs for reverse voltages. They possess two exponential sections, $J\sim\exp(-eV/E_J)$, with energies $E_J\approx0.6$ eV at voltages $3.4<-V<6.8$ eV and $E_J\approx0.96-0.98$ eV at voltages $6.8<-V<10$ V. The values of E_J do not depend on T. These current components can be described as a tunneling breakdown.

At voltages $-eV>10$ eV$\approx3\cdot E_g$(GaN) impact ionization appeared and luminescence due to an electron-hole plasma was observed. Reverse currents and emission spectra accompanying impact ionization will be examined in a following paper.

3.3. Capacitance versus voltage characteristics, field and potential distributions

The measurements of the voltage dependence of the capacitance $C(V)$ and a plot of this dependence in double-logarithmic coordinates showed that the space charge region (SCR) can be represented equivalently as two serially connected capacitances: C_n, whose magnitude depends very little on the reciprocal of the voltage, and C_p, which determines the change in the capacitance of the entire structure. In the absence of a bias voltage, the contribution of the SCR to C_n equals about 45% of the total width of the SCR. This capacitance is due to the charge in the n-layer, whose expansion is limited by the strongly doped n-region of the structure. The change in the total capacitance of the structure is due to an expansion of the structure in the direction of the more lightly doped p-type region (GaAlN:Mg). The part of the contact potential referring to the p-type region, ΔV_p, determined from the $C(V)$ curves, was $\Delta V_p\approx0.5-0.6$ V. The part of the contact potential referring to the n-region was $\Delta V_n\approx0.4=0.5$ V. Therefore, $\Delta V_p+\Delta V_n\approx0.9-1.0$ V. The compensated layers adjoining the active region are of the order of 10–15 nm thick on both sides. A part ΔV_{qn} of the contact potential falls across these quasineutral layers, but the larger part, $\Delta V_i\approx2.0-2.4$ V, falls across the thin (2.5–4 nm) active layer. A potential distribution of this type is formed by the charged walls on the heterojunctions (p-AlGaN/InGaN and InGaN/n-GaN). A model of such walls has been discussed in Ref. 10. The formation of the walls could be due to upward diffusion of impurities as a result of the deformation potential, electric field, and broken bonds at the boundaries of the layers.

4. DISCUSSION

4.1. Potential and field distributions; energy diagram

The model potential and field distributions, obtained from an analysis of the experimental results, in the structure under study is shown in Fig. 5. It should be noted that a strong electric field of up to $\mathscr{E}=6\times10^6$ V/cm exists in the active layer. As the direct voltage increases, this field decreases starting at values $U\approx\Delta V_i\approx2.0-2.2$ V, but the tunneling component of the current still dominates. This situa-

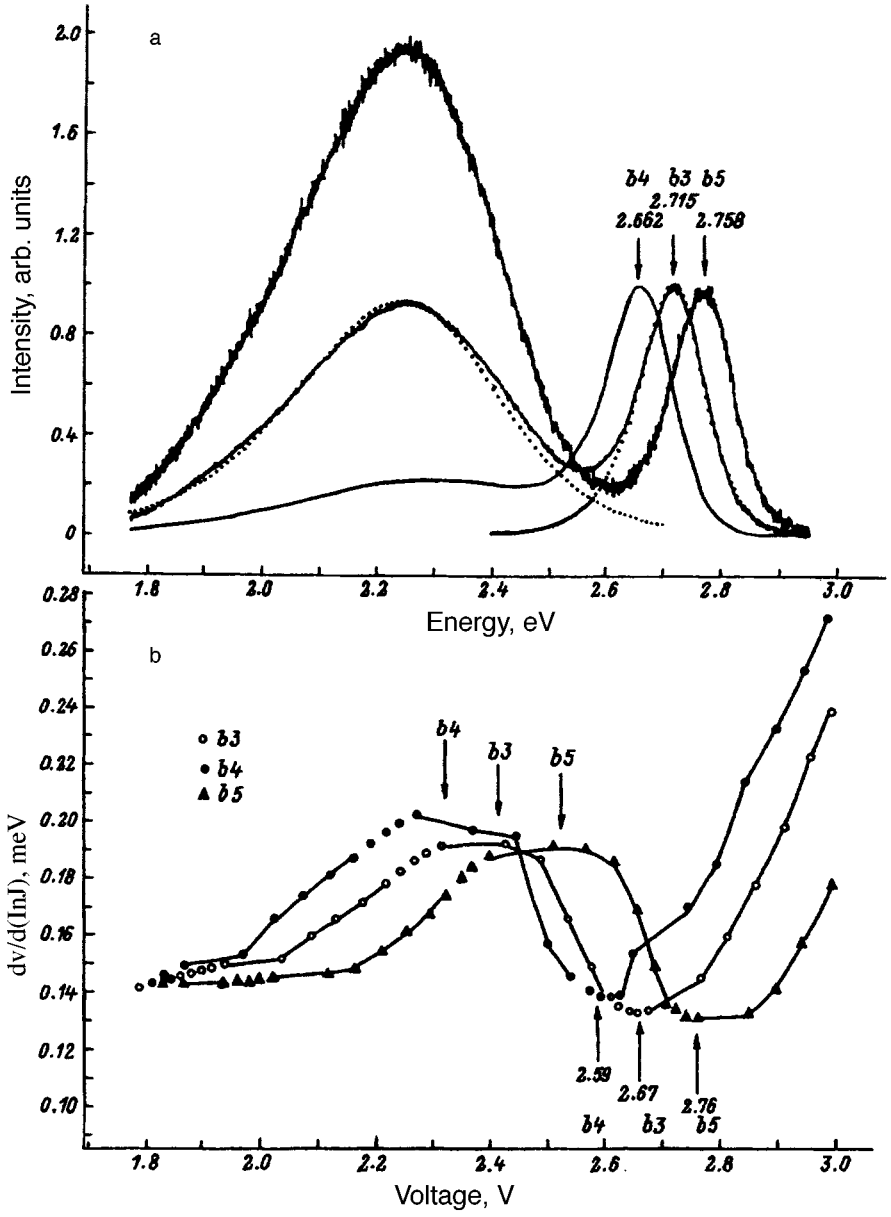

FIG. 2. a—Spectra of blue LEDs at the same voltage $V=2.304$ V. The spectra are normalized to the maximum intensity of the blue emission band. The dots show the approximation of the blue and tunneling lines. b—$dV/d(\ln J)$ versus V for the same LEDs.

tion is illustrated in Fig. 6a. When the voltage increases to values $U \approx \Delta V_i + \Delta V_{qn} \approx 2.4-2.6$ eV, the injection component dominates (Fig. 6b).

4.2. Tunneling radiative recombination

The theory of tunneling radiative recombination was developed for homogeneous $p-n$ junctions which are degenerate on both sides.[6,7] We employed this theory with some modifications for our more complicated case of a multilayer heterojunction. The tunneling radiation spectrum can be described by the formula

$$I(\hbar\omega) \sim [\hbar\omega/(E_g-\hbar\omega)] \times [(\hbar\omega-eU)/(\exp((\hbar\omega-eU)/mkT)-1)] \times [\exp(-(4/3)(E_g-\hbar\omega)/E_0)^{3/2}], \quad (1)$$

where E_g is the effective band gap, m is a dimensionless parameter that depends on the ratio of the electron and hole effective masses,

$$E_0=[(\hbar/(2m_{cv}^*)^{1/2})e\mathscr{E}]^{2/3}. \quad (2)$$

is the exponent in the theory of the Franz–Keldysh effect, m_{cv}^* is the reduced effective mass, and $\mathscr{E}$ is the electric field, which is assumed to be constant in the region of overlapping of the electron and hole wave functions.

The experimental spectra in Figs. 1 and 2 were described by Eq. (1) by fitting the parameters to obtain the best agreement between theory and experiment. The main blue band was first calculated from the sum spectra (Figs. 1 and 2); it was approximated by a theoretical curve in the manner described in Refs. 2–4. One can see that the theoretical curves describe the experimental spectra well. Fitting the parameters showed that eU in Eq. (1) equals, to within the limits of

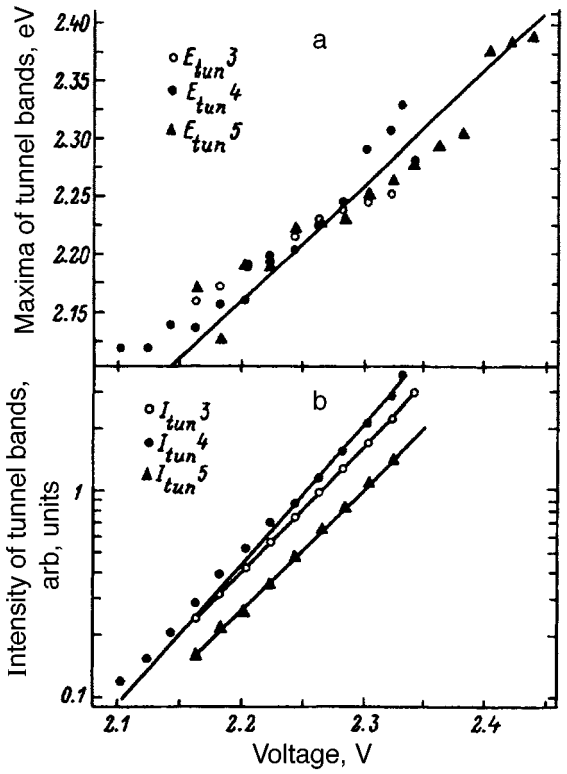

FIG. 3. a—Position of the maxima of the tunneling band versus voltage for three blue LEDs; straight line: $\hbar\omega = eU - eU_0$, $U_0 = 0.04$ eV. b—Tunneling radiation intensity versus voltage for the same LEDs; straight lines—approximation by the function $I_{\text{tun}} = A\exp(|eU|/E_I)$, the values of $E_{I_{(3,4,5)}}$ for LEDs Nos. 3, 4, and 5 are, respectively, 0.0712, 0.0640, and 0.0740 eV.

accuracy, the measured voltage on the structure; the effective band gap required for agreement is $E_g = 2.6-2.9$ eV; the parameter $m = 1.6$.

The most important result was found to be the value of the parameter E_0 required for agreement: $E_0 = 0.35-0.42$ eV. Hence an estimate was obtained for the

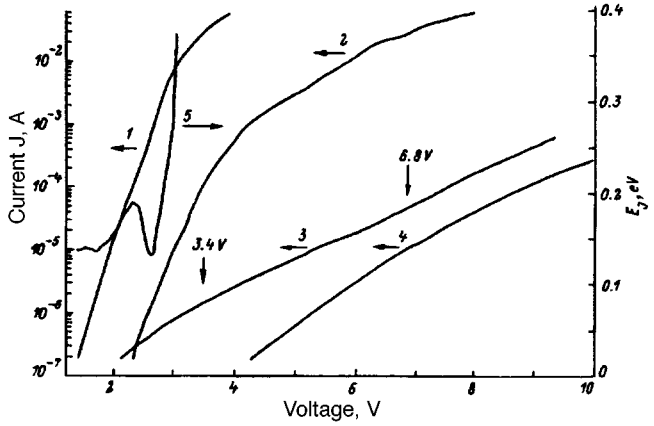

FIG. 4. Current-voltage characteristics of the blue LED No. 3. *1, 2*—Direct voltage, *3, 4*—reverse voltage; *1, 3*—$T = 300$ K; *2, 4*—$T = 77$ K; *5*—$E_J = dV/(\ln J)$.

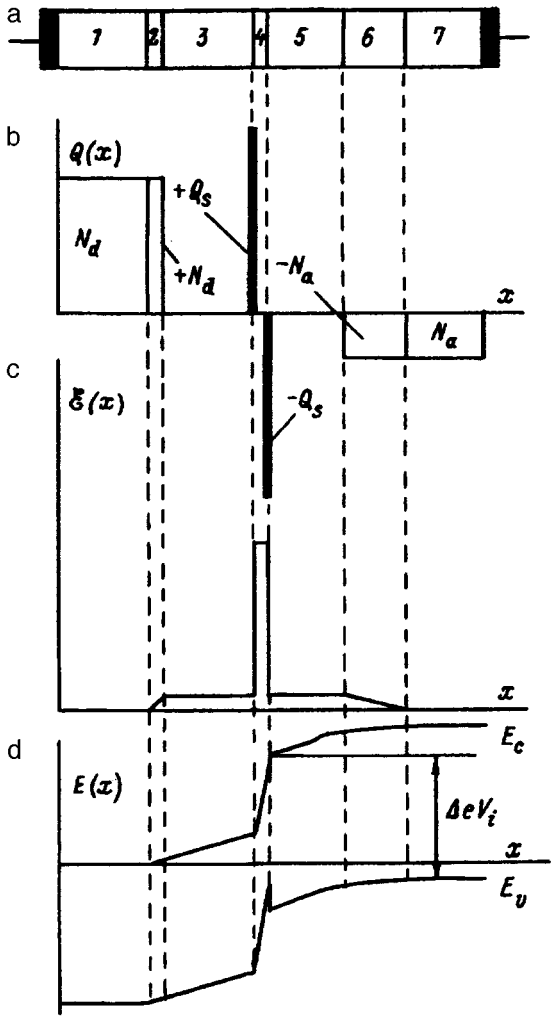

FIG. 5. Diagram of the heterostructure (a), distributions of electrically active centers and space charge (b) and the electric field (c), and energy diagram at equilibrium. *1, 7*—Quasineutral *n*- and *p*-GaN layers; *2, 6*—ionized donors and acceptors in the space charge region; *3, 5*—compensated layers in *n*-GaN and *p*-AlGaN; *4*—active layer—InGaN quantum well.

field required for tunneling radiation: $\mathscr{E} = (4-6)\times 10^6$ V/cm; the effective masses in InGaN were calculated to be proportional to E_g from the values for GaN [$m_c^* = 0.20m_0$ and $m_v^* = 0.54m_0$ (Ref. 11)]. The large values of $\mathscr{E}$ agree with the analysis of the distribution of the fields from capacitance measurements.

4.3. Tunneling effects and fluctuations of the potential

The model of radiative recombination for the main, blue line in the spectra took into consideration the potential fluctuations arising in the two-dimensional active layer as a result of nonuniformities of the solid solution, fluctuations of the well width, and the Coulomb fields of the impurities.[2–4] Estimates of the fluctuation electric fields from this model give $\mathscr{E} \approx (2-3)\times 10^5$ V/cm. The fields due to the fluctuations act together with the electric field of the $p-n$ heterojunction and should affect the tunneling radiation.

We do not discuss here the questions concerning the size-quantization levels in structures with a strong electric field in the quantum well. The role of impurities (acceptors

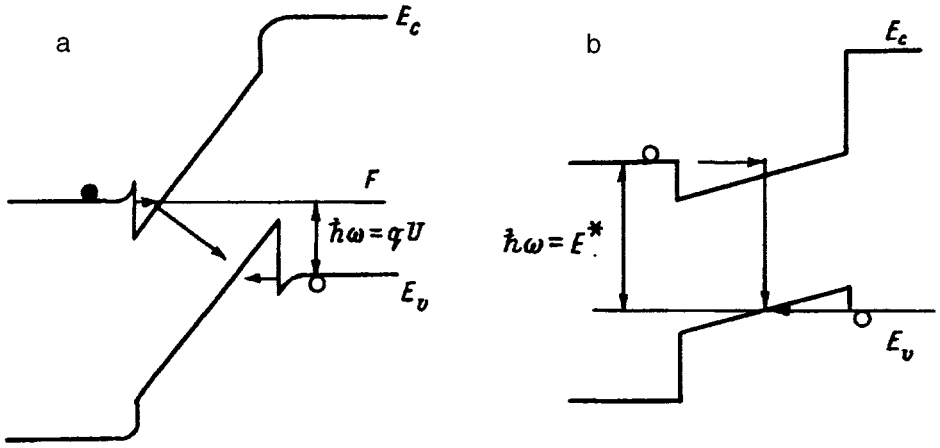

FIG. 6. Energy diagram of a heterostructure under direct bias voltages. a—tunneling, b—injection.

Mg and donors Si) in tunneling junctions also fall outside the scope of the present discussion. In general, the nature of the luminescence band with a maximum at 2.2 eV, which is attributable to defects and which are studied in Ref. 12, must also be taken into account. These questions require a separate analysis.

5. CONCLUSIONS

1. The spectra observed in the region $\hbar\omega = 2.1-2.5$ eV with low currents ($J < 0.2$ mA) from blue InGaN/AlGaN/GaN LEDs with a thin space charge region are due to tunneling radiative recombination of electrons and holes in the InGaN active layer.

2. The charge distribution in these structures includes not only the space charge region, but also the compensated quasi-neutral layers and charged walls at the heterojunctions. This distribution gives rise to a strong electric field in the quantum well, up to $(4-6)\times 10^6$ V/cm.

3. The diagonal-tunneling model describes qualitatively the spectra and their variation as a function of the voltage on the structure.

4. The proposed energy diagram describes the luminescence and electric properties of InGaN/AlGaN/GaN heterostructure light-emitting diodes.

We are deeply grateful to Dr. N. Nakamura for sending the light-emitting diodes to Moscow State University and S. S. Shumilov for assisting in the computer support.

*e-mail: yunovich@scon175.phys.msu.su

[1)]The present work was reported at a meeting of the Materials Research Society, Boston, 1996.[1]

[1] A. E. Yunovich, A. N. Kovalev, V. E. Kudryashov, F. I. Manyachin, A. N. Turkin, and K. G. Zolina in *Abstracts of Mater. Res. Soc. Fall Meeting 1996, Sympos. N* (Boston, USA, 1996) Abstr. No. 9–37, p. 347.
[2] K. G. Zolina, V. E. Kudryashov, A. N. Turkin, A. E. Yunovich, and S. Nakamura, MRS Int. J. Nitride Semic. Res., 1/11; http: nsr. mij. mrs. org 1 11.
[3] A. N. Kovalev, V. E. Kudryashov, F. I. Manyachin, A. N. Turkin, K. G. Zolina, and A. E. Yunovich in *Abstracts 23rd International Symp. on Semiconductor Compounds*, St. Petersburg, 1996), Abstr. 03.P3.04.
[4] K. G. Zolina, V. E. Kudryashov, A. N. Turkin, and A. É. Yunovich, Fiz. Tekh. Poluprovodn. **31** 901 (1997) [Semiconductors **31**, 1055 (1997)].
[5] A. É. Yunovich and A. B. Ormont, Zh. Éksp. Teor. Fiz. **51**, 1292 (1966) [Sov. Phys. JETP **24**, 869 (1967)].
[6] T. N. Morgan, Phys. Rev. **148**, 890 (1966).
[7] S. Nakamura, M. Senoh, N. Iwasa, T. Yamada, and T. Mukai, J. Appl. Phys. **34**, L1332 (1995).
[8] F. I. Manyakhin, Izmer. Tekh. **11**, 49 (1996).
[9] J. Zeller, P. G. Eliseev, P. Sartori, P. Perlin, and M. Osinski, Mater. Res. Soc. Symp. Proc. **395**, 937 (1996).
[10] A. Satta, V. Fiorentini, A. Bosin, and F. Meloni, Mater. Res. Soc. Symp. Proc. **395**, 515 (1996).
[11] U. Kaufmann, M. Kunser, C. Mers, I. Akasaki, and H. Amano, Mater. Res. Soc. Symp. Proc. **395**, 633 (1996).
[12] D. M. Hoggmann, D. Kovalev, G. Steude, D. Volm, B. K. Meyer, C. Xavier, T. Momteiro, E. Pereira, E. N. Mokhov, H. Amano, and I. Akasaki, Mater. Res. Soc. Symp. Proc. **395**, 619 (1996).

Translated by M. E. Alferieff

Electron-structural metastability of cationic donor centers in GaAs

D. E. Onopko and A. I. Ryskin

All-Russia Science Center ''S. I. Vavilov State Optics Institute'' 199034 St. Petersburg, Russia

N. T. Bagraev

A. F. Ioffe Physicotechnical Institute, Russian Academy of Sciences 194021 St. Petersburg, Russia
(Submitted February 27 1997; accepted April 10 1997)
Fiz. Tekh. Poluprovodn. **31**, 1310–1313 (November 1997)

The reconstruction of shallow donors in GaAs–$Ga_{1-x}Al_xAs$ crystals, which is accompanied by the formation of deep cationic *DX* centers, is studied for the first time in a cluster approximation using the self-consistent, scattered-wave method. It is demonstrated that the formation of a C_{3v} DX^- state could be due to the difference in the electronic structure of a shallow donor from the structure of a lattice atom. This difference is the reason why an impurity atom transfers into the nearest tetrahedral interstice. The model proposed for cationic *DX* centers is based on the fundamental possibility of localization of two antibonding electrons on an antobonding orbital of one of the four tetrahedral bonds of an impurity center with arsenic ligands. This greatly weakens the bond and results in a corresponding formation of a trigonal DX^- state. © *1997 American Institute of Physics.* [S1063-7826(97)00411-0]

1. INTRODUCTION

The formation of substitution centers in semiconductors in many cases is accompanied by a reconstruction of both the impurity ion and the surrounding lattice atoms. This is reflected in a corresponding lowering of the full symmetry of the defect. The possible crystallographic avenues for reconstruction of impurity centers as a result of relaxation of the crystal lattice of elementary semiconductors as well as III–V and II–VI compounds have been studied in the cluster approximation.[1–4] The self-consistent scattered-wave method made it possible to determine the most likely symmetry of the defect and substantiate its metastable properties, which arise as a result of the distinguishing features of the electronic structures of the impurity ion and lattice atom.[1–4]

If the electronic structures of the impurity atom differ substantially from that of a lattice atom, then a spontaneous reconstruction of a substitution center is accompanied, as a rule, by a lowering of its symmetry from tetrahedral to trigonal (C_{3v}) or orthorhombic (C_{2v}).[1] In the opposite case, when the electronic structure of the impurity center corresponds to the structure of the corresponding fragment of the regular crystal, the tetrahedral symmetry of a defect either does not change at all or it changes slightly as a result of the Jahn–Teller effect. However, even when the difference in the electronic structures of the impurity and lattice atoms is small, as is the case, for example, for shallow donors in semiconductors, there is a potential for the above-described reconstruction of the impurity substitution center to occur under the influence of external perturbations, such as hydrostatic and uniaxial compression of the crystal or isovalent doping, for the purpose of obtaining solid solutions of III–V and II–VI semiconductors. The reconstruction of shallow donors, which thus far has been studied within the capabilities of the pseudopotential and density functional methods, consists of the formation of deep, negatively charged C_{3v} centers as a result of transition of the impurity ions from lattice sites into positions of tetrahedral interstices.[5–8] Such amphoteric defects, formed on the basis of shallow donors, are so-called *DX* centers,[9] which are metastable impurity centers with negative correlation energy (negative *U* centers), which tunnel, in a charge transfer process, in the semiconductor lattice between positions corresponding to different symmetries.[8,10–14] A direct consequence of their appearance is self-compensation in the system of shallow donors: $2d^0 \rightarrow DX^- + d^+$ (where DX^- is the state corresponding to the reconstructed, negatively charged C_{3v} center, and d^0 and d^+ are the filled and ionized states of the tetrahedral shallow donor), which determines the electrical properties induced by Fermi level pinning of both bulk $Ga_{1-x}Al_xAs$ crystals[5,15] and GaAs–$Ga_{1-x}Al_xAs$-type superlattices.[16]

In our study we have examined for the first time, the reconstruction of shallow donors, which stimulates lowering of the symmetry of an impurity center, from the standpoint of the difference in their electronic structure from that of the regular lattice atoms. This method for studying the problem of the reconstruction of impurity substitution centers does not make it possible to determine the energy characteristics of the deep defects that appear. This is achieved, for example, in calculations of metastable centers by pseudopotential and density functional methods.[6,8,12,13] However, the method employed makes it possible to establish the general quantum-mechanical foundations of the reconstruction of the impurity centers and directly relate them to the symmetry of the reconstructed point defects.

2. CATIONIC DONOR SILICON AND TIN CENTERS IN GaAS AND $Ga_{1-x}Al_xAs$

Cationic donor centers form in GaAs in the process of introducing group-IV impurities. The electronic charge distribution on the valence orbitals of AB_4^{3q-} clusters (q is the absolute magnitude of the ion charge) shows that Si_{Ga} sub-

TABLE I. Distribution of electronic charge in the valence orbitals of GaAs, GaAs:Si, and GaAs:As crystals (AB_4^{3q-} clusters).

Crystal	Γ	ε(Ry)	q_A	q_B	$q_\parallel$
GaAs($GaAs_4^{3q-}$)	4a1	0.129			
	$1t_1$	0.303	0.1	55	38
	$3t_2$	0.323	6.1	59	32
	$1e$	0.364	0.6	46	47
	$2t_2$	0.438	13	40	40
	$2a_1$	0.716	430	35	22
	$1t_2$	1.011	2.4	75	21
	$1a_1$	1.094	16	56	26
GaAs:Si	$4a_1$	0.122			
	$3a_1$	0.156	13	20	48
	$1t_1$	0.319	0.2	59	36
	$3t_2$	0.363	4.8	54	35
	$1e$	0.389	1.2	49	45
	$2t_2$	0.488	19	39	37
	$2a_1$	0.795	36	40	19
	$k1t_2$	1.031	3.4	72	23
	$1a_1$	1.136	23	48	28
GaAs:As	$4a_1$	0.124			
	$3a_1$	0.202	13	45	32
	$1t_1$	0.298	0.2	58	37
	$3t_2$	0.349	4.1	52	39
	$1e$	0.369	1.2	48	45
	$2t_2$	0.519	30	34	32
	$2a_1$	0.881	26	54	17
	$1t_2$	0.015	4.9	70	23
	$1a_1$	1.212	48	28	24

Note: Γ — irreducible representation; ε — single-electron energy; q_A, q_B, $q_\parallel$ — fractions of the orbital electronic charge (%), localized inside a sphere of a central atom, in the ligand atomic spheres and in the interatomic region, respectively. The fraction of the charge in the outer region is: $q_\parallel = 1 - q_A - q_B - q_\parallel$.[1–3] The $4a_1$ orbital corresponds to the conduction band minimum; the $1t_1$orbital corresponds to the valence band maximum.

stitution centers do not significantly change the electronic structure of GaAs (see Table I). The main bonding orbitals (a_1,$2a_1$,$2t_2$) undergo only a very small transformation. The largest difference is the appearance of an antibonding donor state $3a_1$ occupied by one electron.

On this basis, the tetrahedral structure of a Si_{Ga} donor center is very stable in a neutral state as a result of the fact that group-IV atoms predominantly tend to form tetracoordinated compounds. At the same time, the nonisovalent character of the substitutions, which leads to the presence of an unused valence electron, though weakly bound, as well as the existing probability for a group-IV atom to pass into a divalent state, determine the fundamental possibility of reconstruction of a shallow Si_{Ga} donor. The necessary condition for this to happen is that an antibonding additional electron must be trapped at the donor center. This excess electron decreases the binding energy of the center with one of the arsenic ligands, thereby allowing a transition of the impurity silicon atom to a stable bond with the three remaining arsenic ligands. Such a large weakening of the As–Si bond becomes possible only if the impurity atom is displaced into a tetrahedral interstitial position (Fig. 1), which lowers the initial symmetry of the defect to C_{3v} (trigonal) symmetry. It should be noted that the above-described reconstruction of a shallow donor requires that a potential energy barrier separating the position of an impurity center in an interstice and a tetrahedral interstice be overcome.

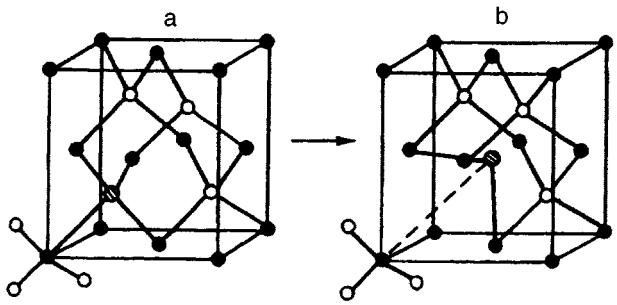

FIG. 1. Model of a DX center based on a shallow silicon donor in GaAs–$Ga_{1-x}Al_xAs$ (a — neutral state of a shallow donor with T_d symmetry, b — DX^- state with C_{3v} symmetry).

After the above-noted compensation of the weakened As–Si bond occurs, the negatively charged silicon center possesses eight electrons, four of which belong directly to the Si atom (s^2p^2), for the formation of bonds with three arsenic ligands. In III–V crystals the cation gives up $0.75e$ per bond and an anion gives up $1.25e$. Therefore, approximately two electrons are required in order to fill the valence s and p shells of the three arsenic atoms. As a result, the two valence electrons of the initial $SiAs_4^{(3q+1)}$ cluster are formally excess electrons. In this case, two different methods are possible for constructing the chemical bond on the basis of a trigonal $SiAs_3^{2q-}$ cluster.

Because of the high covalence of silicon-doped GaAs crystals, the presence of excess electrons can result in higher bond multiplicity in a cluster. This becomes possible if a silicon atom passes into a s^1p^3 excited state and if a free ligand orbital, on which a fourth valence electron of the three arsenic atoms could localize, appears. The realization of the latter condition signifies an appreciable weakening of the bond of the indicated arsenic atoms with their nearest neighbors, gallium atoms. A result of this process is that two electrons, initially located in the corresponding bonding orbital, are transferred into an antibonding orbital of the neighboring gallium atoms. The energy losses due to the excitations listed above are canceled by a gain in energy as a result of an increase in the multiplicity of the As–Si bonds. In the process of the above-described reconstruction a silicon atom passes into a sp^2 hybridization state. The interaction of its fourth valence orbital (p_z type) and the above-mentioned unoccupied orbital of the ligands will form the basis for the increase in bond multiplicity (an additional p bond forms). As a result, the As–Si interatomic distance will decrease substantially when the silicon atom transfers into an interstice. The above-indicated antibonding orbital, whose formation is greatly enhanced by the gallium atoms from the second coordination sphere of the impurity atom, will be the highest filled DX^- state of the negative charged defect studied.

If a silicon atom passes into a divalent state, then the bonds inside a $SiAs_3^{2q-}$ cluster will remain single and the interatomic distance As–Si will not change appreciably. In this case, two excess electrons will be localized in an anti-

bonding orbital which arises on the basis of the $s(p)$ orbital of silicon. This orbital is the last filled DX^- state of the negatively charged impurity center. As a result, the excess electrons form an unshared pair of the impurity atom under conditions such that its sp^3 hybridization is preserved.

In reality, a superposition of the above-described versions of the reconstruction of a defect probably will be realized. As a result, the muliplicity of the As–Si bonds will increase appreciably as the corresponding interatomic distances decrease, and the hybridization state of the impurity silicon atom will be an intermediate state between the sp^2 and sp^3 structures. The orbital of a deep, negatively charged state of the reconstructed DX center will contain an appreciable contribution of gallium cations from the second coordination sphere and a relatively diminished contribution from the atomic functions of the impurity silicon atom. Irrespective of the reconstruction mechanism, this orbital will also be influenced by a ligand with a weakened As–Si bond (Fig. 1), since the displacement of the impurity atom into an interstice cannot completely eliminate the corresponding interaction.

This arsenic ligand will in turn form a trigonal (C_{3v}) cluster with three nearest-neighbor gallium atoms. Inside this cluster the interatomic distances will not change much. The orbital of the weakened As–Si bond is largely determined by this cluster, although it contains a small contribution from the atomic functions of the impurity atom. The corresponding level is localized in the valence band of the crystal.

Reconstruction of a tetrahedral impurity center requires that the occupied level of the C_{3v} DX^- state be quite deep compared with the initial shallow donor level. Otherwise, the lowering of the symmetry of the defect, accompanied by the above-described self-compensation process due to the presence of a negative correlation energy (negative U energy) $2d^0 \Rightarrow d^+ + DX^-$, would be energetically unfavorable. Ionization of the DX^- state of the reconstructed center will in turn be accompanied by a transfer of excess energy to the lattice. This will make it possible for an impurity atom to overcome the potential barrier separating the positions of the T_d and C_{3v} states: $DX^- + d^+ \rightarrow 2d^0$. The presence of a potential barrier separating the positions of the charged states of a DX center will also be reflected in the fact that the optical ionization energy of a DX^- state will be several times higher than its thermal ionization energy.[9,15] The ionization-dependent decrease of the charge of the unshared pair in the cluster $SiAs^{2q-}$ makes its structure much flatter, thereby strengthening the weakened As–Si bond, which results in a shortening of the corresponding interatomic distance and creates conditions for a subsequent transition of the second electron of the unshared pair into a state of a weakly bound electron at a shallow donor.

It was noted above that the deep level of the DX^- state in GaAs crystals is formed largely by cations from the second sphere. This explains the fact that the L valley of the conduction band plays a predominant role in its formation. The position of this level is fixed relative to the L valley by a corresponding change in the structure of the conduction band in the process of hydrostatic compression of the crystal and variation of the composition of the solid solutions $Ga_{1-x}Al_xAs$ For this reason, the self-compensation phenomenon, which is induced by the appearance of DX centers, is most pronounced near the point corresponding to crossing of the $\Gamma - X$ valleys, when the ionization energy of the DX^- state is much higher than that of a shallow donor.[15]

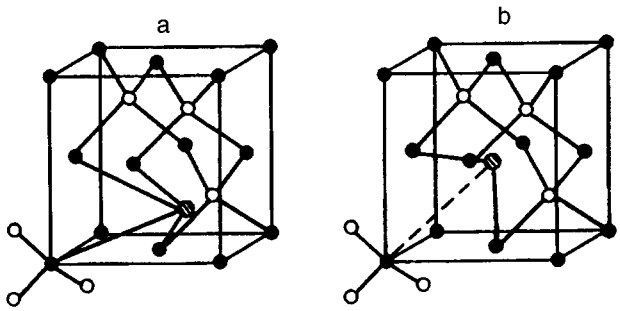

FIG. 2. Model of a DX center based on a shallow tin donor in GaAs–$Ga_{1-x}Al_xAs$ (a — DX^0 state with C_{2v} symmetry, b — DX^- state with C_{3v} symmetry).

The foregoing analysis refers primarily to the system silicon-doped GaAs–$Ga_{1-x}Al_xAs$, where a deep DX^- state forms directly from a tetrahedral shallow donor. The situation is somewhat different in the case of the formation of a DX center in tin-doped GaAs and $Ga_{1-x}Al_xAs$ crystals.[17–19] Electron spin resonance studies under conditions of monochromatic optical pumping[17] and optical detection of magnetic resonance[18,19] have shown that the reconstruction of shallow tin donors proceeds in two steps. First, some shallow tin donors transform into deep neutral centers with C_{2v} symmetry (Fig. 2a). Despite their metastability, these centers dissociate as a result of the negative correlation energy: $2DX^0 \rightarrow DX^- + DX^+$ [where DX^- and DX^+ are states of the DX center that are characterized by C_{3v} (Fig. 2b) and D_{2d} symmetry, respectively[14,20]]. Next, a compensation reaction of nonreconstructed shallow tin donors occurs: $DX^+ + Sn^0 \rightarrow DX^0 + Sn^+$, which is accompanied by the above-described self-compensation reaction in the system of the DX center. In contrast to silicon-doped $Ga_{1-x}Al_xAs$ crystals, whose irradiation with monochromatic light revealed only the ESR of shallow donors,[17] the study of an analogous system containing tin demonstrated in the process of optical pumping regeneration of two centers simultaneously — a shallow tin donor and a deep tin center with C_{2v} symmetry.[17–19] This behavior of tin centers is due to the larger, compared with other group-IV impurity atoms, changes of the electronic structure of GaAs and $Ga_{1-x}Al_xAs$ crystals in the doping process, the direct consequence of which is the observation of the reconstructed neutral state of the DX center.

The proposed description of DX centers in GaAs and $Ga_{1-x}Al_xAs$ crystals containing group-IV impurity centers agrees with the results of the corresponding pseudopotential[6] and density-functional.[21] Specifically, in Ref. 21 it is noted that there is a large similarity in the change in the bond character accompanying the formation of DX centers in GaAs:Si and accompanying a phase transition of diamond into graphite. It is expressed as a change in the state of the hybridization of the carbon atom from sp^3 to sp^2. In contrast to the data of Refs. 6 and 7, we took into account the

contribution of cations from the second sphere to the formation of the DX^- state.

3. CONCLUSIONS

The versions of the reconstruction of shallow silicon and tin donors in GaAs and $Ga_{1-x}Al_xAs$ crystals, which we examined above, suggest the following model of the formation of cationic DX centers. In the initial tetrahedrally symmetric state, a shallow donor is bound with four arsenic ligands by means of two-electron bonds. The weakly bound donor electron is located in a delocalized antiboinding donor orbital. The capture of the second electron in an antibonding orbital can result in a reconstruction of the impurity center with a lowering of its symmetry. It is in principle possible for two antibonding electrons to be localized in antibonding orbitals of one of the four tetrahedral bonds of the impurity atom. As a result, there will be four electrons in the identified As–Si bond. This will greatly weaken the bond and stimulate a displacement of an impurity atom into the nearest tetrahedral interstice, thereby forming a C_{3v} DX^- state. Optical ionization of a trigonal DX^- state transforms the reconstructed deep center into a shallow donor at a lattice site.

[1] D. E. Onopko, N. T. Bagraev, and A. I. Ryskin, Fiz. Tverd. Tela (St. Petersburg) **37**, 2376 (1995) [Phys. Solid State **37**, 1299 (1995)].
[2] D. E. Onopko, N. T. Bagraev, and A. I. Ryskin, Fiz. Tverd. Tela (St. Petersburg) **38**, 142 (1996) [Phys. Solid State **38**, 137 (1996)].
[3] D. E. Onopko, N. T. Bagraev, and A. I. Ryskin, Phys. Lett. A **198**, 58 (1995).
[4] D. E. Onopko and A. I. Ryskin, Fiz. Tverd. Tela (St. Petersburg) **38**, 689 (1996) [Phys. Solid State **38**, 382 (1996)].
[5] P. M. Mooney, J. Appl. Phys. **67**, R1 (1990).
[6] D. J. Chadi and K. J. Chang, Phys. Rev. B **39**, 10063 (1989).
[7] T. N. Morgan, Mater. Sci. Forum **38–41**, 1079 (1989).
[8] D. J. Chadi and K. J. Chang, Phys. Rev. Lett. **61**, 873 (1988).
[9] D. V. Lang in *Deep Centers in Semiconductors*, edited by S. T. Pantelides, Gordon and Breach, N. Y., 1986, p. 489.
[10] G. D. Watkins, Festkoerperprobleme **24**, 163 (1984).
[11] N. T. Bagraev and V. A. Mashkov, Solid State Commun. **65**, 1111 (1988).
[12] J. Dabrpwslo and M. Scheffler, Phys. Rev. Lett. **60**, 2183 (1988).
[13] D. J. Chadi and K. J. Chang, Phys. Rev. Lett. **60**, 2187 (1988).
[14] N. T. Bagraev, Defect Diffus. Forum **103–105**, 67 (1993).
[15] J. C. Bourgoin, S. L. Feng, and H. J. von Bardeleben, Phys. Rev. B **40**, 7663 (1989).
[16] T. Baba, M. Mizuta, T. Fujisawa, J. Yoshino, and H. Kukimoto, J. Appl. Phys. **28**, L.891 (1989).
[17] H. J. von Bardeleben, M. Sheinkman, C. Delerue, and M. Iannoo, Mater. Sci. Forum **83–87**, 784 (1992).
[18] M. Foeckele, J.-M. Spaeth, H. Overhof, and P. Gibart, Mater. Sci. Forum **83–87**, 835 (1992).
[19] M. Linde, T. Pawlik, and J.-M. Spaeth, Mater. Sci. Forum **143–147**, 1041 (1994).
[20] N. T. Bagraev and A. Yusupov, Fiz. Tekh. Poluprovodn. **28**, 198 (1994) [Semiconductors **28**, 119 (1994)].
[21] J. Dabrowski and M. Scheffler, Mater. Sci. Forum **83–87**, 735 (1992).

Translated by M. E. Alferieff

Optical properties of thin n-$Pb_{1-x}Sn_xSe/BaF_2$ epitaxial layers in the plasmon–phonon interaction region

A. A. Kopylov, V. A. Moshnikov, and A. N. Kholodilov

St. Petersburg State Electrical Engineering University, 197376 St. Petersburg, Russia
(Submitted September 20, 1995; accepted for publication April 24, 1997)
Fiz. Tekh. Poluprovodn. **31**, 1314–1320 (November 1997)

The optical reflection and transmission spectra of submicron epitaxial $Pb_{1-x}Sn_xSe/BaF_2$ layers with $x=0.04-0.21$ have been investigated. The parameters of the electron plasma are determined by modeling the shape of the spectra. The interband contribution to the dielectric function of $Pb_{1-x}Sn_xSe$ is estimated. © *1997 American Institute of Physics.* [S1063-7826(97)00711-4]

The band structure and the optical and electrical properties of the lead chalcogenides PbTe, PbSe, and PbS as well as the solid solutions $Pb_{1-x}Sn_xTe$, which are widely used in practice, have now been well studied.[1–3] The properties of solid solutions in the system $Pb_{1-x}Sn_xSe$ have been given much less attention.

In this study we have investigated, the optical reflection and transmission spectra of micron-thick n-$Pb_{1-x}Sn_xSe$ epitaxial layers with $x=0.04-0.21$ on BaF_2 substrates by using the method of infrared-range Fourier spectroscopy.

1. SAMPLES AND MEASUREMENT PROCEDURE

The $Pb_{1-x}Sn_xSe$ layers were grown by the hot-wall method on fresh cleavage faces of BaF_2 substrates with ⟨111⟩ orientation. Growth was conducted in an URM 3279011 apparatus. The construction of the evaporation chamber is similar to that described in Ref. 4. S-0000 lead, ultrapure tin, and analytically pure selenium were employed to synthesize the initial charge. Prior to growth, the charge was subjected to homogenizing isothermal annealing at 850–1000 K for 8–10 h under dynamic vacuum conditions. The composition of the initial charge varied in the range 0.1–0.2 of the molecular fraction of SnSe. The temperatures in the sublimation and substrate zones were equal to 770 and 500–550 K, respectively. The growth rate of the layers was equal to 0.7–1.0 μm/h.

The layers grown possessed ⟨100⟩ orientation. The composition of the solid solution was measured on a DRON-3M diffractometer. A tube with a copper anode (Cu $K\alpha$ radiation) was used. In the operating regime of the tube, the anode potential was equal to 30–35 mV and 15–35 mA the anode current was equal to, depending on the thickness of the layer. The uniformity of the composition of the layers was checked by x-ray spectral microanalysis on a Cameca MS-46 microanalyzer. The basic characteristics of the samples are presented in Table I.

The measurements of the optical reflection spectra in the range $30-650\ cm^{-1}$ were performed at temperatures of 10, 80, and 300 K using a LFS-1000 long-wavelength Fourier spectrometer[5]. The samples were secured on the cold duct of a nitrogen or helium vacuum cryostat. The measurements at $T\approx 10$ K were performed with a R-118 cryostat. No special surface treatment of the samples was performed. Repeated measurements performed every few months showed that the shape of the reflection spectra was stable.

The transmission spectra in the range $500-2700\ cm^{-1}$ were measured on a LAFS-02 rapid-scan Fourier spectrometer at temperatures of 300–520 K using a resistance heater.

2. ANALYSIS OF THE SHAPE OF THE REFLECTION SPECTRA

Figures 1 and 2 show examples of the reflection spectra of the experimental samples at different temperatures. A characteristic feature of all spectra is the presence of structure, due to a band of residual rays from BaF_2, in the region $150-350\ cm^{-1}$. The sharp drop in the frequency range above $300\ cm^{-1}$ is due to plasma oscillations of free charge carriers. An appreciable peak near $40\ cm^{-1}$, due to transverse optical phonons in the solid solution $Pb_{1-x}Sn_xSe$, is also observed for all samples.

The analysis of the reflection spectra was based on the model of an ''epitaxial layer on a semiinfinite substrate.'' To describe the dispersion of the refractive index of the solid solution we used a dielectric function of the form

$$\varepsilon(\omega)=\varepsilon_\infty-\frac{\varepsilon_\infty\omega_p^2}{\omega(\omega+i/\tau)}+\frac{S\omega_T^2}{\omega_T^2-\omega^2-i\omega\gamma}, \tag{1}$$

where ω is the frequency, ε_∞ is the high-frequency permittivity, ω_p and τ are, respectively, the plasma frequency and relaxation time of free charge carriers, and S, γ, and ω_T are, respectively, the oscillator strength, the damping parameter, and the frequency of the transverse optical phonon. The oscillator strength was determined in the form $S=\varepsilon_s-\varepsilon_\infty$, where ε_s is the static permittivity.

The parameters ω_p and τ, which most strongly influence the shape of the model spectrum, were chosen so as to obtain the best agreement between the computed and experimental spectra. Examples of the computed spectra are shown in Figs. 1 and 2 by the dashed lines and demonstrate the degree of agreement with experiment. The values obtained for ω_p and τ are presented in Table II.

TABLE I. Characteristics of the experimental n-$Pb_{1-x}Sn_xSe/BaF_2$ samples.

Sample No.	Composition (x)	Layer thickness, μm
1	0.04	0.19
2	0.11	0.15
3	0.21	0.2
4	0.06–0.08	0.38

3. DETERMINATION OF THE PARAMETERS OF FREE CHARGE CARRIERS

We shall now find a relation between the plasma frequency and the Fermi level. It is known that

$$\omega_p^2=\frac{ne^2}{\varepsilon_0\varepsilon_\infty m_{\text{opt}}}, \tag{2}$$

where n is the charge carrier density, and m_{opt} is the optical effective mass. In a two-band Kane model, the charge carrier density[2] and optical effective mass[6] can be expressed as

$$n=\frac{M}{3\pi\hbar^3}[m_d(0)kT]^{3/2}\,{}^0L_0^{3/2} \quad \text{and}$$

$$m_{\text{opt}}=\frac{3K}{2K+1}K^{-1/2}\frac{{}^0L_0^{3/2}}{{}^0L_{-1}^{3/2}}m_d(0), \tag{3}$$

where M is the number of equivalent extrema in the band ($M=4$), K is the anisotropy factor, $m_d(0)$ is the effective mass of the density of states at the band bottom (per ellipsoid), and

$${}^0L_n^m(\eta,\beta)=\int_0^\infty \frac{\exp(y-\eta)}{[1+\exp(y-\eta)]^2}(y+\beta y^2)^m \times(1+2\beta y)^n dy$$

are the generalized Fermi integrals ($\eta=E_F/kT$ and $\beta=kT/E_g$). Subsituting the expressions (3) into the expression (2), we obtain an equation for the Fermi level

$${}^0L_{-1}^{3/2}(\eta,\beta)=\frac{9\pi^2}{2^{3/2}M}\frac{\hbar^3\varepsilon_0\varepsilon_\infty K^{3/2}\omega_p^2}{e^2 m_d(0)^{1/2}(kT)^{3/2}(2K+1)}. \tag{4}$$

The Fermi level is measured from the conduction band bottom. The band gap as a function of the composition and temperature was calculated from the relation[3]

$$E_g(x,T)=125-1021x+(400+0.256T^2)^{1/2}, \tag{5}$$

where E_g is expressed in meV. The effective mass of the density of states at the conduction band bottom was expressed in terms of the interband interaction parameter P as

$$m_d(0)=\frac{\hbar^2}{2}\frac{E_g}{P^2}, \quad P=\frac{\hbar}{m_0}|\mathbf{p}_{cv}|, \tag{6}$$

where $\mathbf{p}_{cv}$ is the matrix element of the momentum operator. Following Ref. 7, we use the value $p=3.7\times10^8$ eV·cm, and also $K=2$ for $x=0.04-0.11$ and $K=1$ for $x=0.21$.

A method for calculating the parameters of the electron plasma is discussed in the Appendix. The computational results for E_g, E_F, n, and m_{opt} are presented in Table II.

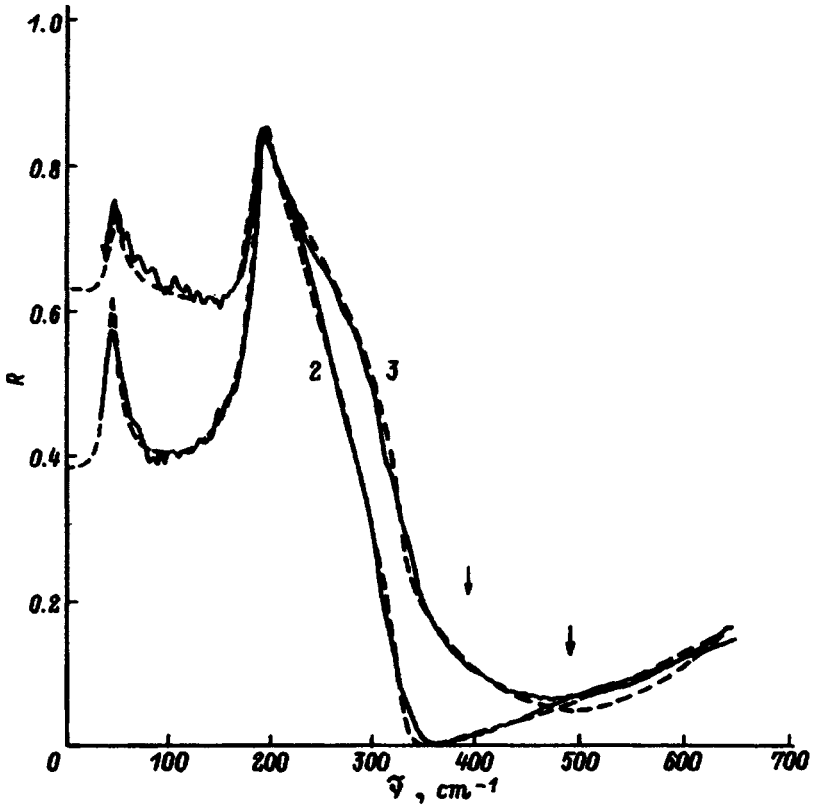

FIG. 1. Optical reflection spectra of n-$Pb_{1-x}Sn_xSe/BaF_2$ samples at $T=300$ K. Solid line—experiment, dashed line—calculation. The numbers on the curves correspond to the numbers of the samples in Tables I and II. The arrows mark the wave numbers corresponding to the plasma frequency; R—reflection coefficient, $\tilde{\nu}$—wave number.

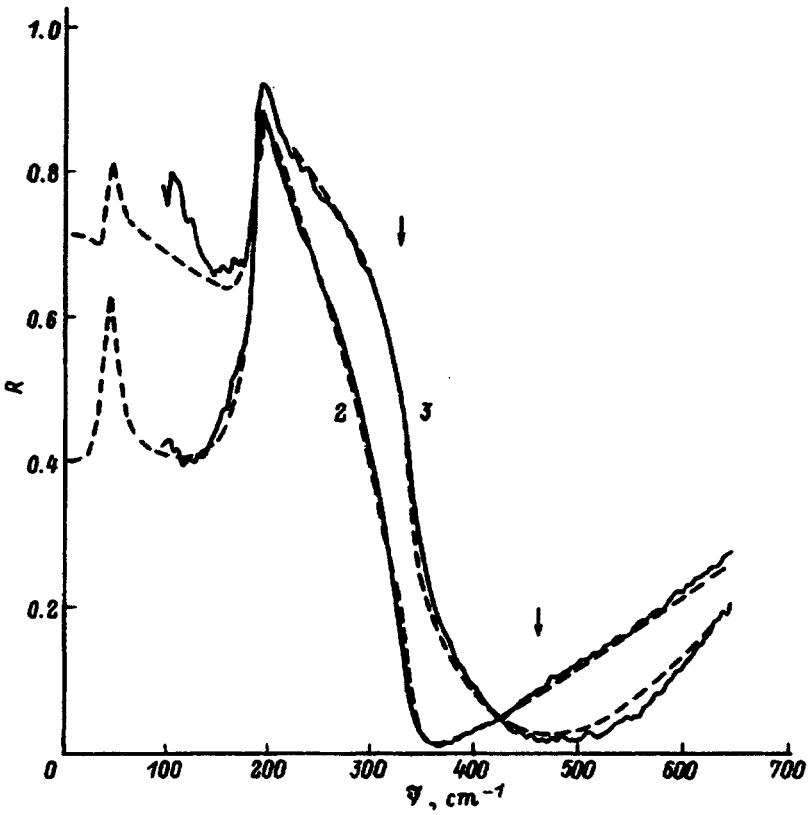

FIG. 2. Optical reflection spectra of n-$Pb_{1-x}Sn_xSe/BaF_2$ samples at $T=80$ K. The labels are the same as in Fig. 1.

4. CALCULATION OF THE INTERBAND CONTRIBUTION

In the random-phase approximation, the expression for the interband contribution for one valley to the imaginary part of the permittivity can be written as[8]

$$\Delta\varepsilon^n_{\text{inter}}(\omega)=\frac{\pi e^2\hbar^2}{\varepsilon_0 m_0^2}\sum_{\mathbf{k}}\frac{|\mathbf{p}_{cv}|^2}{|E_c(\mathbf{k})-E_v(\mathbf{k})|}\,\delta[\hbar\omega-E_c(\mathbf{k})+E_v(\mathbf{k})](f_v-f_c), \tag{7}$$

where

$$f_{c,v}=\left[1+\exp\frac{E_{c,v}(\mathbf{k})-E_F}{kT}\right]^{-1},$$

$$E_{c,v}(\mathbf{k})=-\frac{E_g}{2}\pm\left(\frac{E_g^2}{4}+k^2P^2\right)^{1/2}$$

are the distribution function and dispersion relation for the conduction and valence bands.

Switching from summation to integration in the spherical approximation, making the assumption that the contribution of the four valleys at the point L_6 to the permittivity is additive, and substituting the second expression in (6), we obtain the following relation for the imaginary part of the permittivity:

TABLE II. Parameters of plasma oscillations and the characteristics of the band structure and the electronic plasma for epitaxial layers of n-$Pb_{1-x}Sn_xSe/BaF_2$ structures.

Sample No.	T, K	$\omega_p/2\pi c$, cm^{-1}	$1/2\pi c\tau$, cm^{-1}	E_g, meV	E_F, meV	n, 10^{18}, cm^{-3}	$\frac{m_{\text{opt}}}{m_0}$
1	300	390	250	237	29	4.7	0.107
	80	420	111	129	68	4.4	0.072
	10	460	154	105	83	5.2	0.072
2	300	390	208	166	40	4.2	0.091
	80	330	154	58	64	1.9	0.051
3	300	490	143	64	95	7.2	0.089
	80	465	91	−44	107	5.7	0.073
	10	480	167	−69	103	6.3	0.077
4	300	330	213	207	20	3.0	0.097
	80	350	167	99	59	2.5	0.059

Note. The following initial data were used in modeling the IR reflection spectra: BaF_2: $\omega_T=184$ cm^{-1} ($T=300$ K), $\omega_T=189$ cm^{-1} ($T=80$ K), $\omega_T=190$ cm^{-1} ($T=10$ K), $\varepsilon_s=1.8$, $\varepsilon_\infty=5.75$; $Pb_{1-x}Sn_xSe$: $\varepsilon_\infty(x)=(4.9+2.8x)(T=300\text{ K})$, $\varepsilon_\infty(x)=(5.5+0.8x)$ ($T=10.80$ K),[3] $\varepsilon_s=210$ ($T=300$ K), $\varepsilon_s=231$ ($T=10.80$ K),[2] $\omega_T=44$ cm^{-1}. The composition for sample No. 4 is $x=0.07$.

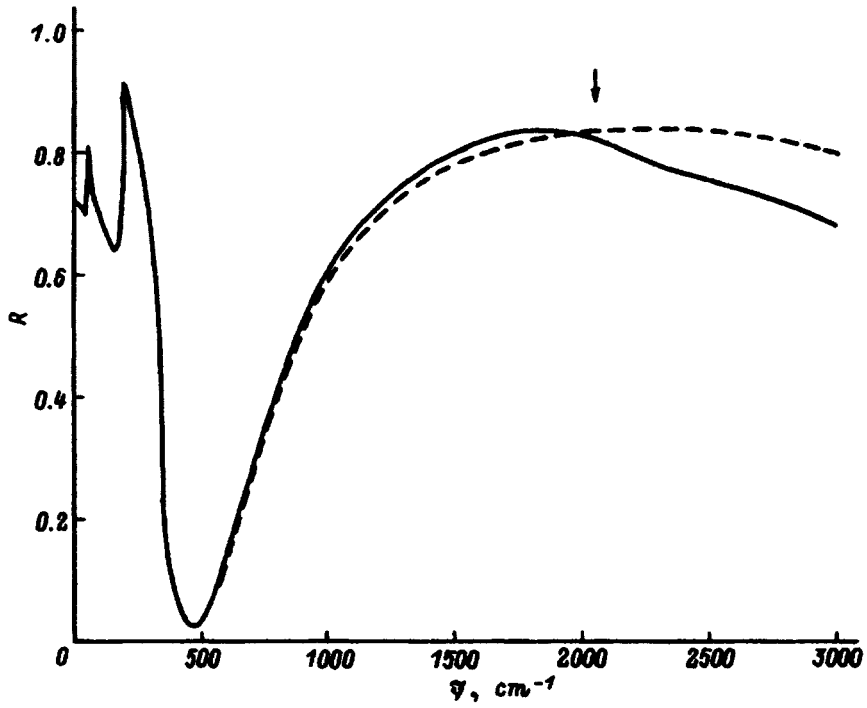

FIG. 3. Computed optical reflection spectra of the structure n-$Pb_{1-x}Sn_xSe/BaF_2$ (R—reflection coefficient). The parameters of the model correspond to sample No. 3, $T=80$ K. Solid line—calculation allowing for the interband contribution, dashed line—neglecting the interband contribution. The arrow marks the wave number $\tilde{\nu}$ corresponding to the energy $|E_g|+2E_F$.

$$\Delta\varepsilon''_{\text{inter}}(\omega)=A\sqrt{1-\left(\frac{E_g}{\hbar\omega}\right)^2}\left[\left(1+\exp\frac{\hbar\omega/2+E_F+E_g/2}{kT}\right)^{-1}-\left(1+\exp\frac{\hbar\omega/2-E_F-E_g/2}{kT}\right)^{-1}\right], \tag{8}$$

where $A=e^2(2\pi\varepsilon_0 P)=7.8$. The Fermi level is measured from the conduction band bottom.

To calculate the real part of the permittivity we employ the approximation of the Kramers–Kronig relation

$$\Delta\varepsilon'_{\text{inter}}(\omega)=\frac{2}{\pi}\int_{E_g}^{E_{\max}}\frac{\omega'}{\omega'^2-\omega^2}\Delta\varepsilon''_{\text{inter}}(\omega)d\omega, \tag{9}$$

where the integral is taken in the principal-value sense.

If $E\gg(\hbar\omega,E_g,E_F)$, then varying $E_{\max}$ in the experimental frequency range will only change the constant component of the real part of the permittivity. This constant component

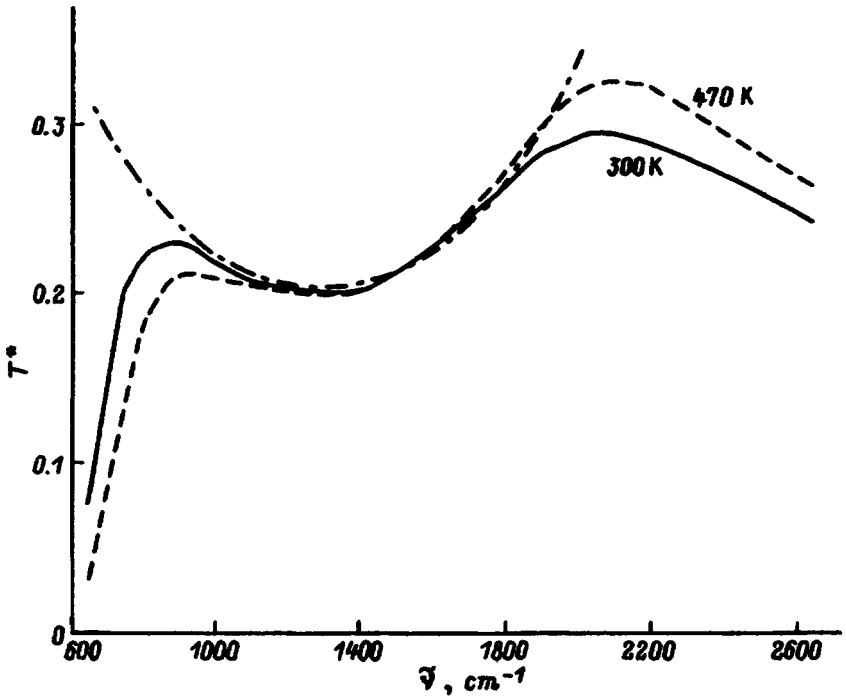

FIG. 4. Optical transmission spectra of n-$Pb_{1-x}Sn_xSe/BaF_2$. Experiment (sample No. 4): Solid line—$T=300$ K, dashed line—$T=470$ K. Dot-dashed line—calculation neglecting absorption in the layer; T*—transmission coefficient.

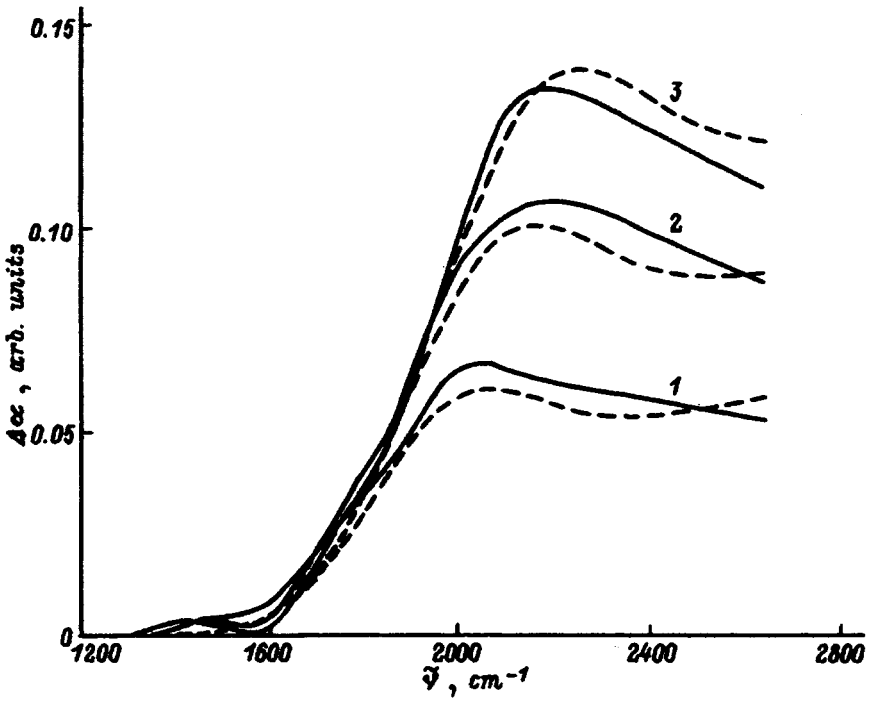

FIG. 5. Optical absorption of n-$Pb_{1-x}Sn_xSe/BaF_2$ in the region of interband transitions. Solid line—experiment (sample No. 4), dashed line—calculation. The numbers on the curves correspond to the temperature T, K: *1*—410, *2*—470, *3*–520. The curves represent the difference in the optical densities for the indicated temperature and $T=300$ K.

can be eliminated by writing the contribution of the interband transitions to the real part of the permittivity as the difference $\Delta\varepsilon'_{\text{inter}}(\omega)-\Delta\varepsilon'_{\text{inter}}(0)$ and assuming that the constant component is now taken into account in the phenomenological parameters ε_∞ and ε_s.

The computed values of $\Delta\varepsilon'_{\text{inter}}(\omega)$ and $\Delta\varepsilon''_{\text{inter}}(\omega)$ were taken into account additively in the expression (1). Figure 3 shows the spectral dependences of the reflection coefficient calculated with and without the interband contribution. We see that the interband contribution makes an appreciable difference only above $1000\ \text{cm}^{-1}$. This makes it possible to determine quite reliably the characteristics of the plasma neglecting the interband contribution.

5. ANALYSIS OF THE TRANSMISSION SPECTRA

Examples of the transmission spectra of sample No. 4, which were obtained at different temperatures, are shown in Fig. 4. The dropoff of transmission at frequencies below $1000\ \text{cm}^{-1}$ is due to absorption by free charge carriers and single-phonon absorption in the substrate. This absorption increases with temperature. The reverse picture is observed at frequencies above $1800\ \text{cm}^{-1}$, where absorption can be due to characteristic interband transitions. This can be explained qualitatively by an increase in the band gap with temperature. The section of the spectrum $1000-1800\ \text{cm}^{-1}$ is virtually temperature-independent, indicating that absorption is weak, and the shape of this section can be explained by interference in the epitaxial layer. The corresponding estimate made for refractive index $n_0=5.1$ and epitaxial layer thickness 0.38 μm is shown in Fig. 4 (dashed line).

The characteristic absorption can be estimated directly from Eq. (8), allowing for the fact that the absorption coefficient is $\alpha(\omega)=2\pi\tilde{\nu}\varepsilon''(\omega)/n_0$, where $\tilde{\nu}=\omega/2\pi c$ is the wave number, and n_0 is the refractive index of the absorbing medium. For convenience, we shall study not the absorption itself but rather its variation with temperature. Figure 5 shows sections of such difference spectra calculated taking into account the interference. The curves obtained using Eq. (8) are shown by dashed lines. The values of E_g and E_F employed in the calculation are given in Table III. Agreement between the experimental and computed optical densities was obtained with $A=5.2$ (instead of $A=7.8$). We note that the values of E_g presented in Table III correspond to a temperature coefficient of the variation of the band gap equal to 2.6×10^{-4} eV/K (Ref. 9) and composition $x\approx0.06$.

In summary, the behavior of the transmission spectra in the range $1000-1800\ \text{cm}^{-1}$ can be attributed to the temperature variation of the band gap of the solid solution.

6. APPENDIX

Equation (4) for the Fermi level can be solved only numerically. The results of such a calculation are presented in Fig. 6 in the form of curves of the plasma frequency versus the position of the Fermi level. As follows from the form of the curves, these functions can be approximated by a comparatively simple expression, which can be convenient for

TABLE III. Characteristics of the band structure and electronic plasma for sample No. 4 at different temperatures.

T, K	E_g, meV	E_F, meV
300	221	20
410	250	0
470	265	−12
520	278	−22

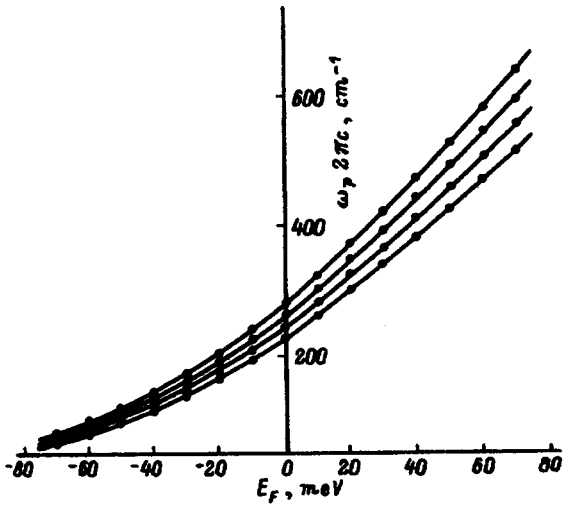

FIG. 6. Relation between the conduction electron Fermi energy and the plasma frequency for $Pb_{1-x}Sn_xSe/BaF_2$ at $T=300$ K. The numbers on the curves correspond to the values of x: *1*—0, *2*—0.04, *3*—0.08, *4*—0.12. Dots—numerical solution of Eq. (4); lines—calculations according to Eq. (10). The parameter values employed for the calculations are discussed in the text.

practical calculations. In particular, at room temperature ($T=300$ K) and for compositions in the range $x=0-0.12$ we can use the following expression:

$$\ln \tilde{\nu}_p = 5.636 - 1.797x - 0.01485E_F - 4.26\times 10^{-5}E_F^2, \tag{10}$$

where $\tilde{\nu}_p=\omega_p/2\pi c$ is expressed in cm^{-1}, and E_F in meV. The error in determining ω_p from Eq. (10) does not exceed 0.5%.

[1] Yu. I. Ravich, B. A. Efimova, and I. A. Smirnov, *Methods of Investigation of Semiconductors in Application to Lead Chalcogenides PbTe, PbSe, and PbS* [in Russian], Nauka, Moscow, 1968.
[2] I. M. Nesmelova, *Optical Properties of Narrow-Gap Semiconductors* [in Russian], Nauka, Novosibirsk, 1968.
[3] H. Preier, Appl. Phys. **20**, 189 (1979).
[4] A. V. Makhin and D. A. Yas'kov, Izv. LÉTI, No. 414, 97 (1989).
[5] V. A. Vasil'ev, P. E. Dyshlovenko, A. A. Kopylov, and A. N. Kholodilov, Prib. Tekh. Éksp. **5**, 174 (1990).
[6] A. G. Belov and E. P. Rashevskaya, Vestn. MGU, Ser. 3, Fiz. **19**, No. 2, 10 (1978).
[7] Yu. V. Kucherenko, Yu. A. Mityagin, L. K. Vodop'yanov, and A. P. Shotov, Fiz. Tekh. Poluprovodn. **11**, 488 (1977) [Sov. Phys. Semicond. **11**, 283 (1977)].
[8] M. Grynberg, R. Le Toullec, and M. Balkanski, Phys. Rev. B **9**, 517 (1974).
[9] T. S. Gertovich, S. I. Grineva, V. G. Gutsulyak, V. B. Orletskiĭ, K. D. Tovstyuk, and S. A. Khramtsova, Ukr. Fiz. Zh. **25**, 1369 (1980).

Translated by M. E. Alferieff

Position of antimony impurity atoms in a PbTe lattice, determined by emission Mössbauer spectroscopy

V. F. Masterov, F. S. Nasredinov, S. A. Nemov, P. P. Seregin, N. N. Troitskaya, and S. I. Bondarevskiĭ

St. Petersburg State University, 195251 St. Petersburg, Russia
(Submitted May 12, 1997; accepted for publication May 15, 1997)
Fiz. Tekh. Poluprovodn. **31**, 1321–1322 (November 1997)

It is shown by emission Mössbauer spectroscopy on ^{119}Sb(^{119m}Sn) that the localization of antimony impurity atoms in a PbTe lattice depends on the conductivity type of the material: Antimony is localized prodominantly in the anionic sublattice in electronic samples and in the cationic sublattice in hole samples. It is noted that the charge state of an antistructural defect ^{119m}Sn formed in the anionic sublattice of PbTe after ^{119}Sb undergoes nuclear decay does not depend on the position of the Fermi level. © *1997 American Institute of Physics.* [S1063-7826(97)00911-3]

Interest in the investigation of the nature of impurity states formed in lead chalcogenides by group-III and -IV atoms has increased substantially in recent years. This is explained mainly by the resonance scattering of current carriers by impurities[1] observed in these systems and the discovery of dielectronic centers with negative correlation energy in these materials.[2] However, virtually no studies are available on the group-V impurities in these compounds. It is known only that As, Sb, and Bi impurities are donors in lead chalcogenides, although the fraction of electrically active atoms is much less than unity.[3] There are two explanations for this: Either an appreciable number of the impurity atoms form in the lattice electrically inactive complexes (of the type Sb_2Te_3) or the impurity is distributed between the cationic sublattice (where it is a donor) and the anionic sublattice (where it is most likely an acceptor). A choice between alternative models can be made if the position of the antimony atoms in the lead chalcogenide lattices is determined. In our study we made such a determination for antimony impurity atoms in lead telluride PbTe by emission Mössbauer spectroscopy on the isotope ^{119}Sb(^{119m}Sn). The arrangement of the Mössbauer level of ^{119m}Sn, obtained using the parent isotope ^{119}Sb (half-life 38 h), is shown in Fig. 1a. Since the recoil energy of the daughter ^{119m}Sn atoms due to electron capture in ^{119}Sb and emission of a neutrino does not exceed 1.4 eV,[4] it can be expected that nuclear decay does not result in a displacement of the tin atoms from the normal sites in the crystal lattice. Therefore, the parameters of the emission Mössbauer spectra of ^{119}Sb(^{119m}Sn) should reflect the valence (charge) state of the ^{119m}Sn atoms localized at the sites occupied by antimony atoms.

The radioactive isotope ^{119}Sb was obtained by the reaction ^{120}Sn$(p,2n)^{119}$Sb. To separate a carrier-free preparation of ^{119}Sb, the target was dissolved in concentrated hydrochloric acid, $SbCl_3$ was extracted with isopropylene alcohol, and the preparation was purified by anionic exchange. The Mössbauer sources were prepared by melting together the PbTe samples and the carrier-free preparation $^{119}SbCl_3$, so that the approximate concentration of the tin impurity atoms did not exceed 10^{17} cm^{-3}. The initial PbTe samples were of the electronic type (with excess lead, $n\sim10^{18}$ cm^{-3}) and hole type (with exces tellurium, $p\sim10^{18}$ cm^{-3}).

The Mössbauer spectra of ^{119}Sb(^{119m}Sn) were measured with a commercial SM-2201 spectrometer at $T=80$ K with a $CaSnO_3$ absorber (surface density with respect to tin was 5 mg/cm^{-2}). The spectrum with such an absorber and a $Ca^{119m}SnO_3$ source consisted of a single line with FWHH $\Gamma=0.79\pm0.01$ mm/s, which was assumed to be the instrumental width of the spectral line. The typical spectra of the PbTe:^{119}Sb samples are presented in Figs. 1b and 1c, and the results of an analysis of the spectra are summarized in Table I.

The spectra of the n- and p-type samples consist of a superposition of two lines, whose relative intensity depends on the conductivity type of the material. The widths of both lines are much larger than the instrumental width, indicating distortion of the cubic symmetry of the local environment of the daughter ^{119m}Sn atoms. This distortion could be due to the difference in the sizes of the replaced and substituent atoms.

One of these lines (it predominates in n-type samples and we designate it as the spectrum I) has an isomeric shift characteristic of intermetallic tin compounds and it should be attributed to $^{119m}Sn^0$ centers in the anionic PbTe sublattice (the nearest-neighbor environment of these centers contains lead atoms and the interaction of tin with the lead atoms results in an isomeric shift typical of metallic tin alloys). It is obvious that the $^{119m}Sn^0$ atoms are formed from ^{119}Sb atoms occupying the anionic sublattice of PbTe.

The second line (it predominates in p-type samples and we designate it as the spectrum II) possesses an isomeric shift characteristic of divalent tin compounds and it should be attributed $^{119m}Sn^{2+}$ centers in the cationic sublattice of PbTe (the nearest-neighbor environment of these centers contains tellurium atoms and the interaction of tin with the tellurium atoms leads to an isomeric shift close to that of the ^{119}Sn spectrum of the compound SnTe). It is obvious that the $^{119m}Sn^{2+}$ atoms form from ^{119}Sb atoms located in the cationic sublattice of PbTe.

Thus, the localization of tin impurity atoms in a PbTe lattice depends on the character of the deviation of the com-

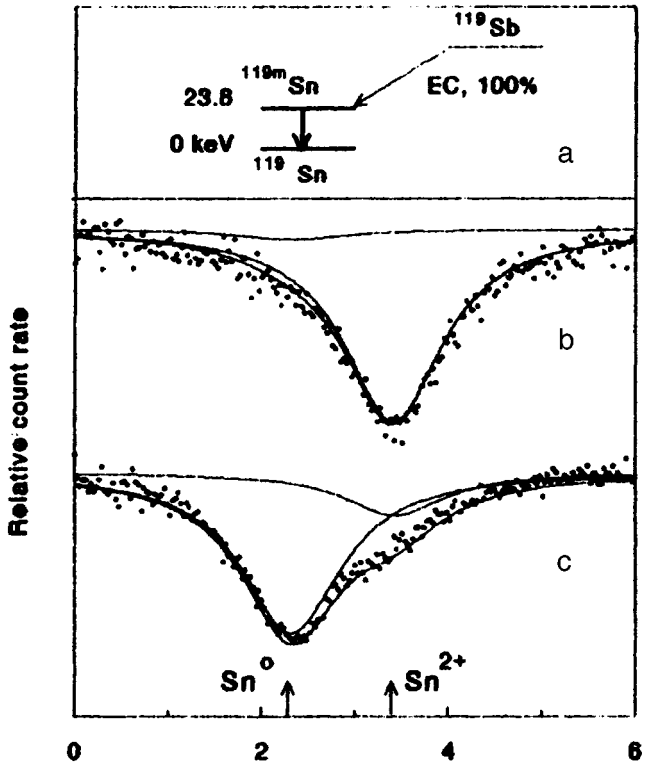

FIG. 1. a—Decay scheme of ^{119}Sb; b, c—^{119}Sb(^{119m}Sn) emission Mössbauer spectra at 80 K of *p*-PbTe (b) and *n*-PbTe (c) samples. The decomposition of the experimental spectra into components corresponding to ^{119m}Sn^{0} and ^{119m}Sn^{2+} is shown.

position from the stoichiometric composition: In samples with excess lead tin is localized predominantly in the anionic sublattice and in samples with excess tellurium it is localized predominantly the cationic sublattice (and plays the role of a donor). The fraction of electrically active antimony atoms depends on the antimony distribution between the sublattices, but it is always less than 1 (this follows from the fact that even in hole samples a significant fraction of the antimony atoms is in the anionic sublattice).

TABLE I. Parameters of the emission Mössbauer spectra of ^{119}Sb(^{119m}Sn) in PbTe at 80 K.

Conductivity type	Spectrum type	Center	mm/sec	mm/sec	*S*, %
n	I	^{119m}Sn^{0}	2.31	1.30	0.79
	II	^{119m}Sn^{2+}	3.41	1.32	0.21
p	I	^{119m}Sn^{0}	2.33	1.32	0.05
	II	^{119m}Sn^{2+}	3.43	1.31	0.95
Errors			±0.01	±0.02	±0.02

Note. I.S.—isomeric shifts with respect to $CaSnO_3$, Γ—width of the spectrum at half-height, *S*—area under the spectrum.

It should be noted that a ^{119m}Sn center in the anionic sublattice of PbTe (it corresponds to a type-I spectrum) consists of an antistructural defect and, as follows from the fact that the isomeric shift of the spectrum I is independent of the conductivity type in the material, the charge state of the antistructural defect does not depend on the position of the Fermi level. A ^{119m}Sn center in the cationic sublattice of PbTe (it corresponds to a type-II spectrum) is an isovalent substitution impurity. According to Ref. 5, such an impurity is electrically inactive, as is confirmed by the independence, which we discovered, of the isomeric shift of the type-II spectrum from the conductivity type in the material.

This work was supported by the Russian Fund for Fundamental Research (Grant 96-02-16957a).

[1] V. I. Kaĭdanov, S. A. Nemov, and Yu. I. Ravich, Fiz. Tekh. Poluprovodn. **26**, 201 (1992) [Sov. Phys. Semicond. **26**, 113 (1992)].
[2] V. F. Masterov, F. S. Nasredinov, S. A. Nemov, and P. P. Seregin, Fiz. Tekh. Poluprovodn. **31**, 197 (1997) [Semiconductors **31**, 100 (1997)].
[3] Yu. I. Ravich, B. A. Efimova, and I. A. Smirnov, *Methods of Investigation of Semiconductors in Application to Lead Chalcogenides* [in Russian], Nauka, Moscow, 1968.
[4] F. Ambe and S. Ambe, J. Chem. Phys. **75**, 2463 (1981).
[5] V. F. Masterov, F. S. Nasredinov, S. A. Nemov, and P. P. Seregin, Fiz. Tekh. Poluprovodn. **30**, 840 (1996) [Semiconductors **30**, 450 (1996)].

Translated by M. E. Alferieff

Extraction of charge carriers in semiconductors with a monopolar component of the photoconductivity

A. I. Vlasenko,[a] Z. K. Vlasenko, and A. V. Lyubchenko

Institute of Semiconductor Physics, Ukrainian National Academy of Sciences, 252650 Kiev, Ukraine
(Submitted August 13 1996; accepted March 5 1997)
Fiz. Tekh. Poluprovodn. **31**, 1323–1326 (November 1997)

Extraction of minority charge carriers in semiconductors with a monopolar component of the photoconductivity has been investigated theoretically and experimentally for the example of $Cd_xHg_{1-x}Te$ ($x \approx 0.2$) at different temperatures. © *1997 American Institute of Physics.* [S1063-7826(97)01011-9]

INTRODUCTION

The amount by which the sensitivity of the semiconductor photoresistive radiation detectors can be increased by increasing the bias voltage is in principle limited by the extraction of minority nonequilibrium charge carriers (MNCs) from the volume of the semiconductor as the electric field intensity E increases above a certain value $E=E^*$. This effect has been studied theoretically and experimentally mainly in connection with the development of threshold infrared (IR) radiation detectors. Specifically, in Refs. 1–3 the operation of photodetectors based on $Cd_xHg_{1-x}Te$ (CMT) ($x \approx 0.2$) is analyzed in the extraction regime, and the corresponding expressions are obtained for the photoresponse signal, the detection power, and other characteristics. In Refs. 4 and 5, the electric field dependences of the photoconductivity (PC) in n-, p-, and mixed-type CMT were investigated. At the same time, it should be noted that the extraction of MNCs has been analyzed theoretically only for the case of a bipolar PC, when the density of nonequilibrium electrons and holes and their lifetimes are equal ($\Delta n=\Delta p,\ \tau_n=\tau_p$). In the opposite case ($\tau_n \neq \tau_p$), the conductivity component which does not depend on the field and which is proportional to the density difference $|\Delta n-\Delta p|$, where the lower quantity determines the density of the nonequilibrium pairs extracted from the volume, should be taken into account. We will analyze the extraction of MNCs in semiconductors with allowance for the monopolar component of the photoconductivity.

1. CURRENT-VOLTAGE CHARACTERISTICS (PHOTOCOMPONENT)

The ratio of τ_n and τ_p is determined by the recombination mechanism realized in the crystal: interband (type A) or impurity (type B). In the first case, the PC is bipolar ($\tau_n=\tau_p$). It can be realized in semiconductors with a low density of recombination levels, when the number of MNCs bound on them can be ignored. In the second case, where these densities cannot be disregarded, the PC is generally monopolar ($\tau_n \neq \tau_p$). In narrow-gap semiconductors which are not strongly compensated ($Cd_xHg_{1-x}Te$, InS, Pb_xSn_{1-x}, Te, and others) at high temperatures, when intrinsic conductivity is realized, interband recombination mechanisms predominate (mechanism A). In materials with a high degree of compensation, at low temperatures the Shockley–Read mechanism (mechanism B) predominates.[6–8] In ''classical'' wide-gap semiconductors (CdS, CdSe) the PC is highly monopolar, since the ratio of the lifetimes reaches $\tau_n/\tau_p \cong 10^4-10^6$ (Ref. 9).

In an arbitrary case the specific photoconductivity ($\Delta\sigma$) and photocurrent (j_{pc}) in a uniform semiconductor

$$\Delta\sigma = e(\mu_n\Delta n+\mu_p\Delta p) \sim e(\mu_n\tau_n+\mu_p\tau_p)G, \qquad j_{pc}=e\Delta\sigma E \tag{1}$$

in the case of the uniform excitation mechanism (with rate G) will consist of two components — monopolar $\Delta\sigma_m$ and bipolar $\Delta\sigma_b$, the latter depending on E,

$$\Delta\sigma=\Delta\sigma_m+\Delta\sigma_b(E)=e\mu_n\Delta n[(1-\varphi)+\varphi(1+b^{-1})], \tag{2}$$

where $b=\mu_n/\mu_p$, and μ_n and μ_p are the electron and hole mobilities. Here we have introduced a parameter that determines the degree of bipolarity of the PC:

$$\varphi=\frac{\Delta p}{\Delta n}=\frac{\tau_p}{\tau_n}\leqslant 1. \tag{3}$$

In Eq. (3) it is assumed that $\tau_p \leqslant \tau_n$. In the opposite case, $\tau_p \geqslant \tau_n$, the parameter $\varphi=\tau_n/\tau_p \leqslant 1$.

In the case of the type A mechanisms the PC is bipolar and $\varphi=1$. In the extraction region, all MNCs are extracted from the volume. As a result, $\Delta\sigma$ drops off with increasing E and the photocurrent (1) saturates.

In the case where several recombination channels — types A and B — participate (compete), $\tau_n \neq \tau_p$ and $\varphi=1$. The quantity φ (3) can be calculated using the probability for trapping of MNCs in recombination levels (A_{rn},A_{rp}) and interband annihilation of the carriers (A_{np}):

$$A_n=1/\tau_n=A_{rn}+A_{np}, \quad A_p=1/\tau_p=A_{rp}+A_{np}. \tag{4}$$

The parameter φ (3) is

$$\varphi=\frac{\tau_p}{\tau_n}=\frac{A_n}{A_p}=\frac{\tau_p'}{\tau' n}\,\frac{\tau_n'+\tau_{np}}{\tau_p'+\tau_{np}}, \qquad \tau_n'=\frac{1}{A_{rn}}, \quad \tau_p'=\frac{1}{A_{rp}}, \quad \tau_{np}=\frac{1}{A_{np}}. \tag{5}$$

The equations (5) allow for the fact that the trapping probabilities are inversely proportional to the corresponding electronic and hole times (τ_n', τ_p'). It is easy to see that in the

absence of a monomolecular impurity recombination channel (A_{rn}, $A_{rp} \ll A_{np}$; $\tau_p', \tau_n' \gg \tau_{np}$) $\varphi = 1$; otherwise, ($A_{np} \ll A_{rn}$, A_{rp}; τ_p', $\tau_n \ll \tau_{np}$) $\varphi = \tau_n / \tau_p \leqslant 1$, and its value is determined by the statistics of Shockley–Read recombination.[10] Making admissable simplifications for a n-type semiconductor, in which the recombination levels (acceptor type) lie near the center of the band gap, we can write φ as follows:

$$\varphi = \frac{a(n_0 + N_{cr}) + N_{vr}}{a(n_0 + N_{cr}) + N_{vr} + N_r} \leqslant 1, \tag{6}$$

where n_0 is the equilibrium electron density, N_r is the density of recombination r levels of defects, $a = c_n / c_p$ (c_n and c_p are electron and hole trapping coefficients, respectively), and N_{cr}, N_{vr} are the free-carrier densities in the bands due to thermal ionization of the r levels.

When the density of r levels is low, $\varphi \cong 1$ at arbitrary temperatures, as noted earlier all MNCs are extracted from the volume in pairs.

For large N_r the degree of bipolarity depends on the temperature. At low temperatures (the traps are completely filled with electrons) the quantities N_{cr} and N_{vr} in Eq. (6) can be disregarded

$$\varphi = \frac{an_0}{an_0 + N_r} = \left(1 + \frac{c_p N_r}{c_n n_0}\right)^{-1} \approx \frac{c_n n_0}{c_p N_r} < 1. \tag{7}$$

If n_0 is large (at least $an_0 \gg N_r$), $\varphi = 1$ and the PC is bipolar. For an_0 comparable to $N_r \varphi < 1$, only some nonequilibrium electrons, whose number is equal to the pair density determined by the quantity $\Delta p = \tau_p G$, are extracted.

Heating increases the thermal transfer between the levels and bands (N_{cr}, N_{vr} becomes comparable to N_r), and the MNC lifetimes τ_n and τ_p increase and become equal to one another. There appears a thermal recombination energy E_r, which is characteristic of Shockley–Read recombination and which is determined by the depth of the r levels

$$\tau_n = \tau_p \approx \exp(-E_r / kT). \tag{8}$$

As follows from Eq. (6), φ increases and approaches 1 at high temperatures T.

The field-independent monopolar part of the PC (2) is actually determined by the difference in the lifetimes of the MNCs, taking into account Eq. (7) for $E < E^*$,

$$\Delta\sigma_m = e\mu_n G(\tau_n - \tau_p) = e\mu_n \Delta n \frac{N_r}{an_0 + N_r}. \tag{9}$$

For $E < E^*$, the monopolar part of the density $\Delta n_m < \Delta n$ corresponds to a constant generation rate G of MNCs, and the effective electron lifetime is determined from the expression

$$\tau = \frac{\Delta n_m}{G} < \tau_n. \tag{10}$$

The electric field dependences of the relaxation times of the PC and the photocurrent, taking into account the degree of bipolarity, can be obtained by simple manipulations:

$$\tau = \tau_0 \left[(1 - \varphi) + \frac{\varphi l}{l + \mu_a \tau_0 \varphi E}\right], \tag{11}$$

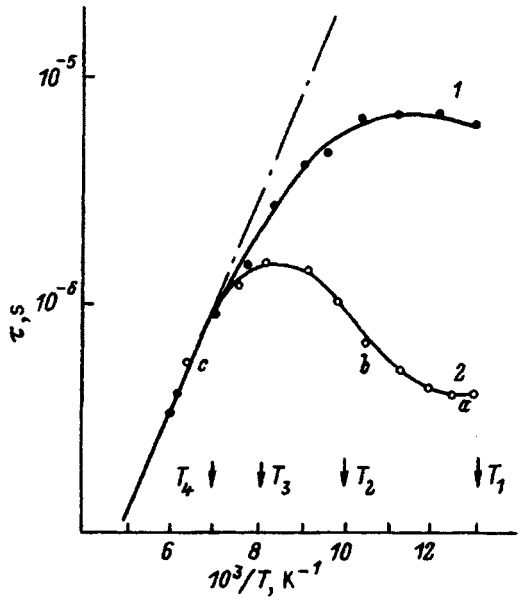

FIG. 1. Temperature dependences of τ for CMT samples 1 and 2 (curves *1* and *2*). Dot-dashed curve — calculation of $\tau(T)$ for Auger recombination in a material with intrinsic conductivity.

$$j_{pc} \approx \left[(1 - \varphi) + \frac{\varphi l}{l + \mu_a \tau_0 \varphi E}\right] E,$$

where τ_0 is the lifetime of the PC with a low bias voltage, μ_a is the ambipolar mobility, and l is the distance between the contacts. Analysis of these expressions shows that the efficiency of extraction of MNCs from the volume in the region of large E depends strongly on the parameter φ and even decreases rapidly for large values of φ ($\leqslant 0.9$).

2. EXTRACTION OF MINORITY NONEQUILIBRIUM CHARGE CARRIERS AT DIFFERENT TEMPERATURES

As an example, let us examine a narrow-gap semiconductor CMT with $x = 0.2$ (band gap $E_g = 0.1$ eV at 77 K) and estimate the degree of bipolarity in different temperature ranges. It is known (see, for example, Ref. 6) that the interband collisional mechanism (type A) dominates in the recombination in highly sensitive n-type CMT crystals in the region of intrinsic and extrinic conductivity (at $T > 77$ K). At the same time, in strongly compensated crystals, the lifetime of MNCs in the region of extrinsic conductivity is limited by the Shockley–Read recombination mechanism.

Figure 1 shows the temperature dependences of the relaxation time of PC for two n-type CMT crystals in which different recombination mechanisms dominate [τ was measured by the PC relaxation method under illumination with Co_3 laser pulses ($\lambda = 10.6$ μm)]. Although $\tau(T)$ for crystal No. 1 is described well by a calculation for the interband collisional recombination in the regions of intrinsic and extrinsic ($n_0 \cong 3 \times 10^{14}$ cm^{-3}) conductivity (solid curve). In this case $\tau_n = \tau_p$ and the PC is bipolar in the entire temperature range 77–300 K. This confirms the character of the electric-field dependences of the photosignal U_c and τ presented in Fig. 2 for this crystal. Saturation of U_c and the decrease of τ in high fields at temperatures from the extrinsic

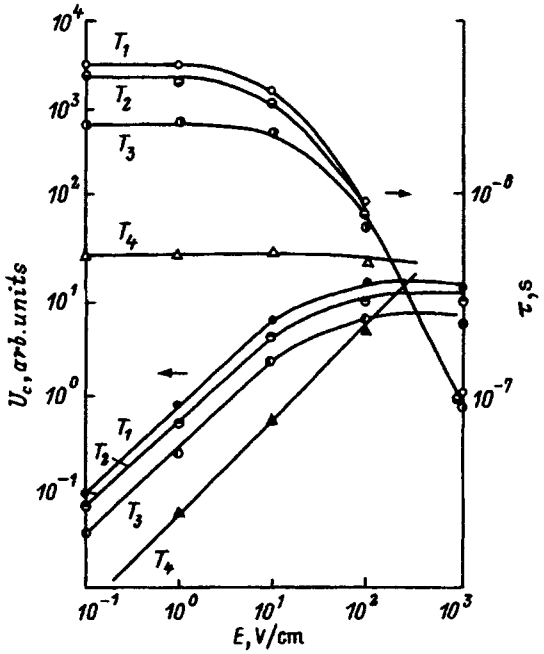

FIG. 2. Electric-field dependences of U_c (filled points) and τ (open points) for sample 1 for the temperatures T_1, T_2, T_3, and T_4 indicated in Fig. 1; solid lines — calculation.

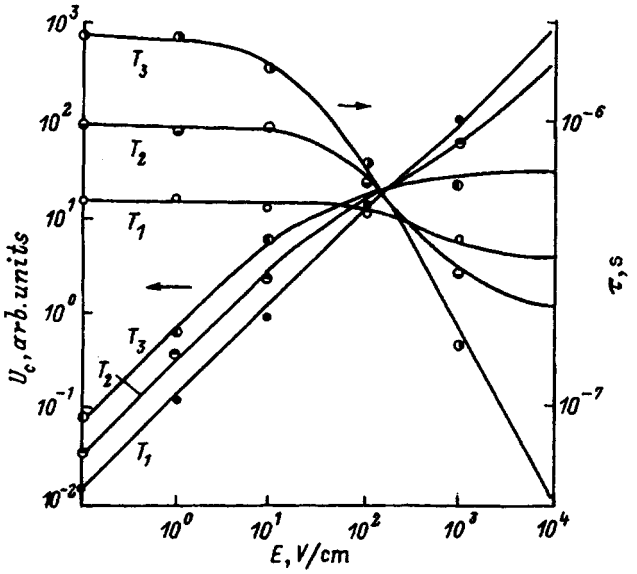

FIG. 3. Electric-field dependences of U_c (filled dots) and τ (open dots) for sample 2 for temperatures T_1, T_2, T_3, and T_4 indicated in Fig. 1; solid lines — calculation for $\varphi \approx 0.5$, 0.9, and 1, respectively.

conduction region (T_1, T_2, T_3) indicates the onset of extraction and a bipolar PC. Obviously, in the intrinsic conductivity temperature range (T_4) the field does not control the MNCs, $\mu_n = 0$, the extraction regime is not realized, and U_c does not saturate.

The situation is more complicated in the case of sample No. 2 (Fig. 1). Here, just as in sample No. 1, for $T > 120$ K the type-A mechanism dominates in recombination in the intrinsic conductivity region. For the temperature range of extrinsic conductivity, the curve $\tau(T)$ can be described by the Shockley–Read recombination theory — the type-B mechanism. Analysis of the published data suggests that Shockley–Read recombination in compensated crystals proceeds via acceptor-type centers[7–9] — doubly charged mercury vacancies V_{Hg}^{2-}.[11,12] Their density in photosensitivity crystals does not exceed $N_r \leqslant 10^{15}$ cm^{-3}.[7,8] The parameters obtained for the r levels from the curves $\tau(10^3/T)$ for sample No. 2 $E_r = 50$ meV and $c_n = 3 \times 10^{-9}$ cm^3/s are in good agreement with the published data [$E_r = 45$–50 meV, $c_n = (1-3) \times 10^{-9}$ cm^3/s].[7,8] The value $N_{vr} \cong 4 \times 10^{14}$ cm^{-3} is comparable to the density n_0, $N_{cr} \ll N_{vr}$. The variance of the published values of c_p reaches several orders of magnitude. However, from considerations of the charge of a r center (holes are trapped in a Coulomb attractive field) $c_n < c_p$, despite the difference in the thermal velocities of the nonequilibrium electrons and holes. For $a = 10^{-1}$ $\varphi \cong 2 \times 10^{-2}$ and remains quite low at low temperatures even for $a \cong 1$. The extraction efficiency should increase with the temperature and n_0. In low-resistivity crystals ($an_0 > N_r$) $\varphi \to 1$, so that the contribution of the bipolar Auger component also increases. In crystals with $n_0 > 10^{15}$ cm^{-3} and $T > 100$ K complete extraction of MNCs pairs should be expected.

Comparison of the temperature and electric field dependences of τ and U_c (Fig. 1, curve *2*; Fig. 3) provides experimental confirmation for this expectation. Indeed, at low temperatures $T < T_C$, when the intensity of heat transfer between the levels and bands can be ignored ($n_0 \gg N_{cr}, N_{vr}$), the PC relaxation time does not depend on the temperature (Fig. 1, section a on curve *2*), $\varphi < 1$ and is determined by the expression (7). The photoconductivity has two components — monopolar and bipolar, and at 77 K saturation of the electric-field dependence of j_{pc}, which is associated with the extraction of MNCs from the volume, is not observed (Fig. 3, T_1). It should be noted that φ can be determined from the curve $\tau(10^3/T)$ (Fig. 1, section b) with $T^* < T_0$ from the ratio of the values of τ extrapolated to the point $10^3/T^*$ and τ on the section a. For crystal No. 2 it amounts to ≈ 0.5 at $T^* \approx 77$ K.

As $T > T_0$ increases (Fig. 1, section b on curve *2*), the contribution of the monopolar component to the PC decreases, $\varphi \to 1$, the electric-field dependence of the PC saturates (Fig. 3, T_2, T_3), and the MNCs are extracted from the volume. In the region of intrinsic conductivity, the Shockley–Read recombination channel is replaced by the interband channel (Fig. 1, section c on curve *2*), but extraction of MNCs does not occur ($\mu_a = 0$), and the electric-field dependences j_{pc} do not saturate (by analogy with the curves for T_4 in Fig. 2).

[a]Fax: (044)-2658342; e-mail: mickle@semicond.kiev.ua

[1] R. L. Williams, Infrared Phys. **8**, 337 (1968).
[2] M. R. Johnson, J. Appl. Phys. **43**, 3090 (1972).
[3] S. P. Emmons and K. L. Ashley, Appl. Phys. Lett. **20**, 162 (1972).
[4] V. I. Ivanov-Omskiĭ, V. K. Ogorodnikov, and T. Ts. Totieva, Fiz. Tekh. Poluprovodn. **14**, 699 (1980) [Sov. Phys. Semicond. **14**, 412 (1980)].
[5] A. I. Vlasenko and A. V. Lyubchenko, Fiz. Tekh. Poluprovodn. **28**, 1219 (1994) [Semiconductors **28**, 695 (1994)].
[6] A. I. Vlasenko, Yu. N. Gavrilyuk, A. V. Lyubchenko, and E. A. Sal'kov,

Fiz. Tekh. Poluprovodn. **13**, 2180 (1979) [Sov. Phys. Semicond. **13**, 1274 (1979)].
[7] L. A. Karachevtseva, A. V. Lyubchenko, and V. D. Sobolev, Ukr. Fiz. Zh. **38**, 1071 (1993).
[8] D. L. Polla and C. E. Jones, J. Appl. Phys. **52**, 5119 (1981).
[9] V. E. Lashkarev, A. V. Lyubchenko, and M. K. Sheĭnkman, *Nonequilibrium Processes in Photoconductors* [in Russian], Kiev, 1981, p. 263.
[10] J. S. Blakemore, *Semiconductor Statistics*, Pergamon Press, N. Y., 1962 [Russian translation, Moscow, 1964].
[11] K. Lischka, Phys. Status Solidi **133**, 17 (1986).
[12] H. R. Vydynath, Electr. Soc. Sol. St. Sci. Technol. **128**, 2609 (1981).

Translated by M. E. Alferieff

Photoluminescence of *n*-type ZnSe crystals doped with donor and acceptor impurities from a LiCl salt melt

G. N. Ivanova, V. A. Kasiyan, and D. D. Nedeoglo

Moldavian State University, 2009 Kishinev, Moldavia
(Submitted February 7, 1997; accepted for publication March 20, 1997)
Fiz. Tekh. Poluprovodn. **31**, 1327–1331 (November 1997)

The photoluminescence spectra and luminescence excitation spectra (LESs) of *n*-type ZnSe single crystals annealed in LiCl melt is investigated in the temperature range from 82 to 420 K. It is established that such heat treatment of the crystals greatly decreases the intensity of the long-wavewlength luminescence bands and intensifies the edge radiation. The excitation spectrum of the long-wavelength photoluminescence bands contains several maxima near the fundamental and impurity absorption edges. it is shown that the complicated structure of the luminescence excitation spectra is due to relocation of a nonequilibrium hole from a shallow acceptor to a deeper acceptor by an Auger process with the participation of carriers localized at these centers. © *1997 American Institute of Physics.* [S1063-7826(97)01111-3]

The problems of modern optoelectronics require the development of devices that operate in the blue-green region of the spectrum. A promising material for these purposes is zinc selenide. However, in addition to edge luminescence, one observes wide, intense, long-wavelength emission bands in the photoluminescence (PL) spectrum of undoped *n*-ZnSe. This raises the problem of identifying the luminescence centers responsible for these bands and searching for dopants that can decrease the number of long-wavelength luminescence centers and increase the intensity of the high-temperature edge luminescence of ZnSe. Since the centers of the long-wavelength luminescence in ZnSe are, as a rule, intrinsic defects (V_{Zn}) or impurities such as Cu, Ag, and Au, which produce deep acceptor centers, the problem of increasing the edge radiation intensity can be solved by decreasing centers of this type in the process of doping of crystals with shallow acceptor and donor impurities.

1. DOPING OF SAMPLES AND EXPERIMENTAL CONDITIONS

We used low-temperature (750 °C) annealing of *n*-type ZnSe crystals in a melt of LiCl salt as a method of doping such crystals simultaneously with shallow donor (Cl_{Se})- and acceptor (Li_{Zn})-type impurities. Annealing was conducted in evacuated cells for 6 to 100 h. When annealing was completed, the cells were rapidly cooled to room temperature. It is known[1] that a melt of LiCl salt is a typical ionic liquid (Li^+ and Cl^-) with a very high electrical conductivity ($6.308\ \Omega^{-1}\cdot cm^{-1}$). It should be expected that during annealing of *n*-ZnSe crystals in a LiCl salt melt the lithium and chlorine ions diffuse into the crystal and occupy sites in the zinc and selenium sublattices, producing, respectively, donor (Cl_{Se}) and acceptor (Li_{Zn}) centers.

The PL spectra of the initial and doped crystals were investigated in the temperature interval from 82 to 420 K. The PL was excited by 337 nm radiation from a LGI-21 laser. Luminescence excitation spectra (LES) were also investigated at 82 K. The PL spectra and LES were investigated using a MDR-23 monochromator with a linear dispersion of 14 Å/mm in the wavelength range from 440 to 700 nm.

2. EXPERIMENTAL RESULTS

The PL spectrum of an undoped *n*-type ZnSe crystal at 82 K, shown in Fig. 1, consists of bands *A* (445 nm) and *C* (540 nm) of equal intensity. A weak band *D* (600 nm), in the form of an inflection, and a clearly expressed band *E* (635 nm) are observed on the long-wavelength shoulder of the band *C*. The band *B* has the lowest intensity.

Short anneal (6 h) of the initial crystals in a LiCl salt melt strongly decreases the intensity of the *C* band (Fig. 1, curve *2*), shifts the maximum of the *E* band to 640 nm, and singles out more clearly the band *D* without changing its spectral position. The PL bands *A* and *B* do not undergo any changes.

A longer anneal (100 h) of the crystals strongly increases the intensity of the edge-radiation band *B* and shifts the maximum of this band to 456 nm (Fig. 1, curve *3*). This band becomes dominant in the PL spectrum. Its intensity is twice that of the shortest wavelength band *A* against the background of the vanishingly low intensities of longer wavelength PL bands. The maximum of the *E* band shifts to 649 nm.

Thus, the intensity of the long-wavelength radiation can be substantially decreased and the edge radiation can be intensified by prolonged annealing of *n*-ZnSe crystals in a LiCl salt melt.

The excitation spectra of the long-wavelength PL bands of an undoped *n*-type ZnSe crystal at 82 K are presented in Fig. 2 (curves *1–3*). A characteristic feature of these spectra is the presence of several excitation bands near the fundamental absorption edge. For example, the LES of the band *E* in the nonannealed crystal consists of three bands with maxima at 420, 445, and 470 nm. The LES of the band *D* possesses approximately the same structure, and only two bands with maxima at 420 and 450 nm are present in the LES of the band *C*. Bands due to excitation of impurity levels dominate in the LES of the band *E* of doped crystals

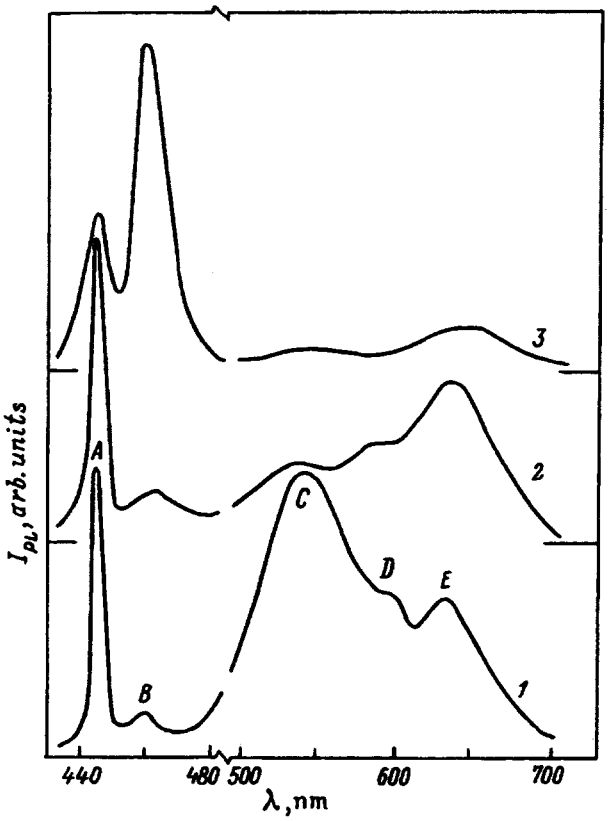

FIG. 1. Photoluminescence spectra of nonannealed *n*-type ZnSe crystals (*1*) and *n*-type ZnSe crystals annealed in melt of a LiCl salt (*2, 3*). $T=82$ K. Annealing time, h: *2* — 6, *3* — 100.

ZnSe:LiCl. Thus, an impurity maximum is observed at 470 nm in the LES of the band *E* of crystals annealed for 6 h (Fig. 2, curve *4*). Annealing for 100 h results in an even larger shift of the LES of the band *E* into the region of impurity excitation and the appearance of two new bands

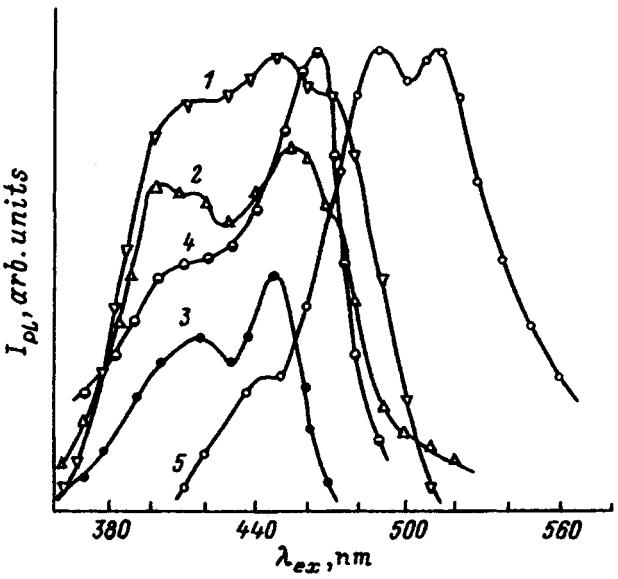

FIG. 2. PL excitation spectra of nonannealed *n*-ZnSe crystals (*1–3*) and *n*-ZnSe crystals annealed in a melt of LiCl salt for 6 h (*4*) and 100 h (*5*). $T=82$ K. LES curves: *1, 4, 5* — *E* band, *2* — *D* band, *3* — *C* band.

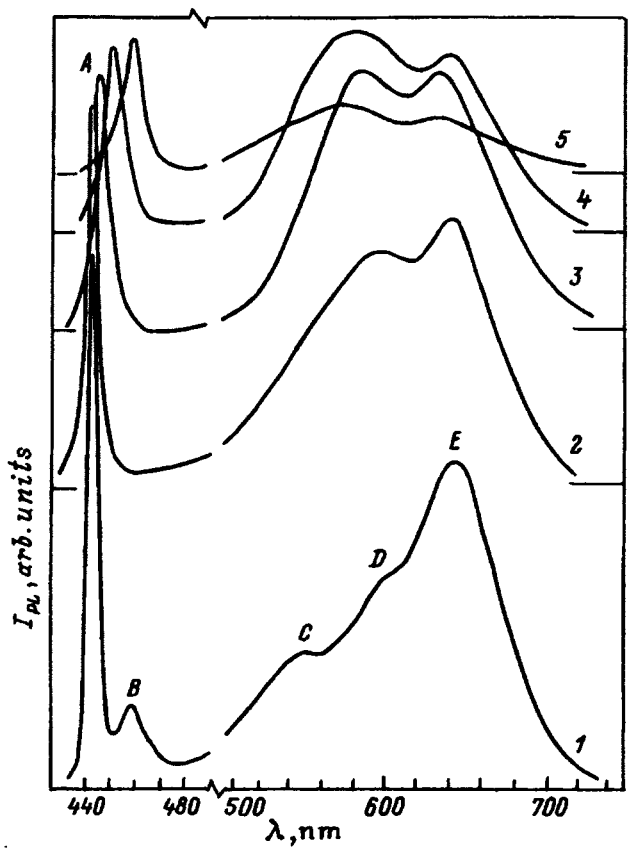

FIG. 3. Temperature evolution of the PL spectra of *n*-ZnSe crystals annealed in LiCl salt for 6 h. *T*, K: *1* — 84, *2* — 133, *3* — 185, *4* — 264, *5* — 350.

with maxima at 490 and 510 nm, which have the highest intensities (Fig. 2, curve *5*). In the doped crystals, light from the fundamental absorption region excites luminescence very weakly.

The large width of the LES, the presence of several maxima, and the change in the energy position of the maxima from sample to sample are consequences of the nonelementary nature of the long-wavelength PL bands.[2]

Investigations of the temperature evolution of the PL spectra (Figs. 3 and 4) showed that the intensities of the bands *A*, *B*, *C*, and *E* decrease with increasing temperature. The temperature dependence of the band *D* is somewhat unusual. At 84 K it is only an inflection on the short-wavelength shoulder of the band *E*, whereas at 93 K this PL band separates into a peak whose intensity is comparable to that of the band *E* at 174 K and becomes dominant in the PL spectrum at 192 K. As the temperature is raised to 330 K, the intensity of the band *D* increases and then decreases, just as the intensity of the other bands in the PL spectrum (Fig. 5). The initial growth in the intensity of this band with increasing temperature is apparently due to the temperature quenching of the more intense, close-lying, neighboring band *E*. Figure 3 shows well the dynamics of this process. The maximum of this band shifts with increasing temperature to shorter wavelengths, and at 350 K the band is centered at 580 nm (Fig. 3, curve *5*). The band *E* shifts very little with increasing temperature. The maximum of the band *A* shifts

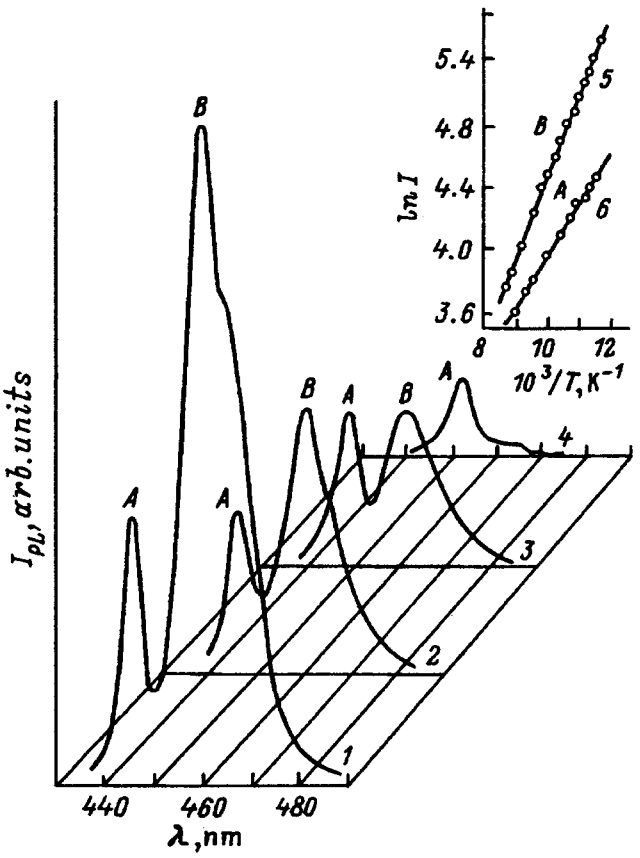

FIG. 4. Effect of temperature on the edge PL spectra of a *n*-ZnSe crystal annealed in LiCl salt for 100 h. *T*, K: *1* — 82, *2* — 101, *3* — 112, *4* — 182. Inset: Curves of temperature quenching of the intensities of the PL bands *B* (*5*) and *A* (*6*).

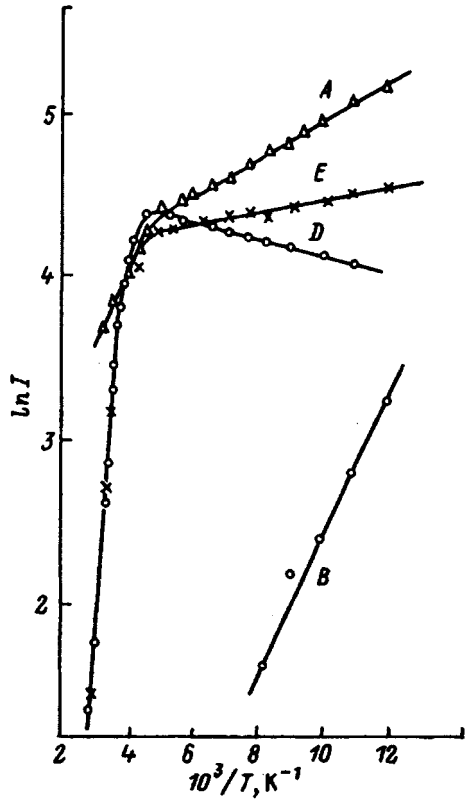

FIG. 5. Temperature dependence of the intensity of the PL of a *n*-ZnSe:LiCl crystal (6 h) at the maxima *A*, *E*, *D*, and *B*.

into the long-wavelength region with the coefficient of the temperature shift equal to -3.8×10^{-4} eV/K and is close in value to the coefficients of the temperature variation of the band gap in ZnSe [-4×10^{-4} eV/K (Ref. 3)]. The half-width of the band *A* increases from 24 meV at 84 K to 80 meV at 350 K. As the temperature increases, the intensity of the band *B* decreases much more rapidly than does the intensity of the band *A* (Fig. 4), and this PL band is virtually undetectable at 180 K. The coefficient of the temperature shift of the band *B* into the long-wavelength region is -3.2×10^{-4} eV/K. The large half-width of this PL band (68 meV at 82 K) is due to the contribution of the phonon repetitions, as is indicated by the appreciable inflection in the long-wavelength shoulder (Fig. 4, curves *1* and *2*).

The activation energy of temperature quenching of the bands *A* and *B* in the temperature interval from 80 to 120 K (Fig. 4, inset) for different samples was found to be 10–27 and 37–39 meV, respectively. At temperatures above 220 K, the intensity in the maximum of the band *A* decreases rapidly and the activation energy of the temperature quenching of this band increases to 39–52 meV (Fig. 5). At temperatures in the range $\sim220-250$ K the temperature quenching of the bands *E* and *D* also changes. The curves $\ln I=f(10^3/T)$ for these bands have two slopes. The activation energies of the temperature quenching of the intensity of the band *E* equal 4–13 meV at low temperatures and 100–150 meV at high temperatures for different samples.

3. DISCUSSION OF THE EXPERIMENTAL RESULTS

The band *A* at low temperatures lies next to a free-exciton emission line and is due to exciton annhilation. As the temperature is raised, shallow donors transfer into an ionized state and at $T>200$ K exciton–impurity complexes, which are associated with ionized donors, whose contribution to the formation of the band *A* becomes dominant, are most likely to form. This introduces an asymmetry in the observed band on the long-wavelength side, broadens the band, shifts the spectrum into the long-wavelength region (Fig. 3), and increases the activation energy of temperature quenching of the intensity of this PL band (Fig. 5). The observed sample-to-sample variance in the values of this energy is evidently due to the presence of several types of shallow donor impurity. In Ref. 4, we made a more detailed analysis of the nature of the bands *A* and *B*. It was found that the structure of the luminescence centers responsible for the band *B* changes with increasing temperature. At low temperatures these are associative centers of the type $V_{Zn}D$. At high temperatures the associative centers decomposed into simple, deeper acceptors V_{Zn} and shallow donors. For this reason, annealing of ZnSe crystals in liquid zinc completely quenched this band and annealing in liquid selenium strongly increased its intensity.[4] The low activation energies of the

temperature quenching of this band do not reflect the depth of the luminescence center, since quenching occurs, as shown in Ref. 4, by an internal mechanism.

The intense band *C*, observed in the luminescence spectra of the starting crystals, with a maximum at 540 nm is ordinarily attributed to the presence of copper in ZnSe.[5,6] The decrease in the intensity of this band after heat treatment of the crystals in LiCl salt (Fig. 1) is explained by extraction of copper from the crystal in the process of such annealing.

The luminescence centers forming the self-activated luminescence band *D* with a maximum at 600 nm consist of the associates $V_{Zn}V_{Se}$.[7,8] The complete vanishing of this band with prolonged annealing of the crystals in LiCl salt (Fig. 1) that we recorded in an earlier work[9] is due to simultaneous filling of the zinc and selenium vacancies by Li_{Zn} and Cl_{Se} atoms, respectively.

The presence of three maxima in the LES of the band *E* (Fig. 2, curves *1* and *5*) and the shift of the PL band itself (Fig. 1) and its excitation spectrum (Fig. 2) into the long-wavelength region when the crystals are annealed in a LiCl salt attest to the complexity of the structure of the luminescence centers responsible for the *E* band and the mechanism leading to the excitation of this band. It was recently shown[2] that the relocation of a nonequilibrium hole from an absorption center (AC) to a deeper luminescence center (LC) occurs in the process of excitation of the 630-nm PL band. This process is accompanied by transfer of excitation energy from the AC to the deeper LC. An Auger process with the participation of carriers localized at AC and LC occurs: After optical excitation of an electron from an AC into the conduction band (or onto a shallow donor) the electron returns nonradiatively into the AC, giving up in the process energy to an electron localized in a deeper LC and exciting the electron into the conduction band.[10] Subsequent trapping of the electron by a luminescence center gives rise to the long-wavelength luminescence.

According to this model, the shorter-wavelength band in the LES of the band *E* (Fig. 2, curve *1*) is due to the excitation of an electron from a relatively shallow acceptor, which is an AC, into the conduction band. The difference in the energy of the absorbed photon at the maximum of this excitation band and the energy of the emitted photon at the maximum of the band *B* is of the order of 0.25 eV and corresponds to a Stokes shift. This suggests that the absorption centers are luminescence centers of the band *B*, i.e., associates $V_{Zn}D$. Assuming that a transition corresponding to the excitation of an electron into the conduction band from a deeper LC of the band *E* as a result of an Auger process is also manifested in the LES, it is logical to attribute the longer wavelength band in the excitation spectrum (Fig. 2, curve *1*) to this optical transition. The difference in the energies in the maxima of this band *E* is 0.45 eV, in good agreement with the Stokes shift of this band, found in Ref. 2.

Adopting as a working hypothesis the idea that the LC of the 630-nm PL band of the band *E* is a three-particle associate consisting of zinc vacancies, a donor, and a shallow acceptor separated from them by a large distance,[2] the annealing of ZnSe crystals in LiCl salt should result in decomposition of these complicated associates for two reasons. First, as we showed earlier,[9] even a short anneal (10 h) of ZnSe crystals in LiCl salt results in extraction of shallow donors (Al, Ga, In) and acceptors (Na) from the crystal. These donors and acceptors probably are the constituents of the associate under study. Second, in such an anneal process zinc vacancies, which are also constituents of the associate, are filled with lithium atoms (Li_{Zn}). According to Ref. 9, increasing the anneal time to 20 h and longer again sharply increases the density of zinc vacancies as a result of departure of lithium atoms from the sites in the zinc sublattice and occupation of the interstitial states. This decreases the number of shallow acceptors Li_{Zn} ($E_A=114$ meV), which impedes repeated formation of LC of the band *E*, despite the high density of V_{Zn} and shallow donors Li_i ($E_D=17-20$ meV). However, this leads to the creation of favorable conditions for the formation of the associates $V_{Zn}Li_i$ which are responsible for the luminescence band *B* in crystals annealed in LiCl. An increase in the density of the associates $V_{Zn}Li_i$ with prolonged annealing of the crystals in LiCl salt and an increase in the probability of radiative transitions on these centers, since nonequilibrium holes under conditions of low density of LC of the band *E* remain localized on $V_{Zn}Li_i$ centers, result in rapid growth of the intensity of the PL band *B* (Fig. 1, curve *3*). An increase in the total density of the impurities (Li_i, Cl_{Se}) and intrinsic defects (V_{Zn}) during a long anneal of the crystals in LiCl salt decreases the possibility of excitonic luminescence, which results in a decrease of the intensity and in broadening of the luminescence band *A*.

[1] *Handbook of Fused Salts* [in Russian], Khimiya, Leningrad, 1970.
[2] B. E. Embergenov, N. E. Korsynskaya, V. D. Ryzhikov, L. P. Gal'chinskiĭ, and E. K. Lisetskaya, Fiz. Tekh. Poluprovodn. **27**, 1240 (1993) [Semiconductors **27**, 686 (1993)].
[3] V. V. Sobolev, V. I. Donetsikh, and E. F. Zagaĭnov, Fiz. Tekh. Poluprovodn. **12**, 1089 (1978) [Sov. Phys. Semicond. **12**, 646 (1978)].
[4] G. N. Ivanova, V. A. Kasiyan, N. D. Nedeoglo, D. D. Nedeoglo, and A. V. Simashkevich, Fiz. Tekh. Poluprovodn. [Semiconductors], submitted for publication.
[5] M. Godlewski, W. E. Lamb, and B. C. Cavenett, Solid State Commun. **39**, 595 (1981).
[6] G. N. Ivanova, V. A. Kasiyan, D. D. Nedeoglo, and S. V. Oprya, Izv. Akad. Nauk RM, Fiz. i Tekh., No. 2, 34 (1995).
[7] P. A. Kukk and N. V. Palmre, Izv. Akad. Nauk SSSR, Neorg. Mater. **16**, 1916 (1980).
[8] M. B. Kotlyarevskiĭ, A. A. Pegov, O. V. Leont'eva, and B. G. Chernyavskiĭ, Dep. N506-B86 (1986).
[9] V. Z. Bolboshenko, G. N. Ivanova, D. D. Nedeoglo, and B. V. Novikov, Opt. Spektrosk. **72**, 149 (1992) [Opt. Spektrosk. **72**, 82 (1992)].
[10] V. V. Dyakin, E. A. Sal'kov, V. A. Khvostov, and M. K. Sheĭnkman, Fiz. Tekh. Poluprovodn. **10**, 2288 (1976) [Sov. Phys. Semicond. **10**, 1357 (1976)].

Translated by M. E. Alferieff

Effect of band-gap narrowing on the diffusion of charged impurities in semiconductors

B. S. Sokolovskiĭ and L. S. Monastyrskiĭ

Iv. Franko L'vov State University 290602 L'vov, Ukraine
(Submitted December 11 1996; accepted April 1 1997)
Fiz. Tekh. Poluprovodn. **31**, 1332–1335 (November 1997)

It is shown theoretically that allowance for the internal electric field due to band-gap narrowing as a result of strong doping of the semiconductor decreases the diffusion of the charged impurity and forms a descending section on its impurity density dependence. © *1997 American Institute of Physics.* [S1063-7826(97)01211-8]

Diffusion of charged impurities in semiconductors, which is important for semiconductor device technology, has been studied extensively, both theoretically and experimentally.[1,2] Despite those studies, there is very little published information on how band-gap narrowing (BGN), which occurs with high levels of doping in a semiconductor,[3–12] influences diffusion of charged impurities. We know of only one work[13] that touches upon some aspects of this problem in application to the diffusion of P in Si. As shown in Ref. 13, the Coulomb interaction of the carriers together with BGN lower the formation energy of vacancies and increase the vacancy diffusion.

In the present paper, we investigate theoretically the basic mechanisms of the effect of BGN on the density dependence of the diffusion of a charged impurity. The approach employed for calculating the density dependence of the diffusion is based on taking into account the internal electric field due to the spatial nonuniformity of the energy diagrams of a heavily doped semiconductor under the conditions of a dopant density gradient.

In the presence of an electric field, the one-dimensional (along the x axis) acceptor q_a and donor q_d fluxes of singly charged impurities with local densities N_a and N_d at an arbitrary time t can be expressed as[2]

$$q_{a,d}(x,t)=-D^0_{a,d}\left(\frac{\partial N_{a,d}}{\partial x}\mp\frac{e}{kT}\frac{\partial\varphi}{\partial x}N_{a,d}\right), \tag{1}$$

where $D^0_{a,d}$ are the diffusion coefficients of the acceptor and donor impurities at low impurity concentrations, φ is the electrostatic potential, e is the elementary charge, T is the temperature, and k is Boltzmann's constant.

We assume that the characteristic length of the spatial distribution of the impurity is much greater than the screening length, and that the impurity density is much higher than the intrinsic density n_i of the charge carriers. The internal electric field can then be found from the equation of electric neutrality

$$N_d(x,t)=N_cF_{1/2}\left[\frac{E_F-\Delta E_c(x,t)+e\varphi(x,t)}{kT}\right] \tag{2}$$

under conditions of donor impurity diffusion and

$$N_a(x,t)=N_vF_{1/2}\left[\frac{\Delta E_v(x,t)-e\varphi(x,t)-E_{g0}-E_F}{kT}\right] \tag{3}$$

in the case of acceptor impurity diffusion. Here N_c and N_ν are the effective density of states in the conduction and valence bands, $F_{1/2}$ is the Fermi integral, ΔE_c and ΔE_ν is the displacement of the edges of the conduction and valence bands as a result of heavy doping, E_{g0} is the band gap in the undoped semiconductor, and E_F is the Fermi energy. In writing the expressions (2) and (3) it was assumed that energy is measured from the conduction band bottom in the undoped semiconductor.

Assuming local equilibrium ($E_F=\text{const}$), we find from Eqs. (2) and (3) the internal electric field

$$-\frac{\partial\varphi}{\partial x}=-\frac{kT}{eN_cF_{-1/2}[F^*_{1/2}(N_d/N_c)]}\frac{\partial N_d}{\partial x}-\frac{\partial\Delta E_c}{\partial x} \tag{4}$$

in a n-type semiconductor and

$$-\frac{\partial\varphi}{\partial x}=\frac{kT}{eN_vF_{-1/2}[F^*_{1/2}(N_a/N_v)]}\frac{\partial N_a}{\partial x}-\frac{\partial\Delta E_v}{\partial x} \tag{5}$$

in a p-type semiconductor, and $F^*_{1/2}$ is the function inverse to the Fermi integral. The derivations of Eqs. (4) and (5) took account of the fact that $dF_{1/2}(z)/dz=F_{-1/2}(z)$.

The second terms in Eqs. (4) and (5) describe the effect on the internal electric field of the change in the positions of the edges of the allowed-energy bands as a result of heavy doping of the semiconductor with a diffusing impurity. A necessary condition for this effect to occur is nonuniformity of doping (evidently, these terms vanish when the impurity distribution becomes uniform). We note that similar terms are present in the internal electric field of variable band-gap semiconductor solid solutions.[14] However, in the latter cases the gradients of the edges of the allowed-energy bands depend not only on the impurity distribution, but also on the chemical composition, whereas the profile of the energy diagram in heavily doped semiconductors is determined uniquely by the coordinate distribution of the impurity.

Substituting the expressions (4) and (5) into Eq. (1), we represent the impurity fluxes in the form of the diffusion fluxes

$$q_{a,d}(x,t)=-D_{a,d}\frac{\partial N_{a,d}}{\partial x} \tag{6}$$

with density-dependent diffusion coefficients

$$D_{a,d}=\left(1+\frac{N_{a,d}}{N_{v,c}F_{-1/2}[F^{*}_{1/2}(N_{a,d}/N_{v,c})]}\mp\frac{1}{kT}\frac{d\Delta E_{v,c}}{dN_{a,d}}N_{a,d}\right)D^{0}_{a,d}. \quad (7)$$

To analyze the characteristic features of the density dependence of the diffusion coefficient under BGN conditions, it is necessary to have expressions for the change in the profiles of the conduction band bottom and valence band top as a function of the impurity density. A number of models of BGN that take into account the possible interactions in the carrier–impurity system have now been proposed (see, for example, Refs. 3–12 and the references cited there). These models are in good agreement with the experimental density dependences of BGN in many semiconductors. The BGN model developed in Refs. 8 and 9 is currently the most widely used model, because this model, in which more interactions are taken into account at the quantum-mechanical level than in other models, gives the correct (specifically, inversely proportional) dependence of the magnitude of the BGN on the effective mass of the charge carriers.[5] The shifts of the band edges in the model of Refs. 8 and 9 is described by the expression

$$\Delta E_{c,v}=\mp R_{c,v}\left[\frac{1.83\Lambda}{\overline{N}^{1/3}_{c,v}r_{d,a}}+\frac{\pi}{2\overline{N}_{c,v}r^{3/2}_{d,a}}\right], \quad (8)$$

where $R_{c,v}=m_{e,h}e^4/2\varepsilon^2\hbar^2$ are the effective Bohr energies for the conduction and valence bands, ε is the relative permittivity of the semiconductor, $m_{e,h}$ are the electron and hole effective masses, $r_{d,a}=(3/4\pi N_{d,a})^{1/3}/a_{e,h}$ are the average donor–acceptor distances normalized to the effective Bohr electron and hole radii $a_{e,h}=\varepsilon\hbar^2/m_{e,h}e^2$, $\overline{N}_{c,v}$ is the number of equivalent extrema in the conduction and valence bands, and Λ is a coefficient of the order of 1, which takes into account the anisotropy of the conduction band in n-type semiconductors and the interaction between the light- and heavy-hole bands in p-type semiconductors. The first term in Eq. (8) describes the displacement of the extremum of the majority charge carrier band as a result of the exchange interaction between the carriers, and the second term characterizes the displacement of the extremum of the same band as a result of an interaction between the carriers and the impurities. According to Refs. 8 and 9, expression (8) can be applied to many semiconductors in a wide temperature range (as a result of the weak temperature dependence of multiparticle interactions[4]) and in the density range corresponding to a degenerate and nondegenerate charge-carrier gas.

Restricting the analysis below to the use of Eq. (8), we note that the diffusion mechanisms established below will be qualitatively satisfied in the case where other models of BGN are used, specifically, the models of Refs. 3 and 10 (in view of the fact that in all models the magnitude of the BGN is a monotonically increasing function of the impurity density).

The expression (8) for the displacement of the edges of the majority carrier bands can be represented as

$$\Delta E_{c,v}=\mp[A_{n,p}N^{1/3}_{d,a}+B_{n,p}N^{1/2}_{d,a}], \quad (9)$$

where $A_{n,p}$ and $B_{n,p}$ are positive coefficients, whose numerical values for Si, Ge, and a number of III–V semiconductors of both types of conductivity are presented in Refs. 8 and 9.

It follows from Eqs. (7) and (9) that when the internal electric field associated with the BGN is taken into account, the diffusion coefficient decreases and, in addition, the correction for band-gap narrowing increases in modulus with the impurity density. This feature of the diffusion coefficient in heavily doped semiconductors has a clear physical explanation. The transformation of the energy diagram as a result of doping, which lowers the energy of the majority carrier in the region with high impurity density, prevents majority carriers from escaping into a more lightly doped region and thereby decreases the internal electric field,[15] which accelerates the diffusing charged impurity.

Since the character of the density dependence of the diffusion coefficient is determined by the ratio of the second and third terms in Eq. (7), which varies with the impurity density (Fermi level), it is useful to examine separately the behavior of $D_{a,d}$ in the range of impurity densities where the charge carriers are not degenerate or the degeneracy is weak, and also in the case where doping results in strong degeneracy. In the case of weak degeneracy ($N_{a,d}\lesssim N_{v,c}$), where the Fermi integral can be represented in the form[16]

$$F_{1/2}=\frac{\exp z}{1+\alpha\exp z}, \quad z<1.3 \quad (10)$$

(here $\alpha=0.27$), the density dependence of $D_{a,d}$ is given by the expression

$$D_{a,d}(N_{a,d})=D^{0}_{a,d}\left[1+\frac{N_{v,c}}{N_{v,c}-\alpha N_{a,d}}-\frac{A_{p,n}}{3kT}N^{1/3}_{a,d}-\frac{B_{p,n}}{2kT}N^{1/2}_{a,d}\right]. \quad (11)$$

It follows from Eq. (11), which holds in the case of a nondegenerate semiconductor, that BGN leads to the formation of a descending section in the density dependence of the diffusion coefficient. The coefficients $D_{a,d}$ decrease with increasing impurity density in the region of the nondegenerate carrier gas and in the region of weak degeneracy. In the first case, the factor $D_{a,d}/D^{0}_{a,d}$ by which the diffusion coefficient increases as a result of the internal electric field, which is not renormalized by the BGN effect, does not depend on the impurity density and equals 2 (we recall that our analysis is limited by the condition $N_{a,d}\gg n_i$).[15] In the second case this factor increases as a result of carrier degeneracy, which in the region where $D_{a,d}$ decreases does not exceed the BGN correction which decreases $D_{a,d}$.

Since the $N_{a,d}$ dependence of the second term in Eq. (11) is superlinear, and since the terms describing the BGN contribution are sublinear, in the region of weak degeneracy a local minimum can form in the functions $D_{a,d}(N_{a,d})$. In the case where $N_{a,d}\ll(2A_{p,n}/3B_{p,n})^6$, the minimum value of $D_{a,d}$ is reached when

$$N^{\min}_{a,d}=\left(\frac{A_{p,n}N_{v,c}}{9\alpha kT}\right)^{3/2}. \quad (12)$$

The position of the minimum of the functions $D_{a,d}(N_{a,d})$ shifts with increasing temperature into the high-density region. In the process, the depth of the minimum decreases somewhat. For example,[1)] for p-type Si the minimum value is $D_a = 1.82D_a^0$ at $T = 600$ °C and $D_a = 1.85D_a^0$ at $T = 900$ °C. This behavior of the diffusion coefficient is attributable to the fact that the BGN correction for $D_{a,d}$ increases with decreasing temperature because of the temperature factor $1/kT$ (in the BGN model of Refs. 8 and 9 the displacements of the band edges are virtually temperature independent). It is obvious that the models of Refs. 3 and 10, where BGN decreases with increasing temperature, will result in a stronger temperature transformation of the density dependences of the diffusion coefficient.

We note that the presence of a descending section in the density dependence of the diffusion coefficient can result in an instability of the diffusion flux. Specifically, it can cause impurities to coagulate into bunches.

As the impurity density increases further ($N_{a,d} > N_{a,d}^{\min}$), the absolute and relative deviations of the diffusion coefficients $D_{a,d}$ and $D'_{a,d}$, calculated with and without BGN, respectively, increase. The calculation of the density dependence of the diffusion coefficient in p-Si using Eq. (7) shows that the ratio $D'_{a,d}/D_{a,d}$ reaches its maximum value, equal to 1.3, at $T = 900$ °C and $N_a = 1.1 \times 10^{21}$ cm^{-3}, which corresponds to the position of the Fermi level in the valence band at a distance of $4kT$ from the valence band top.

Under doping conditions that result in strong degeneracy of the charge carriers ($N_{a,d} \gg N_{v,c}$), we obtain for $D_{a,d}$ from Eqs. (7) and (9) the expression

$$D_{a,d} = D_{a,d}^0 \left[1 + \left(\frac{\pi}{6} \right)^{1/3} \left(\frac{N_{a,d}}{N_{v,c}} \right)^{2/3} - \frac{A_{p,n} N_{a,d}^{1/3}}{3kT} - \frac{B_{p,n} N_{a,d}^{1/2}}{2kT} \right]. \quad (13)$$

In the region of strong degeneracy, the difference $D'_{a,d} - D_{a,d}$ grows monotonically with $N_{a,d}$. As a result of the stronger density nonlinearity of the second term in Eq. (13) than in the case of the BGN terms, the ratio $D'_{a,d}/D_{a,d}$ decreases with increasing doping level.

In summary, we showed in this paper that BGN decreases the diffusion coefficient of a charged impurity. A descending section is observed in the density dependence of the diffusion coefficient in the region of weak degeneracy, and the ratio of the diffusion coefficients, which are calculated with and without allowance for BGN, reaches its maximum value in the intermediate degeneracy range.

[1]For numerical estimates, p-type Si was chosen as a material with one of the strongest density dependences of the edge of the majority carrier band.[8,9]

[1] D. Shaw [Ed.], *Atomic Diffusion in Semiconductors* Plenum Press, N. Y., 1973 [Russian translation, Mir, Moscow, 1975].
[2] B. I. Boltaks, *Diffusion and Point Defects in Semiconductors* [in Russian], Nauka, Leningrad, 1972.
[3] H. P. D. Lanyon and R. A. Tuft, IEEE Trans. Electron Devices **26**, 1014 (1979); S. Sze, *Physics of Semiconductor Devices*, Wiley, N. Y. [Russian translation, Mir, Moscow, 1984, Vol. 1].
[4] H. S. Bennett and J. R. Lowney, J. Appl. Phys. **52**, 5633 (1981).
[5] B. E. Sernelius, Phys. Rev. B **33**, 8582 (1986).
[6] H. S. Bennett and J. R. Lowney, J. Appl. Phys. **62**, 521 (1987).
[7] S. C. Jain, E. Heasell, and D. J. Roulston, Prog. Quantum Electron. **11**, 105 (1987).
[8] S. C. Jain, J. M. McGregor, and D. J. Roulston, J. Appl. Phys. **68**, 3747 (1990).
[9] S. C. Jain and D. J. Roulston, Solid-State Electron. **34**, 453 (1991).
[10] D. I. Bychkovskiĭ, O. V. Konstantinov, and B. V. Tsarenkov, Fiz. Tekh. Poluprovodn. **24**, 1848 (1990) [Sov. Phys. Semicond. **24**, 1151 (1990)].
[11] Z. H. Lu, M. C. Hanna, and A. Majerfeld, Appl. Phys. Lett. **64**, 88 (1994).
[12] B. P. Yan, J. S. Luo, and Q. L. Zhang, J. Appl. Phys. **77**, 4822 (1995).
[13] A. O. Konstantinov, Fiz. Tekh. Poluprovodn. **26**, 339 (1992) [Sov. Phys. Semicond. **26**, 191 (1992)].
[14] L. S. Monastyrskiĭ and B. S. Sokolovskiĭ, Fiz. Tekh. Poluprovodn. **26**, 339 (1992) [Sov. Phys. Semicond. **26**, 191 (1992)].
[15] K. Lehovec and A. Slobodskoy, Solid-State Electron. **3**, 45 (1961).
[16] J. S. Blakemore, *Semiconductor Statistics*, Pergamon Press, N. Y., 1962.

Translated by M. E. Alferieff

Photoconductivity of $CuInSe_2$ films

V. Yu. Rud'

State Technical University 195251 St. Petersburg, Russia

Yu. V. Rud'[a)]

A. F. Ioffe Physicotechnical Institute, Russian Academy of Sciences 194021 St. Petersburg, Russia
(Submitted April 11 1997; accepted April 16 1997)
Fiz. Tekh. Poluprovodn. **31**, 1336–1339 (November 1997)

$CuInSe_2$ thin films were grown by vacuum sputtering of presynthesized material from a single source. The room-temperature photoconductivity spectra of the films were obtained. It was determined that the photoconductivity of these films depends strongly on the preparation conditions and, especially, on the source temperature. A shift of the long-wavelength photoactive absorption edge and the evolution of the photoconductivity spectra of the films were observed. This influence can be explained by allowing for deviations of the composition of the condensed phase from $CuInSe_2$ stoichiometry. The phenomenon established can find application in the production of highly efficient thin-film phototransducers based on $CuInSe_2$. © *1997 American Institute of Physics.* [S1063-7826(97)01311-2]

The ternary semiconductor compound $CuInSe_2$ (CIS) is now one of the most widely used multicomponent materials for highly efficient thin-film solar cells (SCs).[1–3] The efficiency of such SCs has already reached 17%[3–5] and further progress in this field can be made by controlling the optical and electronic properties of CIS films. The band gap, which is the most important parameter for such applications, depends on the atomic composition of the material and also on the degree of ordering of the atoms in the semiconductors of such complex composition.[6,7] In the system Cu–In–Se, the ratio of the copper and indium atom densities directly influences the crystal lattice and the ordering of the Cu and In atoms.[2,8,9] Until now, the spectral position of the long-wavelength limit of photosensitivity in SCs based on CIS thin films was controlled by forming solid solutions by additionally introducing Ga, Te, or S into the films deposited.[2,10–12]

In the present paper we report the results of experimental investigations of the stationary photoconductivity (PC) of CIS films as a function of their vacuum thermal deposition conditions. Photoconductivity measurements give direct information about the character of the photoactive absorption and ultimately have led to the discovery of a new possibility for controlling the spectral position and structure of the long-wavelength photoactive absorption edge exclusively by monitoring the technological parameters of the deposition process, avoiding the need to introduce into the reaction zone new components which are required in order to form solid solutions with the appropriate composition.

Thin polycrystalline CIS films were deposited on glass substrates by evaporation into a vacuum from a single source into which a presynthesized material close to the stoichiometric composition of the ternary compound was placed. The starting material was evaporated in the growth chamber, evacuated to pressures 10^{-6} Torr. A graphite cylinder, heated by an electric current up to a temperature of 1350 °C, was used as the evaporator. The substrate holder was placed 200–400 mm directly above the evaporator. The substrate temperature was regulated by a flat resistance furnace in the range 300–450 °C. To stabilize the parameters of the vapor phase during deposition of the CIS, the evaporator–substrate system was enclosed in a metallic screen. As x-ray and x-ray microprobe investigations showed, the lattice parameters and compositions of the films obtained with evaporation temperatures $T_S = 900-1350$ °C and substrates heated to temperature $T_O = 300-450$ °C corresponded to the initial CIS. The film thicknesses with fixed T_S and T_O were monitored by the evaporation time and reached 1–1.5 μm at $t = 15$ min. The film surfaces were mirror-smooth. All films obtained exhibited, as a rule, rather good adhesion to the surface of the glass substrates.

The PC measurements were performed on samples with average sizes $15-20 \times 3-5$ mm. The samples were prepared by etching off CIS films, deposited on the glass, on the surface which was not coated with lacquer. Ohmic contacts were produced by soldering pure indium. The spectral dependences of the PC were measured in the region where the photocurrent was proportional to the incident radiation flux density, which served as a basis for converting the photoflux into the equivalent number of incident photons. It should be underscored that a photovoltage could not be detected by scanning the obtained film surfaces with a light probe (0.2 mm in diameter). This indicated that the homogeneity of the CIS samples obtained by the method of thermal evaporation was adequate.[13]

Figure 1 shows typical spectral dependences of the stationary PC of CIS films obtained with different evaporation temperatures and a fixed deposition temperature. One can see from the figure that controlling the evaporation temperature makes it possible to influence effectively the spectral contour of the PC. Until now, only a dependence of the resistivity, type of conductivity, and charge carrier density in the CIS films on the deposition conditions was known.[14] According

[a)]e-mail: rudvas@uniys.hop.stn.neva.ru

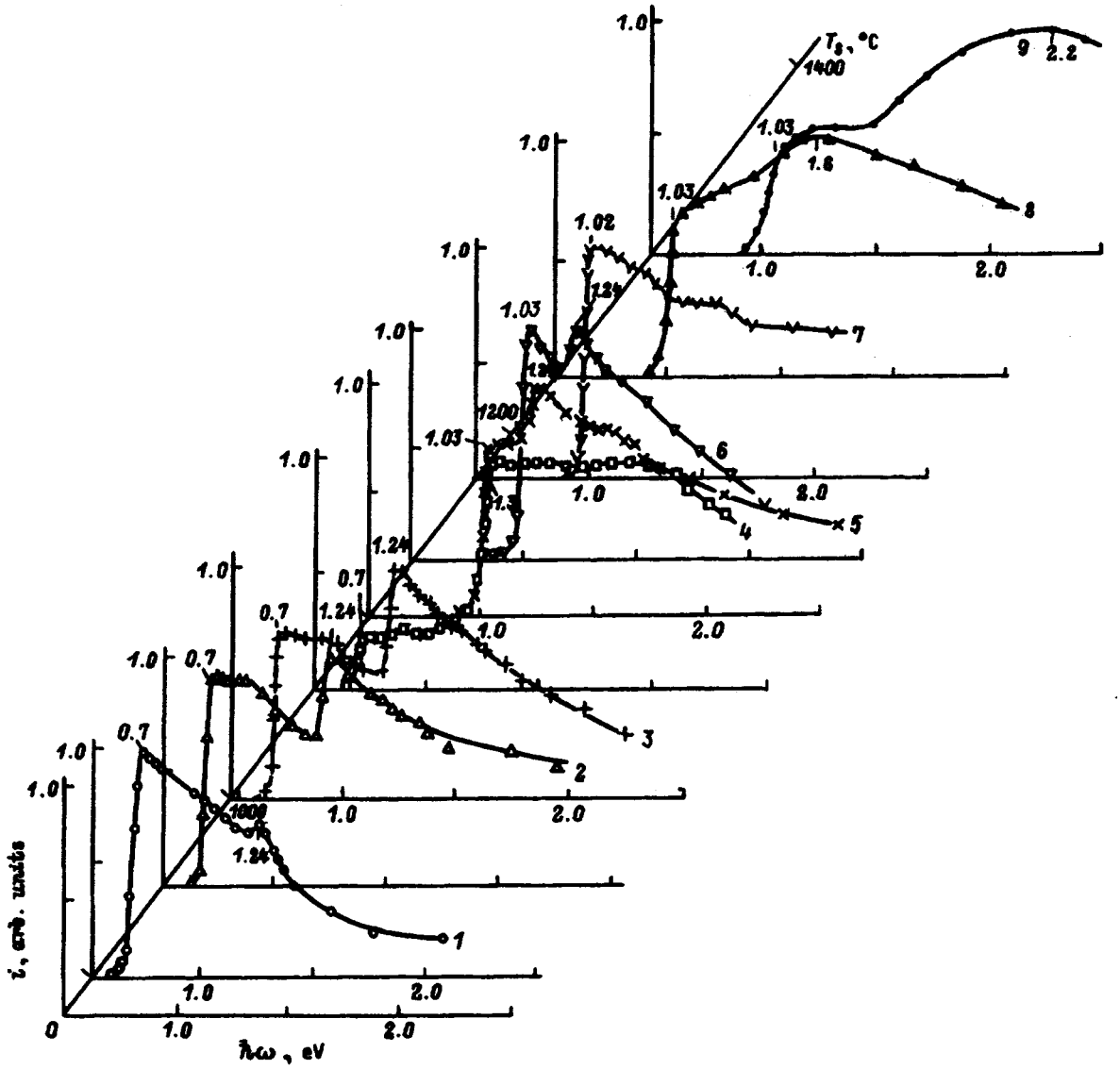

FIG. 1. Photoconductivity spectra of CIS films as a function of the evaporation temperature T_S, °C: *1* — 900, *2* — 950, *3* — 1000, *4* — 1060, *5* — 1100, *6* — 1130, *7* — 1175, *8* — 1230, *9* — 1300. T_O=330 °C.

to Fig. 1, as the evaporation temperature increases, the long-wavelength PC edge shifts into the short-wavelength spectral region and the contribution of the short-wavelength component of the PC increases. At evaporation temperatures up to 1000 °C (Fig. 1, curves *1–3*) the photosensitivity dominates for photon energies $\hbar\omega_1 \approx 0.7$ eV, and the contribution of the short-wavelength component with a maximum at $\hbar\omega_2 \approx 1.24$ eV increases with T_S and becomes dominant at $T_S = 1060$ °C (Fig. 1, curve *4*). As T_S increases further, $T_S \geqslant 1100$ °C, a component, which is typical for CIS,[2,15] with a maximum at $\hbar\omega_3 \approx 1.03$ eV appears in the PC spectra and intensifies (Fig. 1, curves *6–9*). It should be noted that when the evaporation temperature increases above 1175 °C, even shorter wavelength maxima form at $\hbar\omega_4 \approx 1.6$ eV (Fig. 1, curves *7–8*) and $\hbar\omega_5 \approx 2.2$ eV (Fig. 1, curve *9*). Therefore, on the basis of the regularities examined above, the spectral contour of the photoactive absorption of CIS films can be controlled by varying T_S with the deposition temperature held fixed. As investigations showed, variations of T_O in the range from 300 to 420 °C do not introduce any fundamental changes in the character of the evolution of the spectral contour of PC examined above. Variations of T_O give rise only to a shift of the temperature ranges where the maxima studied above dominate. All these maxima undergo the same evolution as that shown in Fig. 1 with increasing T_S and T_O=const.

As one can see from Fig. 2, even small changes of the deposition temperature give rise to appreciable shifts of the long-wavelength edge and maximum of PC in CIS films. This shows how important it is to stabilize the process parameters under deposition conditions. The observed displacements of the long-wavelength edge and absolute maximum $\hbar\omega_3$ of the PC into the short-wavelength spectral region with increasing T_S could be due to changes in the deviation of the composition of the solid phase from CIS stoichiometry, which in turn gives rise to a change in the density and nature of lattice defects as well as the band gap in the films. Figure 2 also shows how an increase in T_S is accompanied by a

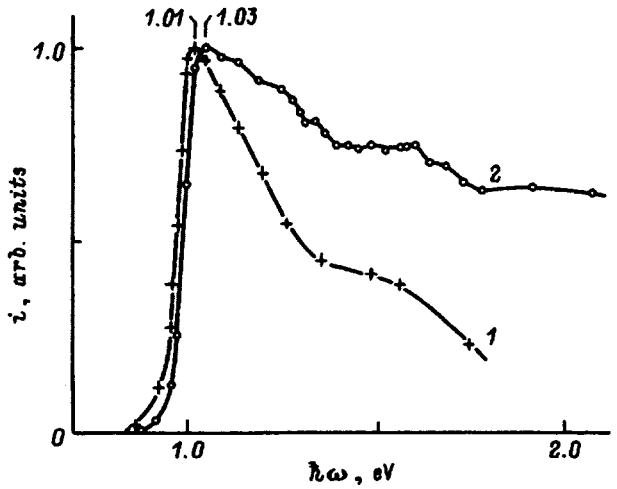

FIG. 2. Photoconductivity spectra of CIS films at $T=300$ K. T_S, °C: *1* — 1150, *2* — 1175. $T_O=335$ °C.

simultaneous decrease in the short-wavelength dropoff of the PC. This could be due to a decrease in the surface recombination rate of nonequilibrium charge carriers.[15]

The long-wavelength PC edge in the films obtained with different T_S remains exponential, despite the large shift of the energy position of the edge from 0.7 to 1.2 eV (see Fig. 3 and Table I). The slope of the long-wavelength PC edge $s=\delta(\ln i)/\delta(\hbar\omega)$ remains quite large in all cases, suggesting that interband transitions in such films are direct. If the energy of the interband transitions is estimated from the spectral position of the absolute maximum of the photocurrent, then according to the results presented it can be assumed that

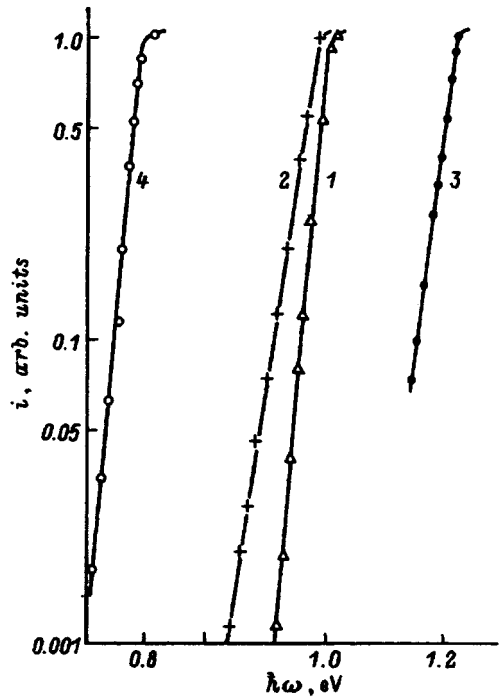

FIG. 3. Photoconductivity spectra of CIS films near the long-wavelength photoactive absorption edge at $T=300$ K. T_S, °C: 1 — 1175, *2* — 1150, *3* — 1130, *4* — 900. $T_O=330$ °C.

TABLE I. Photoelectric properties of CIS thin films at $T=300$ K.

N	T_s, °C ($T_0=330$ °C)	$\hbar\omega^m$, eV	S^m, cm/W	$\delta_{1/2}$ meV	s, eV^{-1}	η
107	900	0.71	10^{-6}	670	48	4
46	1060	1.24	10^{-7}	1500	35	0.7
36	1150	1.02	10^{-3}	270	58	4
95	1150	1.01	10^{-4}	320	41	2.7
92	1170	1.03	4×10^{-5}	670	38	1.4
2	1170	1.02	2×10^{-4}	2200	40	0.6

as a result of changes occurring under conditions of deposition the band gap of the film material can take on discrete values near 0.7, 1.0, and 1.24 eV. In a number of films, these maxima are present in the PC spectrum in some combination simultaneously (Fig. 1). Changes of the deposition conditions could give rise to corresponding deviations from stoichiometry, which gives rise to a corresponding transformation of the PC spectra. Since according to the investigations performed in these samples the crystal lattice parameters and composition of the films are close to the values known for CIS,[16] it can be concluded that PC measurements could be preferable for choosing conditions of growth of thin CIS films with prescribed properties. Indeed, as one can see from Table I, measurements of the evaporation temperature make it possible to monitor photoelectric parameters of the films, such as the energy position of the long-wavelength maximum, the specific photosensitivity S^m, the FWHH $\delta_{1/2}$ of the spectral band of PC, the slope s, and the relative surface recombination rate η.

In summary, the spectral contour of photoactive absorption of thin CIS films can be controlled by varying the conditions of thermal deposition of the CIS, without resorting to the production of quaternary solid solutions, the standard method for such purposes. This could find applications for producing high-efficiency, CIS-based, thin film solar cells.

This work was supported by the International Program INTAS.

[1] S. Wanger, J. L. Shay, P. Migliorato, and H. M. Kasper, Appl. Phys. Lett. **25**, 434 (1974).
[2] T. J. Coutts, L. L. Kazmerskii, and S. Wagner, *Copper Indium Diselenide for Photovoltaic Applications*, Elsevier, Amsterdam, 1986, Vol. 37.
[3] J. Hedstrom, H. Olsen, M. Bodegard, A. K. Klyner, L. Stolt, D. Hariskos, M. Ruch, and H.-W. Schock in *Proceedings 23rd IEEE Photovoltaic Spec. Conference*, IEEE, N. Y., 1993, p. 864.
[4] L. Stolt, J. Hadstrom, J. Kessler, M. Ruch, K. O. Velthaus, and H.-W. Schock, Appl. Phys. Lett. **62**, 597 (1993).
[5] J. R. Tittle, M. A. Contreras, J. S. Word, A. M. Gabor, K. R. Ramanathan, A. L. Tennant, L. Wang, J. Keane, and R. Noufi in *1st World Conference On Photovoltaic Energy Conversion*, Hawaii, 1994.
[6] J. E. Jaffe and A. Zunger, Phys. Rev. B **29**, 1882 (1984).
[7] S.-H. Wei and A. Zunger, Cryst. Res. Technol. **31**, 81 (1996).
[8] H. Yamaguchi, Y. Kuwachara, H. Oyanagi, H. Nakanishi, and T. Irie, J. Appl. Phys. **33**, 567 (1994).
[9] J. Parkers, R. D. Tomlinson, and M. J. Hampshire, J. Appl. Crystallogr. **6**, 414 (1973).
[10] B. M. Keyes, J. Tuttle, J. Sites, A. Tennant, S. Asher, M. Contreras, K. Ramanathan, A. Gabor, J. Webb, R. Ahzenkiel, and R. Noufi, Cryst. Res. Technol. **31**, 439 (1996).
[11] T. Ohashi, A. Jager-Waldau, T. Miyazawa, Y. Hashimoto, and K. Ito, Cryst. Res. Technol. **31**, 435 (1996).

[12] R. Herberholz, T. Walter, and H.-W., Schock, Cryst. Res. Technol. **31**, 449 (1996).
[13] V. Yu. Rud', Author's Abstract of Candidate's Dissertation, Physicotechnical Institute, Russian Academy of Sciences, St. Petersburg, 1995.
[14] M. A. Magomedov, G. A. Medvedkin, I. K. Polushina, and Yu. V. Rud', Zh. Neorg. Mater. **28**, 679 (1992).
[15] N. N. Konstantinova, M. A. Magomedov, V. Yu. Rud', and Yu. V. Rud', Fiz. Tekh. Poluprovodn. **25**, 2047 (1991) [Sov. Phys. Semicond. **25**, 1233 (1991)].
[16] *Reference Date on the Physicochemical Properties of Semiconductors* [in Russian], Nauka, Moscow, 1979.

Translated by M. E. Alferieff

Relaxation properties of a metal–chalcogenide glassy semiconductor

V. T. Avanesyan, V. A. Bordovskiĭ, and R. A. Castro

A. I. Gertsen Russian State Pedagocial University, 191186 St. Petersburg, Russia
(Submitted January 21, 1997; accepted for publication April 14, 1997)
Fiz. Tekh. Poluprovodn. **31**, 1340–1341 (November 1997)

The results of a study of the temperature dependence of the capacitance of an Al-As_2Se_2 contact at infralow frequencies are reported and the values of the parameters characterizing charge accumulation processes are estimated. © *1997 American Institute of Physics.* [S1063-7826(97)03311-5]

1. INTRODUCTION

The capacitance spectroscopy method applied to chalcogenide glassy semiconductors (CGSs) makes it possible to investigate the effect of different excitation conditions on the form of the density of localized states.[1] At the same time, the effect of the temperature on the capacitance of the Al-As_2Se_3 barrier has been established by the method of dynamic current voltage charcteristics (DCVCs). This effect is correlated with the idea that there exists a quasi-continuous spectrum of localized states in the band gap.[2] An investigation of a prolonged relaxation of the photoconductivity (PC) of glassy As_2Se_3 (Ref. 3) has shown that its chief characteristics can be described in a model that takes into account the dispersion character of the charge transfer mechanism. However, the prolonged PC relaxation processes are associated with current relaxation effects which are characteristic of high-resistivity materials and arise in the sample as a result of the accumulation and redistribution of bound charge.

We have developed a method of capacitance spectroscopy for the purpose of further studying the properties that reflect the dynamical characteristics of the metal–CGS barrier region.

2. EXPERIMENTAL PROCEDURE

The investigation was performed on $\sim$1.0-μm-thick As_2Se_3 films prepared by the method of thermal evaporation in vaccum. The samples possessed a sandwich configuration with aluminum electrodes and a contact area of 14.0 mm^2. The curves of the isothermal relaxation currents were recorded using an electrometric amplifier (the measured currents of both polarities range from 10^{-15} to 10^{-7} A), a stabilized-voltage source ($U=0.1$ V), and a X–Y potentiometer. During the measurements the temperature varied in the range $T=294-344$ K.

3. RESULTS AND DISCUSSION

The current relaxation curves for As_2Se_3 at different temperatures (Fig. 1) are characterized by a single section with a hyperbolic drop off $I(t)\sim t^{-n}$ ($n=0.8-0.1$) corresponding to the time interval $\Delta t=1-100$ s.

The theory of the relay mechanism of charge transfer in metal–insulator–metal (MIS) structures gives for the time-dependence of the current[5]

$$I=UC_c\tau/(\tau+t)^2 \tag{1}$$

for $\tau=L^3/\mu d_c U$, where τ is the characteristic time constant, L is the thickness of the insulating layer, μ is the effective charge carrier density, d_c is the width of the region of charge accumulation near the contact, and U is the applied voltage. The instantaneous relaxation time $\tau_i=I/(dI/dt)$ of the process is characterized by the relation[6]

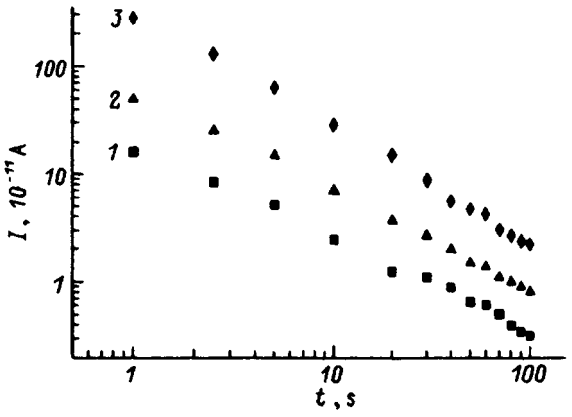

FIG. 1. Relaxation curves of the dark current in As_2Se_3 at different temperatures, K: *1*—294, *2*—314, *3*—344.

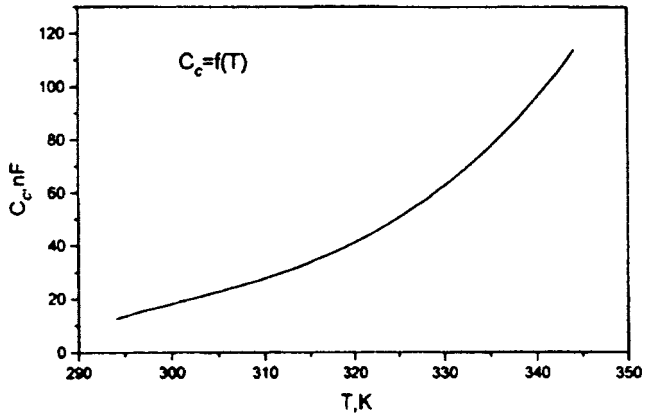

FIG. 2. Temperature dependence of the contact capacitance calculated from Eq. (3).

$$\tau_i = I/(dI/dt) = (\tau + t)/2. \quad (2)$$

Taking into account the experimental dependence $n(T)$ for the family of curves $I(t)$ (Fig. 1) and the expressions (1) and (2), the capacitance C_c of the contact as a function of the temperature can be determined as

$$C_c = 4I_0 \exp(bT) t_0 / U n_0 T (2a + 2 - n_0 T), \quad (3)$$

where I_0, n_0, a, and b are constants, and t_0 is the polarization time corresponding to the termination of the relaxation process ($t_0 = 100$ s). The obtained temperature dependence $C_c(T)$ (Fig. 2) is characterized by the activation energy $E_A \sim 1.3$ eV and agrees with the dependence established in Ref. 1 for an ac current.

Taking into consideration the relation between the instantaneous relexation time for a hyperbolic drop off and the constant τ, it is possible to switch to the time dependence of the charge-accumulation region

$$d_c = nL^3/(2-n)t\mu U. \quad (4)$$

It follows from the last expression that the thickness of the capacitance layer of the contact decreases and the electric field E_c increases with time in the region near the contact. Specifically, the termination of the relaxation process ($t_0 = 100$ s) is characterized by the values $d_c = 1.24 \times 10^{-2}$ m and $E_c = 8.06 \times 10^3$ V/cm.

4. CONCLUSIONS

The character of the relaxation processes in As_2Se_3 films indicates the existence of a non-Debye mechanism of dispersion that corresponds to an asymmetric distribution of the relaxation times and determines the effect of contact phenomena on charge relaxation processes. The high value of the activation energy E_A (of the order of the band gap) indicates that even the deepest states participate in the formation of the barrier capacitance.

[1] G. A. Bordovskiĭ and M. R. Kanichev, Fiz. Tekh. Poluprovodn. **24**, 527 (1990) [Sov. Phys. Semicond. **24**, 330 (1990)].
[2] A. A. Simashkevich and S. D. Shutov, Fiz. Tekh. Poluprovodn. **28**, 611 (1994) [Semiconductors **28**, 367 (1994)].
[3] K. Shimakawa, Y. Yano, and Y. Katsuma, Philos. Mag. B **54**, 285 (1986).
[4] N. Anisimova, V. Avenesyan, G. Bordovski, R. Castro, and A. Nagayteev in *Proceedings 8th Int. Symp. on Electrets*, Paris, France, 1994, p. 136.
[5] B. L. Timan, Fiz. Tekh. Poluprovodn. **7**, 225 (1973) [Sov. Phys. Semicond. **7**, 163 (1973)].
[6] A. M. Andriesh and M. R. Chernyĭ in *Crystalline and Glassy Semiconductors* [in Russian], Shtinitsa, 1977, p. 127.

Translated by M. E. Alferieff

Electrical and photoelectric properties of an anisotypic $Pb_{0.93}Sn_{0.07}Se/PbSe$ heterojunction

T. A. Gavrikova and V. A. Zykov

St. Petersburg State Technical University 195251 St. Petersburg, Russia
(Submitted December 24 1996; accepted March 18 1997)
Fiz. Tekh. Poluprovodn. **31**, 1342–1346 (November 1997)

The electrical and photoelectric properties of sharp anisotypic p-$Pb_{0.93}Sn_{0.07}Se/n$-PbSe heterojunctions with hole densities in the crystal of the solid solution $1\times10^{16}-2\times10^{18}$ cm^{-3} and electron densities in the PbSe film $1\times10^{17}-5\times10^{18}$ cm^{-3} were investigated. The heterojunctions were fabricated by the method of vacuum epitaxy of a PbSe film on a single crystal of the solid solution. The conditions for preparation of sharp anisotypic heterojunctions with the lowest density of states (4×10^{10} cm^{-2}) on the metallurgical boundary were determined. The dependences of the photoresponse signal on the current-carrier density in the base regions and the characteristic features of the spectral distribution of the photosensitivity were analyzed. The direct and inverse current-voltage characteristics were investigated. A band diagram was constructed in the approximation of an ideal heterojunction model. © *1997 American Institute of Physics.* [S1063-7826(97)01411-7]

Narrow-gap solid solutions of lead and tin chalcogenides ($Pb_{1-x}Sn_xSe$, $Pb_{1-x}Sn_xTe$) are promising materials for infrared (IR) radiation detectors in the atmospheric window 10–14 μm.[1] Until recently, the use of materials from this group was limited by the possibilities of the technology used to grow high-quality crystals with the properties required for photoelectric applications. For this reason, device development was limited to the most technologically efficient solid solutions $Pb_{1-x}Sn_xTe$.[1,2] At the same time, a comparative theoretical analysis of the characteristics of the materials shows that solid solutions in the selenide system have a number of advantages for the development of photodiode structures.[3] The present level of crystal-growing technology (mainly on the basis of vapor-phase methods[4,5]) and of stoichiometry monitoring[6] makes it possible to obtain $Pb_{1-x}Sn_xSe$ crystals of the required quality and set the prerequisites for investigating experimentally the properties of the photovoltaic structures based on them.

In the present paper we report the results of an investigation of the electrical and photoelectric properties of anisotypic heterojunctions (HJs) p-$Pb_{0.93}Sn_{0.07}Se/n$-PbSe. The tin content in the narrow-gap solid solution $x=0.07$ corresponds to the band gap $E_g=0.104$ eV at 80 K and a red limit in the region 10–12 μm; for PbSe $E_g=0.165$ eV.[7] Structurally, the components of the HJ form an ideally matched pair for epitaxy — the crystal lattices are isomorphic, the lattice parameters differ by 0.15%, and the thermal expansion coefficients are virtually identical.[7,8]

The heterojunction was prepared by epitaxial growth of a lead selenide film on a substrate consisting of the solid solution. PbSe films were deposited by vacuum sputtering using the ''hot-wall'' method.[9] The sputtering conditions and technique are described in Ref. 10. The density and type of majority current carriers in the crystals and films were determined by the ratio of the intrinsic defects (deviation from stoichiometry). The current carrier density in the PbSe layers on single-crystalline $Pb_{0.93}Sn_{0.07}Se$ substrates were estimated from Hall effect measurements on control samples of PbSe films on (111) BaF_2 and were equal to $n=2\times10^{17}-5\times10^{18}$ cm^{-3}. The quality of the crystals of the solid solution and the composition and electrical parameters were monitored by comprehensive investigation of the Hall coefficient, electrical conductivity, thermoelectric power, and transverse Nernst–Ettingshausen effect in the temperature range 77–300 K, as well as by optical methods, by investigating the absorption coefficient near the fundamental absorption edge. The wafers of p-$Pb_{0.93}Sn_{0.07}Se$ with hole density $p=1\times10^{16}-2\times10^{18}$ cm^{-3} and oriented in the (100) plane were used as substrates for the heterostructures. Prior to deposition, the $Pb_{0.93}Sn_{0.07}Se$ substrates were subjected to chemical-dynamic polishing in a ferrocyanide etchant.[11] Mesa structures with junction area $A=10^{-3}$ cm^2 were separated for investigation of electrochemical etching.[8] The junction was illuminated on the wide-gap material side.

Analysis of the effect of the parameters of the crystals on the electrical and photoelectric properties of the heterojunctions was performed on structures similar to Schottky diodes, where a strongly doped PbSe film was used as the metallic electrode. Estimates show that for current carrier densities in the film exceeding 10^{18} cm^{-3}, the diffusion potential is almost completely concentrated in the solid-solution crystal. Figure 1 shows the experimental dependence of the photoresponse signal (photo-emf) on the hole density in p-$Pb_{0.93}Sn_{0.07}Se$ for a heterojunction with a strongly doped PbSe film. For all experimental heterojunctions, the electron density in the lead selenide film was $n=(2-3)\times10^{18}$ cm^{-3}. The photo-emf signal (S) reaches the highest values for a hole density in the crystal $p=3\times10^{16}-1\times10^{17}$ cm^{-3} and remains nearly constant in this range. For $p>2\times10^{17}$ cm^{-3}, S decreases rapidly with increasing hole density and there is virtually no photoresponse at $p=1\times10^{18}$ cm^{-3}. As the density decreases from $p=3\times10^{16}$ cm^{-3}, the photoresponse likewise drops, but much more slowly.

The spectral characteristics of the heterojunctions with a

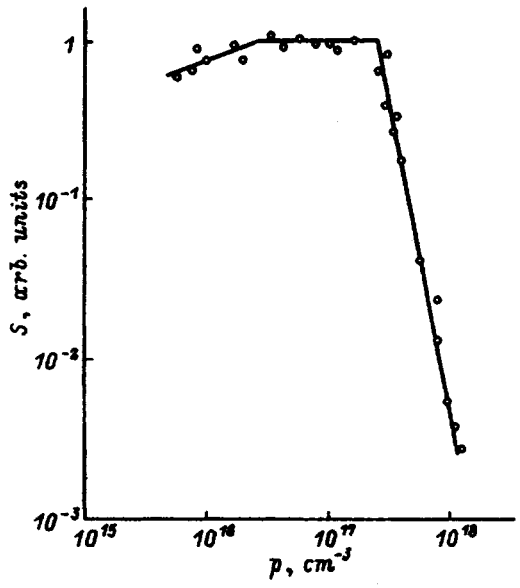

FIG. 1. Photoresponse signal of a p-$Pb_{0.93}Sn_{0.07}Se$/n-PbSe heterojunction versus the hole density in the solid solution. $T=80$ K.

strongly doped lead selenide film exhibit a photoresponse only in the wavelength range 10–12 μm (Fig. 2, curve *2*). For hole density $p=(1-3)\times10^{16}$ cm^{-3} in $Pb_{0.93}Sn_{0.07}Se$, the maximum spectral sensitivity is attained at the wavelength $\lambda=11.9$ μm, corresponding to the band gap in the solid solution at 80 K. As the hole density in the crystals increases from 3×10^{16} to 1×10^{17} cm^{-3}, the red boundary in the spectral distribution of the sensitivity shifts into the short-wavelength region. This shift, taking into account the small values of the effective masses of the density of states in the solid solution,[7] is attributable to the Burshteĭn–Moss effect.

The qualitative experimental hole density dependence of the photo-emf obtained for the heterojunctions agrees satisfactorily with the theoretical calculations[3] of the dependence

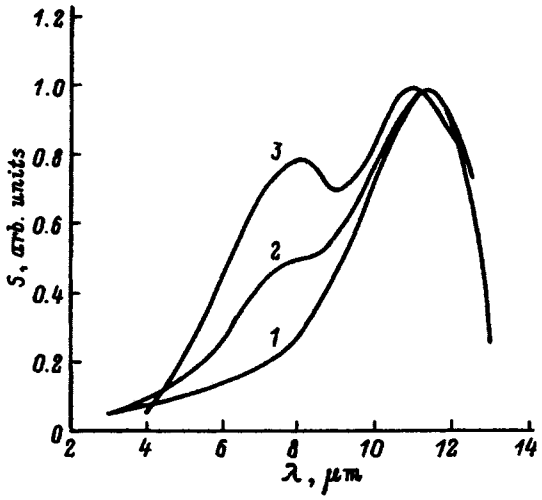

FIG. 2. Spectral characteristics of a p-$Pb_{0.93}Sn_{0.07}Se$/n-PbSe heterojunction with hole density in the crystal $p=8\times10^{16}$ cm^{-3} and electron density in the film n, 10^{17} cm^{-3}: 1 — 10, 2 — 6, 3 — 2. $T=80$ K.

of R_0A (R_0 is the dark resistance of the junction with zero bias) for a device with a unilateral $Pb_{1-x}Sn_xSe$-based $p-n$ junction on the hole density in the crystal. This agreement concerns the characteristic values of the densities, for which a change is observed in the dependence of the photoresponse signal on the current carrier density in $Pb_{0.97}Sn_{0.07}Se$. The photoresponse signal was recorded in the hole density range ($p<2\times10^{17}$ cm^{-3}) corresponding to diffusion current flow in the heterojunctions; here the highest photoresponse is reached in the density range where Auger recombination dominates. In the region $p>2\times10^{17}$ cm^{-3}, R_0A and the photoresponse decrease rapidly with increasing hole density as a result of an increase in the tunneling component of the conductivity.

As the current carrier density in the PbSe film decreases, a photosensitivity peak appears in the spectral characteristics of the response of the heterojunctions in the short-wavelength region of the spectrum with a maximum at $\lambda=8$ μm (Fig. 2, curves *2* and *3*). In the epitaxial technology employed for preparing the heterojunctions, the current carrier density in the film is decreased by adding selenium into the main vapor flux. The efficiency of this technique for controlling the defect composition and the electronic properties of the films depends on the degree to which the conditions of growth deviate from the equilibrium, i.e., on the vapor supersaturation and condensation temperature T_c.[8,9] Experiment shows that for $T_c<350$ °C it is impossible to achieve current carrier densities below $(1-2)\times10^{17}$ cm^{-3}, even with the lowest vapor supersaturations in the crystallization zone. This is due to the nonequilibrium defects, whose number is controlled mainly by T_c.[9] However, an increase in T_c, accompanied by a decrease in the density of nonequilibrium defects in the film, simultaneously stimulates atomic diffusion processes in the contact region of the components of the heterojunctions. An Auger spectroscopy analysis of the distribution of the elements near the metallurgical boundary of the heterojunction shows that at condensation temperatures above 350 °C, tin diffusion from the substrate into the growing lead selenide layer becomes appreciable. This diffusion causes a broadening of the metallurgical boundary of the heterojunction, which at high T_c can reach several tens of microns over the film deposition time. In application to the epitaxial heterostructure under study, for $T_c>350$ °C, the characteristic geometric dimensions of the regions of broadening become comparable to the width of the space charge regions, and the heterojunction acquires characteristics of a variable-gap structure. This circumstance is reflected in, specifically, the spectral characteristics of the heterojunction, resulting in a shift of the maximum of the photoreponse in the region of sensitivity of the solid solution into the short-wavelength region (Fig. 3). At the same time, the sensitivity peak in the region of the variable band gap component of the heterojunction shifts into the region of longer wavelengths. Thus, in the vacuum epitaxial technology for preparing p-$Pb_{0.93}Sn_{0.07}Se$/nPbSe heterojunctions, it is possible to obtain two types of heterojunctions — a sharp anisotypic heterojunction with spectral distributions of the photosensitivity ($T_c<300$ °C) which are determined by the characteristics of the components of the heterojunction in the base regions and

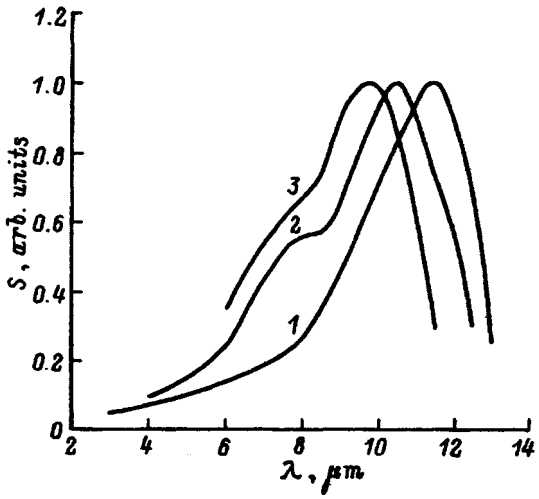

FIG. 3. Spectral characteristics of a p-$Pb_{0.93}Sn_{0.07}Se$/n-PbSe heterojunction prepared at condensation temperatures T_c, °C: *1* — 300, *2* — 350, *3* — 400. $T=80$ K.

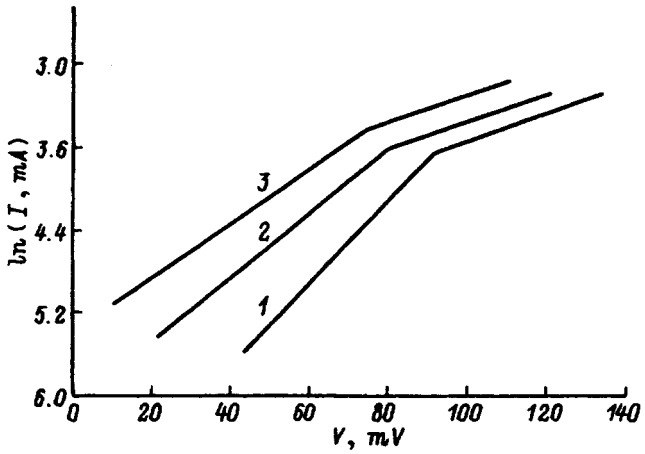

FIG. 4. Straight branches of the IVC of a p-$Pb_{0.93}Sn_{0.07}Se$/n-PbSe heterojunction with $p=8\times10^{16}$ cm^{-3} and $n=6\times10^{17}$ cm-3. T, K: *1* — 80, *2* — 100, *3* — 125.

variable-gap structures ($T_c>350$ °C), in which the character of the spectral distribution reflects the characteristics of the materials in the region of the metallurgical boundary. The properties of devices of the first type will be examined below.

In contrast to an idealized unilateral junction, a heterojunction possesses fundamental features associated with the effect of the metallurgical interface of the components of the heterojunction on the distribution of the contact electric fields and recombination processes and, correspondingly, on the electrical and photoelectric properties. This influence is due to the surface charges due to different surface imperfections near the metallurgical boundary of the heterojunction — misfit dislocations, contamination with foreign impurities — and variations in the electrical properties of the boundaries as a result of the presence of oxide dielectric phases. Evidently, the degree of influence of these factors depends on the structural features of the components of the heterojunction and the level of the surface technology.

The main types of technological contaminants in the heterojunctions which we studied were found by analyzing the Auger spectra of PbSe films systematically etched off in steps (by Ar ion beams) down to the metallurgical boundary, as well as near-contact regions of the solid solution. Ordinarily, carbon and oxygen atoms are found in lead selenide films and at the metallurgical boundary of the heterojunction. Carbon is distributed uniformly over the thickness of the film and is absent in the crystal of the solid solution. The carbon concentration depends on the pressure of the residual gases in the evaporation chamber and can be decreased to the level of sensitivity of the method of determination at $P=5\times10^{-7}$ Torr and lower. The appearance of oxygen in the film is also associated with the effect of the residual gases in the evaporation chamber. However, in contrast to carbon, oxygen is distributed nonuniformly over the thickness of the film. A high oxygen content on the outer surface, which is in contact with the atmosphere, is observed for all films. At the same time, in some samples, oxygen is present in appreciable quantities on the metallurgical boundary of the heterojunction. The content of this oxygen is correlated mainly with the conditions of surface treatment of the solid-solution crystals prior to film deposition, and with the correct combination of conditions of chemical-dynamical polishing, accurate maintenance of the concentrations of the etchant ingredients and, especially, strict control of the pH of the solution, the amount of surface oxygen can be reduced to a level determined by contaminations from the residual gases. At $P=5\times10^{-7}$ Torr oxygen is essentially not detected at the metallurgical boundary. Thus, in the epitaxial technology employed to prepare the heterojunctions, it is possible to achieve a combination of process parameters, for which the density of the surface states at the interface of the components of the heterojunction is determined by the magnitude of the mismatch of the lattice parameters. For the sharp $Pb_{0.93}Sn_{0.07}Se$/PbSe HJs studied, the density of states associated with the mismatch of the lattice parameters equals 4×10^{10} cm^{-2}, i.e., a value at which the heterojunction can be regarded as ideal.[12] This conclusion is confirmed by the results of an investigation of the electrical properties of the heterojunction.

Sharp anisotypic heterojunctions with current carrier density $n=(0.5–5.0)\times10^{18}$ cm^{-3} in the film and $p=(0.3–3.0)\times10^{17}$ cm^{-3} in the substrate exhibit rectifying properties, and at higher hole densities in the substrate the current-voltage characteristics are linear. The straight branches of the nonlinear I–V characteristics contain two exponential sections (Fig. 4). Both sections remain when the measurement temperature is increased from 80 to 125 K. In the presence of low direct biases, the total current through the junction is limited by carrier recombination at the interface and the straight branch of the I–V characteristic is described by the relation

$$I=qs_0N_D\exp\left\{-\frac{q(V_{Dn}-BV)}{kT}\right\},$$

where s_0 is the recombination rate at the interface, H_D is the donor density in the wide-gap material, N_D is the contact

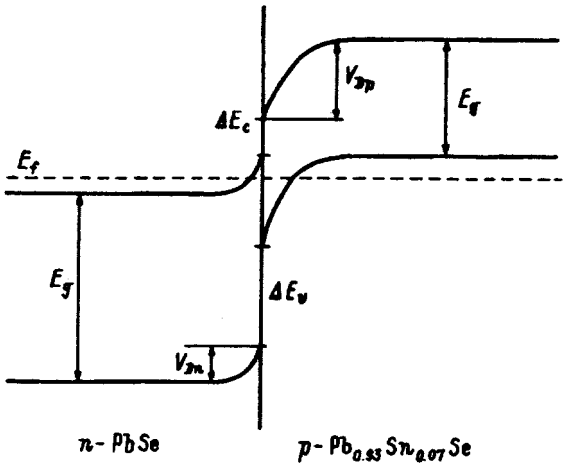

FIG. 5. Diagram of the energy bands of the anisotypic p-$Pb_{0.93}Sn_{0.07}Se$/n-PbSe heterojunction with $p=2.3\times10^{17}$ cm^{-3} and $n=6.6\times10^{17}$ cm^{-3}. $T=80$ K.

potential difference across the n-type region, and $B=1/\beta_1$. At 80 K $\beta_1=2-3$ and increases with temperature.

At high direct biases the current flow is determined by tunneling and is described by the formula

$$I=I_0\ \exp(CV),$$

where $C=1/\beta_2$; here $\beta_2=10$ and is independent of temperature (Fig. 4).

The reverse branches of the I–V characteristic are described by a power-law dependence. Calculations show that the direct currents are modeled satisfactorily by a recombination-tunneling mechanism at the interface.[11] A thermal-emission current flows in the wide-gap material and a tunneling current flows in the narrow-gap material. The magnitudes of the currents are determined by current carrier recombination at the interface.

Investigations of the electrical and photoelectric properties of heterojunctions (I–V characteristics, saturation photo-emf), supplemented by measurements of the electric and optic properties of crystals and films, yield the information required to construct diagrams of the energy bands of heterojunctions. Figure 5 shows a diagram of the energy bands of a typical sharp anisotypic heterojunction p-$Pb_{0.93}Sn_{0.07}Se$/n-PbSe, obtained under conditions when the diffusion broadening of the metallurgical interface can be ignored. For the heterojunction which we studied, the current carrier densities in the base regions of the solid-solution crystal and the epitaxial lead selenide film, $p=2.3\times10^{17}$ cm^{-3} and $n=6.6\times10^{17}$ cm^{-3}, respectively, were determined from Hall effect measurements. The equilibrium diffusion potential $V_D=0.059$ eV and the partial potentials are $V_{Dp}=0.040$ eV and $V_{Dn}=0.013$ eV. The conduction and valence band offsets are $\Delta E_c=0.059$ eV and $\Delta E_v=0.118$ eV. All data for the band diagram are presented for 80 K.

Investigations of the saturation photo-emf in heterojunctions made it possible to determine the current carrier density in the base region of the constituent lead selenide film of the heterojunction. After the saturation photo-emf is determined experimentally in the long-wavelength part of the spectrum (for the heterojunction studied this quantity is 40 meV), the equilibrium band bending in the region of PbSe and the electron density in the film can be easily calculated. It turns out to be 6.6×10^{17} cm^{-3}. This value agrees well with the electron density in the lead selenide film, grown under the same conditions on a (111) BaF_2 dielectric substrate — $n=6.9\times10^{17}$ cm^{-3}. The satisfactory agreement between the densities shows that estimation of the current carrier densities in the film of the heterojunction from Hall effect measurements in control samples — PbSe films on (111) BaF_2 substrates — is a correct procedure.

[1] R. J. Keyes, *Optical and Infrared Detectors*, Springer-Verlag, N. Y., 1977 [Russian trans., Moscow, 1985].
[2] F. F. Sizov, Zarubezh. Élektron. Tekhn. **24**, 31 (1977).
[3] H. Preier, Infrared Phys. **18**, 43 (1978).
[4] V. P. Slomanov and A. V. Novoselova, *P-T-x Phase Diagrams of Metal–Chalcogen Systems* [in Russian], Moscow, 1987.
[5] G. A. Kalyuzhnaya and K. V. Kiseleva, Tr. FIAN **177**, 5 (1987).
[6] G. Nimtz and B. Schliht, Springer Tracts in Mod. Phys. **98** (1983).
[7] T. C. Harman and I. Mendailis, Sol. St. Sci. **4**, 1 (1974).
[8] A. Lopez-Otero, Thin Solid Films **49**, 3 (1978).
[9] T. A. Gavrikova and V. A. Zykov, Elekton. Tekhn. Materialy, No. 7, 35 (1990).
[10] B. Bretsameter, W. Harman, and H. Lane, Krist. Tech. **15**, 497 (1978).
[11] A. Milnes and D. Feucht, *Heterojunctions and Metal-Semiconductor Junctions*, Academic Press, N. Y., 1972 [Russian trans., Mir, Moscow, 1975].

Translated by M. E. Alferieff

Excitonic electroluminescence of 6*H*-SiC *p*–*n* structures obtained by sublimation epitaxy

A. A. Lebedev and N. K. Poletaev

A. F. Ioffe Physicotechnical Institute, Russian Academy of Sciences, 194021 St. Petersburg, Russia

M. Z. doKarmo

Aveiro University, Aveiro, Portugal

(Submitted January 30, 1997; accepted for publication April 22, 1997)
Fiz. Tekh. Poluprovodn. **31**, 1347–1349 (November 1997)

The electroluminescence spectra of 6*H*-SiC *p*–*n* structures obtained by sublimation epitaxy have been investigated. It has been found that the intensity of the excitonic band increases rapidly with increasing direct current density, and that this band dominates the emission spectrum of the diode at high direct-current densities and elevated temperatures. Investigation of the shift of the maximum of this band with increasing temperature shows that this band is most likely due to the recombination of a free exciton. © *1997 American Institute of Physics.* [S1063-7826(97)01511-1]

1. INTRODUCTION

Despite the publication of many papers on the edge photoluminescence and electroluminescence (i.e., radiation with photon energy close to the band gap) of 6*H*-SiC,[1–6] many questions concerning the nature of the observed radiation still have not been answered definitively. For example, it remains unclear whether the edge radiation is due to the annihilation of a free or bound exciton.[5] Moreover, investigations of the short-wavelength part of the emission spectrum of 6*H*-SiC *p*–*n* structures yield important information about the band structure of silicon carbide.

In our study we investigated 6*H*-SiC *p*–*n* structures obtained by sublimation epitaxy (SE) in an open system.[7] On the one hand, such structures are widely used for fabricating different SiC-based semiconductor devices[8] and, on the other, their excitonic electroluminescence (EL) radiation has never been studied in detail.

2. PRELIMINARY REMARKS

The excitonic band in 6*H*-SiC was previously investigated mainly by photoluminescence and at low temperatures, $T \leqslant 300$ K.[2,6] This method of investigations was attributable to the fact that wide bands, due to carrier recombination against a background of deep acceptor levels and superimposed on the excitonic emission, dominate the EL spectrum of 6*H*-SiC *p*–*n* structures. In the case of *p*–*n* structures prepared by SE, at room temperature the maximum of the radiation falls in the yellow-green region of the spectrum. This radiation is due mainly to carrier recombination at *D* centers ($E_v + 0.58$ eV), whose presence is due to uncontrollable boron-doping of epitaxial layers grown by this method.[9] (The boron impurity is contained in the graphite fixtures used for growth.)

In *p*–*n* structures obtained by liquid and containerless liquid epitaxy,[4,5] the *D*-center densities are several orders of magnitude lower, but in such structures the *n*-type base, as a rule, has a background aluminum density, which gives radiation in the blue region of the spectrum. The ionization energy of the center—EL activator (~ 0.27 eV) is much lower in this case. As a result, the temperature quenching of EL is substantial even at $T \simeq 300$ K. However, the spectral position of the EL due to the aluminum impurity is much closer to the excitonic peak and the EL can interfere with observations even at low intensity. For this reason, from our point of view, it was important to investigate the excitonic EL in *p*–*n* structures obtained by SE and having a low density of background acceptor levels.

3. SAMPLES

The *p*–*n* junctions which are investigated were formed on the (0001) Si face of single-crystalline n^+ substrates of the 6*H* polytype of silicon carbide. Al (*p*-type) and N (*n*-type) served as dopants. The *p*-type epitaxial layers were 1–2 μm thick and the *n*-type layers were 5–10 μm thick. The area of the *p*–*n* structures was equal to $\sim 2.5 \times 10^{-3}$ cm^2. To decrease the background concentration of deep acceptor levels in the *n*-type layer, prior to epitaxy the growth cell was subjected to prolonged vacuum annealing at temperatures >2000 °C.

4. EXPERIMENT

DLTS measurements showed that the densities of *i* and *D* centers in the experimental *p*–*n* structures was two to three times lower than in the samples studied in Refs. 7 and 8. Correspondingly, the intensity of the yellow-green band was low and the excitonic electroluminescence could be observed at currents $>10^{-3}$ A (Fig. 1). The spectral position of the excitonic band ($\lambda_{max} \simeq 425 \pm 1$ nm) agreed well with the data obtained by other authors for both photoluminescence and electroluminescence spectra. The intensity of the excitonic peak increased with current more rapidly than that of any other part of the EL spectrum (Fig. 2). A more detailed analysis showed that the intensity I_{ex} of the excitonic line increased with the current J as $I_{ex} = J^n$, where $n = 2 \pm 0.2$. The intensity of the excitonic band increased especially rap-

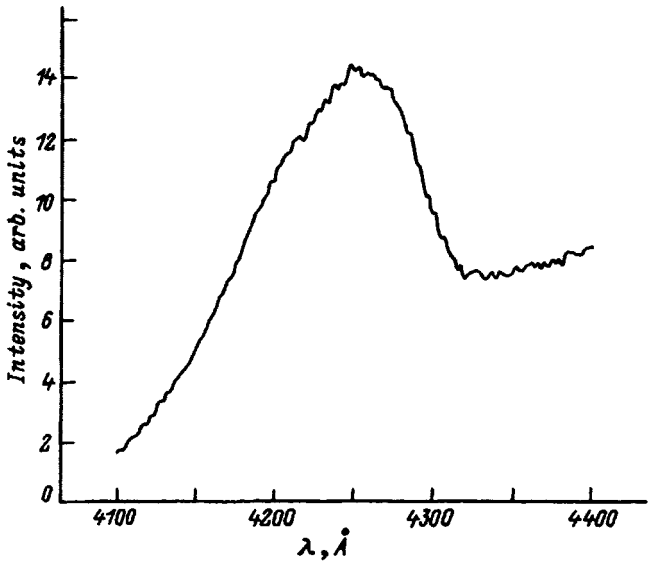

FIG. 1. Edge electroluminescence spectrum of $p-n$ structures at room temperature. $J=30$ mA.

idly at low currents $J=(1-6)\times 10^{-2}$ A. This could be due to an increase in the hole diffusion length with increasing injection level.[10]

As the sample temperature and the direct current increased, the excitonic peak became dominant in the emission spectrum of the diode (Fig. 3). This occurred for the following reasons: 1) more rapid growth of I_{ex} with J than any other EL bands; 2) increase of the hole diffusion length with temperature;[11] and 3) temperature quenching of all EL bands except the excitonic band. At 650 K the intensity of excitonic band exhibited the same dependence on the direct current density with $n=2$ as previously. As the temperature was

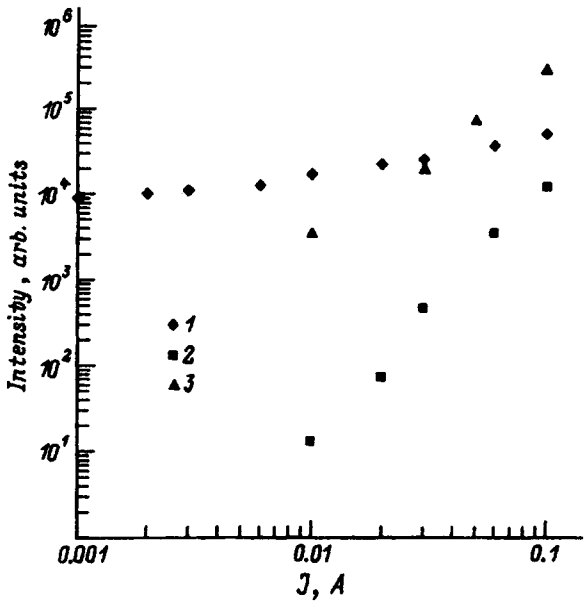

FIG. 2. Electroluminescence band intensities versus direct current: yellow-green band at 300 K (*1*); excitonic band at 300 K (*2*) and 650 K (*3*).

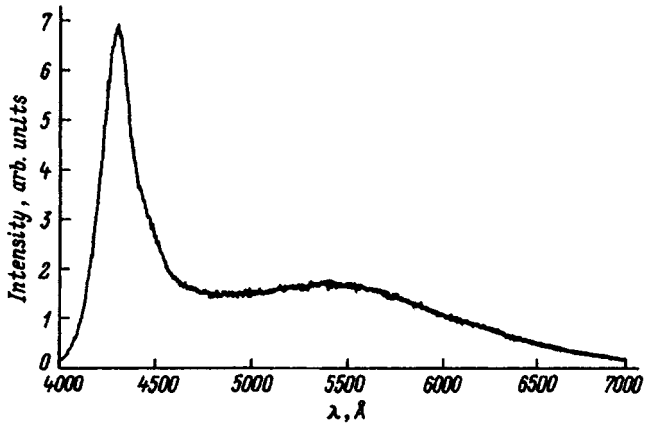

FIG. 3. Electroluminescence spectrum of $p-n$ structures at $T=450$ K. $J=500$ mA.

raised, the position of the maximum of the excitonic EL shifted into the long-wavelength region (Fig. 4).

5. DISCUSSION

There are several papers devoted to determining the band gap in 6*H*-SiC and its temperature dependence. The results of the three best-known studies are presented in Fig. 4 (Refs. 12–14). The figure also shows experimental data, which were obtained by us, on the temperature dependence of the maximum of the excitonic EL. As one can see from the figure, even at room temperature the experimental data lie above the curve obtained in Ref. 12, and at 650 K they

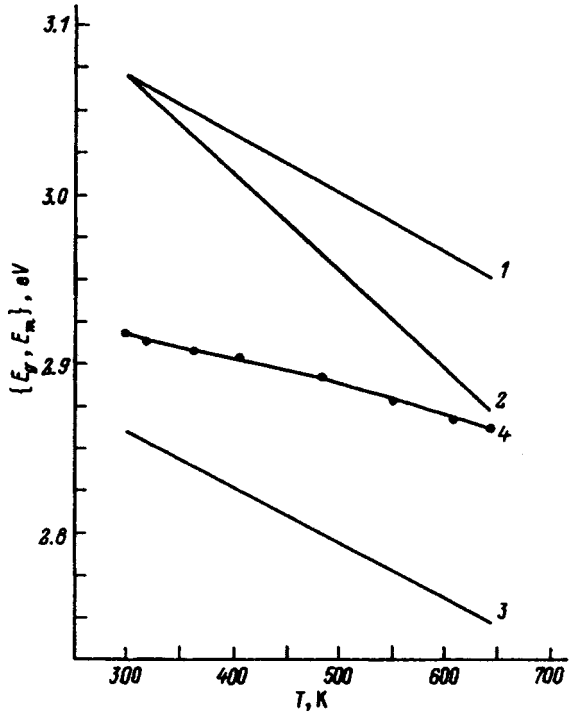

FIG. 4. Temperature dependence of the band gap E_g in 6*H*-SiC according to data from different studies: *1*—Ref. 13, *2*—Ref. 14, *3*—Ref. 12. *4*—experimental temperature dependence of the position of the excitonic electroluminescence maximum E_m.

agree with the band gap obtained in Ref. 14. In our opinion, the experimental data obtained in the present work agree only with the results of Ref. 13, since the energy of the excitonic radiation cannot exceed the band gap at any temperature. As one can see from Fig. 4, the energy of the maximum of the excitonic EL decreases more slowly with increasing temperature than the band gap E_g; i.e., there exists a temperature dependence $E_g - h\nu_{\max} \simeq -kT$ which is characteristic of radiation due to free-exciton annihilation.[2]

6. CONCLUSIONS

We can draw the following conclusions from our study:

1. The position of the maximum of the edge electroluminescence of 6*H*-SiC $p-n$ structures and its temperature dependence, which were obtained in the present work, agree only with the results of measurements, presented in Ref. 13, of the temperature dependence of E_g in 6*H*-SiC.

2. The quadratic dependence of the intensity of the edge EL of $p-n$ structures, just as the temperature dependence $E_g - h\nu_{\max} \simeq -kT$, indicate that the EL is most likely due to free-exciton recombination in 6*H*-SiC.

This work was sponsored by the University of Arizona (USA).

[1] É. E. Violin and G. F. Kholuyanov, Fiz. Tverd. Tela (Leningrad) **6**, 593 (1964) [Sov. Phys. Solid State **6**, 465 (1964)].
[2] M. Ikeda, T. Haykava, H. Matsunami, and T. Tanaka, J. Appl. Phys. **50**, 8215 (1979).
[3] W. v. Münch and W. Kürzinger, Solid-State Electron. **21**, 1129 (1978).
[4] V. A. Dmitriev, P. A. Ivanov, Ya. V. Morozenko, I. V. Popov, and V. E. Chelnokov, Pis'ma Zh. Tekh. Fiz. **11**, 246 (1985) [Sov. Tech. Phys. Lett. **11**, 101 (1985)].
[5] M. M. Anikin, A. M. Strel'chuk, A. L. Syrkin, V. E. Chelnokov, and A. E. Cherenkov, Fiz. Tekh. Poluprovodn. **28**, 284 (1994) [Semiconductors **28**, 171 (1994)].
[6] A. M. Danishevskiĭ and A. Yu. Rogachev, Fiz. Tekh. Poluprovodn. **30**, 17 (1996) [Semiconductors **30**, 9 (1996)].
[7] M. M. Anikin, A. A. Lebedev, S. N. Pyatko, A. M. Strel'chuk, and A. L. Syrkin, Mater. Sci. Eng. B **11**, 113 (1992).
[8] M. M. Anikin, P. A. Ivanov, A. A. Lebedev, S. N. Pyatko, and A. M. Strel'chuk in *Semiconductor Interfaces and Microstructures*, Edited by Z. C. Feng, World Scientific, Singapore, p. 280.
[9] A. A. Lebedev and V. E. Chelnokov, Diamond Relat. Mater. **3**, 1393 (1994).
[10] A. A. Lebedev, Fiz. Tekh. Poluprovodn. **30**, 999 (1996) [Semiconductors **30**, 531 (1996)].
[11] A. M. Strel'chuk, Fiz. Tekh. Poluprovodn. **29**, 1190 (1995) [Semiconductors **29**, 614 (1995)].
[12] H. R. Philipp and E. A. Taft in *Silicon Carbide–A High-Temperature Semiconductor*, Edited by J. R. O'Connor and J. Smiltens, Pergamon Press, N. Y., 1960, p. 306.
[13] W. J. Choyke, Mater. Res. Bull. **4**, S141 (1968).
[14] A. N. Pikhtin and D. A. Yas'kov, Fiz. Tverd. Tela (Leningrad) **12**, 1597 (1970) [Sov. Phys. Solid State **12**, 1267 (1970)].

Translated by M. E. Alferieff

Passivation of GaAs in alcohol solutions of ammonium sulfide

V. N. Bessolov, E. V. Konenkova, and M. V. Lebedev

A. F. Ioffe Physicotechnical Institute, Russian Academy of Sciences, 194021 St. Petersburg, Russia

D. R. T. Zahn

Institute für Physik, TU Chemnitz D-09107 Chemnitz, Germany
(Submitted April 28, 1997; accepted for publication April 29, 1997)
Fiz. Tekh. Poluprovodn. **31**, 1350–1356 (November 1997)

The chemical composition and position of the surface Fermi level in n- and p-type GaAs (100) under conditions of passivation in alcohol solutions of ammonium sulfide were studied by x-ray photoelectron and Raman spectroscopies. It is shown that sulfidizing GaAs decreases the amount of oxides on the surface, forms a sulfide coating on the surface, and decreases the surface barrier; in n-GaAs the surface Fermi level shifts in the direction of the conduction band and in p-GaAs it shifts in the direction of the valence band. It was established that as the permittivity of the sulfide solution decreases, the rate constant of the reaction, which leads to the formation of sulfides on the surface, and the magnitude of the shift of the surface Fermi level increase. The shift equals 0.53 eV in n-GaAs and 0.27 eV in p-GaAs in the case of passivation in a solution of ammonium sulfide in tret-butanol. A model explaining these experimental results on the basis of the reactivity of the sulfide ion in solution is proposed.
© *1997 American Institute of Physics.* [S1063-7826(97)01711-0]

1. INTRODUCTION

One of the main problems holding back the development of semiconductor electronics based on GaAs and other III–V compounds is the presence of a natural oxide layer, which results in a high density of surface states and pinning of the Fermi level near the center of the band gap. In this connection, there has appeared in recent years an avenue of research on surface passivation whose goal is to decrease the density of surface states in the band gap and, ideally, to remove such states completely.

Intensive development of sulfide passivation started with the work of Sandroff *et al.*,[1] where it was shown that treatment of GaAs/AlGaAs bipolar transistors in a water solution of sodium sulfide improves the transistor characteristics and, moreover, sulfide passivation initiated investigations of the interaction of sulfur with GaAs and other III–V semiconductor surfaces in solutions and in the gas phase. Sulfur passivation results in the removal of the natural oxide layer from the surface and formation of a thin sulfide coating on the surface. These chemical processes appreciably decrease the surface nonradiative recombination rate, which is manifested as a strong increase in the edge photoluminescence of sulfidized GaAs.

Investigations of the electronic properties of GaAs surfaces showed that the surface Fermi level (E_{Fs}) can shift in the direction of the conduction band[2–5] and in the direction of the valence band[6] in the case of sulfidization in water solutions[2,3,6] or from the gas phase.[4,5] Later investigations of GaAs surfaces sulfidized in water solutions showed that sulfidization changes very little the position of the Fermi level at the surface.[7,8]

Passivation of a GaAs surface in alcohol sulfide solutions is a highly promising technology for modifying surface properties. It has been shown that the intensity of the edge photoluminescence of both n- and p-GaAs can be greatly increased by using as solvents alcohols whose permittivity is lower than that of water (for example, isopropanol, tret-butanol, and so on).[9–12]

We will investigate the atomic structure (chemical composition) and electronic properties of a GaAs (100) surface (position of the surface Fermi level) sulfidized in different alcohol solutions of ammonium sulfide.

2. EXPERIMENTAL PROCEDURE

The chemical composition of the GaAs surface was studied by x-ray photoelectron spectroscopy (XRPS). The photoelectron spectra were measured with a Perkin–Elmer PHI 5400 spectrometer, using 300-W Mg $K\alpha$ x-rays ($h\nu = 1253.6$ eV). The structures were placed in a vacuum chamber no later than 10 min after sulfidization was completed. The spectra were decomposed using a standard Perkin–Elmer computer program.

To determine the position of the surface Fermi level, the surface barrier of the semiconductor was studied by Raman spectroscopy. The Raman spectra were recorded at room temperature in the range from 200 to 400 cm^{-1} with a Dilor XY spectrometer equipped with a CCD camera for multichannel detection and an optical microscope, which made it possible to focus a laser beam into a 1 μm in diameter spot.[1,3] Excitation was performed with the $\lambda = 457.9$-nm line of a Ar^+ laser (the penetration depth of the radiation in GaAs was equal to 50.3 nm (Ref. 14)); the laser power was equal to 2.5 mW. In accordance with the selection rules,[15] only optical LO phonons should be observed in the spectra. The spectra were recorded in air.

The objects of investigation were GaAs:Te (100) wafers with electron density $n = 1 \times 10^{18}$ cm^{-3} and GaAs:Zn wafers with hole density $p = 2 \times 10^{18}$ cm^{-3}.

Before sulfidization, the plates were treated in HCl at room temperature for 100 s. Sulfidization was performed for 15 min at room temperature. Ammonium sulfide solutions $[(NH_4)_2S\ (20\%)]$ in different alcohols with permittivity ε were used:[16] methanol (CH_3OH), $\varepsilon=33.0$; ethanol (C_2H_5OH), $\varepsilon=25.3$; isopropanol (i-C_3H_7OH), $\varepsilon=20.18$; and, tret-butanol (t-C_4H_9OH), $\varepsilon=12.47$. The volume content of ammonium sulfide $[(NH_4)_2S\ (20\%)]$ in the alcohol solutions was equal to 10%. For this reason, the effective permittivity ε^* of the solution was determined as $\varepsilon^*=0.1\varepsilon_{aqe}+0.9\varepsilon_{alc}$. For comparison, sulfidization was also performed in pure $[(NH_4)_2S\ (20\%)]$, which is a solution of ammonium sulfide in water (H_2O, $\varepsilon=80.1$). To remove the sulfide solution, the sample was placed into a centrifuge and rotated in air at a speed of 1000 rpm.

3. RESULTS

3.1. Chemical composition of a sulfidized surface

The chemical composition of a surface sulfidized in pure ammonium sulfide (i.e., in a water solution) and in alcohol solutions of ammonium sulfide (in isopropanol and tret-butanol) was investigated by XRPS.

The panoramic x-ray photoelectron spectra of all surfaces contain Ga, As, C, and O peaks, and the spectra of sulfidized surfaces also contain a S peak. Sulfidization greatly diminishes the intensity of the C and O peaks. Nonsulfidized surfaces and surfaces sulfidized in a water solution were enriched with gallium, while surfaces sulfidized in alcohol solutions were virtually stoichiometric.

It is evident from the decomposition of the As3d peaks of the investigated surfaces that a peak due to elemental arsenic As^0 (binding energy about 41.55 eV) and a peak due to arsenic oxides (electron binding energy 43.6 eV) are present together with a component due to As–Ga bonds (electron binding energy 40.8 eV) in the spectrum of the nonsulfidized surface (Fig. 1a). An additional peak with electron binding energy $\sim$42.6 eV appears in the spectra after sulfidization. This peak is apparently due to the formation of arsenic sulfides (Fig. 1b–d).

Sulfidization in all solutions greatly diminishes the amount of arsenic oxides and elemental arsenic. The intensity of the peak due to sulfides is different for different solvents: The highest intensity is obtained with sulfidization in a tret-butanol solution. The thickness of the sulfide coating on different surfaces ranges from 0.47 monolayers (ML) (in the case of sulfidization in ammonium sulfide) up to 0.7 ML (sulfidization in a solution based on tret-butanol).

The sulfidization reaction rate constant, i.e., the thickness of the sulfide coating formed per unit time, divided by the sulfur concentration in the solution, increases with decreasing permittivity of the solution.

3.2. Electronic properties of a sulfidized surface

The penetration depth D of $\lambda=457.9$ nm laser radiation in a semiconductor is much greater than the depth δ of the depleted region in both n-GaAS ($\delta_n=33.6$ nm) and p-GaAs ($\delta_p=19.0$ nm). For this reason, two peaks are clearly seen in the Raman spectra (Figs. 2 and 3). The L^- (268.6 cm^{-1}) peak is due to scattering of free carriers by a paired phonon-plasmon mode in the volume of the semiconductor. The LO (291.3 cm^{-1}) peak is associated with the depleted layer on the semiconductor surface. In nonsulfidized n-GaAs the LO peak is two times more intense than the L^- peak (Fig. 2a), while in nonsulfidized p-GaAs the L^- and LO peaks have virtually the same intensity (Fig. 3a).

Sulfidization of semiconductors in different solutions changes the ratio of the volume L^- and surface LO peaks in both n-GaAs (Fig. 4a) and p-GaAs (Fig. 4b), attesting to the change in the surface barrier. This effect is small in the case of sulfidization in a water solution. The ratio of the LO and L^- peak intensities decreases with the permittivity of the

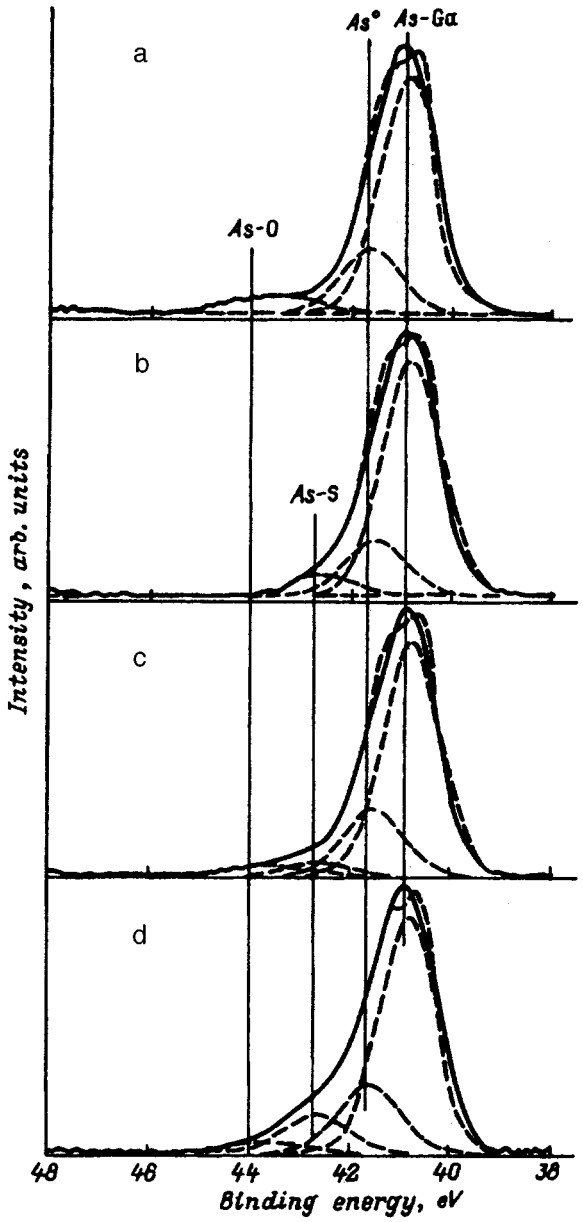

FIG. 1. As3d photoelectron spectra of four different GaAs (100) surfaces pre-etched in HCl and washed in deionized water: a—Nonsulfidized surface; b—sulfidized in a water solution of ammonium sulfide $[(NH_4)_2S\ (20\%)]$; c—sulfidized in a $[(NH_4)_2S\ (20\%)]$ solution in isopropanol (C_3H_7OH); d—sulfidized in a $[(NH_4)_2S\ (20\%)]$ solution in tret-butanol (t-C_4H_9OH).

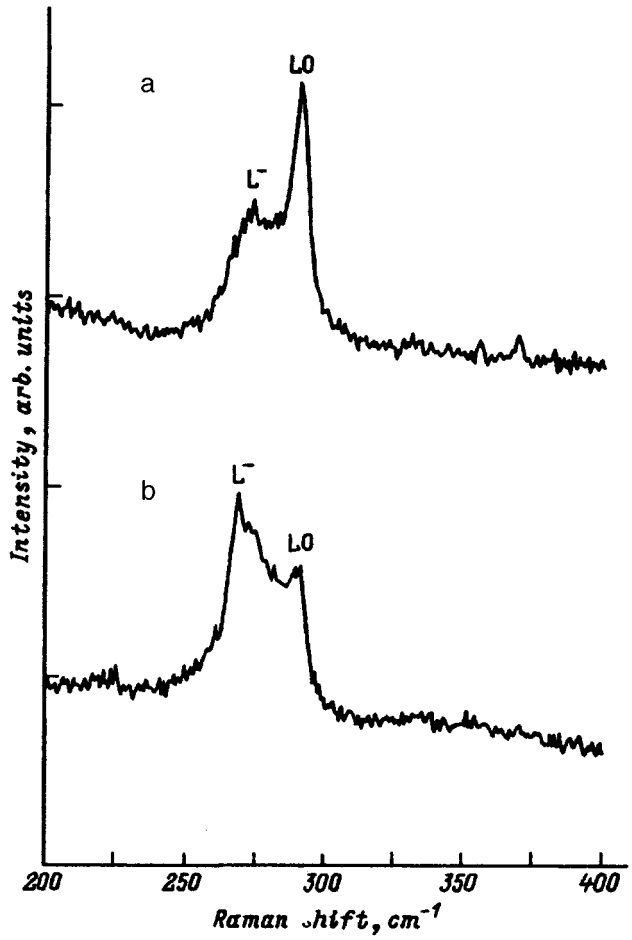

FIG. 2. Raman spectra of n-GaAs with $N_D=1\times10^{18}$ cm^{-3} nonsulfidized (a) and sulfidized in a [$(NH_4)_2S$ (20%)] solution in tret-butanol (b).

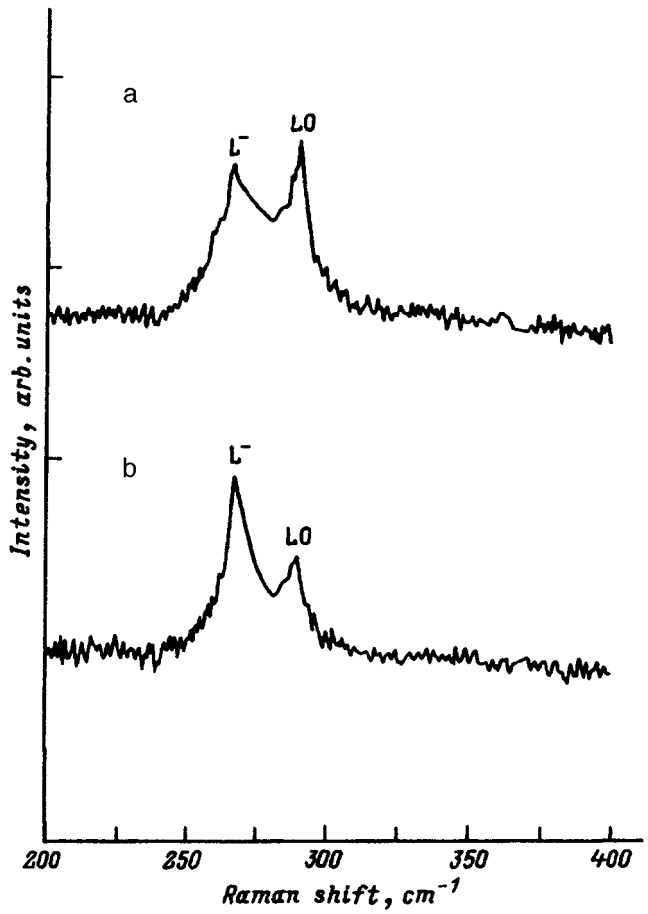

FIG. 3. Raman spectra of p-GaAs with $N_A=2\times10^{18}$ cm^{-3} nonsulfidized (a) and sulfidized in a [$(NH_4)_2S$ (20%)] solution in tret-butanol (b).

solvent. In the case of sulfidization in a solution based on tret-butanol (which has the lowest permittivity ε of all solutions employed in this work), the LO peak becomes much smaller than the L^- peak in both n-GaAs (Fig. 2b) and p-GaAs (Fig. 3b).

The depth δ of the depleted region in the sulfidized samples was calculated from the intensity ratio $I(LO)/I(L^-)$ of the peaks in accordance with Ref. 17

$$\frac{I(LO)}{I(L^-)}=\frac{I_0(LO)}{I_0(L^-)}\cdot\frac{(1-e^{-2\delta/D})}{e^{-2\delta/D}}, \tag{1}$$

where D is the penetration depth of the laser radiation in GaAs, $I_0(LO)$ is the intensity of the LO-phonon peak in the nondoped semiconductor, and $I_0(L^-)$ is the intensity of the L^- peak in the absence of a depleted region. The ratio $I_0(LO)/I_0(L^-)$ was determined from the Raman spectrum of nonsulfidized semiconductors similarly to Ref. 2.

The surface barrier height V_s was calculated from the formula

$$V_s=eN_{D(A)}\delta^2/2\varepsilon_0\varepsilon_s, \tag{2}$$

where e is the electron charge, $N_{D(A)}$ is the donor (acceptor) density in GaAs, ε_0 is the permittivity of free space, and $\varepsilon_s=13.1$ is the static permittivity of GaAs.

Calculations were performed for carrier densities in the semiconductor $N_D=1\times10^{18}$ cm^{-3} and $N_A=2\times10^{18}$ cm^{-3} and the barrier height in nonsulfidized GaAs was assumed to be $V_0=0.78$ eV (Ref. 18) for n-GaAs and $V_0=0.5$ eV (Ref. 19) for p-GaAs. Passivation decreases the surface barrier height V_s and depth δ of the depleted region in both n-GaAs and p-GaAs (see Table I): The lowest values were obtained for surfaces sulfidized in a tret-butanol solution: $V_s=0.25$ eV and $\delta=19.9$ nm in n-GaAs and $V_s=0.23$ eV and $\delta=13.3$ nm in p-GaAs.

Sulfidization of GaAs in alcohol solutions shifts the surface Fermi level relative to its initial position (Fig. 5). In n-GaAs the Fermi level shifts in the direction of the conduction band and in p-GaAs it shifts in the direction of the valence band of the semiconductor. The magnitude of this shift increases in n-GaAs and p-GaAs with decreasing permittivity of the passivating solution.

4. MODELS

The experimentally observed dependence of the position of the surface Fermi level E_{Fs} on the permittivity of the solution can be explained as follows. As is well known,[19] both donor and acceptor states are present in the band gap on the oxidized GaAs surface, and in n-GaAs the Fermi level is pinned on an acceptor state and in p-GaAs it is pinned on a

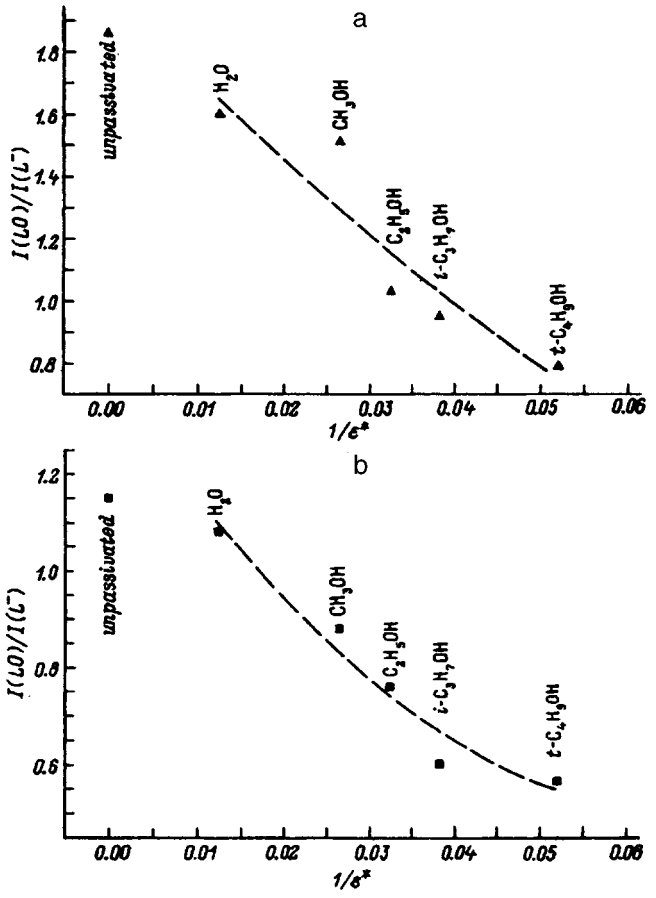

FIG. 4. Ratio of the LO and L^- peak intensities for n-GaAs ($N_D=1\times10^{18}$ cm^{-3}) (a) and p-GaAs ($N_A=2\times10^{18}$ cm^{-3}) (b) sulfidized in different solutions versus the effective permittivity of the solution employed.

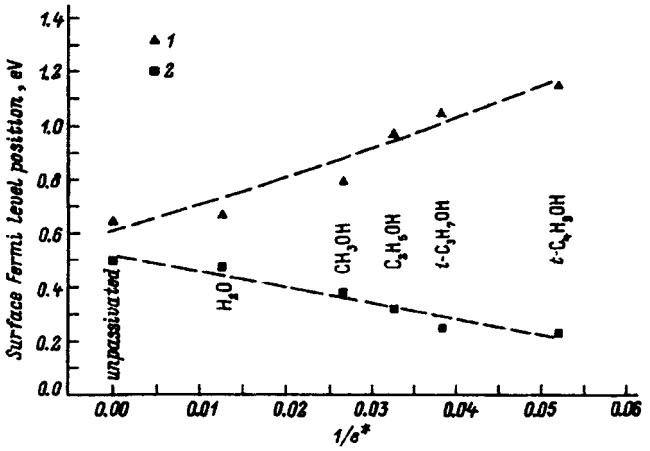

FIG. 5. Position of the surface Fermi level relative to the edges of the conduction bands for n-GaAs and p-GaAs passivated in ammonium sulfide solutions in different solvents versus the effective permittivity of the solution employed.

donor state. Correspondingly, when a covalent bond is formed between an adatom and the surface, in the case of n-GaAs the surface will strive to accept electrons and in the case of p-GaAs it will strive to give up electrons.

If the surface states are represented as molecular orbitals (similar to the molecular orbitals of the sulfide ion), then in the case of sulfidization of n-GaAs in solution (Fig. 6a) an interaction will occur between the lowest (in energy) unoccupied orbital (LUMO) of the GaAs surface and the highest occupied molecular orbital (HOMO) of the sulfide ion. As a result of this interaction, there arises a GaAs–S complex, whose HOMO energy is less than that of the nonsulfidized semiconductor by an amount ΔE, which in turn is determined, according to Ref. 20, as

$$\Delta E=-\frac{Q_sQ_i}{\varepsilon R}+\frac{\mu Q_i}{\varepsilon RR^*}+\frac{2(c_sc_i\beta)^2}{E_{\mathrm{HOMO}(i)}-E_{\mathrm{LUMO}(s)}},$$

where Q_s and Q_i are the charges of the surface atom of the semiconductor and sulfide ion, respectively; ε is the permittivity of the medium, R is the distance between the reacting atoms, μ is the dipole moment of the semiconductor surface, R^* is the effective length of the dipole, c_s and c_i are orbital coefficients, β is the interaction integral, and E_{HOMO} and E_{LUMO} are the HOMO and LUMO energies (the subscripts i and s refer to the ion and surface).

The first and second terms on the right-hand side of Eq. (3) are due to the Coulomb interaction between the sulfide ions in solution and the surface atoms of the semiconductor and (or) the dipole layer on its surface. The third term de-

TABLE I. Depth δ of the depleted region and height V_s of the surface barrier of GaAs sulfidized under different conditions.

	n-GaAs		p-GaAs	
Solution	δ, nm	V_s, eV	δ, nm	V_s, eV
$(NH_4)_2S+H_2O$	33.1	0.76	18.6	0.48
$(NH_4)_2S+CH_3OH$	30.2	0.63	16.6	0.38
$(NH_4)_2S+C_2H_5OH$	25.8	0.46	15.3	0.32
$(NH_4)_2S+i-C_3H_7OH$	23.5	0.38	13.4	0.25
$(NH_4)_2S+t-C_4H_9OH$	19.9	0.25	13.3	0.23

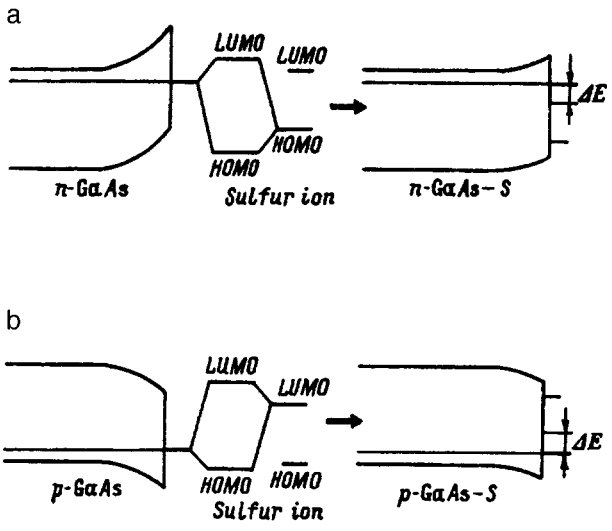

FIG. 6. Schematic diagram of the interaction between the molecular orbitals of the sulfide ion and the surface states of n-GaAs (a) and p-GaAs (b).

scribes the energy gain due to the formation of a covalent bond between the sulfur atoms (ions) and the surface atoms of the semiconductor.

A decrease in the HOMO energy of the semiconductor surface correspondingly results in a decrease of the band bending at the surface and therefore a shift of the Fermi level in the direction of the conduction band. It is evident from Eq. (3) that the shift of the HOMO energy of the n-GaAs surface and therefore the surface Fermi level as a result of adsorption of a sulfide ion should be proportional to $1/\varepsilon$ of the solution, as is in fact observed experimentally (Fig. 5).

Conversely, sulfidization of p-GaAs (Fig. 6b) will result in an interaction between the HOMO of the semiconductor surface and the LUMO of the sulfide ion. Such an interaction likewise lowers the energy of the HOMO of the semiconductor surface by an amount ΔE and, correspondingly, decreases the band bending at the surface and results in a shift of the Fermi level but this time in the direction of the valence band. Just as in the case of n-GaAs, when p-GaAs is sulfidized, the shift of the surface Fermi level should be proportional to $1/\varepsilon$ of the solution, as is also observed experimentally (Fig. 5).

The following assumption can be made from Eq. (3): The maximum shift of the Fermi level (minimum surface recombination rate) should be obtained when sulfur atoms (and/or ions) with the highest reactivity are used for passivation. To obtain the maximum energy gain ΔE, not only can the permittivity of the solution be decreased but the third term in Eq. (3) can be increased by using in the passivation process other sulfides characterized by a higher heat of formation of S–GaAs bonds (and therefore a higher rate of the reaction leading to the formation of sulfides on the semiconductor surface).

5. DISCUSSION

In the case of sulfidization in solutions, the position of the Fermi level on the GaAs surface depends on the permittivity of the solution: As ε decreases, the shift of the surface Fermi level with respect to its initial position in a nonsulfidized semiconductor increases. On the other hand, as ε decreases, the rate of the reaction leading to the formation of a sulfide coating, i.e., the reactivity of the sulfide ion with respect to the GaAs surface, increases. Therefore, the maximum shift of the surface Fermi level in both n-GaAs and p-GaAs is obtained by using sulfide ions with the highest reactivity, i.e., with the maximum ΔE of the reaction leading to the formation of S–GaAs covalent bonds.

Sulfidization of the surface of n-GaAs and p-GaAs in alcohol solutions lowers the surface barriers by a larger amount than sulfidization in water solutions and therefore gives more effective surface passivation. These results are in good agreement with the increase in the photoluminescence intensity of GaAs passivated in alcohol solutions of sodium sulfide[9,10] and ammonium sulfide.[11] The absence of an appreciable passivation effect in the case of sulfidization of a GaAs surface in a water solution agrees with the results of synchrotron photoemission investigations of such surfaces.[7,8]

The decrease in the HOMO energy and increase in the LUMO energy in the process of sulfidization, as follows from the model proposed above, is in agreement with the results of molecular-orbital calculations of the electronic properties of a GaAs (100) surface covered with sulfur adatoms.[21] This also means that sulfide passivation increases the surface band gap, in agreement with pseudopotential calculations of the properties of such a surface.[22,23] We note that in order to understand the effect of a solvent on the position of the surface Fermi level, the change in the reactivity of the sulfide ion in different solutions must be taken into account.

The following experimental results support the model assumption that the effectiveness of sulfide passivation of a GaAs surface is linked with the reactivity of the passivating sulfur atom (ion). First, the intensity of the edge photoluminescence of sulfidized GaAs increases as the logarithm of the rate constant of the reaction leading to the formation of sulfides on the surface[14] (the reactivity of the sulfur atom or ion with respect to the GaAs surface). Second, the sulfidized GaAs surface is annealed,[5,7,8] which results in a restructuring of the As–S bonds into thermodynamically more stable Ga–S bonds and is accompanied by a shift of the Fermi level by an amount approximately equal to the energy gain due to this restructuring.

We note that the dependence of the position of the surface Fermi level on the permittivity of the solution is much stronger for n-GaAs than p-GaAs. This is apparently due to the difference in the dipole moments for n- and p-GaAs.

6. CONCLUSIONS

The chemical composition and position of the surface Fermi level in n- and p-GaAs (100) in the case of passivation in alcohol solutions of ammonium sulfide were studied by x-ray photoelectron and Raman spectroscopies. It was shown that sulfidization decreases the amount of oxides on the surface and results in the formation on the surface of a sulfide coating which consists mainly of arsenic sulfides. The rate constant of the reaction leading to the formation of sulfides on the surface increases with decreasing permittivity of the sulfide solution employed. It was determined that sulfidization of a GaAs surface lowers the surface barrier. In n-GaAs the surface Fermi level shifts in the direction of the conduction band and in p-GaAs it shifts in the direction of the valence band. The magnitude of this shift in both n- and p-GaAs increases with decreasing permittivity of the sulfide solution employed. In the case of sulfidization of ammonium sulfide solutions in tret-butanol, the Fermi level shifted by 0.53 eV in n-GaAs and 0.27 eV in p-GaAs. A model explaining these experimental results on the basis of the reactivity of the sulfide ion in solution was proposed.

This work was supported in part by the Russian Fund for Fundamental Research (Grant No. 95-03-09330) and the Volkswagen–Stiftung Foundation (Germany).

[1] C. J. Sandroff, R. N. Nottenburg, J.-C. Bischoff, and R. Bhat, Appl. Phys. Lett. **51**, 33 (1987).
[2] L. A. Farrow, C. J. Sandroff, and M. C. Tamargo, Appl. Phys. Lett. **51**, 1931 (1987).
[3] C. J. Sandroff, M. S. Hegde, L. A. Farrow, C. C. Chang, and J. P. Harbinson, Appl. Phys. Lett. **54**, 362 (1989).
[4] G. J. Hughes, L. Roberts, M. O. Henry, K. McGuigan, G. M. O'Connor,

F. G. Anderson, G. P. Morgan, and T. Glynn, Mater. Sci. Eng. B **9**, 37 (1991).
[5] P. Moriarty, B. Murphy, L. Roberts, A. A. Cafolla, L. Koenders, and P. Bailey, Phys. Rev. B **51**, 14 237 (1994).
[6] V. L. Berkovits, V. N. Bessolov, T. V. L'vova, E. B. Novikov, V. I. Safarov, R. V. Khasieva, and B. V. Tsarenkov, J. Appl. Phys. **70**, 3707 (1991).
[7] H. Sugahara, M. Oshima, H. Oigawa, H. Shigekawa, and Y. Nannichi, J. Appl. Phys. **69**, 4349 (1991).
[8] H. Sugahara, M. Oshima, R. Klauser, H. Oigawa, and Y. Nannichi, Surf. Sci. **242**, 335 (1991).
[9] V. N. Bessolov, A. F. Ivankov, E. K. Konenkova, and M. V. Levedev, Pis'ma Z. Tekh. Fiz. **21**, No. 46 (1995) [Tech. Phys. Lett. **21**, 20 (1995)].
[10] V. N. Bessolov, E. V. Konenkova, and M. V. Lebedev, J. Vac. Sci. Technol. B **14**, 2761 (1996).
[11] V. N. Bessolov, E. V. Konenkova, and M. V. Lebedev, Fiz. Tverd. Tela (St. Petersburg) **39**, 63 (1997) [Phys. Solid State **39**, 54 (1997)].
[12] V. N. Bessolov, E. V. Konenkova, and M. V. Lebedev, Pis'ma Zh. Tekh. Fiz. **22**(18), 37 (1996) [Tech. Phys. Lett. **22**, 749 (1996)].
[13] G. Bauer and W. Richter, *Optical Characterization of Epitaxial Semiconductor Layers*, Springer, Berlin, 1996.
[14] D. E. Aspnes and A. A. Studna, Phys. Rev. B **27**, 985 (1983).
[15] W. Haes and R. London, *Scattering of Light by Crystals*, Wiley, N. Y., 1978.
[16] D. R. Lide, *CRC Handbook of Chemistry and Physics*, CRC Press, Boca Raton, Florida, 1995.
[17] J. Geurts, Surf. Sci. Rep. **18**, 1 (1993).
[18] G. P. Schwartz and G. J. Gualtieri, J. Electrochem. Soc. **133**, 1266 (1986).
[19] N. Newman, W. E. Spicer, T. Kendelewicz, and I. Lindau, J. Vac. Sci. Technol. B **4**, 931 (1986).
[20] G. Klopman, J. Am. Chem. Soc. **90**, 223 (1968).
[21] J. Guo-Ping and H. E. Ruda, J. Appl. Phys. **79**, 3758 (1996).
[22] T. Ohno and K. Shiraishi, Phys. Rev. B **42**, 11 194 (1990).
[23] K. N. Ow and X. W. Wang, Phys. Rev. B **54**, 17 661 (1996).

Translated by M. E. Alferieff

Heating of a two-dimensional electron gas by the electric field of a surface acoustic wave

I. L. Drichko, A. M. D'yakonov, V. D. Kagan, A. M. Kreshchuk, T. A. Polyanskaya, I. G. Savel'ev, I. Yu. Smirnov, and A. V. Suslov

A. F. Ioffe Physicotechnical Institute, Russian Academy of Sciences, 194021 St. Petersburg, Russia
(Submitted May 16, 1997; accepted for publication June 20, 1997)
Fiz. Tekh. Poluprovodn. **31**, 1357–1366 (November 1997)

The heating of a two-dimensional electron gas by an rf electric field generated by a surface acoustic wave, which can be described by an electron temperature T_e, has been investigated. It is shown that the energy balance of the electron gas is determined by electron scattering by the piezoelectric potential of the acoustic phonons with T_e determined from measurements at frequencies $f=30$ and 150 MHz. The experimental curves of the energy loss Q versus T_e at different SAW frequencies depend on the value of $\omega\overline{\tau_e}$ compared to 1, where $\overline{\tau_e}$ is the relaxation time of the average electron energy. Theoretical calculations of the heating of a two-dimensional electron gas by the electric field of the surface acoustic wave are presented for the case of thermal electrons ($\Delta T \ll T$). The calculations show that for the same energy losses Q the degree of heating of the two-dimensional electrons (i.e., the ratio T_e/T) for $\omega\overline{\tau_e}>1$ ($f=150$ MHz) is less than for $\omega\overline{\tau_e}<1$ ($f=30$ MHz). Experimental results confirming this calculation are presented. © *1997 American Institute of Physics.*
[S1063-7826(97)02011-5]

1. INTRODUCTION

The investigation of nonlinear (with respect to the input power) effects in the absorption of piezoelectrically active ultrasonic waves, arising due to the interaction of the waves with three-dimensional electron gas (in the case of Boltzmann statistics), has shown that the mechanisms of the nonlinearity depend on the state of the electrons. If electrons are free (delocalized), then the nonlinearity mechanism for moderately high sound intensities is usually due to the heating of the electrons in the electric field of an ultrasonic wave. The character of the heating depends on the quantity $\omega\tau_\varepsilon$, where ω is the sound frequency, and τ_ε is the energy relaxation time.[1,2] If the electrons are localized, then the nonlinearity mechanism is due to the character of the localization (on an individual impurity or in the wells of a fluctuation potential). In Ref. 3, it was shown that in the case where the electrons are localized on individual impurities, the nonlinearity was determined by impurity breakdown in the electric field of the sound wave. When the electrons occupied the conduction band as a result of this effect, their temperature started to grow as a result of heating in the electric field of the wave.[4]

The study of structures with a two-dimensional electron gas (2DEG) opens up a unique possibility of studying in one series of measurements performed on the same sample the mechanisms of nonlinearity in delocalized and localized electron states, since under quantum Hall effect conditions both states are realized by varying the magnetic field. The change in the absorption coefficient for a piezoelectrically active surface acoustic wave (SAW) interactimg with a 2DEG as a function of the SAW intensity in GaAs/AlGaAs structures was previously observed in Refs. 5 and 6 only in the magnetic field range corresponding to small integer filling numbers—the quantum Hall effect regime, when the two-dimensional electrons are localized. The authors explained the data which they obtained by heating of a 2DEG.

In the present paper we report some of our investigations concerning nonlinear effects accompanying the interaction of delocalized two-dimensional electrons with the electric field of a SAW for the purpose of investigating nonlinearity mechanisms.

2. EXPERIMENTAL PROCEDURE

We investigated the absorption coefficient for a 30–210 MHz SAW in a two-dimensional electron gas in $GaAs/Al_{0.75}Ga_{0.25}As$ heterostructures as a function of the temperature in the range $T\simeq 1.4-4.2$ K in the linear regime (the input power did not exceed 10^{-7} W) and the SAW power at $T=1.5$ K in magnetic fields up to 30 kOe. Samples studied previously in Ref. 7 with Hall density $n_s^H=6.7\times10^{11}$ cm^{-2} and mobility $\mu_H=1.28\times10^5$ cm^2/(V·s) at $T=4.2$ K were used for the investigations. The technology used to fabricate the heterostructures is described in Ref. 8 and the procedure for performing the sound absorption experiment is described in Ref. 7. Here we only note that the experimental structure with 2DEG was located on the surface of the piezodielectric (lithium niobate $LiNbO_3$), along which the SAW propagates. The SAW was excited in a pulsed regime by sending radio pulses with filling frequency 30–210 MHz from an rf oscillator into the excited interdigital transducer. The pulse duration was of the

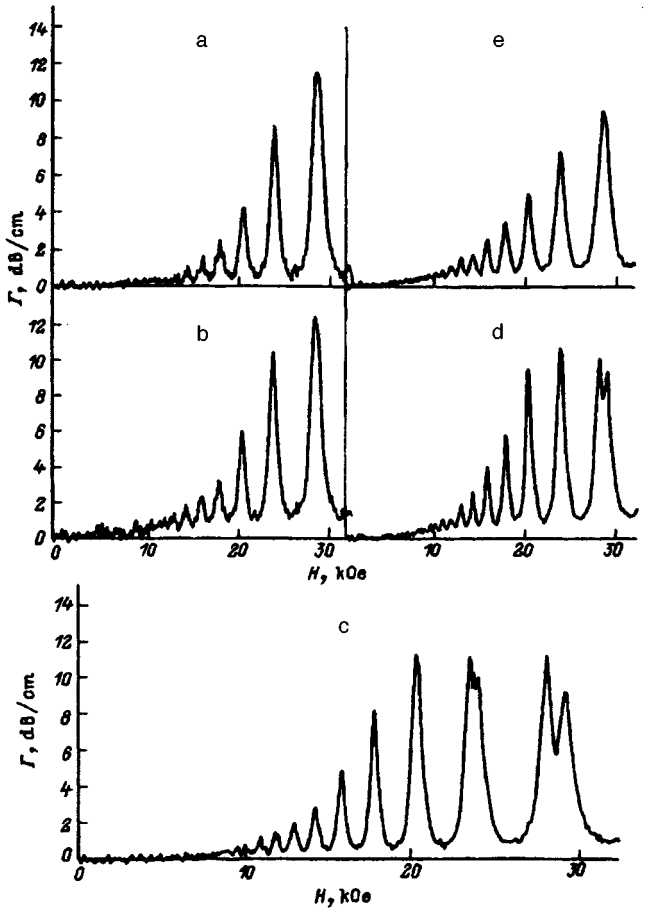

FIG. 1. Absorption coefficient Γ versus magnetic field H at frequency $f=30$ MHz at temperatures T, K: a—4.2, b—3.8, c–e—1.5 and wave power at the oscillator output P, W: a–c—10^{-5}, d—10^{-4}, e—10^{-3}.

order of 1 μs and the pulse repetition frequency was equal to 50 Hz. In the present paper the SAW power is the power in a pulse.

An ac electric field with the frequency of the SAW, which accompanies the deformation wave, penetrates into a channel containing two-dimensional electrons, giving rise to electrical currents and, correspondingly, Joule losses. As a result of this interaction, energy is absorbed from the wave. The SAW absorption in a magnetic field is measured in the experiment. Since the measured absorption is determined by the conductivity of the 2DEG, quantization of the electronic spectrum, which leads to Shubnikov-de Haas oscillations, gives rise to oscillations in the SAW potential as well.

3. EXPERIMENTAL RESULTS AND ANALYSIS

Curves of the absorption coefficient Γ versus the magnetic field H are presented in Fig. 1 for different temperatures and powers of the 30-MHz SAW. Similar curves were also obtained for other SAW frequencies. The character of the curves $\Gamma(H)$ is analyzed in Ref. 7. The absorption maxima Γ_{max} as a function of the magnetic field for $H<25$ kOe are equally spaced as a function of $1/H$, and the splitting of the maxima $\Gamma(H)$ for $H>25$ kOe into two peaks with the values of Γ_M at the maxima[1)] is due to the relaxational character of the absorption. The temperature and

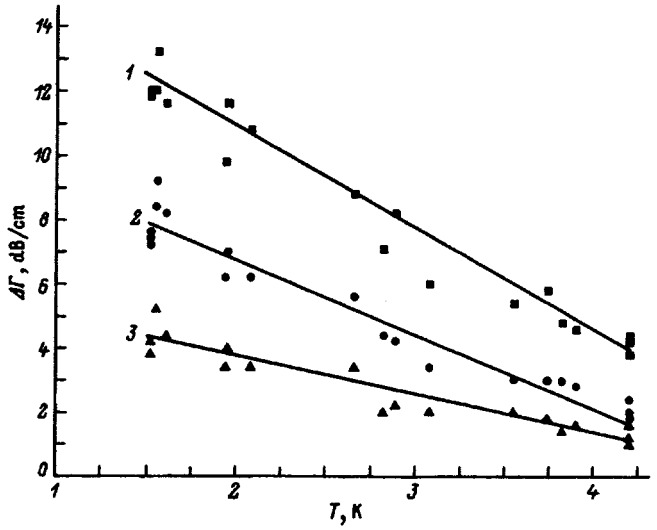

FIG. 2. $\Delta\Gamma=\Gamma_{max}-\Gamma_{min}$ versus temperature T in the linear regime at a frequency of 150 MHz in a magnetic field H, kOe: *1*—17.5, *2*—15.5, *3*—14.1.

SAW power dependences of Γ, shown in Figs. 2 and 3, were extracted from the experimental curves of the same type as in Fig. 1 for the corresponding frequencies in a magnetic field $H<25$ kOe for large filling numbers $\nu=n_s hc/2eH>7$.

Figure 2 shows the temperature dependence of the quantity $\Delta\Gamma=\Gamma_{max}-\Gamma_{min}$ measured in the linear regime at a frequency of 150 MHz in different magnetic fields. Here Γ_{max} and Γ_{min} are the values of Γ on the upper and lower lines, which envelop the oscillatory dependence $\Gamma(H)$ for $H<25$ kOe. Figure 3 shows $\Delta\Gamma$ versus P—the power of the SAW (frequency 150 MHz) at the oscillator output at $T=1.5$ K. We see from Figs. 2 and 3 that $\Delta\Gamma$ decreases with increasing temperature and with increasing SAW power.

In Ref. 7 it was shown that in the range of magnetic fields where the quantum Hall effect is still not observed (in

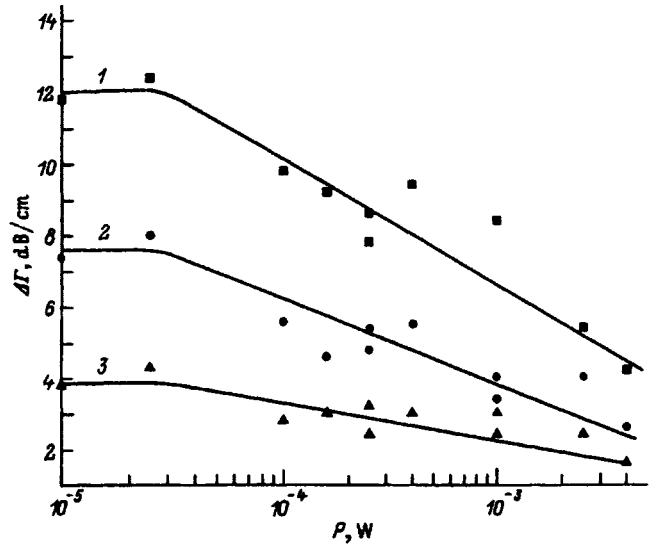

FIG. 3. $\Delta\Gamma=\Gamma_{max}-\Gamma_{min}$ versus the power P at the oscillator output in the linear regime at a frequency of 150 MHz in a magnetic field H, kOe: *1*—17.5, *2*—15.5, *3*—14.1.

our case $H<25$ kOe) the dissipative conductivities are

$$\sigma_{xx}^{ac}=\sigma_{xx}^{dc},$$

where σ_{xx}^{dc} is the conductivity calculated from the measured dc resistivities $\rho_{xx}(H)$ and $\rho_{xy}(H)$, and σ_{xx}^{ac} is the conductivity found from the absorption coefficient $\Gamma(H)$ measured in the linear regime. This result gave us the basis for assuming that in this range of magnetic fields the electrons are in a delocalized state. As we have already indicated in the introduction, we shall analyze here nonlinearity only in this case.

In a previous work[9] we showed that if the electrons are delocalized, then the characteristics of the 2DEG, such as the carrier density n_s, the transport relaxation time τ, and the quantum[2)] relaxation time, can be determined from the magnetic field dependences $\sigma_{xx}^{ac}(H)$. In addition, the mobility $\mu=e\tau/m$ and the concentration n_s at $H=0$ are close to the values obtained from dc measurements: the Hall density and mobility of the electrons, as well as n_s found from the Shubnikov–de Haas oscillations. For this reason, it was natural to assume that Γ depends on the SAW power, just as in the static case, because of the heating of the 2DEG but in the electric field of the SAW. The heating of the 2DEG in a static electric field in similar heterostructures was investigated in Refs. 11–15. In those papers it was shown that at liquid-helium temperatures the electron energy relaxation processes are determined in a wide range of 2DEG densities by the piezoacoustic electron-phonon interaction under small-angle scattering and weak screening conditions.

We shall employ, by analogy with Refs. 11–14, the concept of the temperature T_e of two-dimensional electrons and determine it by comparing the curves of the absorption coefficient Γ versus the SAW power with the curves of Γ versus the lattice temperature T. Such a comparison makes it possible to establish a correspondence between the temperature of the two-dimensional electrons and the output power of the oscillator. The values of T_e were extracted by two methods: 1) by comparing the curves of the amplitude of the oscillations $\Delta\Gamma=\Gamma_{\max}-\Gamma_{\min}$ versus the temperature T (Fig. 2) and versus the power P (Fig. 3) for the same value of the magnetic field H; 2) by comparing curves of the ratios $\Gamma_{\max}/\Gamma_M=f(T)$ and $\Gamma_{\max}/\Gamma_M=f(P)$ versus the lattice temperature T and the power P. Here the values of $\Gamma_{\max}(T)$ and $\Gamma_{\max}(P)$ were also taken for the same value of H, and Γ_M is the absorption at $H=28$ kOe (Fig. 1). The use of the ratios instead of the absolute values of Γ decreased the effect of the experimental variance in Γ on the error in determining T_e. As a result, the accuracy in determining T_e by these two methods was no worse than 10%.

To determine the absolute energy losses as a result of absorption of SAW in the case of interaction with electrons ($\overline{Q}$), the following calculations must be performed. The intensity E of the electric field, in which the two-dimensional electrons of the heterostructure are located during the propagation of a SAW in a piezoelectric material placed at a distance a from a high-conductivity channel, is

$$|E|^2=K^2\frac{32\pi}{v}(\varepsilon_1+\varepsilon_0)\,\frac{bq\exp(-2qa)}{1+\left(\frac{4\pi\sigma_{xx}}{v\varepsilon_s}\right)^2 c^2}W, \qquad (1)$$

where K^2 is the electromechanical coupling constant; $v=3.5\times10^5$ cm/s and q are, respectively, the velocity and wave number of sound in $LiNbO_3$; a is the width of the vacuum gap between the sample and the $LiNbO_3$ plate; ε_0, ε_1, and ε_s are the permittivities of free space, $LiNbO_3$, and the semiconductor with the 2DEG, respectively; and W is the input SAW power scaled to the width of the sound track. The functions b and c are

$$b=[\varepsilon_1^+\varepsilon_s^+-\varepsilon_1^-\varepsilon_s^-\exp(-2qa)]^{-2},$$

$$c=\frac{1}{2}\{1+b^{1/2}[\varepsilon_1^+\varepsilon_s^--\varepsilon_1^-\varepsilon_s^+\exp(-2qa)]\},$$

$$\varepsilon_1^+=\varepsilon_1+\varepsilon_0,\quad \varepsilon_s^+=\varepsilon_s+\varepsilon_0,$$

$$\varepsilon_1^-=\varepsilon_1-\varepsilon_0,\quad \varepsilon_s^-=\varepsilon_s-\varepsilon_0.$$

The magnitude of the electric losses is defined as $\overline{Q}=\sigma_{xx}E^2$. Multiplying both sides of Eq. (1) by σ_{xx}, we obtain $\overline{Q}=4W\Gamma$, where Γ is the absorption measured in the experiment. The power W at the entrance to the sample is not measured very accurately in acoustic measurements. The problem is that this quantity is determined by, first, the quality of the interdigital transducers; second, by the losses associated with the mismatch of the line that feeds electric power into the transmitting transducer as well as the line that removes electrical power from the detecting transducer, where the losses in the receiving and transmitting parts of the line may not be the same; and, third, by absorption of the SAW in the susbtrate, whose absolute magnitude is difficult to measure in our experiment. The effect of these losses decreases with frequency, so that in determining W at 30 MHz we assumed that both the conversion losses for the transmitting and receiving transducers as well as the losses in the transmitting and receiving lines are identical. The total losses were found to be $\Delta P=16$ dB, if SAW absorption in the heterostructure substrate is ignored. If it is assumed that nonlinear effects at 150 MHz start at the same value of $\overline{Q}$ as at 30 MHz, then the ''threshold'' value of $\overline{Q}$ at which the deviation of $\Gamma_{\max}(\overline{Q})/\Gamma_M$ at 30 MHz from a constant value becomes appreciable [we recall that $\Gamma(H)/\Gamma_M\sim1/\sigma_{xx}(H)$ in the region of delocalized electronic states, i.e., $H<25$ kOe[7]] can be used to determine the total losses at 150 MHz. An estimate of the total losses by this method at 150 MHz gives $\Delta P=18$ dB. Therefore, the power W at the entrance to the sample is determined by the output power P of the oscillator, taking into account the total losses ΔP.

With the results of Refs. 11–14 in mind, we constructed the curves

$$Q=\overline{Q}/n_s=f(T_e^3-T^3),$$

which correspond to the energy balance equation in the case of the interaction of electrons with the piezoelectric potential of the acoustic phonons (PA scattering) under the condition of weak screening at frequencies of 30 and 150 MHz in different magnetic fields

$$Q_{PA}=e\mu E^2=A_3(T_e^3-T^3). \qquad (2)$$

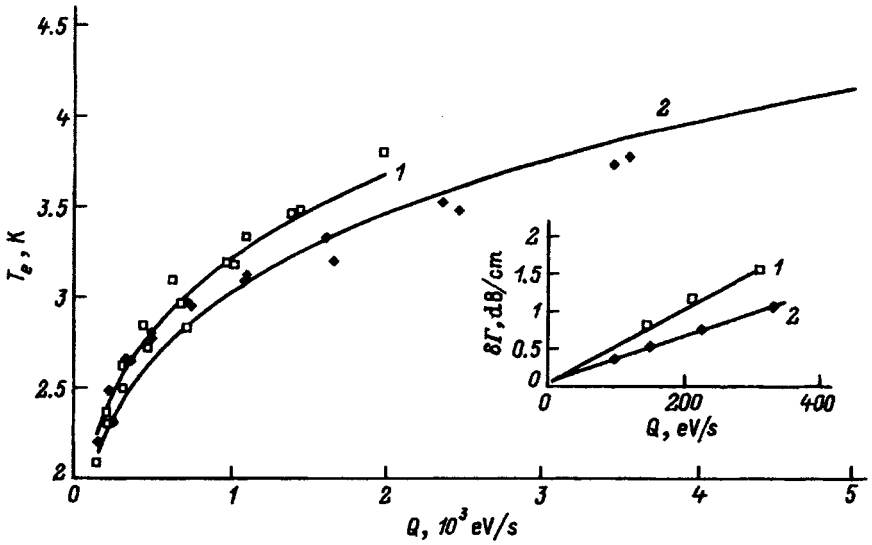

FIG. 4. Electron temperature T_e versus the energy losses Q at SAW frequencies f, MHz: *1*—150 and *2*—30. Inset: $\delta\Gamma=\Gamma(T_e)-\Gamma_0(T)$ versus Q at SAW frequencies f MHz: *1*—150, *2*—30.

But since the condition for weak screening was not satisfied for this sample, the curves $Q=f(T_e^5-T^5)$, corresponding to the energy balance equation in the case of PA scattering but with the condition of strong screening for the same frequencies 30 and 150 MHz and the same magnetic fields, were also constructed:

$$Q_{PA}=A_5(T_e^5-T^5), \tag{3}$$

A least-squares analysis showed that the expression (3) gives a better description of the experimental curves. Figure 4 shows the experimental points and theoretical curves of the expressions of the type (3) with $A_5=3.0\pm0.5$ eV/(s·K^5) and $f=30$ MHz, where f is the SAW frequency (see curve *1* in Fig. 4), and $A_5=4.0\pm0.6$ eV/(s·K^5) and $f=150$ MHz (see curve *2* in Fig. 4).

4. THEORY OF HEATING OF TWO-DIMENSIONAL ELECTRONS WITH CONTROL OF RELAXATION ON THE LATTICE BY ELECTRON-ELECTRON COLLISIONS

To describe the heating of an electron gas by means of a temperature T_e different from the lattice temperature T, the electron-electron collisions must occur more often than collisions with the lattice; i.e., the condition $\tau_{ee}\ll\tau_\varepsilon$, must be satisfied. Here τ_e and τ_{ee} are, respectively, the electron energy relaxation time on phonons and the electron-electron (ee) interaction time.

In a weakly disordered 2DEG in GaAs/AlGaAs heterostructures, momentum is dissipated mainly on the Coulomb charge of the residual impurity near the interface. As a result, the relaxation times satisfy the inequalities

$$\tau_p\ll\tau_{ee}\ll\tau_\varepsilon, \tag{4}$$

where τ_p is the electron momentum relaxation time.

4.1. Static regime

When the inequalities (4) are satisfied, the nonequilibrium part of the distribution function has the form

$$f_p=-e\mathbf{E}\cdot\mathbf{v}\tau_p\frac{\partial f_0(\varepsilon_p)}{\partial\varepsilon_p}, \tag{5}$$

where $\mathbf{E}$ is the electric field, $\mathbf{v}$ is the electron velocity, $f_0(\varepsilon_p)$ is the principal part of the distribution function of electrons with energy $\varepsilon_p=p^2/2m$, where p and m are, respectively, the electron momentum and effective mass. Because of the rapid ee collisions, a Fermi distribution is established for $f_0(\varepsilon_p)$, but the Fermi level ε_F and the temperature T_e must be determined from the conservation equations for the electron density and average energy, while the electron-phonon collisions give rise to energy transfer from the electrons to the lattice.

The results of a calculation of the energy balance equation in a 2DEG in the case of electron scattering by piezoelectric material and deformation potentials of the acoustic phonons are presented in Refs. 16 and 17. The numerical coefficients in the relations, taken from Ref. 16 and presented below, refer to a 2DEG on the (001) surface of GaAs if the following condition is satisfied:

$$k_F<\pi/d, \tag{6}$$

where the electron localization width d in a quantum well can be estimated for a heterojunction by the relation

$$d=\left[\left(\frac{3}{4}\right)\frac{a_B^*}{\pi N^*}\right]^{1/3},\quad N^*=N_{\text{depl}}+\frac{11}{32}n_s. \tag{7}$$

Here N_{depl} is the density of the residual impurity near the heterojunction, and $a_B^*=\hbar^2\varepsilon_s me^2$ is the effective Bohr radius.

In the case of weak screening, the intensity of the energy losses due to PA scattering is determined by the expression[16]

$$Q_{PA}=b_1Q_1\left(\frac{k_BT}{\hbar k_Fs_t}\right)^3\left(\frac{T_e^3}{T^3}-1\right),$$

$$Q_1\equiv\frac{2ms_t^2}{\tau_0},\quad b_1=\frac{\zeta(3)}{2}\frac{13}{16}\left[1+\frac{9}{13}\left(\frac{s_t}{s}\right)^2\right], \tag{8}$$

where $1/\tau_0=(e\beta_{14})^2m/2\pi\rho\hbar^2s_t$, β_{14} is the piezoelectric constant, ρ is the density of the semiconductor (in our case GaAs, s and $s_t=0.59s$ are, respectively, the longitudinal and transverse sound speeds in GaAs, $k_F=(2\pi n_s)^{1/2}$ is the wave

number of an electron with Fermi energy ε_F, $\zeta(x)$ is the Riemann ζ-function, and k_B is Boltzmann's constant.

In the case of electron scattering by the deformation potential of acoustic phonons (DA scattering) the corresponding expression has the form

$$Q_{DA}=b_2Q_2\left(\frac{k_BT}{2ms^2}\right)^2\left(\frac{k_BT}{\hbar k_Fs}\right)^3\left(\frac{T_e^5}{T^5}-1\right),$$

$$Q_1\equiv\frac{2ms^2}{l_0/s},\quad b_2=12\zeta(5), \tag{9}$$

where $l_0\equiv\pi\hbar^4\rho/2m^3E_1^2$, and E_1 is the deformation potential.

The relations (8) and (9) hold for small-angle scattering when

$$k_BT\ll 2\hbar k_Fs\equiv k_BT_{sma}, \tag{10}$$

and weak screening when

$$k_BT\gg 2\hbar s_t/a_B^*\equiv k_BT_{scr}. \tag{11}$$

In the case of strong screening, when an inequality opposite to the (11) holds,

$$k_BT\ll 2\hbar s_t/a_B^*\equiv k_BT_{scr}, \tag{12}$$

for PA scattering[16]

$$Q_{PA}^{scr}=\zeta(5)\frac{3}{4}\frac{59}{64}\left[1+\frac{45}{59}\left(\frac{s_t}{s}\right)^4\right]\frac{2ms_t^2}{\tau_0}\frac{\varepsilon_F}{\varepsilon_B}\times\left(\frac{k_BT}{\hbar k_Fs_t}\right)^5\left(\frac{T_e^5}{T^5}-1\right), \tag{13}$$

where $\epsilon_B=\hbar^2/2m(a_B^*)^2$ is the Bohr energy.

4.2. Heating of electrons by a surface acoustic wave

When the relations (4) between the times are satisfied, the nonequilibrium part of the distribution function, which depends on the electron momentum, relaxes rapidly and its current part, which is antisymmetric in the momentum, has the usual form (5) but $E(x,t)=E_0\cos(qx-\omega t)$, where $\omega=2\pi f$. As a result, $f_0(\varepsilon_p)$ is the Fermi function but the chemical potential $\varepsilon_F(x,t)$ and temperature $T(x,t)$ can be functions of the coordinates and time. These functions must also be determined from the conservation equations for the density and average energy of the electrons. Slow electron-phonon (e-ph) collisions, which are responsible for energy transfer from electrons to the lattice, appear only in the last equation and they fall out of the equation for the density, since the e-ph interaction preserves the total number of electrons.

The main part of the chemical potential is given by the normalization condition for the total electron density, i.e., it is a constant. True, there are corrections, which are proportional to the amplitude of the wave, but the nonlinear contribution from these corrections, scaled to the main value of the chemical potential, is small and can be ignored. For this reason, we write only the equation for the change in the average energy

$$\frac{\pi^2}{6}\rho\frac{\partial(T_e^2)}{\partial t}-\sigma_{xx}E_0^2\frac{\omega^2}{\omega^2+(q^2D)^2}\cos^2(qx-\omega t)+\overline{Q}(T_e)=0, \tag{14}$$

where T_e is the electron temperature, ρ_0 is the two-dimensional density of states, σ_{xx} is the electric conductivity, D is the diffusion coefficient, and $\overline{Q}(T_e)$ is the energy transferred to the lattice. The harmonic variations of the chemical potential with wave number q and frequency ω lead to a variation of the Joule heat source for the wave and to the appearance in it of the cofactor

$$\frac{\omega^2}{\omega^2+(q^2D)^2}.$$

Since in the experiment $q^2D\ll\omega$ (see Ref. 7), the spatial variation of the Joule heat source can be disregarded. For this reason, we also disregard the spatial variation of the temperature but allow for a variation of the temperature correction for the average energy in time. The quantity $\overline{Q}(T_e)$ depends on the e-ph interaction mechanism. For PA scattering $\overline{Q}(T_e)=n_sQ_{PA}(T_e)$, where $Q_{PA}(T_e)$ are given by Eq. (8) or (13) and in a simplified form by the expression (2) or (3); $n_s=\rho_0\varepsilon_F$ is the total density of the two-dimensional electrons.

We shall examine first the condition for weak heating

$$\Delta T=T_e-T\ll T. \tag{15}$$

In this case

$$\frac{\partial\Delta T}{\partial t}+\frac{\Delta T}{\tau_\varepsilon}=\frac{3\sigma_{xx}E_0^2\cos^2(qx-\omega t)}{\pi^2\rho_0T}, \tag{16}$$

where for small-angle PA scattering under strong screening conditions

$$\frac{1}{\tau_\varepsilon}=\frac{15}{\pi^2}\varepsilon_FA_5T^3, \tag{17}$$

and the coefficient A_5 is determined by Eq. (13) written in the form (3). The equation (16) is easily solved. The temperature correction nonlinear in the electric field must be substituted into the expression for the electrical conductivity and the latter into the expression for the damping coefficient Γ of the surface acoustic wave

$$\delta\Gamma=\Gamma(W)-\Gamma_0=\frac{\partial\Gamma}{\partial\sigma_{xx}}\frac{\partial\sigma_{xx}}{\partial T}\times\frac{3\sigma_{xx}E_0^2\tau_\varepsilon}{2\pi^2\rho_0T}\left(1+\frac{1/2}{1+4\omega^2\tau_\varepsilon^2}\right). \tag{18}$$

Here $\Gamma_0\equiv\Gamma(T)$ as $W\to 0$ is the absorption in the linear region at fixed lattice temperature T, and $\delta\Gamma$ is the nonlinear correction to $\Gamma(W)$. The SAW electric field is expressed in terms of the input power W and the absorption Γ is expressed as $\sigma_{xx}E_0^2=4\Gamma W$. It follows from the expression (18) that when $\omega\tau_e\gtrsim 1$ and Eq. (15) holds, the second harmonic in the heating function decreases rapidly as a result of oscillations in time, and the heating is determined by the average power

of the wave. This last assertion is also valid for the case of strong heating. The quasistatic balance condition holds in this case:

$$A_5(T_e^5-T^5)=\sigma_{xx}E_0^2/2n_s. \tag{19}$$

The temperature T_e found from the relation (19) determines the electrical conductivity and the absorption of the SAW. For strong heating, the difficulty of solving the nonlinear equation (14) analytically makes it impossible to obtain simple formulas for an arbitrary value of the parameter $\omega\tau_\varepsilon$.

For $\omega\tau_\varepsilon\ll 1$, the heating of the 2DEG is completely determined not by the average power but by the instantaneously varying field of the wave. As a result, in the case of slight heating, we see an increase in the degree of heating of the 2DEG [see the cofactor in parentheses in the expression (18) for $\omega\tau_\varepsilon\to 0$]. For $\omega\tau_\varepsilon\to 0$ the following expression can be written out, assuming the time derivative in the relation (16) to be a small term. For the PA interaction under strong screening conditions

$$T_e(x,t)=\left[T^5+\frac{\sigma_{xx}E_0^2\cos^2(qx-\omega t)}{A_5 n_s}\right]^{1/5}.$$

This expression must be substituted into the temperature-dependent part of the electric conductivity, which in a strong magnetic field is determined by the expression for the Shubnikov oscillations

$$\Delta\sigma_{xx}=C\frac{2\pi^2T_e(x,t)/\hbar\omega_c}{\sinh[2\pi^2T_e(x,t)/\hbar\omega_c]}\cos\left(\frac{2\pi\varepsilon_F}{\hbar\omega_c}\right),$$

where C is a slowly varying function of temperature and magnetic field, and ω_c is the cyclotron frequency. In this case, only the part of the current corresponding to the first harmonic in the 2DEG layer participates in the absorption of the SAW. The effective temperature appearing in the expression for $\Gamma(W)$ is also determined correspondingly:

$$\frac{T_e}{\sinh(2\pi^2T_e/\hbar\omega_c)}=\int_0^{2\pi}\frac{d\varphi}{\pi}(\cos^2\varphi)\times\frac{[T^5+(\sigma_{xx}E_0^2/A_5n_s)\cos^2\varphi]^{1/5}}{\sinh\{(2\pi^2/\hbar\omega_c)[T^5+(\sigma_{xx}E_0^2/A_5n_s)\cos^2\varphi]^{1/5}\}}.$$

This expression is quite difficult to use in the case of strong heating.

4.3. Determination of the relaxation times

4.3.1. *Electron-electron interaction time* τ_{ee}. In the theoretical studies[18,19] it was shown that the quasiparticle lifetime in a 2DEG under conditions of large momentum transfers is determined by the quantity

$$\frac{\hbar}{\tau_{ee}^{(p)}}=\frac{\pi^2T^2}{2\varepsilon_{F0}}\ln\left(\frac{\varepsilon_{F0}}{T_m}\right),\quad T_m=\max\{T,\hbar/\tau_p\}, \tag{20}$$

where ε_{F0} is the Fermi energy at $T=0$, and $\tau_{ee}^{(p)}$ is called the ''pure'' electron-electron (ee) interaction time.

As the temperature is lowered, the so-called ''dirty'' or ''Nyquist'' time $\tau_{ee}^{(N)}$ with small momentum transfer (in the process of electron diffusion) $\Delta q\approx 1/L_T$, (Ref. 20 and 22) where $L_T=(D\hbar/k_BT)^{1/2}$ is the diffusion length over time $k_BT/\hbar$, often called the coherence length, plays an increasingly larger role in the ee interaction as the degree of disordering of the 2DEG increases. The ee collision frequency is determined by the quantity

$$\hbar/\tau_{ee}^{(N)}=(TR_\square e^2/h)\ln(h/2e^2R_\square), \tag{21}$$

where $R_\square=1/\sigma_{xx}$ is the resistance of the film per unit area.

4.3.2. *Relaxation time* $\overline{\tau_\varepsilon}$ *of the average electron energy.* If the heating of the 2DEG is characterized by an electron temperature T_e, then the energy losses Q (per electron) can be written in the form[10]

$$Q=[\overline{\varepsilon}(T_e)-\overline{\varepsilon}(T)]/\overline{\tau_\varepsilon}, \tag{22}$$

where $\overline{\varepsilon}(T_e)$ and $\overline{\varepsilon}(T)$ are the average electron energy at T_e and T, respectively, and $\overline{\tau_\varepsilon}$ is the energy relaxation time. The change in the average kinetic energy of a two-dimensional electron with $\varepsilon_F\ll k_BT$ is

$$\Delta\varepsilon=\overline{\varepsilon}(T_e)-\overline{\varepsilon}(T)=\frac{\pi^2k_B^2}{6}\frac{(T_e^2-T^2)}{\varepsilon_{F0}}\bigg|_{\Delta T\ll T}=\frac{\pi^2k_B^2}{3}\frac{T\Delta T}{\varepsilon_{F0}}. \tag{23}$$

The latter equality in Eq. (23) corresponds to the condition of weak heating (15). If a dependence $Q(T_e,T)$ of the type (2) or (3) can be represented in an expansion in $\Delta T/T$ as

$$Q(T,\Delta T)=\gamma A_\gamma T^{\gamma-1}\Delta T,$$

where γ is the exponent of T_e and T in the expression the following expression (2) or (3), then we obtain the following expression for $\overline{\tau_\varepsilon}$:

$$\overline{\tau_\varepsilon}|_{\Delta T\ll T}=\frac{\pi^2k_B^2}{3\gamma A_\gamma\varepsilon_{F0}T^{\gamma-2}}. \tag{24}$$

For the case (3), i.e., $\gamma=5$, we obtain the expression (17) for $1/\overline{\tau_\varepsilon}=1/\tau_\varepsilon$.

5. DISCUSSION OF THE EXPERIMENTAL RESULTS

Let us examine the condition of applicability of the heating theories presented in the preceding section to our results. The typical values of the residual impurity density N_{depl} in the region of the 2DEG for our heterostructures is of the order of 10^{10} cm^{-2}. Therefore $N_{\text{depl}}\ll n_s$. For the parameters of GaAs $m=0.07m_0$, permittivity $\varepsilon_s=12.8$, and Bohr radius $a_B^*=97$ Å, we obtain from Eq. (7)

$$d=85\text{ Å},\quad dk_F/\pi\cong 0.3<1.$$

In other words, the condition (6) is satisfied.

The momentum relaxation time for the experimental sample was estimated from the Hall mobility $\tau_p\simeq\mu_Hm/e$; it is $\tau_p=5.1\times10^{-12}$ s.

It was shown experimentally in Ref. 23 that at liquid-helium temperatures and low 2DEG mobilities the ee inter-

action with small momentum transfer (21) predominates in quantum wells at the GaAs/GaAlAs heterojunction. For our structure, with $R_{\square}=73\ \Omega$, $\hbar/\tau_{ee}^{(N)}=1.46\times10^{-2}\ T$ and varies in the range

$$\hbar/\tau_{ee}^{(N)}=0.02-0.06\ \text{K} \tag{25}$$

for $T=1.5-4.2$ K.

In the expression (20) we employed the value $T_m=T$, since $\hbar/\tau_p\simeq1.5\ \text{K}\leqslant T$. In the case $\varepsilon_{F0}\simeq266$ K, for our sample $\hbar/\tau_{ee}^{(p)}$ in the same temperature range is

$$\hbar/\tau_{ee}^{(p)}=0.07-0.4\ \text{K} \tag{26}$$

The sum of the contributions (25) and (26) gives for the experimental sample

$$1.5\times10^{-11}\ \text{s}<\tau_{ee}<8.4\times10^{-11}\ \text{s} \tag{27}$$

in the interval $T=1.5-4.2$ K.

To estimate the energy relaxation time $\overline{\tau_\varepsilon}$ (24) it is necessary to know the coefficient A_γ in relations of the type (2) or (3):

$$Q=A_\gamma(T_e^\gamma-T^\gamma).$$

A calculation according to Eqs. (8), (9), and (13) gives for a 2DEG in our structure [$\beta_{14}=0.12\ \text{C/m}^2$ (Ref. 24) and the same values of all other parameters as in Ref. 16] for small-angle scattering and weak screening, when $T_{scr}\ll T\ll T_{sma}$ [see Eqs. (10), (11), (8), and (9)],

$$Q_{\text{PA}}[eV/s]=67.5[eV/(s\cdot\text{K}^3)](T_e^3-T^3),$$

$$Q_{\text{DA}}[eV/s]=13.7[eV/(s\cdot\text{K}^5)](T_e^5-T^5), \tag{28}$$

and in the case of strong scattering with $T\ll T_{scr}\ll T_{sma}$ [see Eqs. (10), (12), and (13)]

$$Q_{\text{PA}}^{scr}[eV/s]=16.2[eV/(s\cdot\text{K}^5)](T_e^5-T^5). \tag{29}$$

As indicated in Ref. 16, PA scattering in the region of strong screening predominates with ''certainty'' over DA scattering.

It should also be noted that for such a sample with $n_s=6.75\times10^{11}\ \text{cm}^{-2}$ and $\mu_H=1.5\times10^5\ \text{cm/(V}\cdot\text{s)}$ in dc investigations (i.e., in the static regime)[11,14] at $T=1.86$ K up to $T_e\simeq4$ K the heating was described by a law of the type (2), which is valid for PA scattering, and under weak screening conditions the value $A_3=130\ \text{eV/(s}\cdot\text{K}^3)$ was found for sample 1 from Ref. 11, which is higher than the value indicated for Q_{PA} in Eq. (28).[3)] However, irrespective of the values of A_γ and γ which we used to estimate $\overline{\tau_\varepsilon}$ on the basis of Eq. (24)—the theoretical values (28) and (29) or the experimental value $A_3=130\ \text{eV/(s}\cdot\text{K}^3)$ $\gamma=3$—we obtained for the energy relaxation time estimates in the range $\overline{\tau_\varepsilon}=(2-50)\times10^{-9}$ s.

Comparing the values presented above for τ_p and τ_{ee} (27) and the range of values for $\overline{\tau_\varepsilon}$, we see that the relations (4) are satisfied.The concept of an electron temperature T_e could therefore be introduced and the heating theories presented in Sec. 4 could be used.

Let us examine the estimates of the critical temperatures T_{sma} (10) and T_{scr} (12) at which the energy relaxation mechanisms change in the case of the e-ph interaction. We determined these temperatures using the value $s_t=3.03\times10^5$ cm/s (see Ref. 16) and the value given above for a_B^*. The results are

$$T_{sma}=9.5\ \text{K}\quad\text{and}\quad T_{src}=4.6\ \text{K}. \tag{30}$$

Since the phonon temperature in our experiments $T=1.55$ K, we have

$$T<T_{scr}<T_{sma}. \tag{31}$$

Therefore, the inequalities (10) and (12) are satisfied in our experiment, though not as strongly, especially the inequality (12), as assumed in the theory of Ref. 16 for application of the expression (13).

Finally, observation of a law of the type (3) with $\gamma=5$ (see Sec. 3 and Fig. 4) and the ratio (31) of the temperatures presented above allows us to assert that in the case of heating of two-dimensional electrons by the electric field of a SAW ($f=30$ and 150 MHz) the electron energy relaxation is determined by PA scattering with strong screening (13), which for the parameters employed by us gives the theoretical relation (29).

At the same time, as noted above, in the investigation in the static regime [with phonon temperature $T\simeq1.86$ K (Refs. 11–15), i.e. the inequalities (31) hold], the law (2) with $\gamma=3$ was observed, indicating that PA scattering dominates in the electron energy relaxation mechanisms in the case of weak screening (8). Besides the indicated discrepancy between the results of investigations of the heating of a 2DEG in high-frequency (rf) and dc electric fields, it should be noted that there is also a discrepancy in the experimental values $A_5\simeq3\ \text{eV/(s}\cdot\text{K}^5)$ at $f=30$ MHz and $A_5\simeq4\ \text{eV/(s}\cdot\text{K}^5)$ at $f=150$ MHz (see Sec. 3). In addition, these values are not greater than (as the experimental value of A_3 is the static regime) but less than the theoretical value $A_5\simeq16.2\ \text{eV/(s}\cdot\text{K}^5)$—Eq. (29), calculated according to the theory of Ref. 16.

Since the calculations in Ref. 16 were performed for a constant electric field, they obviously cannot explain the above-noted discrepancies, especially the difference in the functions $Q(T_e)$ at different frequencies. Apparently, the difference is due to the different values of $\omega\tau_\varepsilon$ with respect to 1. Taking into consideration the approximate nature of the computed parameters and the uncertainty in the input power in our measurements, we took as the value of the energy relaxation time τ_ε estimated from the theoretical value $A_5\simeq16.2\ \text{eV/(s}\cdot\text{K}^5)$ with $\gamma=5$ (29), which gives in the case of a calculation based on Eq. (17) or (24) $\tau_\varepsilon\simeq3.3\times10^{-9}$ s. At frequency $f=30$ MHz $\omega\tau_\varepsilon\simeq0.6<1$ and at $f=150$ MHz $\omega\tau_\varepsilon\simeq3>1$, which leads to a different heating for the same energy losses. In this connection, we attempted to study this question theoretically (see Sec. 4.2) and to compare the results obtained with experiment. As a result, we can demonstrate the validity of Eq. (18), obtained under the assumption of weak heating, $\Delta T\ll T$. We present in the inset in Fig. 4 the experimental values of the difference $\delta\Gamma=\Gamma(W)-\Gamma_0$ as a function of Q for two frequencies, 30 and 150 MHz, in a field $H=15.5$ kOe. We see from the figure that in accordance with Eq. (18), these dependences are linear and for the same energy losses Q the quantity $\delta\Gamma_1$ ($f_1=30$ MHz) is

greater than $\delta\Gamma_2$ ($f_2=150$ MHz), the ratio $\delta\Gamma_1/\delta\Gamma_2$ is equal, to within 10%, to the theoretical value

$$\left(1+\frac{1/2}{1+4\omega_1^2\tau_\varepsilon^2}\right)\Bigg/\left(1+\frac{1/2}{1+4\omega_2^2\tau_\varepsilon^2}\right)$$

with $\omega_{1,2}=2\pi f_{1,2}$. A similar result was also obtained for $\delta\Gamma_1/\delta\Gamma_2$ in the magnetic field $H=14.1$ kOe. Therefore, experiment confirms the theoretical conclusion that for $\Delta T \ll T$ the energy losses depend on $w\tau_\varepsilon$.

It should be noted that in determining Q at $f=150$ MHz it was assumed that $\delta[\Gamma(W)/\Gamma_M]$ is frequency-independent (see Sec. 3), which is at variance with the result presented above. However, Q and $\delta\Gamma$ are so small at the onset of the nonlinear effects that their differences at different frequencies fall within the limits of error of our measurements.

As one can see from the theory (see Sec. 4.2), an analytical expression could not be obtained in the case of strong heating of a 2DEG in an rf electric field of a SAW, but it can be assumed that, by analogy with the case of weak heating, the difference in the coefficients A_5 remains also in the case of heating up to $T\simeq 4$ K.

A more accurate numerical development of the theory of heating of a 2DEG for arbitrary values of $\omega\tau_\varepsilon$ from $\omega=0$ up to $\omega\tau\varepsilon\gg 1$, including in the transitional regions $T\simeq T_{scr}$ and $T\simeq T_{sma}$, could explain the discrepancy in the experimental results obtained in constant and rf electric fields with the same direction of the inequalities (31).

5. CONCLUSIONS

In our study we observed heating of a 2DEG by a rf electric field generated by a surface acoustic wave (SAW). The heating could be described by an electron temperature T_e exceeding the lattice temperature T.

It was shown that the experimental dependences of the energy losses Q on T_e at different SAW frequencies depend on the value of $\omega\tau_\varepsilon$ with respect to 1, where τ_ε is the energy relaxation time of two-dimensional electrons. Theoretical calculations of the heating of a two-dimensional electron gas by the electric field of a SAW were presented for the case of warm electrons ($\Delta T \ll T$). The results showed that for the same energy losses Q the degree of heating (i.e., the ratio T_e/T) with $\omega\tau_\varepsilon>1$ ($f=150$ MHz) is less than with $\omega\tau_\varepsilon\leqslant 1$ ($f=30$ MHz). Experimental results confirming this calculation were presented.

It was shown that the electron energy relaxation time τ_ε is determined by energy dissipation in the piezoelectric potential of the acoustic phonons under conditions of strong screening for the SAW frequencies employed in the experiment.

This work was supported by the Russian Fund for Fundamental Research (Grants 95-02-04066a and 95-02-04042a) and by the Fund of International Associations (Grant INTAS-1403-93-ext).

[1)] In Ref. 7 it is shown that the values of Γ_M do not depend on the conductivity of the 2DEG, and that they are determined, within the limits of the experimental error, only by the SAW characteristics and the gap between the sample and $LiNbO_3$.

[2)] We take this term to mean the so-called escape time τ_0, which is inversely proportional to the almost total scattering cross section.[10] In experiments on quantum oscillations it is defined as $\tau_0=\hbar/2\pi T^*$, where T^* is the Dingle temperature.

[3)] As V. Karpus has shown,[16] the experimental data of Ref. 11 in the region $T_e \gg T$ fall well within the general picture of $Q(T_e,T)$ (see Fig. 4 from Ref. 16). It should be noted that the value $\beta_{14}=0.12$ C/m^2 (Ref. 24), which we used for calculation of Eqs. (28) and (29), corresponds to $h_{14}=1.06\times 10^7$ V/cm (in the notation of Ref. 16). For this reason, the theoretical value of A_γ ($\gamma=3$ or 5) in Refs. 11, 14, and 16 for PA scattering (see, for example, $\alpha\equiv I_3$ for the theoretical curve in Fig. 3 from Ref. 11) is 1.3 times higher than the corresponding values for $Q_{\rm PA}$, presented in the relations (28) and (29), for similar values of n_s.

[1] Yu. M. Gal'perin, I. L. Drichko, and B. D. Laĭkhtman, Fiz. Tverd. Tela (Leningrad) **12**, 1437 (1970) [Sov. Phys. Solid State **12**, 1128 (1970)].
[2] I. L. Drichko, Fiz. Tverd. Tela (Leningrad) **27**, 499 (1985) [Sov. Phys. Solid State **27**, 305 (1985)].
[3] Yu. M. Gal'perin, I. L. Drichko, and L. B. Litvak-Gorskaya, Fiz. Tverd. Tela (Leningrad) **28**, 3374 (1986) [Sov. Phys. Solid State **28**, 1899 (1986)].
[4] Yu. M. Gal'perin, I. L. Drichko, and L. B. Litvak-Gorskaya in *Proceedings of a Conference on Plasma and Instabilities in Semiconductors* [in Russian], Vil'nyus, 1986, p. 186.
[5] A. Wixforth, J. Scriba, M. Wassermeir, J. P. Kotthaus, G. Weimann, and W. Schlapp, Phys. Rev. B **40**, 7874 (1989).
[6] A. Schenstrom, M. Levy, B. K. Sarma, and H. Morkoc, Solid State Commun. **68**, 357 (1988).
[7] I. L. Drichko, A. M. D'yakonov, A. M. Kreshchuk, T. A. Polyanskaya, I. G. Savel'ev, I. Yu. Smirnov, and A. V. Suslov, Fiz. Tekh. Poluprovodn. **31**, 451 (1997) [Semiconductors **31**, 384 (1997)].
[8] M. G. Blyumina, A. G. Denisov, T. A. Polyanskaya, I. G. Savel'ev, A. P. Senichkin, and Yu. V. Shmartsev, Fiz. Tekh. Poluprovodn. **19**, 164 (1985) [Sov. Phys. Semicond. **19**, 102 (1985)].
[9] I. L. Drichko and I. Yu. Smirnov, Fiz. Tekh. Poluprovodn. **31**, 1092 (1997) [Semiconductors **31**, 933 (1997)].
[10] V. F. Gantmakher and I. B. Levinson, *Current Carrier Scattering in Metals and Semiconductors* [in Russian], Nauka, Moscow, 1984.
[11] M. G. Blyumina, A. G. Denisov, T. A. Polyanskaya, I. G. Savel'ev, A. P. Senichkin, and Yu. V. Shmartsev, JETP Lett. **44**, 331 (1986).
[12] I. G. Savel'ev, T. A. Polyanskaya, and Yu. V. Shmartsev, Fiz. Tekh. Poluprovodn. **21**, 2096 (1987) [Sov. Phys. Semicond. **21**, 1271 (1987)].
[13] A. M. Kreshchuk, M. Yu. Martisov, T. A. Polyanskaya, I. G. Savel'ev, I. I. Saĭdashev, A. Yu. Shik, and Yu. V. Shmartsev, Fiz. Tekh. Poluprovodn. **22**, 604 (1988) [Sov. Phys. Semicond. **22**, 377 (1988)].
[14] A. M. Kreshchuk, M. Yu. Martisov, T. A. Polyanskaya, I. G. Savel'ev, I. I. Saĭdashev, A. Yu. Shik, and Yu. V. Shmartsev, Solid State Commun. **65**, 1189 (1988).
[15] A. M. Kreshchuk, E. P. Laurs, T. A. Polyanskaya, I. G. Savel'ev, I. I. Saĭdashev, and E. M. Semashko, Fiz. Tekh. Poluprovodn. **22**, 2162 (1988) [Sov. Phys. Semicond. **22**, 1364 (1988)].
[16] V. Karpus, Fiz. Tekh. Poluprovodn. **22**, 439 (1988) [Sov. Phys. Semicond. **22**, 268 (1988)].
[17] V. Karpus, Fiz. Tekh. Poluprovodn. **20**, 12 (1986) [Sov. Phys. Semicond. **20**, 6 (1986)].
[18] A. V. Chaplik, Zh. Éksp. Teor. Fiz. **60**, 1845 (1971) [Sov. Phys. JETP **33**, 997 (1971)].
[19] H. Fukuyama and E. Abrahams, Phys. Rev. B **27**, 5976 (1983).
[20] B. L. Al'tshuler and A. G. Aronov, JETP **30**, 482 (1979).
[21] F. Schmid, Z. Phys. **217**, 251 (1979).
[22] B. L. Altshuler, A. G. Aronov, and D. E. Khmelnitskii, J. Phys.: Condens. Matter **15**, 73 (1982).
[23] I. G. Savel'ev and T. A. Polyanskaya, Fiz. Tekh. Poluprovodn. **22**, 1818 (1988) [Sov. Phys. Semicond. **22**, 1150 (1988)].
[24] A. R. Hutson and D. L. White, J. Appl. Phys. **33**, 40 (1962).

Translated by M. E. Alferieff

Optical spectroscopy of two-dimensional electronic states in modulation-doped *N*-AlGaAs/GaAs heterostructures

A. V. Guk, V. É. Kaminskiĭ, V. G. Mokerov, Yu. V. Fedorov, and Yu. V. Khabarov

Institute of Radio Engineering and Electronics, Russian Academy of Sciences, 103907 Moscow, Russia
(Submitted October 22, 1996; accepted for publication March 18, 1997)
Fiz. Tekh. Poluprovodn. **31**, 1367–1374 (November 1997)

Photoluminescence spectra, associated with the two-dimensional electron gas in modulation-doped *N*-AlGaAs/GaAs heterostructures with different thicknesses d_s of the undoped spacer layer, have been investigated at 77 K. All experimental samples possessed an undoped superlattice buffer layer (as the second heterojunction), located at a distance d_a below the main heterojunction. The data obtained are subjected to a theoretical analysis by comparing with spectra calculated on the basis of a self-consistent solution of the Schrödinger and Poisson equations. For $13 \leqslant d_a \leqslant 40$ nm the photoluminescence spectra possessed two lines with photon energies $h\nu_1$ and $h\nu_2$ ($h\nu_2 > h\nu_1$) and intensities I_1 and I_2, respectively. This doublet structure is due to optical transitions between the bottom electronic subbands E_e^1 and E_e^2 and the lowest heavy-hole E_{hh}^1, E_{hh}^2 and light-hole E_{lh}^1 subbands. It is shown that the increase in the intensity ratio I_2/I_1 with decreasing d_s is due to an increase in the population of the upper subband E_e^2 and a decrease in the probability of optical transitions from the lower subband E_e^1. The shift of both lines in this case in the direction of lower energies is due to an increase in the band bending. It is shown that the change in the distance d_a influences differently the intensities I_1 and I_2 and the spectral position of the components $h\nu_1$ and $h\nu_2$ of the doublet. This is due to the large difference in the spatial extent of the electron wave functions $\Psi_e^1(z)$ and $\Psi_e^2(z)$.
© *1997 American Institute of Physics.* [S1063-7826(97)02111-X]

Optical investigations of the two-dimensional electron gas (2DEG) in AlGaAs/GaAs heterostructures (HSs) yield direct information about the basic parameters of the electronic subbands (energy, width, degree of filling, and so on),[1–4] supplementing and sometimes exceeding the information supplied by galvanomagnetic measurements. However, thus far they have been directed mainly toward studying the quantum Hall effect and Wigner crystallization, so that they have been performed at very low temperatures and, as a rule, were limited to low 2DEG densities ($<10^{11}$ cm^{-2}).

At the same time, it has been shown[5,6] for the pseudomorphic heterostructures AlGaAs/InGaAs/GaAs that the investigation of the photoluminescence (PL) spectra at liquid-nitrogen temperatures and even room temperature is an effective method for studying electronic states in modulation-doped HSs (MDHSs).

However, such investigations have not been performed for the system AlGaAs/GaAs. This is due to the difficulty of revealing effects associated with the 2DEG because they are masked by intense photoluminescence corresponding to interband radiative recombination of three-dimensional current carriers.

The present work is devoted to a study of the two-dimensional electron states in the MDHS *N*-AlGaAs/GaAs by the PL method, including their characteristic behavior accompanying the introduction of a second (nondoped) heterobarrier (HB) on the substrate side (at a distance d_a from the main HB) into a standard HS. Using such double-barrier MDHSs, we were able to weaken substantially (for small d_a) the contribution of three-dimensional carriers to the PL spectrum and to investigate the PL spectra due to radiative recombination of 2DEG and holes in the system AlGaAs/GaAs at liquid-nitrogen temperature.

In the present paper, we discuss the theoretical approaches describing the main regularities observed in the PL spectra and we calculate the wave functions and energies of the electronic and hole subbands, the populations of the subbands, and the matrix elements of optical transitions as a function of the density n_{2d} of the 2DEG and the distance d_a between the heterobarriers (HBs).

1. EXPERIMENTAL PROCEDURE

Double-barrier MDHSs were grown by molecular-beam epitaxy (MBE) on semi-insulating (001) GaAs substrates. They included a 0.5-μm-thick undoped GaAs buffer layer, an undoped 20-period $Al_{0.25}Ga_{0.75}As$ (1.5 nm)/GaAs (1.2 nm) superlattice (forming the bottom heterobarrier), an active undoped GaAs layer with thickness d_a and then an undoped $Al_{0.25}Ga_{0.75}As$ spacer layer of thickness d_s and a 60-nm-thick silicon-doped ($N=1\times10^{18}$ cm^{-3}) *n*-$Al_{0.25}Ga_{0.75}As$ layer forming the main MDHB. The structure was completed with a 10-nm-thick undoped GaAs layer at the top. The profile of the conduction band of the structure obtained is shown in Fig. 1. The distance d_a between the heterobarriers ranged from 6.5 nm up to 1 μm and more. To investigate the contribution of size quantization in the GaAs active layer, due to its confinement exclusively by the walls of the heterojunctions HSs in which no layer was doped were also grown so as to form a square quantum well (QW). The measurements of the PL spectra

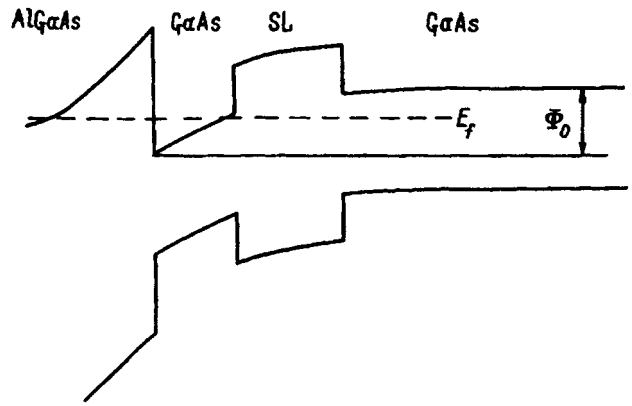

FIG. 1. Band diagram (the effective barrier is shown for the superlattice).

were performed at $T=77$ K. An Ar^+ laser with irradiation density ~ 100 W/cm^2 was used as the source for excitation of the PL.

The PL spectra of MDHSs with different values of d_a and d_s are presented in Fig. 2. For samples with $d_a > 50$ nm, only one line was observed in the PL spectrum (Fig. 2a), irrespective of the degree of doping and thickness d_s. The spectral position of the line $h\nu_0 = 1.508$ eV was independent of d_a in the range 50–1000 nm and larger and corresponded to interband radiative recombination of three-dimensional carriers in GaAs at 77 K; i.e., it equalled the band gap $E_g = 1.508$ eV at this temperature.

Figure 3 shows the maximum intensity I_M of this line versus d_a. As one can see from Fig. 3, I_M increases with d_a. It is interesting that although the rate of increase of $I_M(d_a)$ with increasing d_a slows down somewhat, the saturation expected for $d_a > 0.4$ μm, where $\alpha d_a \gg 1$ ($\alpha \approx 10^4$ cm^{-1} is the absorption coefficient in GaAs at the wavelength of the exciting laser) should be satisifed, does not occur. The absence of saturation in $I_M(d_a)$ could be due to the decrease in the

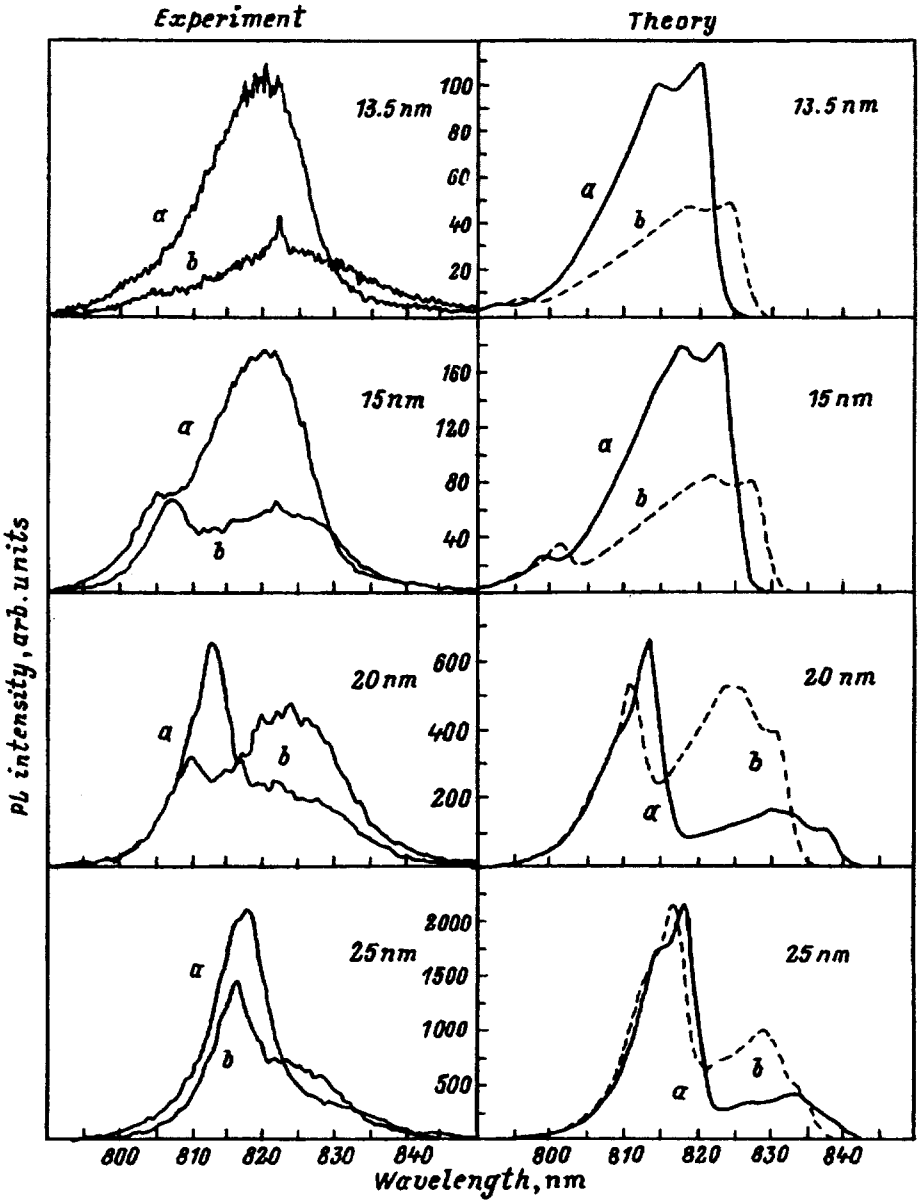

FIG. 2. Experimental and computed PL spectra for different values of the quantum well width (a—$d_s = 3$ nm, b—$d_s = 10$ nm).

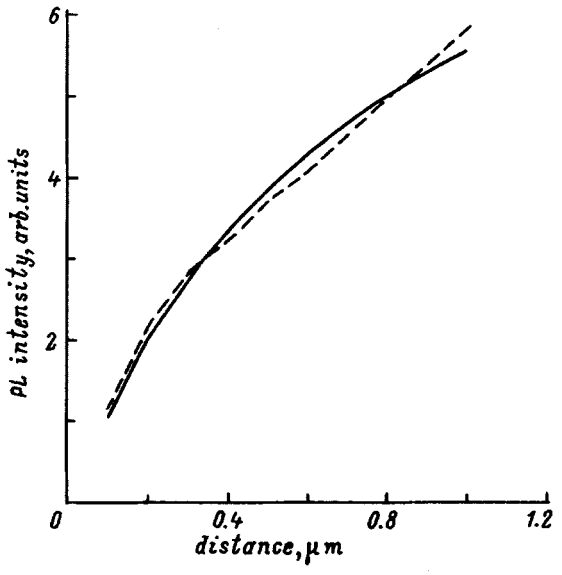

FIG. 3. Experimental (dashed line) and computed (solid line) curves of the PL intensity (at the maximum) for $3D$ electrons versus the distance between the heterobarriers.

TABLE I.

d_a, nm	d_s, nm	$h\nu_1$, eV	$h\nu_2$, eV	$h\nu_0$, eV	$h\Delta\nu_{21}$, meV	I_2/I_1
30	10	1.496	1.510		13.5	7
	3	1.490	1.512	1.509	22	12
25	10	1.503	1.419		17	2
	3	1.492	1.517	1.511	25	7.7
22.5	10	1.503	1.520	1.512	17	1.8
	3	1.493	1.518		25	4.27
20	10	1.506	1.531	1.515	25	0.75
	3	1.500	1.526		26	3.47
18	10	1.509	1.532	1.517	23	0.7
	3	1.503	1.526		23	1.93
15	10	1.511	1.538	1.521	27	0.41
	3	1.508	1.536		28	1.27
13.5	10	1.512	1.545	1.523	33	0.18
	3	1.506	1.540		34	0.39
12	10	1.515	1.553	1.528	38	0.09
	3	1.513	-		-	-
10	10	-	-	1.535	-	-
	3	1.523			-	-
8.5	10	-	-	1.545	-	-
	3	1.536	-		-	-
6.5	10	-	-	1.5609	-	-
	3	1.547	-		-	-

fraction of photocarriers participating in nonradiative surface recombination at the heterojunctions.

It was observed that for small d_a, near $d_a \approx 40-50$ nm and below, the form of the PL spectrum of MDHSs undergoes fundamental changes. Specifically, the initial line at $h\nu_0 = 1.508$ eV transforms into a doublet structure (Fig. 2) consisting of a high-energy peak at $h\nu_2$ and a low-energy ''shoulder'' (or peak) at $h\nu_1$. This fact is attributed to the transition from PL of three-dimensional carriers to PL from sections of the 2DEG. The doublet structure arising is attributed to optical transitions from the bottom two subbands of the 2DEG localized at the top MDHB into the subbands of a hole well located at the bottom heterobarrier (Fig. 1). This structure arises when most photoexcited carriers are trapped in the above-mentioned electronic and hole wells and when the overlapping of the carrier wave functions becomes sufficient for appreciable radiative recombination to occur.

In the case of undoped HSs, in which the band bending associated with the 2DEG is small, the doublet structure in the PL spectrum does not arise when $d_s \leqslant 40$ nm. In such structures a nearly square QW is formed and, accordingly, only one PL line is observed. The spectral position of this line shifts with decreasing d_a to high values of $h\nu$ as a result of size quantization due to the heterobarriers. This line always occupies an intermediate spectral position between the components of the doublet in MDHS (Fig. 2).

As one can see from Fig. 2, the intensities of the components of the doublet structure in MDHS and the shape and spectral position of the components depend on d_a and d_s. Table I gives the main characteristics of the doublet structure for MDHSs ($d_a \leqslant 30$ nm) with different values of d_a and d_s.

Here I_2 and I_1 are the maximum intensities of the high- and low-energy components of the doublet, respectively, and $h\nu_1$ and $h\nu_2$ are their spectral positions, $h\Delta_{12} = h\nu_2 - h\nu_1$ is the spectral splitting of the components of the doublet, and $h\nu_0$ is the spectral position of the PL line in the undoped HSs (the concept of d_s is meaningless for these structures).

It follows from Fig. 2 and Table I that as the spacer-layer thickness d_s decreases (and, correspondingly, the 2DEG density n and the associated self-consistent band-bending potential increase) the following occur for all MDHSs (with $d_a \leqslant 30$ nm):

—the intensity ratio I_2/I_1 increases due to both a strong decrease in I_1 and an increase in I_2;

—a spectral shift of both components of the doublet in the direction of lower energies. Here the $h\nu_1$ peak is shifted more strongly than $h\nu_2$, which increases the spectral splitting $h\Delta\nu_{12}$ of the doublet with decreasing d_a.

It is interesting that for MDHSs with $18\ \text{nm} \leqslant d_a \leqslant 30-40$ nm the component $h\nu$ lies at photon energies lower than the band gap E_g in GaAs at 77 K.

Clear regularities are also observed for the dependence of the PL spectra on the distance d_a between the heterobarriers (for $d_a \leqslant 30$ nm). As d_a decreases, these regularities consist of the following:

—both components of the doublet in a MDHS shift in the direction of high energies; the line $h\nu_0$ in undoped HSs also shifts to higher values of $h\nu$;

—the energy splitting between the components of the doublet increases as a result of the stronger shift in the $h\nu_2$ peak to higher values of $h\nu$ (compared with the shift of the component $h\nu_1$);

—the intensity ratio I_2/I_1 decreases as a result of an increase in I_1 and decrease in I_2.

We present below the results of theoretical calculations performed for the purpose of substantiating the experimental results.

The following will be examined separately:

1. ''Wide wells'' ($d_a > 50$ nm), where because of the large distance between the electronic and hole QWs, the overlapping of the wave functions of the two-dimensional

electrons and holes is small, so that only interband recombination of three-dimensional carriers contributes to the PL spectrum.

2. Quantum wells (for $d_a \leqslant 30-40$ nm), for which the PL spectrum corresponds to optical transitions with the participation of a 2DEG.

2. THEORETICAL MODELS

1. We shall analyze first the dependence of the PL intensity on d_a in wide wells (Fig. 3). As is well known, the main mechanism of relaxation of the energy of nonequilibrium carriers in GaAs at temperatures $T \geqslant 77$ K is the emission of optical phonons. The characteristic energy relaxation length for such processes is ~ 50 nm. For this reason, in the case of wide wells all photoexcited carriers must recombine inside a well. In the case of stationary pumping and weak excitation the distribution of excess electrons δn and holes δp ($\delta n = \delta p$) over the coordinate z (in the direction of growth of the layers) is described by the equation

$$D\frac{d^2(\delta n)}{dz^2} = Ge^{-\alpha z} + \frac{\delta n}{\tau}, \tag{1}$$

where D is the ambipolar diffusion coefficient, G is the photogeneration rate at $z=0$, and τ is the effective lifetime

$$\frac{1}{\tau} = \frac{1}{\tau_r} + \frac{1}{\tau_{nr}},$$

where τ_r is the lifetime for interband radiative recombination, and τ_{nr} is the total lifetime for all other types of nonradiative and radiative volume recombination processes. It is obvious that the PL intensity I is given by

$$I \sim \int_0^{d_a} \delta n(z)\,dz. \tag{2}$$

If it is assumed that the surface recombination rate S_0 is the same for both heterojunctions, then integrating Eq. (1) and substituting the result into Eq. (2), we obtain

$$I = B\frac{S[\cosh(d_a/L)-1]+\sinh(d_a/L)}{(1+S^2)\sinh(d_a/L)+2S\cdot\sinh(d_a/L)}\,[(\alpha L+S) \times(\alpha L-S)\exp(-\alpha d_a)]-[1-\exp(-\alpha d_a)]/\alpha L, \tag{3}$$

where $S = S_0 L/D$, $L = \sqrt{D\tau}$ is the ambipolar diffusion length, and B is a proportionality coefficient.

In the case of our experiments the conditions $d_a/L \ll 1$ and $\alpha L \gg 1$ are satisfied. Comparing the experimental values of I in Fig. 3 with the computational results shows that the best agreement with experiment is attained for $S \ll 1$ and Eq. (3) can be written in the simplified form

$$I = B\alpha L\frac{d_a}{d_a+2SL}(1-e^{-\alpha d_a}). \tag{4}$$

Least-squares analysis of the experimental results, using Eq. (4), gives $S = 2.7\times 10^{-3}$, which corresponds to $S_0 = 10$ cm/s. This means that the surface recombination rate in the HSs investigated is very low and the expression (4) describes well the well-width dependence of the PL intensity (Fig. 2).

2. Quantum wells ($d_a \leqslant 30-40$ nm).

The calculation of the PL characteristics revealed that in order to obtain good agreement with experiment it is necessary to determine accurately the effective height of the superlattice (SL) barrier. This height was calculated according to the Kronig–Penney model. The results are $0.48\Delta E_c$ and $0.44\Delta E_v$ for electrons and holes, respectively, where ΔE_c and ΔE_v are the conduction and valence band offsets at the GaAs/$Al_{0.25}Ga_{0.75}$As heterojunction, respectively.

If it is assumed in the calculations for undoped HSs that the QW is square, then agreement with experiment cannot be obtained. The reason is band bending (Fig. 1). The energies, wave functions, and populations of the subbands of the 2DEG in the MHDS were calculated in the approximation $\delta n \ll n$ (quasiequilibrium situation) by solving the system of equations (the Kohn–Sham system[7])

$$-\frac{\hbar^2}{2m_c}\frac{d^2\Psi_e^i}{dz^2} + U_e(z)\Psi_e^i = E_e^i\Psi_e^i, \tag{5}$$

$$\chi\frac{d^2\varphi}{dz^2} = q[n-N(z)], \tag{6}$$

where z is the direction perpendicular to the heterojunctions, $\Psi_e^i(z)$ is the envelope wave function, $U_e(z)$ is the potential energy, χ is the permittivity, $\varphi(z)$ is the electrostatic potential which is determined by the equilibrium electron distribution, E_e^i is the energy of electron motion along z, $N(z)$ is the impurity density,

$$U_e(z) = \Delta E_c(z) - q(\varphi+\varphi_{xc}), \tag{7}$$

where $\varphi_{xc} = q/3\pi\chi n^{1/3}$ is the exchange-correlation electron interaction potential, and

$$n = \int n_{s_E}|\Psi_e|^2 dE, \tag{8}$$

where n_{s_E} is the layer density of electrons with energy E.

In Eq. (8) the integration extends over both the discrete and continuous sections of the spectrum. For holes, Eq. (5) has the same form as for electrons with the potential energy

$$U_p(z) = \Delta E_v(z) + q(\varphi+\varphi_{xc}). \tag{9}$$

The motion of electrons and holes is unbounded in the plane of the heterojunction and the wave functions are plane waves. The new aspect of the expression (9) is that an exchange-correlation interaction potential φ_{xc}, which depends only on the electron density, is introduced into the hole potential energy. The calculations showed that satisfactory agreement with experiment cannot be obtained without it. The introduction of φ_{xc} is strictly justified in Ref. 7 for electrons. We know of no justification for the introduction in Eq. (9) of a potential φ_{xc} that depends only on the electron density.

The problem of calculating the optical-transition energies was systematically solved by first solving the self-consistent system of equations (5)–(8) for the electrons and then, using the values obtained for the potential (9), the system of equations (5) and (9) for holes. This simplified approach is possible in our case since $\delta p \ll n$.

In the case $\delta n \sim n$, it would be necessary to solve self-consistently the complete system of equations for electrons and holes. This does not present any special difficulties, if the carrier energy distribution functions are known.

It should be noted that in the case of electrons the MDHS studied consists of two almost independent potential wells (in front of and behind the superlattice heterobarrier). For this reason, to simplify the calculations the system of equations (5)–(8) were solved separately for each well, and the coupling equation for the potentials at the SL boundaries was obtained from the solution of Eq. (6) in the region of the SL with $n=0$.

The solution was obtained numerically by an iteration method. This procedure is described in detail in Ref. 8.

After these calculations are completed, it is quite easy to calculate the PL spectrum. The Fermi–Dirac functions with electron and hole quasi-Fermi levels $E_{F,e}=E_F-\delta_e kT$ and $E_{F,n}=E_F-\delta hkT$ for electrons and holes, respectively (E_F is the equilibrium value of the Fermi energy) were taken as the carrier energy distribution functions. It can be shown that $\delta h \gg \delta_e$ in the case $\delta n \ll n$. We can then obtain from the Boltzmann collision integral the following expression for the PL intensity:

$$I(h\nu)=B(e^{\delta_n}-1)$$

$$\times \sum_{i,j} \frac{W_{ij}}{1+m_e/m_h} \frac{\exp\left(-\dfrac{h\nu-E_g}{kT}\right)}{1+\exp\left(\dfrac{E_F-E_e^i-E^{ij}}{kt}\right)} \Theta(E^{ij}/kT), \tag{10}$$

where E_e^i is the energy of the ith quantum-well subband of the 2DEG, $h\nu$ is the energy of the emitted photons,

$$E^{ij}=\frac{h\nu-E_g-E_e^i-E_h^j}{1+m_e/m_h}, \tag{11}$$

E_h^j is the energy of the jth hole quantum-well subband, Θ is the theta function, and W_{ij} is the squared overlap integral of the envelopes of the electron and hole wave functions Ψ_e^i and Ψ_h^j.

It should be noted that, in contrast with the case of wide wells, B in Eq. (10) depends on d_a and d_s. This is due to the fact that the number of electrons and holes trapped in a QW depends on the size of the well and the magnitude of the band bending and, correspondingly, the 2DEG density n_{2d}.[9] For this reason, the expression (10) is admissable, strictly speaking, only for qualitative comparison of the peak intensities of the PL spectrum of MDHSs with different values of d_a or d_s.

3. DISCUSSION

Since the intensity of the PL in wide wells has already been analyzed, here we shall discuss only the results for a QW.

We start with an analysis of undoped HSs. As one can see from Fig. 4, the picture of an ideally square quantum well makes it impossible to explain the experimental dependence $h\nu_0(d_a)$ (curve *1*). Satisfactory agreement between theory and experiment is achieved if the presence of band bending φ_0 is taken into account (Fig. 4, curve *3*). As an exact calculation shows, the magnitude of φ_0 in an undoped HS (with background impurity density $\sim 1\times 10^{14}$ cm^{-3}) equals approximately 20 meV. In this case, the energy of optical transitions can be approximated by the expression

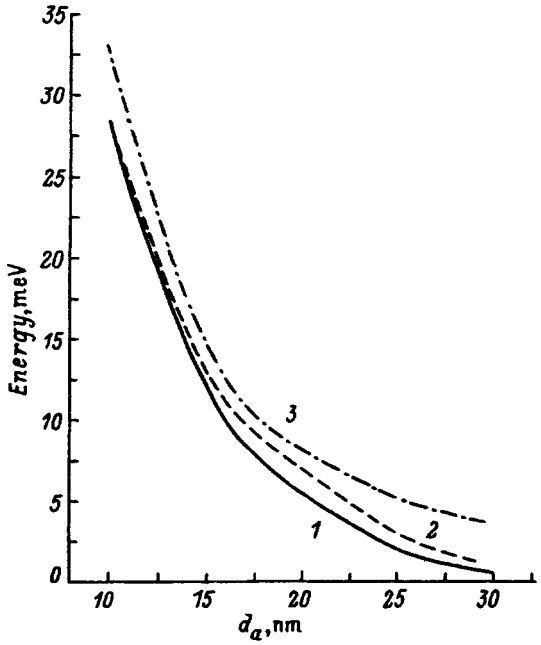

FIG. 4. $E_1^e-E_1^{hh}-E_g$ versus the width of undoped well (*1*—self-consistent calculation, *2*—experiment, *3*—calculation in the square-well model).

$$h\nu_0=E_g+E_e^i+E_h^j-qFd_a, \tag{12}$$

where $E_e^i+E_h^j \sim 1+m_e/m_h/d_a^2$ is the total energy of the bottom electron and hole subbands, and qFd_a is the band-bending potential inside the QW, where F is the effective band-bending electric field.

Since the deviation of the QW from a square shape is not large, the selection rules $W_{ij}\approx 1$ for $i=j$ and $W_{ij}\approx 0$ for $i\neq j$ (for heavy and light holes) hold approximately, as the calculation shows. Since there is no special doping, the population of all subbands $i>1$ should be close to zero. Therefore, only one line corresponding to the optical transition $E_e^1 \rightarrow E_{hh}^1$ should be observed in the PL spectrum of undoped HSs.

For MDHSs, band bending is substantial, $\varphi_0 \approx 80-120$ meV and, correspondingly, the electric field in the QW is strong. This lifts the restriction on the optical transitions between different electron and hole subbands. The high 2DEG density $n_{2d}\sim(6-10)\times 10^{11}$ cm^2 ensures that two bottom electronic subbands, E_e^1 and E_e^2, are filled in most MDHSs. Calculations showed that six types of optical transitions between electronic subbands E_e^1 and E_e^2, on the one hand, and hole subbands E_{lh}^1 and E_{hh}^2, on the other (E_{lh} and E_{hh} are the light- and heavy-hole subbands, respec-

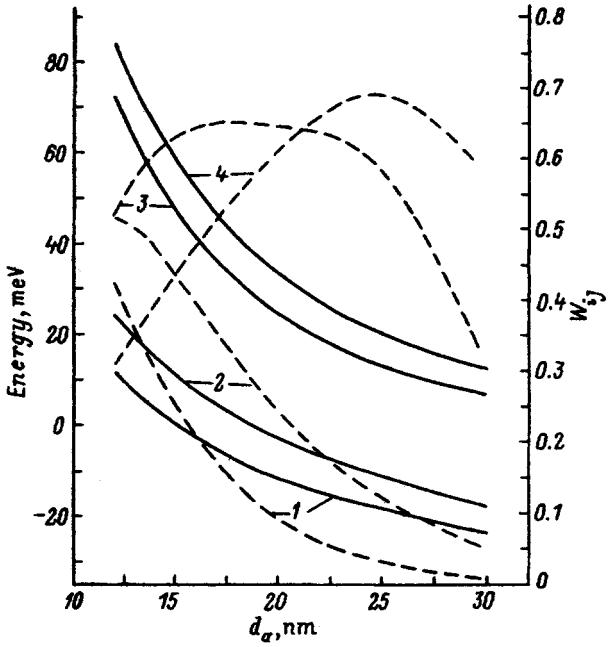

FIG. 5. $E_j^e - E_j^h - E_g$ (solid lines) and squared overlap integrals (dashed lines) versus spacer-layer thickness (transitions: *1*—$1e-1hh$, *2*—$1e-2hh$, *3*—$2e-1hh$, *4*—$2e-1lh$) for $d_s = 10$ nm.

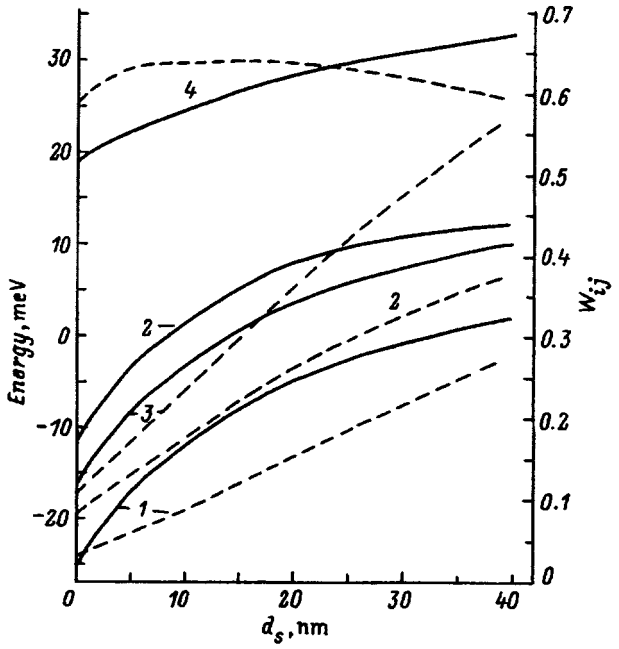

FIG. 6. $E_i^e - E_j^h - E_g$ (solid lines) and squared overlap integrals (dashed lines) versus well width (transitions: *1*—$1e-1hh$, *2*—$1e-2hh$, *3*—$2e-1hh$, *4*—$2e-1lh$) for $d_a = 20$ nm.

tively), can make an appreciable contribution to the doublet structure in the PL spectrum of a MDHS. In addition, the contributions of each depend on d_a and d_s.

The optical transition $E_e^1 \rightarrow E_{hh}^1$ as well as the transitions $E_e^1 \rightarrow E_{hh}^1$ and $E_e^2 \rightarrow E_{hh}^2$ make the main contribution to the low-energy component $h\nu$ of the doublet.

The transitions $E_e^2 \rightarrow E_{lh}^1$ and $E_e^2 \rightarrow E_{hh}^2$ contribute to the high-energy peak at $h\nu_2$; the contribution of the latter transition decreases with decreasing d_a. It should be noted that the peak I_2 should appear only when the E_e^2 subband is appreciably filled with electrons, i.e., when the Fermi level E_F lies either above or slightly below E_e^2 (so that optical pumping would ensure that it is filled).

The experimental and computed PL spectra for $d_a = 20$ nm are shown in Fig. 2. Comparing them shows that the theoretical model explains, at least qualitatively, the shape of the PL spectra, including the spectral position and intensity ratio of the components of the doublet and the character of their variation with decreasing d_s.

The energies and squared overlap integrals computed as functions of d_s for different optical transitions are presented in Fig. 5. In accordance with experiment, here the components of the doublet shift to lower values of $h\nu$ with decreasing d_s. This is due to an increase in the band bending (as a result of an increase in the 2DEG density n_{2d}), which results in a decrease of the effective energy gaps between the electron and hole subbands. The theory also explains the decrease in I_1 and the increase in I_2 and, correspondingly, the increase in the ratio I_2/I_1 with decreasing d_s. In this case, the decrease in I_1 is due to a decrease in the overlap integral of the wave function of the ground state Ψ_e^1 of the 2DEG with the hole wave functions because of the narrowing and ''sharpening'' of the lower part of the quasitriangular well that contains the 2DEG, which decrease the extent of $\Psi_e^1(z)$ in the z direction. The intensity I_2 increases because the population of the state E_e^2 increases as a result of an increase in n_{2d}. At the same time, because of the large extent of the wave function $\Psi_e^2(z)$, its overlap integrals with the hole wave functions are virtually independent of d_s.

The theoretical curves of the energies of optical transitions and the corresponding overlap integrals W_{ij} versus the distance d_a between the heterobarriers are shown in Fig. 6.

According to these results, the observed increase in the intensity of the peak I_1 with decreasing d_a is due to an increase in the overlap integral of the wave function Ψ_e^1 with the wave functions of the bottom heavy- and light-hole subbands. The decrease in the intensity of the peak I_2, which occurs in this case, must be attributed to the decrease in the population of the E_e^2 subband, since the corresponding overlap integrals are virtually independent of d_a. The theory predicts, in agreement with experiment (Fig. 6), that the energies of all optical transitions studied increase with decreasing d_a; here the predicted shift is larger for the $h\nu_2$ peak than for the $h\nu_1$ peak. This results in an increase of the spectral splitting $h\Delta\nu_{12} = h\nu_2 - h\nu_1$ of the doublet. As a result of the rapid increase in the energy E_e^2 relative to the Fermi energy E_F, the population of this subband decreases with d_a.

The results presented demonstrate clear differences in the behavior of the wave functions of the subbands E_e^1 and E_e^2 of the 2DEG. The weaker dependence on d_a of the overlap integrals for optical transitions from the E_e^2 subband than for transitions from the E_e^1 subband and the opposite situation for the d_a dependences of the energies of these subbands are due to differences in the extent of wave functions $\psi_e^2(z)$ and $\Psi_e^1(z)$ in the z direction. It follows from the results obtained that the spatial extent of $\Psi_e^1(z)$ equals about 12–15

nm, while the spatial extent of $\Psi_e^2(z)$ is estimated to be $\sim$30 nm. The small extent of $\Psi_e^1(z)$ is responsible for the weak effect of the approach of the second heterobarrier (for $d_a \geqslant 15$ nm) on the energy of the subband E_e^1, on the one hand, and a strong effect of this heterobarrier on the overlap integral of $\Psi_e^1(z)$ with the hole wave functions, on the other. At the same time, the approach of the second heterobarrier strongly influences the more extended state described by the wave function $\Psi_e^2(z)$, increasing its energy E_e^2 and correspondingly decreasing its population.

In this connection, measurements of the dependence $I_1(d_a)$ can be used to obtain an experimental estimate of the spatial extent of the wave function $\Psi_e^1(z)$ and measurements of I_2 can be used to estimate the population of the E_2^2 subband. The latter makes it possible to use the PL method to investigate the electron distribution over the two-dimensional subbands (this is usually done by means of low-temperature Shubnikov–de Haas measurements), even at high temperatures.

In conclusion, we note that a transition from PL of three-dimensional carriers to PL with the participation of a 2DEG is observed in the PL spectra of double-barrier MDHSs with decreasing distance d_a between the heterobarriers. Near $d_a \approx 40$ nm the $h\nu_0$ line, which corresponds to interband recombination of three-dimensional electrons and holes, in the PL spectrum vanishes and is replaced by a new doublet structure with components at $h\nu_1$ and $h\nu_2$. This PL in MDHSs with different distances d_a and spacer-layer thicknesses d_s was investigated experimentally and were the experimental data were analyzed theoretically on the basis of a self-consistent solution of the Schrödinger and Poisson equations.

It was found that the doublet structure in the PL spectrum is due to optical transitions between the two lowest subbands with a 2DEG E_e^1 and E_e^2 and hole subbands E_{hh}^1, E_{lh}^1, and E_{hh}^2. The relative contributions of each transition depend on d_a and d_s. The observed increase in the intensity ratio I_2/I_1 of the doublet components with decreasing d_s is due to an increase in the populations of the E_e^2 subband, on the one hand, and a decrease in the probability of optical transitions from the subband E_e^1, on the other. The accompanying increase in the band bending gives rise to a shift of all optical transitions in the direction of lower values of $h\nu$ as a result of a decrease in the effective interband gap.

It was found that a decrease in the distance d_s influences differently the spectral position and intensity of the components of the doublet in the PL spectrum. For the $h\nu_2$ peak, a much larger shift is observed in the direction of large $h\nu$ than for the $h\nu_1$ peak. The intensity of the first peak decreases and that of the second peak increases. This behavior is attributable to the large differences in the spatial extent of the wave functions $\Psi_e^1(z)$ and $\Psi_e^2(z)$, which account for the different d_a dependences of the energies of the subbands, of their populations, and of the overlap integrals with the hole wave functions.

The results which we obtained in our study are undoubtedly of interest which we for understanding size-quantization phenomena in a 2DEG and for developing effective methods for diagnostics of the parameters of a 2DEG.

This work was supported by the Ministry of Science of the Russian Federation as part of the program ''Physics of solid-state nanostructures.''

[1] Y. K. Yuan, K. Mohammed, M. A. A. Pudensi., and J. L. Mezz, Appl. Phys. Lett. **45**, 739 (1984).
[2] Zh. I. Alferov, A. M. Vasil'ev, and P. S. Kop'ev, [JETP Lett. **44**, 669 (1986)].
[3] P. D. Altukhov, A. A. Bakun, B. K. Medvevdev, V. G. Mokerov, A. A. Rogachev, and G. P. Rubtsov, Fiz. Tekh. Poluprovodn. **21**, 449 (1987) [Sov. Phys. Semicond. **21**, 279 (1987)].
[4] I. V. Kukushkin, K. V. Klitzing, and K. Ploog, Phys. Rev. B **37**, 8509 (1988).
[5] S. K. Lyo and E. D. Jones, Phys. Rev. B **38**, 4113 (1988).
[6] H. J. Polland, K. Leo, K. Rother, and K. Ploog, Phys. Rev. B **38**, 7635 (1988).
[7] S. Lundqvist and N. March [Eds.], *Theory of Inhomogeneous Electron Gas*, Plenum Press, N. Y., 1983 [Russian translation, Mir, Moscow, 1987].
[8] V. É. Kaminskiĭ, Fiz. Tekh. Poluprovodn. **23**, 662 (1989) [Sov. Phys. Semicond. **23**, 414 (1989)].
[9] V. A. Solov'ev, I. N. Yassievich, and V. M. Chistyakov, Fiz. Tekh. Poluprovodn. **29**, 1264 (1995) [Semiconductors **29**, 654 (1995)].

Translated by M. E. Alferieff

Effect of the spin-orbit interaction on the optical spectra of an acceptor in a semiconductor quantum dot

A. F. Polupanov, V. I. Galiev, and M. G. Novak

Institute of Radio Engineering and Electronics, Russian Academy of Sciences, 103907 Moscow, Russia
(Submitted August 15, 1996; accepted for publication March 20, 1997)
Fiz. Tekh. Poluprovodn. **31**, 1375–1382 (November 1997)

The energy levels and oscillator strengths of optical dipole transitions from the ground state into odd excited states of a shallow acceptor located at the center of a spherical quantum dot are calculated as functions of the spin-orbit splitting Δ of the valence bands for different values of the radius of the dot and ratio β of the heavy- and light-hole effective masses. It is established that the spin-orbit interaction strongly influences some states of the acceptors in the case of real, large values of β and small values of the dot radius. The spin-orbit interaction influences most the lower Γ_6^- state, since it changes from a heavy-hole ($\Delta=0$) to a light-hole ($\Delta=\infty$) state. The problem is solved exactly within the approximations employed, specifically, exact analytic expressions are used for the wave functions of the acceptor. © *1997 American Institute of Physics.* [S1063-7826(97)02211-4]

1. The states of shallow impurities in semiconductor structures with quantum wells and their optical properties have been studied extensively in recent years (see, for example, the review article in Ref. 1). This is attributable to the great interest shown in new structures such as quantum wires and quantum dots and, correspondingly, the need to investigate impurity states in them and attempts to obtain more accurate computational results using more accurate approximations and methods. Starting with the first calculation,[2] the impurity levels for shallow donors and shallow acceptors have been calculated repeatedly in different approximations in the case of impurities located in quasi-two-dimensional quantum wells (see, for example, Refs. 3–6) and in quasi-one-dimensional quantum wires.[7–9] Numerous calculations of the exciton and ''free'' hole energy levels have been performed[10–14] for the case of semiconductor quantum dots or semiconductor microcrystals in a dielectric matrix (we note that in the case of spherical quantum dots with small radii, when the exciton as a whole is quantized, these problems are equivalent; see Ref. 12), and calculations of the states of shallow donors and acceptors in them appeared recently.[9,15–17] It should be noted that in the overwhelming majority of calculations of impurity states in structures with quantum wells only the energies of the ground state and the lowest excited state were calculated. These calculations were performed by a variational method, which possesses well-known deficiencies (specifically, the accuracy of the variational wave functions is unknown). However, in order to identify optical transitions correctly it is necessary to know, in addition to the energy levels, one other very important spectral characteristic—the oscillator strengths of the transitions, which is especially important in the case of nonhydrogen-like impurities.[18] Such impurities (nonhydrogen-like) include, in particular, acceptors in semiconductors with a degenerate valence band: In contrast to the case of hydrogen-like impurities, the oscillator strengths of optical transitions from the ground state of an acceptor vary nonmonotonically with increasing number of the excited level (with decreasing binding energy of the excited states), even for a series of transitions into a state of the same symmetry.[19,16] In Ref. 16, we calculated the energies of the ground state and a number of excited states, as well as the oscillator strengths of optical dipole transitions of shallow donors and acceptors as a function of the radius of a spherical quantum dot by means of a new numerical-analytical method for solving singular, multicomponent, Schrödinger equations.[20,21] This new method made it possible to solve the problem exactly within the approximations employed. In the case of acceptors, the approximation of an infinitely large spin-orbit splitting of the valence bands was used to calculate their optical spectra. This approximation holds well in the case of the calculation of the spectra of acceptors in the volume of many semiconductors, but in the case of a quantum dot, as the radius of the dot decreases, spin-orbit interaction effects between the Γ_8^+ valence band and the spin-orbit split off Γ_7^+ band increase because the kinetic energy of the charge carriers increases. In the present paper we employ the method of Refs. 20 and 21 to investigate the energies of the ground state and a number of excited states, as well as the oscillator strengths of optical dipole transitions of a shallow acceptor located at the center of a spherical quantum dot as a function of the magnitude of the spin-orbit splitting of the valence bands for different values of the radius of the dot and ratio of the heavy- and light-hole effective masses. We shall employ the numerical-analytical method of Refs. 20 and 21, which will make it possible to solve the problem exactly, in particular, to obtain exact analytical expressions for the wave functions of the acceptor.

2. For definiteness, we shall study an acceptor impurity atom located at the center of a spherical semiconductor quantum dot with radius R_0. We shall assume the potential barrier at the boundary of the quantum dot to be infinitely high. In the spherical approximation,[22] the Hamiltonian which approximates the effective mass of the acceptor and which takes into account exactly the finite magnitude of the spin-orbit splitting of the valence bands, can be represented as

$$H=p^2-3\mu(P^{(2)}I^{(2)})+\frac{2}{3}\left(\frac{1}{2}-\mathbf{I}\cdot\mathbf{S}\right)\Delta+\frac{2Z}{r}. \tag{1}$$

Here $\hbar\mathbf{p}$ is the momentum operator, $P^{(2)}$ and $I^{(2)}$ are rank-2 irreducible spherical tensor operators consisting of, like in Ref. 18, the components of the vector $\mathbf{p}$ and the angular momentum vector $\mathbf{I}$ with $I=1$, $\mathbf{S}$ is the spin operator, $\mu=(4\gamma_2+6\gamma_3)/5\gamma_1$ (where γ_i are the Luttinger parameters of the valence band), Δ is the spin-orbit splitting of the valence bands, the energy and distances are measured, respectively, in the units $R_a=m_0e^4/2\hbar\kappa^2\gamma_1$ and $a=\hbar\kappa\gamma_1/m_0e^2$ (where m_0 is the free-electron mass), κ is the static permittivity of the crystal, and Z is the charge of the impurity ion.

We seek the wave function corresponding to the Hamiltonian (1) in the form

$$\Psi=\sum_{JL} R_{LJ}(r)|LJFF_z\rangle, \tag{2}$$

where $|LJFF_z\rangle$ are the known $L-J$ coupling wave functions, F is the quantum number of the total angular momentum $\mathbf{F}=\mathbf{L}+\mathbf{J}$ (where $\mathbf{J}=\mathbf{I}+\mathbf{S}$), and $R_{LJ}(r)$ are the radial wave functions. The quantum number J assumes the values $J_1=3/2$, which corresponds to a degenerate Γ_8^+ valence band, and $J_2=1/2$, which corresponds to the spin-orbit split off Γ_7^+ band. It is obvious that just as in the case $\Delta=\infty$, (Ref. 22), the states of the Hamiltonian (1) are classified according to the values of the total angular momentum $F=1/2,\ 3/2,\ldots$, which is a good quantum number, and in what follows we shall designate them in the manner adopted in the spherical approximation in the limit[22] $\Delta=\infty$. Substituting the expression for the wave function into the Schrödinger equation with the Hamiltonian (1), we obtain the following system of three coupled equations for the radial functions ($F>1/2$):

$$\begin{aligned}
&\left\{\left(1+\frac{1-\beta^2}{1+\beta^2}\mu\right)\left[\frac{d^2}{dr^2}+\frac{2}{r}\frac{d}{dr}-\frac{L_1(L_1+1)}{r^2}\right]\right.\\
&\quad\left.+\frac{2Z}{r}+E\right\}R_{L_1J_1}+\frac{2\beta\mu}{1+\beta^2}\left[\frac{d^2}{dr^2}+\frac{2L_1+5}{r}\frac{d}{dr}\right.\\
&\quad\left.+\frac{(l_1+1)(L_1+3)}{r_2}\right]R_{L_1+2J_1}\\
&\quad+\mu(L_1J_1|P^{(2)}\cdot I^{(2)}|L_2J_2)R_{L_2J_2}=0;\\
&-\frac{2\beta\mu}{1+\beta^2}\left[\frac{d^2}{dr^2}-\frac{2L_1+1}{r}\frac{d}{dr}+\frac{L_1(L_1+2)}{r^2}\right]R_{L_1J_1}\\
&\quad+\mu[(L_1+2)J_1|P^{(2)}\cdot I^{(2)}|L_2J_2]R_{L_2J_2}\\
&\quad+\left\{\left(1+\frac{1-\beta^2}{1+\beta^2}\mu\right)\left[\frac{d^2}{dr^2}+\frac{2}{r}\frac{d}{dr}-\frac{(L_1+2)(L_1+3)}{r^2}\right]\right.\\
&\quad\left.+\frac{2Z}{r}+E\right\}R_{L_1+2,J_1}=0;\\
&-\mu(L_2J_2|P^{(2)}\cdot I^{(2)}|L_1J_1)R_{L_1J_1}-\mu[L_2J_2|P^{(2)}\cdot I^{(2)}|\\
&\quad\times(L_1+2)J_1]R_{L_1+2,J_1}+\left\{\frac{d^2}{dr^2}+\frac{2}{r}\frac{d}{dr}-\frac{L_2(L_2+1)}{r^2}\right.\\
&\quad\left.+\frac{2Z}{r}+E-\Delta\right\}R_{L_2J_2}=0.
\end{aligned} \tag{3}$$

Here $\beta=3^{L_1-F+1}[(F+3/2)/(F-1/2)]^{1/2}$. The matrix elements appearing in these equations are

$$\begin{aligned}
(LJ|P^{(2)}\cdot I^{(2)}|L'J')&=\sqrt{30}(-1)^{F+J+L}\begin{Bmatrix}F & J & L\\ 2 & L' & J'\end{Bmatrix}\\
&\quad\times(L\|P^{(2)}\|L').
\end{aligned} \tag{4}$$

Here the table in the braces is a $6j$-symbol and $(L\|P^{(2)}\|L')$ is a reduced matrix element, which is nonvanishing only for $L=L'$ and $L=L'\pm2$,

$$\begin{aligned}
&(L\|P^{(2)}\|L')=(-1)^{(L'-L)/2}\\
&\times\left(\frac{(L+L'+2)(L+L')(4L+2-|L'-L|)(4+|L'-L|)}{24(L+L'-1+|L'-L|)(4L+6-3|L'-L|)}\right)\\
&\times\left(\frac{d^2}{dr^2}+\frac{[(L'+1/2)(L'-L)+2-|L-L'|]}{r}\right.\\
&\times\left.\frac{d}{dr}+(-1)^{(L'-L)/2}\right.\\
&\times\left.\frac{[4-2|L-L'|-(L'-3L+2)(5L'-L+2)]}{16r^2}\right).
\end{aligned} \tag{5}$$

Just as in the limit of an infinitely large spin-orbit splitting of the valence bands,[22] the case $F=1/2$ must be studied separately. In this case, as follows from the addition rules for angular momentum, the radial equation is a system of two coupled equations. The odd states with $F=1/2$, which are of interest to us, are described by the equations

$$\begin{aligned}
&\left\{(1+\mu)D+\frac{2Z}{r}+E\right\}R_{1J_1}-D\sqrt{2}\mu R_{1J_2}=0,\\
&\left\{D+\frac{2Z}{r}+E-\Delta\right\}R_{1J_2}-D\sqrt{2}\mu R_{1J_1}=0.
\end{aligned} \tag{6}$$

We note that the systems of equations for the radial wave functions, which describe the states of a ''free'' hole in a spherical quantum dot, taking into account the finite magnitude of the spin-orbit splitting, and which are obtained from Eqs. (3) and (6) by setting $Z=0$ in them, were obtained earlier in Ref. 14. However, in Ref. 14 the operator employed in writing these equations was incorrect. The correct form of this operator is

$$A_l^+=\frac{d^2}{dr^2}-\frac{2l+1}{r}\frac{d}{dr}+\frac{l(l+2)}{r^2}.$$

Since we are interested in the dependence of the acceptor states on Δ for all $0\leqslant\Delta\leqslant\infty$, it is interesting to follow the limits $\Delta\to0$ and $\Delta\to\infty$ for the equations describing these states. It is obvious that as $\Delta\to\infty$, the acceptor states are described by the system consisting of the first two equations in (3) and the first equation in (6), where the radial function with the subscript J_2 must be set equal to zero. The equations describing the state of the acceptor with $\Delta=0$ were obtained in Ref. 22 [Eqs. (30a)–(30d)], but here the following remarks must be made. First, in the system (30d) from Ref. 22,

describing the state $\Phi(P_2)$, $\Phi(P_2)=F_3(r)|L=1,\ I=1,\ F=2,\ F_z\rangle+G_3(r)|L=3,\ I=1,\ F=2,\ F_z\rangle$ the relative signs of the radial functions $F_3(r)$ and $G_3(r)$ were not chosen correctly. This does not affect the calculation of the energies but leads to incorrect results in calculation of the matrix elements. The correct equations for these functions are

$$\begin{bmatrix} \left(1+\frac{1}{5}\mu\right)\left(\frac{d^2}{dr^2}+\frac{2}{r}\frac{d}{dr}-\frac{2}{r^2}\right)+\frac{2}{r}+E & -\frac{3}{5}\sqrt{6}\mu\left(\frac{d^2}{dr^2}+\frac{7}{r}\frac{d}{dr}-\frac{8}{r^2}\right) \\ -\frac{3}{5}\sqrt{6}\mu\left(\frac{d^2}{dr^2}-\frac{3}{r}\frac{d}{dr}+\frac{3}{r^2}\right) & \left(1+\frac{4}{5}\mu\right)\left(\frac{d^2}{dr^2}+\frac{2}{r}\frac{d}{dr}-\frac{12}{r^2}\right)+\frac{2}{r}+E \end{bmatrix}\begin{bmatrix} F_3(r) \\ G_3(r) \end{bmatrix}=0. \tag{7}$$

In addition, it is important to note that the spin-orbit interaction removes the degeneracy of some states and as $\Delta\to 0$, the systems of equations (3) and (6) for some different states reduce to identical equations. As $\Delta\to 0$, the systems of coupled radial equations (3) and (6) decouple and reduce, correspondingly, to a system of two equations and one equation and as of two uncoupled equations. As $\Delta\to 0$, Eqs. (3) reduce to the system (7), for the radial functions of the lower state with $F=5/2$, $L_2=L_1+2=3$ $(2P_{5/2})$ and for the first excited state with $F=3/2$, $L_2=L_1=1$ $(3P_{3/2})$. However, Eq. (3), which describes the lower state with $F=3/2$, $L_2=L_1=1$ $(2P_{3/2})$, and Eq. (6), also for the lower state with $F=1$, $L_2=L_1=1$ $(2P_{1/2})$, reduce in the limit $\Delta\to 0$ to the equation

$$\left\{(1-\mu)\left[\frac{d^2}{dr^2}+\frac{2}{r}\frac{d}{dr}-\frac{2}{r^2}\right]+\frac{2}{r}+E\right\}F_2(r)=0, \tag{8}$$

whose solution determines for $\Delta=0$ the radial function for the state $\Phi(P_1)=F_2(r)|L=1,\ I=1,\ F=1,F_z\rangle$.[22]

3. As is obvious from the expressions for the matrix elements (4) and (5), the equation (3) can be represented in the form

$$wr^2\frac{d^2R}{dr^2}+p_0r\frac{dR}{dr}+(q_0+q_1r+q_2r^2)R=0, \tag{9}$$

where w, p_0, and q_i are constant 3×3 matrices, and $R=R(r)$ is a three-component vector function. The most important feature of the problem at hand [just as other problems leading to a solution of equations of the type (9)] is the presence of singular points in the multicomponent radial Schrödinger equation (9). Since we seek the solution of Eq. (3) on a finite interval of variation of r, in our case there is only a regular singular point at $r=0$. A numerical–analytical method for constructing all solutions from the fundamental system of equations of the type (9) was developed in Ref. 21 (where equations of a more general form are studied) for an arbitrary finite dimension of the equations in the case of general matrices w, p_0, and q_i. In our case of simple matrices of coefficients, using the result of Refs. 20 and 21, we can immediately write all solutions from the fundamental system of solutions of Eq. (3).

We define the following sequence of matrices:

$$\Gamma_k(\rho)=w(k+\rho)(k+\rho-1)+p_0(k+\rho)+q_0,$$

$$k=0,\ 1,\ldots \tag{10}$$

Both the behavior of the solutions of Eq. (3) in the limit $r\to 0$ and the structure of the solutions are determined by the roots of the equation[20,21]

$$\det\Gamma_0(\rho)=0. \tag{11}$$

In the case of Hamiltonians which are quadratic in the momentum, the solutions of Eq. (11) are known exactly for any dimension of the system of radial equation (9).[20] In our case of the Hamiltonian (1) the solutions of Eq. (11) and, correspondingly, the form of the solutions of Eqs. (3) are different for the two types of states. Indeed, since the Hamiltonian (1) preserves the quantum number for the total angular momentum and parity (we ignore weak effects associated with the absence of a an inversion center in semiconductors with the zinc blende lattice), and the quantum number J assumes the values $J_1=3/2$ and $J_2=1/2$, for a given value of F and parity the quantum number L_1 equals either $F-3/2$ and then $L_2=L_1+2$ or $F-1/2$ and then $L_2=L_1$. Using this property, which follows simply from the addition rules for angular momentum, and explicit expressions for the matrix elements (4) and (5), it is easy to see that in these two cases Eqs. (3) differ somewhat and they must be studied separately.

a) $L_1=F-3/2$, $L_2=L_1+2$. In this case the operators acting on the functions R_{L_1+2,J_1} and $R_{L_2J_2}$ which determine the behavior of the functions in a neighborhood of $r=0$, i.e., operators of the form

$$P_L(r)\equiv\frac{d^2}{dr^2}+\frac{a_L}{r}\frac{d}{dr}+\frac{b_L}{r^2}, \tag{12}$$

are identical to within a constant. The nonnegative solutions of Eq. (11), which correspond to solutions of Eq. (3) that are regular at $r=0$, will then be $\rho_1=\rho_2=L_1+2$, $\rho_3=L_1$, and the solutions of Eq. (3) will have the form

$$R^{(1)}=r^{\rho_1}\sum_{k=0}^{\infty}R_k^{(1)}r^k,\quad R^{(2)}=r^{\rho_2}\sum_{k=0}^{\infty}R_k^{(2)}r^k,$$

$$R^{(3)}=r^{\rho_3}\sum_{k=0}^{\infty}R_k^{(3)}r^k+(K_1R^{(1)}+K_2R^{(2)})\ln r, \tag{13}$$

where the coefficients $R_k^{(i)}$ and the constants $K_{1,2}$ are determined from the recurrence relations

$$\Gamma_0(\rho_1)R_0^{1,2}=0,$$

$$\Gamma_k(\rho_1)R_k^{1,2}+q_1R_{k-1}^{1,2}+q_2R_{k-2}^{1,2}=0,$$

$$k=1,2,\ldots(R_l=0,l<0); \tag{14a}$$

$$\Gamma_0(\rho_3)R_0^{(3)}=0,$$

$$\Gamma_1(\rho_3)R_1^{(3)}+q_1R_0^{(3)}=0,$$

$$\Gamma_k(\rho_3)R_k^{(3)}+q_1R_{k-1}^{(3)}+q_2R_{k-2}^{(3)}+\{2(\rho_3+k)+q_0-1\}\times(K_1R_{k-\rho_1+\rho_3}^{(1)}+K_2R_{k-\rho_1+\rho_3}^{(2)})=0,\quad k\geqslant 1. \tag{14b}$$

We note that the recurrence relations for the coefficients $R_k^{(1)}$ and $R_k^{(2)}$ are identical but the solutions $R_0^{(1,2)}$ of the first equation in (14a) are chosen to be linearly independent.

b) $L_1=F-1/2$, $L_2=L_1$. In this case the operators (12) acting on $R_{L_1J_1}$ and $R_{L_2J_2}$ are identical to within a constant. The solutions of Eq. (3) that are regular at $r=0$ correspond to the roots of Eq. (11) $\rho_1=L_1+2$, $\rho_2=\rho_3=L_1$, and the solutions have the form

$$R^{(1)}=r^{\rho_1}\sum_{k=0}^{\infty}R_k^{(1)}r^k,$$

$$R^{(2)}=r^{\rho_2}\sum_{k=0}^{\infty}R_k^{(2)}r^k+(K_2R^{(1)})\ln r,$$

$$R^{(3)}=r^{\rho_3}\sum_{k=0}^{\infty}R_k^{(3)}r^k+(K_3R^{(1)})\ln r, \tag{15}$$

where the coefficients $R_k^{(i)}$ and constants $K_{2,3}$ are determined from the recurrence relations

$$\Gamma_0(\rho_1)R_0^{(1)}=0,$$

$$\Gamma_k(\rho_1)R_k^{(1)}+q_1R_{k-1}^{(1)}+q_2R_{k-2}^{(1)}=0,$$

$$k=1,2,\ldots(R_l=0,l<0); \tag{16a}$$

$$\Gamma_0(\rho_3)R_0^{(2,3)}=0,$$

$$\Gamma_1(\rho_3)R_1^{(2,3)}+q_1R_0^{(2,3)}=0,$$

$$\Gamma_k(\rho_3)R_k^{(2,3)}+q_1R_{k-1}^{(2,3)}+q_2R_{k-2}^{(2,3)}+\{2(\rho_3+k)+q_0-1\}K_{2,3}R_{k-\rho_2+\rho_3}^{(1)}=0,\quad k\geqslant 1. \tag{16b}$$

We see that the recurrence relations for the coefficients $R_k^{(2)}$ and $R_k^{(3)}$ are identical, but the solutions of the first equation in (16b) for $R_0^{(2,3)}$ are chosen to be linearly independent.

It is obvious that Eq. (6) can also be represented in the form (9) with the corresponding 2×2 matrices, but its solutions differ from those obtained in Ref. 16. Since in this case Eq. (11) has degenerate roots that are regular at $r=0$, the solutions of Eqs. (6) do not contain a logarithmic function and have the form

$$R^{(1)}=r^{\rho_1}\sum_{k=0}^{\infty}R_k^{(1)}r^k,\quad R^{(2)}=r^{\rho_2}\sum_{k=0}^{\infty}R_k^{(2)}r^k, \tag{17}$$

where $\rho_1=\rho_2=1$. The coefficients $R_k^{(1,2)}$ are determined from the recurrence relations

$$\Gamma_0(\rho_1)R_0^{(1,2)}=0,$$

$$\Gamma_k(\rho_1)R_k^{(1,2)}+q_1R_{k-1}^{(1,2)}+q_2R_{k-2}^{(1,2)}=0,$$

$$k=1,2,\ldots(R_l=0,l<0), \tag{18}$$

where two linearly independent solutions of the first equation in (18) are chosen.

As we have proved in Ref. 21, the power series in Eqs. (13), (15), and (17) have an infinite convergence radius. Therefore, the expressions (13)–(18) completely determine the wave functions of all states of the Hamiltonian (1) both in the volume of the semiconductor (see Ref. 20) and in the quantum dot, and to calculate the energies of the levels and the wave functions of the acceptor it is only necessary to satisfy the corresponding boundary conditions. We note that these expressions determine the acceptor wave functions not only in a spherical approximation, but also when account is taken of the irregularities of the valence bands to first order in the ''irregularity'' parameter $\delta=(\gamma_3-\gamma_2)/\gamma_1$, to which the terms of cubic symmetry, which are added to Eq. (1) when the cubic symmetry is taken into account, are proportional.[18,22] Indeed, in this approximation the irregularities have no effect at all on states with $F<5/2$ and lead to splitting of states with $F=5/2$ (since dipole transitions from the ground state into states with $F>5/2$ are forbidden,[18] we shall not consider them). The wave functions are now characterized according to one of the representations $\Gamma=\Gamma_8^{\pm}$, $\Gamma_7^{\pm}$, and $\Gamma_6^{\pm}$ of the group $T_d\times C_i$ of the Hamiltonian and the state $2P_{5/2}$ of interest to us splits into the states $2\Gamma_8^-$ and $1\Gamma_7^-$. However, the equations for the radial functions of these states have the previous form (3) except with different

TABLE I. Energy levels E and oscillator strengths f of optical transitions from the ground state into excited states of a shallow acceptor in a quantum dot as a function of the spin-orbit splitting Δ. $\mu=0.8$, $R_0=3$.

Δ	$E(Z=0)$	$E(1S_{3/2})$	$E(2P_{3/2})$	f	$E(3P_{3/2})$	f	$E(2P_{5/2})$	f	$E(2P_{1/2})$	f
0	0.449	−3.22	−1.25	0.041	−0.663	1.75	−0.663	15.8	−1.25	0.008
0.1	0.464	−3.21	−1.23	0.065	−0.607	1.79	−0.646	15.8	−1.18	0.020
0.5	0.511	−3.17	−1.19	0.151	−0.371	2.53	−0.595	15.8	−0.921	0.126
1	0.548	−3.12	−1.17	0.217	−0.255	2.52	−0.558	15.7	−0.608	0.390
2	0.592	−3.05	−1.14	0.265	−0.205	2.31	−0.520	15.9	−0.028	1.54
3	0.616	−3.00	−1.13	0.274	−0.177	2.34	−0.502	16.2	0.476	2.95
5	0.644	−2.92	−1.12	0.269	−0.147	2.42	−0.485	16.9	1.22	6.91
10	0.672	−2.81	−1.11	0.245	−0.117	2.56	−0.469	18.1	2.01	13.2
∞	0.677	−2.57	−1.10	0.21	−0.073	2.90	−0.450	20.5	2.78	21.3

TABLE II. Energy levels E and oscillator strengths f of optical transitions from the ground state into excited states of a shallow acceptor in a quantum dot as a function of the spin-orbit splitting Δ. $\mu=0.8$, $R_0=1$.

Δ	$E(Z=0)$	$E(1S_{3/2})$	$E(2P_{3/2})$	f	$E(3P_{3/2})$	f	$E(2P_{5/2})$	f	$E(2P_{1/2})$	f
0	4.04	−1.52	0.076	1×10^{-4}	4.76	1.79	4.76	16.1	0.076	2×10^{-5}
1	4.19	−1.42	0.228	3×10^{-6}	5.30	2.50	4.92	16.2	0.738	0.015
5	4.64	−1.16	0.639	0.001	6.79	7.26	5.15	16.5	3.29	0.479
10	4.99	−0.999	0.927	0.004	7.31	8.30	5.24	17.1	6.27	1.85
20	5.38	−0.854	1.23	0.010	7.72	8.65	5.29	17.8	11.4	6.20
50	5.84	−0.720	1.55	0.023	8.15	9.09	5.32	18.5	21.0	21.4
100	6.08	−0.659	1.72	0.034	8.37	9.33	5.33	18.8	26.8	34.0
∞	6.09	−0.58	1.95	0.05	8.69	9.66	5.35	19.1	32.6	45.8

constant coefficients in front of operators of the type (12), and just as for the $2P_{5/2}$ state their solutions are given by Eqs. (13) and (14).

In the case of an acceptor in a quantum dot, the boundary conditions must be satisfied at $r=R_0$, i.e., it is necessary to find energies E and linear combinations of solutions such that $R|_{r=R_0}=0$. This is most conveniently done as follows. We construct from the solutions (13) or (15) (depending on the state of interest) at the point R_0 a 3×3 matrix A

$$A(E)=(R^{(1)},R^{(2)},R^{(3)})_{r=R_0}.$$

Then the procedure for calculating the energies of the levels in some interval $[E',E'']$ reduces to solving the equation $\det A(E)=0$ numerically by ''ranging.'' If for some $E=E_0$ the condition $\det A(E_0)=0$ holds, then

$$(R^{(1)})_{r=R_0}=\alpha_1(R^{(2)})_{r=R_0}+\alpha_2(R^{(3)})_{r=R_0},$$

where the constants $\alpha_{1,2}$ correspond to the eigenvalue E_0. Then the normalized solution, which corresponds to this energy and which satisfied the boundary conditions will have the form

$$\varphi(r)=C(R^{(1)}-\alpha_1R^{(2)}-\alpha_2R^{(3)}),$$

and the constant C is determined from the normalization condition

$$\int_0^{R_0}(\varphi^T\varphi)dr=1.$$

We note that in this approach the calculation of the energy levels and wave functions of a ''free'' hole in a quantum dot, i.e., a hole in the absence of an acceptor in the well, is comlpetely analogous. We now must set $Z=0$ in Eq. (3). The expressions (13)–(18), as before, are exact solutions of Eqs. (3) and the coefficients in front of the logarithmic terms in Eqs. (13) and (15) vanish—they are proportional to Z.[20]

4. Knowing the wave functions of the acceptor, it is easy to calculate the oscillator strengths of the transitions between impurities. Since the system under study is spherically symmetric, the oscillator strengths of the optical dipole transitions between the bound states a and b of the acceptor in a quantum dot are given by the standard expression valid in the volume of the semiconductor:[23]

$$f(a\to b)=\frac{2m_0}{\hbar^2\gamma_1}\frac{E_b-E_a}{g_a}\sum_{m=1}^{g_a}\sum_{n=1}^{g_b}|(\mathbf{e}\cdot\mathbf{r})_{\mathbf{mn}}|^2. \qquad (19)$$

Here E_a, E_b and g_a, g_b are, respectively, the energies and degeneracies of the levels a and b, and $\mathbf{e}$ is a unit polarization vector of the radiation. The coefficient in front of the double sum in Eq. (19) is determined by the sum rule for oscillator strengths for acceptor impurities, which depends only on the single Luttinger parameter γ_1[23,18] and equals 1, if energy and distances are measured, respectively, in the units R_a and a, just as in Eq. (1). Then, substituting into Eq. (19) the expression (2) for the wave functions and applying the Wigner–Eckart theorem and the orthogonality of the $3j$ symbols, we obtain

$$f(a\to b)=\frac{E_b-E_a}{3g_a}\left\{\sum_{JL}(L_aJ_aF_a\|r\|L_bJ_bF_b)\right\}^2, \qquad (20)$$

where the reduced matrix element is

TABLE III. Energy levels E and oscillator strengths f of optical transitions from the ground state into excited states of a shallow acceptor in a quantum dot as a function of the spin-orbit splitting Δ. $\mu=0.5$, $R_0=3$.

Δ	$E(Z=0)$	$E(1S_{3/2})$	$E(2P_{3/2})$	f	$E(3P_{3/2})$	f	$E(2P_{5/2})$	f	$E(2P_{1/2})$	f
0	1.03	−1.35	−0.222	3.20	0.621	4.32	0.621	38.9	−0.222	0.640
0.1	1.03	−1.34	−0.207	3.46	0.692	4.09	0.629	39.0	−0.156	0.826
0.5	1.04	−1.33	−0.165	4.19	0.989	3.56	0.654	39.4	0.095	1.83
1	1.04	−1.31	−0.136	4.67	1.35	3.85	0.675	40.0	0.377	3.673
2	1.04	−1.29	−0.108	5.06	1.71	4.72	0.701	40.8	0.829	8.77
3	1.04	−1.28	−0.095	5.20	1.75	4.06	0.715	41.5	1.14	14.3
5	1.05	−1.26	−0.081	5.30	1.78	3.70	0.730	42.4	1.50	22.6
10	1.05	1.23	0.069	3.32	1.79	3.48	0.746	43.6	1.81	30.7
∞	1.05	−1.19	−0.054	5.3	1.81	3.22	0.76	45.6	2.10	37.7

TABLE IV. Energy levels E and oscillator strengths f of optical transitions from the ground state into excited states of a shallow acceptor in a quantum dot as a function of the spin-orbit splitting Δ. $\mu=0.5$, $R_0=1$.

Δ	$E(Z=0)$	$E(1S_{3/2})$	$E(2P_{3/2})$	f	$E(3P_{3/2})$	f	$E(2P_{5/2})$	f	$E(2P_{1/2})$	f
0	9.29	3.49	6.30	2.85	14.6	4.36	14.6	39.3	6.30	0.570
1	9.30	3.51	6.46	3.13	15.3	4.04	14.7	39.6	6.96	0.830
5	9.34	3.58	6.87	3.92	18.3	3.23	14.9	40.5	9.46	2.33
10	9.36	3.63	7.16	4.43	21.8	3.01	15.0	41.2	12.2	5.12
20	9.38	3.69	7.43	4.87	24.7	2.33	15.1	42.1	16.3	12.3
50	9.41	3.76	7.70	5.20	25.2	1.66	15.3	43.1	22.0	28.2
100	9.42	3.79	7.82	5.32	25.4	1.54	15.4	43.6	24.3	35.9
∞	9.44	3.84	7.98	5.4	25.4	1.46	15.4	44.3	26.6	41.9

$$(L_aJ_aF_a\|r\|L_bJ_bF_b)=\delta_{J_aJ_b}(-1)^{F_b+J+L_a+1}[(2F_a+1)\times(2F_b+1)]^{1/2}\begin{Bmatrix} L_b & J & F_b \\ F_a & 1 & L_a \end{Bmatrix}\times(L_a\|r\|L_b). \quad (21)$$

Since some different excited states become degenerate (they are described by identical equations; see Sec. 2) in the limit $\Delta\to 0$, it is interesting to determine how the oscillator strength, which corresponds at $\Delta=0$ to a transition into a given degenerate state, is distributed between transitions into the excited states which make up the oscillator strength in the limit $\Delta\to 0$. A direct calculation from Eqs. (20) and (21) shows that the oscillator strength of a transition from the ground state ($1S_1$ in the notation of Ref. 22, $\Delta=0$) into the excited state $2P_1$ is divided between the transitions $1S_{3/2}(1\Gamma_8^+)\to 2P_{3/2}(1\Gamma_8^-)$ and $1S_{3/2}(1\Gamma_8^+)\to 2P_{1/2}(1\Gamma_6^-)$ as $\Delta\to 0$ in the ratio 5:1, and the oscillator strength of the transition into the state $2P_2$ is divided between the transitions $1S_{3/2}(1\Gamma_8^+)\to 2P_{5/2}(2\Gamma_8^-+1\Gamma_7^-)$ and $1S_{3/2}(1\Gamma_8^+)\to 3P_{3/2}(3\Gamma_8^-)$ in the ratio 9:1. Here the symbols in parentheses designate the states into which the given states transfer when the irregularities are taken into account.

5. The computational results for the energy levels and oscillator strengths of optical dipole transitions from the ground state into odd excited states of a shallow acceptor in a spherical quantum dot as a function of the spin-orbit splitting Δ of the valence bands are presented in Tables I–IV. The Δ-dependence of the energy E $(Z=0)$ of the lower level of a free hole is also presented here (second column in the tables). In the tables, the energies are indicated in units of R_a and oscillator strength in units of 10^{-2}. We have calculated these quantities for different values of the radius of the dot and the parameter μ. This makes it possible to estimate them for acceptors in quantum dots consisting of different materials. Indeed, in a spherical approximation the parameters μ and Δ in dimensionless units completely characterize the valence band of the semiconductor; this is evident from, in particular, Eqs. (1) and (3). It should be noted that the ratio β of the heavy- and light-hole effective masses (Γ_8^+ band) is expressed only in terms of μ: $\beta=(1+\mu)/(1-\mu)$. The tables give the most interesting computational results for $\mu=0.8$ and 0.5, which are characteristic of many semiconductors, and $R_0=1.3$. The corresponding data obtained in the limit $\Delta=\infty$ in Ref. 16 are also presented here. The states in the tables are designated in the manner adopted in the spherical approximation.[22] It should be noted that, as shown in Ref. 14, in small-radius quantum dots in the case of large β and sufficiently small Δ inversion of the order of the s- and p-type free-hole states can occur. Indeed, in our calculation with $\mu=0.8$ in a quantum dot with radius $R_0=3$ and $0\leqslant\Delta\leqslant 12$ and in a dot with radius $R_0=1$ and $0\leqslant\Delta\leqslant 103$, the bottom quantum-well level of a free hole is the state $P_{3/2}$, while for large Δ and in the case $\mu=0.5$ for all $0\leqslant\Delta\leqslant\infty$ the bottom quantum-well level is the state $S_{3/2}$. Inversion of the acceptor states does not occur for any of the parameters investigated, as is evident from the tables and from the figure, which shows the computational results for the energies of the lower levels of a free hole and acceptor levels as a function of the squared reciprocal of the radius of a quantum dot for the ''critical'' values $\Delta=0$ and $\mu=0.8$, when inversion of the order of s-p type hole states occurs for all finite dot radii. It is evident from the tables that the ratios obtained above (Sec. 4) between the oscillator strengths in the limit $\Delta\to 0$ hold exactly in the numerical calculation. It is also evident that the energies of both the ground state and a number of the excited states of the acceptor are virtually independent of Δ even for small radii of a quantum dot, but in this case the oscillator strengths of the transitions can change substantially—by several orders of magnitude. The computational results show that the spin-orbit interaction most strongly affects the energy spectra and oscillator

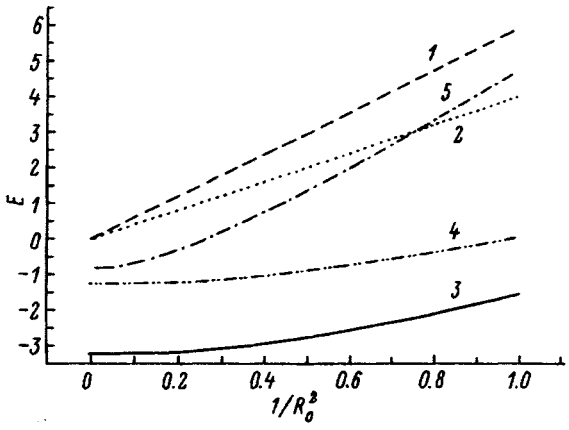

FIG. 1. Energies E of the lower levels of a free hole and acceptor as a function of the squared reciprocal of the radius R_0 of the quantum dot. $\mu=0.8$, $\Delta=0$. *1*—$S_1(Z=0)$, *2*—$P_1(Z=0)$, *3*—$1S_1$, *4*—$2P_1$, *5*—$2P_2$. The energy E is given in units of R_0 and the radius R_0 of the quantum dot is given in units of a.

strengths of optical transitions for large values of β and small dot radii. It is obvious that for small β, i.e., in the limit $\mu \to 0$, the acceptor states no longer depend on Δ—this is easy to see from Eqs. (3) and (6). The spin-orbit interaction affects most strongly the energy and oscillator strength of a transition into the lower Γ_6^- state (designated as $2P_{1/2}$ in the spherical approximation), since its character changes from heavy-hole (for $\Delta = 0$) to light-hole (for $\Delta = \infty$). Indeed, as one can see from Eqs. (6) and (8), in the spherical approximation and in first order of perturbation theory in the parameter δ, to which terms describing the irregularities of the valence bands are proportional, the corresponding equation has in these limits a purely 'hydrogen-like'' form with $L = 1$ and strongly different masses, proportional to $1/(1-\mu)$ and $1/(1+\mu)$, respectively. This is why for small quantum-dot radii the approximation of infinitely large spin-orbit splitting of valence bands, which is widely used in calculations, becomes applicable for these states only for very large Δ.

This work was supported in part by the Russian Fund for Fundamental Research.

[1] S. Fraizzoli and A. Pasquarello, Physica Scripta T **39**, 182 (1991).
[2] G. Bastard, Phys. Rev. B **24**, 4714 (1981).
[3] C. Mailhiot, Y.-C. Chang, and T. C. McGill, Phys. Rev. B **26**, 4449 (1982).
[4] R. L. Green and K. K. Bajaj, Phys. Rev. B **34**, 961 (1986).
[5] W. T. Masselink, Y.-C. Chang, and H. Morkoc, Phys. Rev. B **32**, 5190 (1985).
[6] S. Fraizzoli and A. Pasquarello, Phys. Rev. B **44**, 1118 (1991).
[7] G. W. Bryant, Phys. Rev. B **29**, 6632 (1984).
[8] J. Lee and H. N. Spector, J. Vac. Sci. Technol. B **16** (1984).
[9] D. S. Chuu, C. M. Hsiao, and W. N. Mei, Phys. Rev. B **46**, 3898 (1992).
[10] Al. L. Éfros and A. L. Éfros, Fiz. Tekh. Poluprovodn. **16**, 1209 (1982) [Sov. Phys. Semicond. **16**, 772 (1982)].
[11] L. E. Brus, J. Chem. Phys. **80**, 4403 (1984).
[12] A. I. Ekimov, A. A. Onushchenko, A. G. Plyukhin, and Al. L. Éfros, Zh. Éksp. Teor. Fiz. **88**, 1490 (1985) [Sov. Phys. JETP **61**, 891 (1985)].
[13] M. Sweeny and J. Xu, Solid State Commun. **72**, 301 (1989).
[14] G. B. Grigoryan, É. M. Kazaryan, Al. L. Éfros, and T. V. Yazeva, Fiz. Tverd. Tela (Leningrad) **32**, 1772 (1990) [Sov. Phys. Solid State **32**, 1031 (1990)].
[15] J.-L. Zhu, Phys. Rev. B **39**, 8780 (1989); J.-L. Zhu, J.-J. Xiong, B.-L. Gu. Phys. Rev. B **41**, 6001 (1990).
[16] V. I. Galiev and A. F. Polupanov, Fiz. Tekh. Poluprovodn. **27**, 1202 (1993) [Semiconductors **27**, 663 (1993)].
[17] J.-L. Zhu and X. Chen, J. Phys.: Condens. Matter **6**, L123 (1994).
[18] Sh. M. Kogan and A. F. Polupanov, Zh. Éksp. Teor. Fiz. **80**, 394 (1981) [Sov. Phys. JETP **53**, 201 (1981)].
[19] A. F. Polupanov and Sh. M. Kogan, Fiz. Tekh. Poluprovodn. **13**, 2338 (1979) [Sov. Phys. Semicond. **13**, 1368 (1979)].
[20] V. I. Galiev and A. F. Polupanov, Preprint N 18(519), Institute of Radio Electronics of the Soviet Academy of Sciences, Moscow, 1989.
[21] V. I. Galiev, A. F. Polupanov, and I. E. Shparlinski, J. Comput. Appl. Math. **39**, 151 (1992).
[22] A. Baldereschi and N. O. Lipari, Phys. Rev. B **8**, 1525 (1973); Phys. Rev. B **9**, 1525 (1974).
[23] Sh. M. Kogan and A. F. Polupanov, Solid State Commun. **27**, 1281 (1978).

Translated by M. E. Alferieff

Photoluminescence of porous gallium arsenide

D. N. Goryachev and O. M. Sreseli

A. F. Ioffe Physicotechnical Institute, Russian Academy of Sciences, 194021 St. Petersburg, Russia
(Submitted June 10, 1997; accepted for publication June 11, 1997)
Fiz. Tekh. Poluprovodn. **31**, 1383–1386 (November 1997)

Photoluminescence in the visible and infrared regions of the spectrum is investigated for porous gallium arsenide prepared by the electrolytic or chemical etching of GaAs. The IR luminescence band of porous GaAs is shifted from the maximum for crystalline GaAs into the long-wavelength region of the spectrum and has a greater width. All the samples are characterized by a broad emission band in the visible region; the intensity and shape of the band depend on the layer preparation conditions. Two maxima are discernible in the band in the vicinity of 420 nm and 560 nm. An explanation is given for both the visible luminescence and the modification of the IR band of porous GaAs. It is concluded from a comparison of the visible luminescence of porous GaAs with emission from hydrated oxides of arsenic and gallium that the visible-range luminescence of porous GaAs, especially when prepared by chemical etching, is determined in large measure by the presence of oxides. Considerations are set forth as to ways of creating quantum-size formations on the surface of GaAs. © *1997 American Institute of Physics.* [S1063-7826(97)02511-8]

INTRODUCTION

The escalation of research on the photoluminescence properties of porous silicon (*por*-Si) in recent years, beginning with the work of Canham,[1] holds encouraging prospects for many investigators seeking an inexpensive, relatively simple, and ultimately a universal technique for the preparation of low-dimensional semiconductor materials. The role of quantum-well effects in the evolution of at least part of the photoluminescence spectrum was in fact first demonstrated in the example of *por*-Si. More recently, attempts have been undertaken to create similar porous layers by electrolytic etching on binary and more complex materials: GaAs, GaP, etc.[2–5] We have not found any published data on attempts to form similar structures by chemical etching, which is also used extensively for the preparation of *por*-Si.

Existing accounts of research on the photoluminescence spectra of porous layers on GaAs are highly conflicting. For example, Schmuki *et al.*[3] report a slight short-wavelength shift of the infrared maximum of porous GaAs (*por*-GaAs), whereas Lebedev and Rud'[4] deny the existence of such a shift. Substantial disparities are observed in the positions of the visible photoluminescence maximum (Fig. 1). Finally, nothing is really known about the nature of visible photoluminescence. In principle, it can be characterized either as quantum-well effects or as the presence of new chemical compounds on the sample surface.

We have investigated the photoluminescence of surface layers formed by electrolytic and by chemical etching of GaAs.

EXPERIMENTAL CONDITIONS

Electrolytic anodic etching of *n*-type GaAs(100) with carrier densities from 1×10^{16} cm^{-3} to 8×10^{18} cm^{-3} was performed either in a 1.0 N HCl solution or in a 40% HF solution with a 1% HNO_3 additive. In some of the experiments the samples were illuminated by white light from an incandescent lamp. For the chemical etching of *p*-type and *n*-type GaAs with $n,p=10^{16}$–10^{19}cm^{-3}, 65% HNO_3 was used, in some cases with concentrated H_2SO_4 additives to bind water or acetic acid as a means of slowing down the etching process. After etching, the samples were carefully washed in water and air-dried at 30–40 °C.

Photoluminescence was stimulated by laser pulses of wavelength $\lambda=337$ nm, duration 10 ns, and frequency 100 Hz. The photoluminescence spectra were measured at room temperature by means of a computerized system using an MDR-2 monochromator. The radiation detectors were photomultipliers of the type FÉU-79 (visible range of the spectrum) and FÉU-62 (IR range).

EXPERIMENTAL RESULTS AND DISCUSSION

In the electrolytic etching of *n*-type GaAs ($n=1.4\times10^{18}$ cm^{-3}) in HCl solutions, beginning with a current density $J\approx5$ mA/cm^2, a dark, dense film forms on the surface of the sample, firmly bonding with the substrate. At higher current densities the layer breaks up and disperses into a fine powder even while electrolysis is still in progress. The replacement of the solvent (water) by an alcohol-water mixture (1:1) lowers the ''dispersal'' current threshold by roughly one half.

Instead of a thick layer, only inhomogeneous thin films form on *n*-GaAs with $n=1\times10^{16}$ cm^{-3} over a wide range of current densities in darkness.

An electrolyte composition containing $HF+HNO_3$ forms a thin, dark film on the surface of GaAs only a few seconds after immersion of the sample in the solution at zero current, i.e., the electrolyte acts as a chemical etchant. Sub-

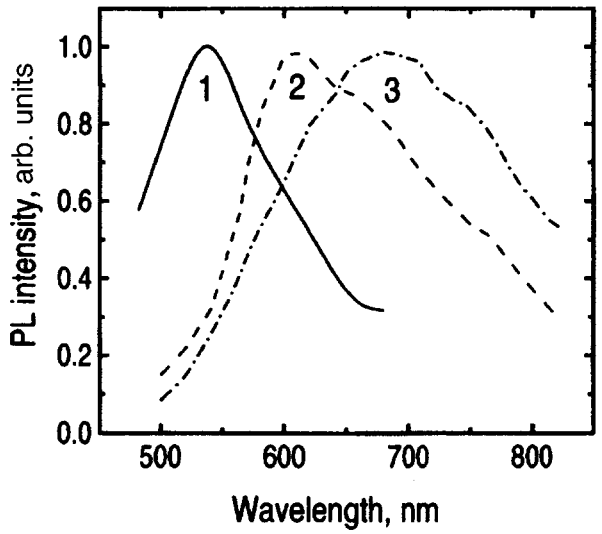

FIG. 1. Visible photoluminescence (PL) spectra of *por*-GaAs. *1*) From Ref. 3; *2–3*) from Ref. 4 (different samples).

sequent electrolysis in this medium produces thick *por*-GaAs layers as in the case of electrolysis in HCl solutions.

Finally, chemical etching results in the formation of homogeneous, thin, dark layers, whose thickness is essentially independent of the etch time. All the prepared layers are characterized by the presence of photoluminescence in the IR region of the spectrum, near the emission band of the substrate. The same IR emission band is observed in the spectra of free (detached from any substrate) films and in powdered *por*-GaAs. These observations, together with published results of x-ray and microscope examinations,[2] indicate that the layers obtained by electrolytic etching are porous formations consisting mainly of GaAs. For all the layers grown on substrates with $n=10^{16}$ cm^{-3} the IR peak is observed to shift into the long-wavelength region of the spectrum, and the photoluminescence band broadens (Fig. 2a). The same shift of the peak, but without broadening of the band, is observed for samples with $n=10^{18}$ cm^{-3} (Fig. 2b). All the *por*-GaAs samples exhibit photoluminescence in the visible region of the spectrum (Fig. 3a). The intensity and shape of the band depend on the conditions of preparation of the layers. The ''chemical'' layers, despite their thinness, have the highest intensity. Their photoluminescence occurs predominantly in the IR region of the spectrum (Fig. 3a, curve *1*). The ''electrolytic'' layers are characterized by a double-humped curve with a more pronounced short-wavelength maximum (Fig. 3a, curves *2* and *3*).

In analyzing the nature of the photoluminescence of *por*-GaAs, it is essential to bear in mind that the etching of binary semiconductors is a far more complicated process than the etching of simple substances, especially silicon. This difficulty stems from the very high degree of ionicity of the lattices of binary semiconductors and from the difference in the rates at which two different semiconductor components enter into solution. As a result, the surface of the sample is enriched with a preponderance of one element, usually in hydrated oxide form. The degree of enrichment depends on the composition of the etchant and, in the case of electrolytic etching, on the electrolysis regime as well. It is also possible for oxides to form during the sample washing and drying stage. The physicochemical properties of such formations differ from those of the untreated semiconductor. Consequently, the luminescence characteristics of its surface can also change.

To discern the nature of the possible influence of oxides on the visible photoluminescence of *por*-GaAs, we have measured the photoluminescence spectra of hydrated arsenic and gallium oxides prepared by chemical means not on the surface of GaAs (Fig. 3b, curves *4* and *5*, respectively). The spectral intensities observed here are very similar to the visible photoluminescence bands of *por*-GaAs. The following conclusions can be drawn from a comparison of these curves with the spectra of *por*-GaAs layers prepared by diverse methods. The photoluminescence of chemical layers is determined in large measure by the presence of gallium oxide on their surface, consistent with well-documented data which show that predominantly gallium oxide is formed on the surface of GaAs subjected to chemical etching in strong HNO_3 solutions.[6] The surface oxidation of *por*-GaAs in electrolytic

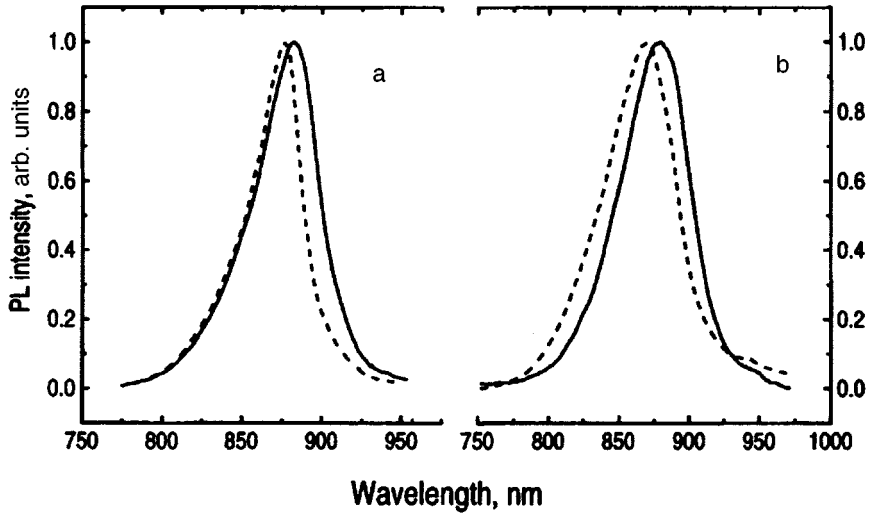

FIG. 2. Infrared photoluminescence spectra of as-prepared GaAs (dashed curves) and *por*-GaAs (solid curves). a) $n=1\times10^{16}$ cm^{-3}; b) $n=1.4\times10^{18}$ cm^{-3}.

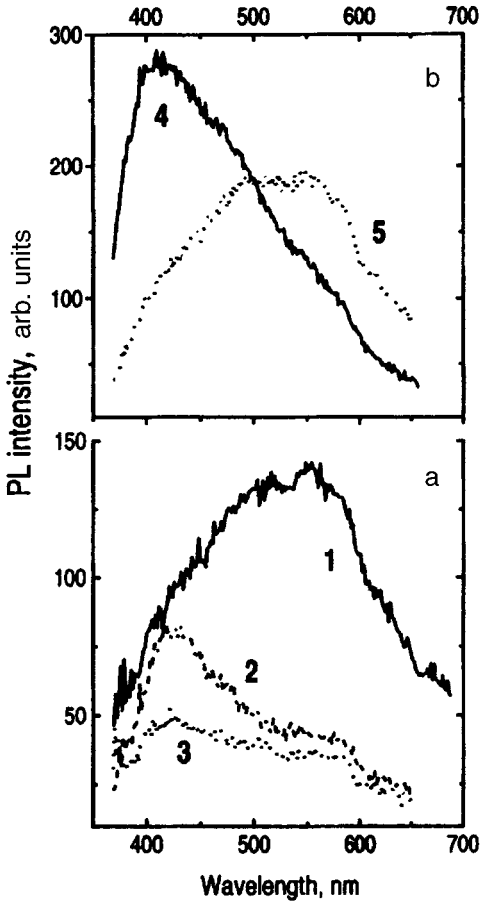

FIG. 3. Visible photoluminescence spectra of: a) *por*-GaAs layers; b) hydrated oxides. *1*) ''chemical'' layer; *2*) ''electrolytic'' layer, $HF+HNO_3$ electrolyte; *3*) the same, HCL electrolyte; *4*) $As_2O_3 \cdot nH_2O$; *5*) $Ga_2O_3 \cdot nH_2O$.

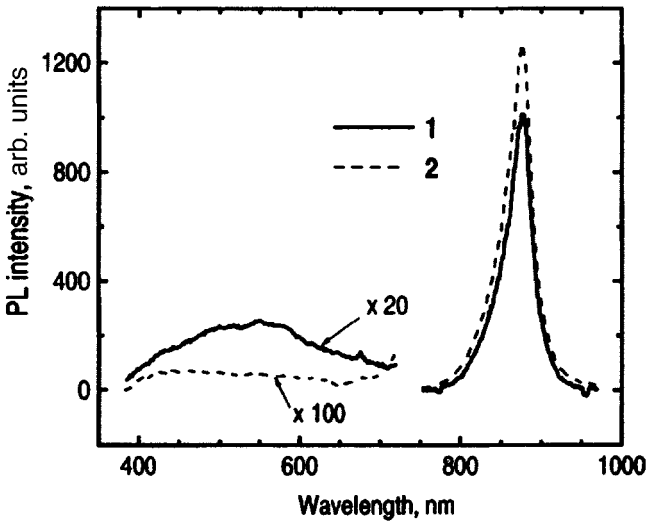

FIG. 4. Photoluminescence spectra of *por*-GaAs (chemical layers). *1*) Before sulfidation; *2*) after sulfidation.

etching is less pronounced than in chemical etching; both oxides are formed, but with a preponderance of arsenic oxide, as is also confirmed by published data.[2]

We have conducted experiments on the removal of oxides from the surface of *por*-GaAs by chemical means. Newly formed oxides of both Ga and As are known to dissolve slightly in alkali solutions with *pH* 12–14. For the latter we used 1N Na_2CO_3 or Na_2S solutions. We discovered that the intensity of visible photoluminescence decreased by more than an order of magnitude after such treatment of chemical *por*-GaAs layers (Fig. 4), corroborating the foregoing conclusions. The IR emission intensity, conversely, increases after the oxides are dissolved in Na_2CO_3 solution and is still further enhanced by immersion of the sample in Na_2S solution for 5–10 s. Similar results are obtained in the removal of oxides directly in Na_2S solution. The enhancement of IR emission after treatment in Na_2S solutions is attributable to the well-known passivation of the surface of GaAs after sulfidation.[7] The influence of this treatment on electrolytic layers is much weaker. The nature of the residual, weak, visible luminescence of *por*-GaAs after dissolution of the oxide needs to be studied further.

The variation of the characteristic (IR) photoluminescence of GaAs during the formation of the porous layer can be attributed to large band-edge fluctuations in *por*-GaAs or, in other words, to growth of the tails of the density of states in the bands. The fluctuations arise both from the large curvature of the inner surfaces of fine *por*-GaAs formations and from the generation of surface defects and irregularities as a result of selective etching. As the tails of the bands become larger, the energy of the emitted photons decreases, and the photoluminescence maximum is observed to shift into the long-wavelength region, i.e., toward lower energies. Radiative recombination between the band tails also accounts for the broadening of the emission band in lightly doped samples.

CONCLUSIONS

We have described the preparation of porous gallium arsenide layers by electrolytic and chemical etching of the semiconductor. On the basis of an investigation of the photoluminescence spectra we have concluded that the prepared layers comprise GaAs crystallites having well-developed surfaces and surrounded by a large quantity of hydrated gallium and arsenic oxides. Quantum-well effects in the photoluminescence of porous GaAs layers have not been observed in the present stage of our experimental work. The visible photoluminescence of the porous layers, particularly those prepared by the chemical etching of GaAs, is largely attributable to emission from hydrated oxides of gallium and arsenic. This fact indirectly confirms the previously stated conclusion regarding the special mechanism underlying the formation of low-dimensional structures on silicon in connection with its unique chemical properties.[8] However, our observed appreciable reduction in the crystallite dimensions with the introduction of alcohol into the electrolyte and the implementation of additional measures for passivation of the *por*-GaAs surface foster the belief that quantum-well effects will eventually be detected on *por*-GaAs.

This work has received partial support from the Russian Fund for Fundamental Research (RFFI Grant 96-02-17903) and the Ministry of Science Program ''Physics of Solid State Nanostructures'' (Projects 96-1012 and 97-1035).

[1] L. T. Canham, Appl. Phys. Lett. **57**, 1046 (1990).
[2] P. Schmuki, J. Frazer, C. M. Vitus, M. J. Graham, and H. S. Isaacs, J. Electrochem. Soc. **143**, 3316 (1996).
[3] P. Schmuki, D. J. Lockwood, H. J. Labbé, and J. W. Frazer, **69**, 1620 (1996).
[4] A. A. Lebedev and Yu. V. Rud', Pis'ma Zh. Tekh. Fiz. **22**, 484 (1996) [Tech. Phys. Lett. **22**, 483 (1996)].
[5] B. H. Erne, D. Vanmeakelbergh, and J. J. Kelly, Adv. Mater. **7**, 739 (1995); A. V. Zoteev, P. K. Kashkarov, A. N. Obraztsov, and V. Yu. Timoshenko, Fiz. Tekh. Poluprovodn. **30**, 1473 (1996) [Semiconductors **30**, 775 (1996)].
[6] B. Schwartz, Crit. Rev. Solid State Sci. **5**, 4, 609 (1975).
[7] C. J. Sandroff, R. N. Nottenburg, J.-C. Bischoff, and R. Bhat, Appl. Phys. Lett. **51**, 33 (1987).
[8] D. N. Goryachev, L. V. Belyakov, O. M. Sreseli, and I. D. Yaroshetskii, Semicond. Sci. Technol. **10**, 373 (1995).

Translated by James S. Wood

Polarization memory in an oxidized porous SiC layer

A. M. Danishevskiĭ, A. Yu. Rogachev, V. B. Shuman, and E. G. Guk

A. F. Ioffe Physicotechnical Institute, Russian Academy of Sciences, 194021 St. Petersburg, Russia
(Submitted January 21, 1997; accepted for publication February 25, 1997)
Fiz. Tekh. Poluprovodn. **31**, 1387–1391 (November 1997)

Polarization and polarization memory of pulsed photoluminescence are observed on porous layers prepared on microcrystalline, cubic SiC films deposited on silicon substrates. The porous layer is oxidized by electrochemical means. A qualitative model is proposed to account for the mechanism underlying the onset of polarization of photoluminescence for linearly polarized excitation. © *1997 American Institute of Physics.* [S1063-7826(97)02611-2]

Porous nanodimensional semiconductor materials are alluring to researchers for the possibility of observing strong, wideband photoluminescence resulting from quantum-well effects in nanocrystals. Studies of the polarization and polarization memory of photoluminescence in porous Si samples[1–4] have enabled investigators to draw conclusions about the crystallite geometries (the model of more or less prolate ellipsoids) for a particular material preparation technique, and also about the distribution of crystallites in the formation of porous layers on various crystallographic planes of the original material. However, the theoretical model set forth in Ref. 3 to describe the mechanism underlying the origin of the polarization of photoluminescence is purely classical (randomly arrayed ellipsoidal crystallites in the field of a light wave) and does not account for either the spectral or the time dependence of the degree of polarization of photoluminescence.

Polarization memory has also been observed in several amorphous semiconductors such as *a*-$Si_{1-x}C_x$:H, *a*-C:H, and *a*-As_2S_3 (Refs. 5–7). The authors of the cited papers attribute the nature of the phenomenon to the presence of small clusters having a narrower-gap composition and residing in a matrix of a wider-gap material. This is the case, for example, in *a*-C:H (Ref. 6) or *a*$Si_{1-x}C_x$:H (Ref. 5), where clusters incorporating graphite-like (sp^2) carbon bonds are built into a structural grid matrix with sp^3 carbon bonds. The authors believe that if photoexcited pairs are localized in small crystallites, polarization memory can persist for a long time, so that the emitted photoluminescence is polarized. Consequently, polarization memory ostensibly reflects the degree of localization of photoexcited carriers.[5] It is suggested in Ref. 5 that the primary cause of the polarization dependence of photoluminescence is anisotropy of the valence bonds, because the valence bond of amorphous SiC is made up of Si and C *p* orbitals. In essence, therefore, this interpretation characterizes the phenomenon of ''alignment'' of nonequilibrium carriers, investigated in bulk crystalline semiconductors of the GaAs (Ref. 8) and $Ga_{1-x}Al_xAs$ type. In the latter material, however, polarization is observed only for ''hot'' photoluminescence, because the emission of a few phonons is sufficient to eradicate polarization memory. A fairly high degree of polarization has been recorded for the photoluminescence of thermalized carriers in *a*-SiC, and it was found not to have a very strong dependence either on the exciting photon energy or on the luminescing photon energy. In our opinion, this consideration diminishes the likelihood of the given explanation.

The investigation of porous SiC from the standpoint of the above-stated problems has important bearing on the issue of the existence of polarization memory and its characteristics. The existence of polarization memory has never been discussed in any of the papers published to date on porous SiC (Refs. 9–13). On the other hand, the investigation of this problem could help to resolve the question of the existence and geometry of nanostructural crystallites responsible for the onset of quantum-well effects in photoluminescence. Specifically, in Refs. 9–13 the spectral maximum of the observed radiation from porous layers occurred in the interval 2.45–2.6 eV. Since the given layers were prepared on 6*H*-SiC crystals, whose band gap has a width of the order of 3.1 eV, it has been concluded[13] that the appearance of the given photoluminescence band is attributable to the formation of defects during anodic etching of the crystal. In our previous work[14,15] we have advanced the hypothesis that the nature of the given luminescence is associated with nanodimensional layers of a cubic phase, which appear at the void boundaries during electrolytic etching of the hexagonal 6*H*-SiC used to create the porous layer. The broadening of the photoluminescence band toward shorter wavelengths, achieved by varying the conditions attending the preparation of the layer, can be linked to quantum-well effects in this case, but now in cubic crystallites (the width of the band gap of bulk 3*C*-SiC is $E_g = 2.3$ eV).

Pursuant to the discussion in Ref. 15, we have undertaken an investigation of porous layers prepared from cubic polycrystalline SiC films grown on silicon substrates.[16] The layers were coated with an oxide film by an electrolytic process in an aqueous HCl solution for passivation of the reticulated porous surface. Strong, very wideband photoluminescence is observed in this case, its short-wavelength edge attaining 3.4–3.5 eV.

Anodic oxidation of the surface of a porous layer was also used repeatedly in the preparation of porous Si samples emitting in the blue-green region ($h\nu_{\max} = 2.4$ eV). The photoluminescence intensity increased by several orders of magnitude in this case. However, in the earliest studies the phenomenon was thought to be associated with passivation of the surface layer[17] and a significant reduction in the surface recombination rate, whereas the authors of later papers (see, e.g., Ref. 18) concluded that the emission sources exist in

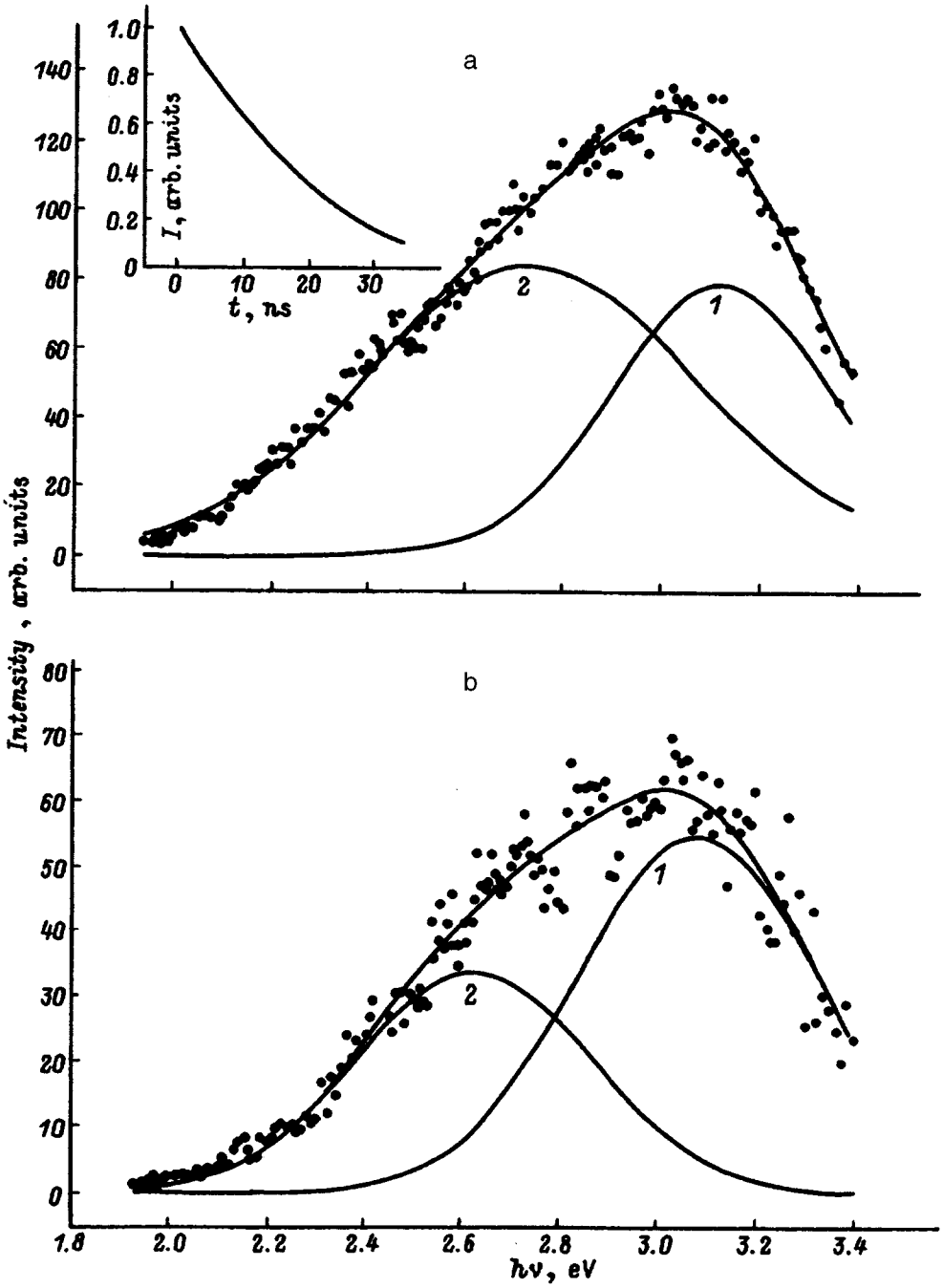

FIG. 1. Photoluminescence spectra of porous SiC at two temperatures and their approximation by two Gaussian profiles. a) $T=90$ K; b) $T=300$ K. Inset: Transient decay characteristic of the photoluminescence pulse.

the oxide layer or at its interface with crystallites. This conclusion was based on investigations of time-resolved spectra and also the kinetics of photoluminescence at various exciting photon energies. The polarization characteristics of the photoluminescence were not investigated in Ref. 18. However, the very presence of polarization memory, along with the dependence (differing considerably for different crystallographic planes of Si) of the degree of polarization on the direction of polarization of the exciting radiation (an investigation of these characteristics for porous Si is reported in Ref. 19) indicates that the main source of emission in the oxidized layers of porous Si lies in geometrically anisotropic nanodimensional crystallites.

In the present study, therefore, we have investigated not only the photoluminescence spectra, but also polarization memory effects and the emission-wavelength and time dependence of the degree of polarization.

EXPERIMENTAL PROCEDURE

The sample for the photoluminescence investigations was excited by a pulsed nitrogen laser beam ($h\nu=3.68$ eV) with a pulse duration of 10 ns and a repetition rate of 50 pulses/s. The emission spectra (Fig. 1) were analyzed by means of a DFS-12 dual spectrometer and an FÉU-79 photomultiplier. After wideband amplification and synchronous detection with a 4-ns gate the signals were fed into a computer. To measure the polarization characteristics, a film ana-

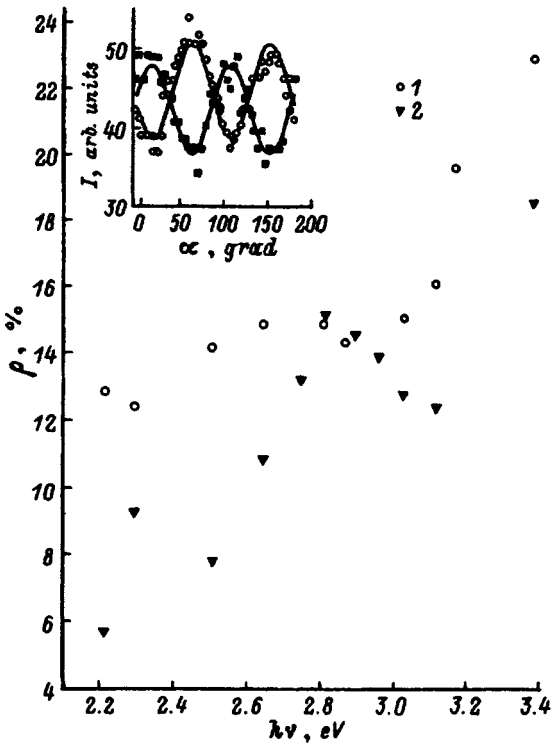

FIG. 2. Spectral dependence of the degree of polarization of photoluminescence of porous SiC at two temperatures. *1*) $T=90$ K; *2*) $T=300$ K. Inset: Photoluminescence intensity ($h\nu_{per}=2.88$ eV) versus angle of rotation of the half-wave plate for two mutually perpendicular analyzer positions.

lyzer was placed in front of the spectrometer entrance slit, and a Glan prism and half-wave phase filter were inserted in the path of the exciting beam. Rotation of the polarization of the laser beam induced rotation of the polarization plane of photoluminescence, causing the photoluminescence intensity to be modulated after passage through the analyzer. The analyzer was then rotated 90°, and the photoluminescence intensity was again measured as a function of the angle of rotation of the phase plate. The inset in Fig. 2 shows typical plots, which can be used to determine the degree of polarization of the photoluminescence at a given wavelength. The gap between the central lines of the two sine curves is associated with the polarization dependence of the spectrometer sensitivity.

The measurements were performed on a porous layer prepared on a polycrystalline film of cubic SiC of thickness 2.15 μm, which was deposited on a silicon substrate. The as-prepared film was far from stoichiometric. The width of its band gap, determined from edge-absorption spectra, was equal to 1.76 eV (Ref. 16). The anodic etching of the film was performed in a water-alcohol solution of HF for 1 min. The porous layer which was obtained was then electrochemically oxidized in an aqueous solution of HC1 for 8 min. The oxidized films were highly luminescent when observed in a Lyumam R-2 luminescence microscope. We had previously[16] observed substantial degradation of photoluminescence as a result of exposing a sample to ultraviolet radiation from a pulsed nitrogen laser,[16] and for this reason the sample was held under the laser beam for 20 min prior to the measurements, whereupon the photoluminescence signal changed only slightly with time.

TABLE I.

T, K	Peak No.	$h\nu_{max}$, eV	$\Delta h\nu$, eV	I_{max}, arb. u.	$\tilde{I}$, arb. u.
90	1	3.12	0.447	78.07	43.74
	2	2.727	0.679	83.76	71.26
300	1	3.081	0.486	54.68	33.29
	2	2.626	0.483	33.66	20.39

Note: Here $h\nu_{max}$ denotes the position of the luminescence peak, $\Delta h\nu$ is its width, I_{max} is the luminescence intensity at $h\nu_{max}$, and $\tilde{I}$ is the total photoluminescence (area under the calculated spectral curves).

EXPERIMENTAL RESULTS AND DISCUSSION

Figure 1 shows photoluminescence spectra obtained from the experimental sample at $T=90$ K (a) and 300 K (b) at a time corresponding to the maxima of the excitation and photoluminescence pulses (the maxima of these pulses and their transient decay characteristics — see the inset to Fig. 1a — essentially coincide within the time-resolution limits of the recording system, of the order of 15 ns). The indicated spectra are quite similar and are well described by two Gaussian profiles with maxima at energies in the vicinity of 2.7 eV and 3.1 eV. However, the parameters of the profiles (see Table I) differ appreciably for the two temperatures at which the spectra were obtained.

The temperature shifts of the peaks differ significantly: 0.101 eV for the longer-wavelength blue band (curves *2* in Figs. 1a and 1b) and 0.039 eV for the shorter-wavelength violet band (curves *1*), implying a difference in the basic physical nature of the particular system of emitters. The temperature variations of the width $\Delta h\nu$ and amplitude I_{max} of these profiles also differ markedly. As T is lowered, both the amplitude and the width of band *2* increase substantially, whereas the amplitude of the short-wavelength band *1* increases insignificantly, and its width changes only slightly. The relatively weak temperature dependence of band *1* indicates a localization of excess carriers contributing to radiative, probably ''geminate,'' recombination, and the energy characteristics reveal the major role of quantum-well effects.

Figure 2 shows the dependence of the degree of polarization ρ on the photoluminescence photon energy at $T=90$ K and 300 K. At the maximum photon energy (3.4 eV) the maximum degrees of polarization are recorded for both temperatures. They gradually decay from 0.23 to 0.13 (at 300 K) as the emitted photon energy decreases from 3.4 eV to 2.2 eV, with a higher value of ρ at 300 K, and they decay more slowly. At 90 K the decay is not fully monotonic.

The sum-total of several factors — the comparatively weak temperature dependences of the degree of polarization and the amplitude of the broad band distinguished in the photoluminescence spectra, with its maximum at an energy of the order of 3.12 eV, and the rapid decay of the photoluminescence pulses with time — leads to the conclusion that the emission sources in the given situation are electron-hole pairs localized in small, anisotropic crystallites, i.e., local-

ized excitons. The significant broadening of the spectrum into the short-wavelength range indicates the presence of quantum-well effects in these crystals.

Ellipsometric measurements in a study of porous Si (Ref. 20) have revealed that the dielectric constants $\varepsilon_{\parallel}$ and $\varepsilon_{\perp}$ are not equal for a porous layer formed on the (100) plane. We know from electron microscope measurements[21,22] that the elongated crystallites in the given situation are oriented predominantly in the [100] direction, so that the inequality of $\varepsilon_{\parallel}$ and $\varepsilon_{\perp}$ is most likely indicative of a difference in the structure of the electron energy spectrum along and across the crystallite axis. It is reasonable to assume that the same difference accounts for the existence, degree, and long-time ($\sim 10\ \mu$s) retention of the polarization of photoluminescence. For the SiC samples investigated in the present study the carrier lifetime is fairly short (<15 ns). Nonetheless, taking into account the other noted features of the photoluminescence behavior, we can assume that the mechanism underlying the origin of polarization memory is unique. Photon-excited electrons with velocities perpendicular to the crystallite axis are scattered by lattice vibrations and become thermalized predominantly into lower energy states, changing the direction of their velocities. The same carriers with velocities oriented along the crystallite axis under the influence of photoexcitation must acquire additional energy to overcome the energy barrier before they can have the direction of their velocities changed by scattering. As a result, an excess-carrier distribution oriented in momentum space is created in each crystallite. Allowance must be made for the fact that the carrier generation rate depends on the angle between the direction of polarization of the exciting light and the long axis of the crystallite. The recombination rate must depend on the carrier density (in the case of predominantly radiative recombination) and on the direction of the carrier velocity.

The degree of polarization of photoluminescence is given by the expression

$$\rho \sim \frac{\langle \tau_{\mathrm{rel}} \rangle}{\langle \tau_{\mathrm{rel}} + \tau_0 \rangle},$$

where τ_{rel} is the relaxation time of the oriented state of carriers in a crystallite, and τ_0 is their lifetime; the angle brackets signify averaging over the ensemble of crystallites. For thermalized excess carriers the indicated quantities can be of the same order of magnitude, in principle, but their temperature dependences will probably differ and should dictate the temperature dependence of ρ. The decrease in the degree of polarization with increasing photoluminescence wavelength can be attributed to emission from larger crystallites (it is also conceivable that larger crystallites have lower geometrical anisotropy). Also possible, of course, are radiative processes associated with impurity levels, defects, and crystallite boundary states. Future studies will be aimed at elucidating and tracing the process by which the polarization of photoluminescence is retained in this case as well.

We wish to thank V. E. Chenokov for interest in this investigation.

This work has received financial support from the Russian Fund for Fundamental Research (RFFI Grant 95-02-04115) and partial support from the Ministry of Science of Russia (Project 1-079/4) and the University of Arizona, USA.

[1] A. V. Andrianov, D. I. Kovalev, N. N. Zinov'ev, and I. D. Yaroshetskiĭ, JETP Lett. **58**, 427 (1993).
[2] A. V. Andrianov, D. I. Kovalev, and I. D. Yaroshetskiĭ, Fiz. Tverd. Tela (St. Petersburg) **35**, 2677 (1993) [Phys. Solid State **35**, 1323 (1993)].
[3] D. Kovalev, M. Ben Chorin, J. Diener, F. Koch, Al. L. Efros, M. Rosen, M. A. Gippius, and S. G. Tikhodeev, Appl. Phys. Lett. **67**, 1585 (1995).
[4] H. Koyama and N. Koshida, Phys. Rev. B **52**, 2649 (1995).
[5] V. Masumoto, H. Kunitomo, S. Shinoya, H. Munekata, and H. Kukimoto, Solid State Commun. **51**, 209 (1984).
[6] Rusli, G. A. J. Amaratunga, and J. Robertson, Phys. Rev. B **53**, 16306 (1996).
[7] K. Murayama and M. A. Bösch, Phys. Rev. B **25**, 6542 (1982).
[8] V I. Zemskiĭ, B. P. Zakharchenya, and D. M. Mirlin, JETP Lett. **24**, 82 (1976).
[9] T. Matsumoto, J. Takahashi, T. Tamaki, T. Futaki, H. Mimura, and Y. Kanemitsu, Appl. Phys. Lett. **64**, 226 (1994).
[10] A. O. Konstantinov, C. I. Harris, and E. Yanzen, Appl. Phys. Lett. **65**, 2699 (1994).
[11] J. S. Shor, L. Bemis, A. D. Kurtz, M. McMillan, W. J. Choyke, I. Grimberg, and B. Z. Weiss, in *Institute of Physics Conference Series, No. 137, Silicon Carbide and Related Materials, Proceedings of the Fifth International Conference*, edited by M. G. Spencer *et al.* (IOP Publ., Bristol-Philadelphia, 1993), p. 193.
[12] A. A. Lebedev, A. A. Lebedev, and Yu. V. Rud', Pis'ma Zh. Tekh. Fiz. **21**(3), 64 (1995) [Tech. Phys. Lett. **21**, 117 (1995)].
[13] A. O. Konstantinov, A. Henry, C. I. Harris, and E. Yanzen, Appl. Phys. Lett. **66**, 2250 (1995).
[14] A. M. Danishevskiĭ, V. B. Shuman, A. Yu. Rogachev, and P. A. Ivanov, Fiz. Tekh. Poluprovodn. **29**, 2122 (1995) [Semiconductors **29**, 1106 (1995)].
[15] A. M. Danishevskiĭ, V. B. Shuman, A. Yu. Rogachev, E. G. Guk, P. A. Ivanov, A. A. Mal'tsev, Fiz. Tekh. Poluprovodn. **30**, 1064 (1996) [Semiconductors **30**, 564 (1996)].
[16] A. M. Danishevskiĭ, V. B. Shuman, E. G. Guk, and A. Yu. Rogachev, Fiz. Tekh. Poluprovodn. **31**, 420 (1997) [Semiconductors **31**, 354 (1997)].
[17] A. Bsiesy *et al.*, Surf. Sci. **254**, 195 (1991).
[18] S. Komuro, T. Kato, and T. Morikava, J. Appl. Phys. **80**, 1749 (1996).
[19] F. Koch, in *Digests of the Second Russian Conference on the Physics of Semiconductors* [in Russian], St. Petersburg-Zelenogorsk (1996), p. 118.
[20] P. Basmaji, V. S. Bagnato, V. Grivickas, G. I. Surdotovich, R. Vitlina, Thin Solid Films **223**, 131 (1993).
[21] A. G. Cullis, L. T. Canham, G. H. Williams, P. W. Smith, and O. D. Dosser, Mater. Res. Soc. Symp. Proc. **283**, 257 (1993).
[22] O. Teschke, F. Alvarez, L. Tessler, and M. U. Kleinke, Appl. Phys. Lett. **63**, 1927 (1993).

Translated by James S. Wood

Current tuning of the emission wavelength of low-threshold mesa stripe lasers utilizing InAsSb/InAsSbP double heterostructures and emitting in the vicinity of 3.3μm

T. N. Danilova, A. P. Danilova, O. G. Ershov, A. N. Imenkov, M. V. Stepanov, V. V. Sherstnev, and Yu. P. Yakovlev

A. F. Ioffe Physicotechnical Institute, Russian Academy of Sciences, 194021 St. Petersburg, Russia
(Submitted March 3, 1997; accepted for publication March 6, 1997)
Fiz. Tekh. Poluprovodn. **31**, 1392–1395 (November 1997)

Diode lasers based on InAsSb/InAsSbP double heterostructures with a low threshold current ($\sim$12 mA) and a narrow mesa stripe (of width $\sim$10 μm) are investigated over a wide range of currents up to five times the threshold current. The modes of such lasers in the measured current range are observed to shift toward shorter wavelengths by approximately the amount of the spacing between modes as a result of an increase in the density of nonequilibrium carriers in the active zone. The rate at which the modes shift with the current differs in different current intervals, depending on the degree of single-mode dominance of the laser emission spectrum. © *1997 American Institute of Physics.* [S1063-7826(97)02911-6]

1. The creation of tunable injection lasers operating in the spectral interval 3–4 μm looks exceptionally promising for high-resolution molecular spectroscopy, because this spectral interval encompasses many strong characteristic absorption lines of natural and industrial gases. The present study is a continuation of work begun by us on the construction and design of InAsSb/InAsSbP-based tunable lasers[1–5] and is devoted to an investigation of current-controlled tuning of the emission wavelength of low-threshold lasers having a narrow mesa stripe and emitting in the absorption region of methane and hydrocarbons ($\lambda = 3.3$ μm).

We have investigated lasers based on N-$InAs_{0.52}Sb_{0.18}P_{0.30}$/$n$-$InAs_{0.95}Sb_{0.05}$/$p$-$InAs_{0.52}Sb_{0.18}P_{0.30}$ heterostructures prepared by liquid-phase epitaxy. The wide-gap emitters had a thickness $\sim$3 μm each, with an active zone of thickness $\sim$1 μm. The N-InAsSbP layer was doped with Sn to an electron density of $(2-5)\times10^{18}$ cm^{-3}, and the P-InAsSbP layer was doped with Zn to a hole density $\sim1\times10^{18}$ cm^{-3}. The active zone was not specially doped, and its electron density was $\sim10^{16}$ cm^{-3}. Mesa stripes of width $\sim$10 μm were formed on the as-grown structure by standard photolithography. Lasers with a cavity length of 225–300 μm were created by cleaving.

We have investigated the emission spectrum, the radiation pattern, and the total emission intensity of the lasers in a quasi-continuous-wave regime. The lasers were pumped by meander-type rectangular current pulses with a repetition rate of 80 Hz. The measurements were performed at liquid-nitrogen temperature. An MDR-2 monochromator was used as a dispersing instrument to obtain the spectra.

2. The coherent emission spectra of the lasers were measured in the current range from threshold (I_{th}) to $I\cong5I_{th}$. The radiation pattern and the total emission intensity were measured in the same current range.

The threshold current for the better lasers is $\sim$12 mA, and the threshold current density $J_{th}\equiv530$ A/cm^2 at 77 K. The mode composition of the coherent emission spectrum at various pumping points is shown in Fig. 1 (V-12192 laser No. 1). The mode spacing is $\simeq$60 Å. At the threshold current the laser has two consecutive dominant modes with an intensity more than double that of all the other modes, but not far above the threshold a single mode emerges as the dominant one $I=1.25I_{th}$. The single-mode regime persists up to currents $I\cong3.5I_{th}$, above which the spectrum acquires another mode on the short-wavelength side at four mode spacings from the first and with approximately the same intensity. As the current is increased, this second mode assumes dominance, but a single-mode spectrum no longer exists.

The fraction of emission of the dominant mode relative to the emission of all modes in the spectrum ($F_{max}/\Sigma F_i$) is estimated numerically in Fig. 2. We see that the ratio $F_{max}/\Sigma F_i$ depends on the current and has values from 0.8 to $\sim$1 in the current interval where $I/I_{th}\cong1.5$–3. At $I=I_{th}$ we have $F_{max}/\Sigma F_i\cong0.3$. At high currents, such that $I/I_{th}>3.5$, $F_{max}/\Sigma F_i$ does not vary with the current and has a value $\sim$0.45.

Characteristics of the laser emission are plotted as functions of the current I (or I/I_{th}) in Fig. 3 for the same laser. Figure 3a shows the current dependence of the increment $\Delta\lambda$ of the spectral position of the dominant mode in the current interval $1.5I_{th}$–$3I_{th}$ and a comparison with its position at the threshold current. Figure 3b shows the current dependence of the full width at half maximum (FWHM) $\Delta\Theta$ of the radiation pattern in the plane of the p–n junction (curve *1*) and in the plane perpendicular to the plane of the p–n junction (curve *2*). Figure 3c shows the current dependence of the total emission intensity F_Σ.

It is evident (Fig. 3a) that the mode position in the spectrum shifts toward shorter wavelengths as the pump current is increased, and in the measured current range the total shift is $\sim$55 Å. However, the rate of this shift differs in different current intervals. The $\Delta\lambda(I)$ curve has the greatest slope in the current interval from I_{th} to $1.5I_{th}$. In this interval

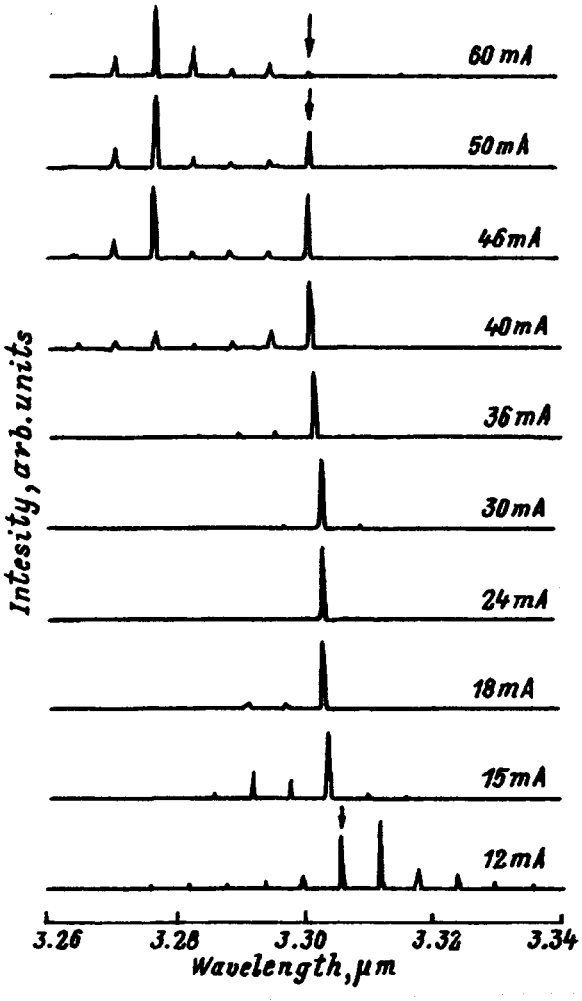

FIG. 1. Emission spectra of a laser (V12192 No. 1) at a temperature of 77 K for various pump currents.

$F_{\max}/\Sigma F_i$ varies from 0.3 to 0.8 (Fig. 2). The total mode shift in this interval is ~ 30 Å. In the same current interval the FWHM of the radiation pattern (Fig. 3b) in the plane of the p–n junction (curve *1*) continues to decrease, but at a

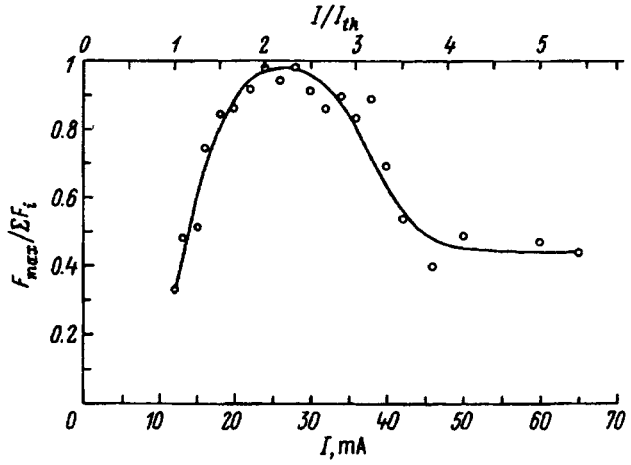

FIG. 2. Ratio of the intensity of the strongest mode to the sum of the intensities of all modes $F_{\max}/\Sigma F_i$ versus current I.

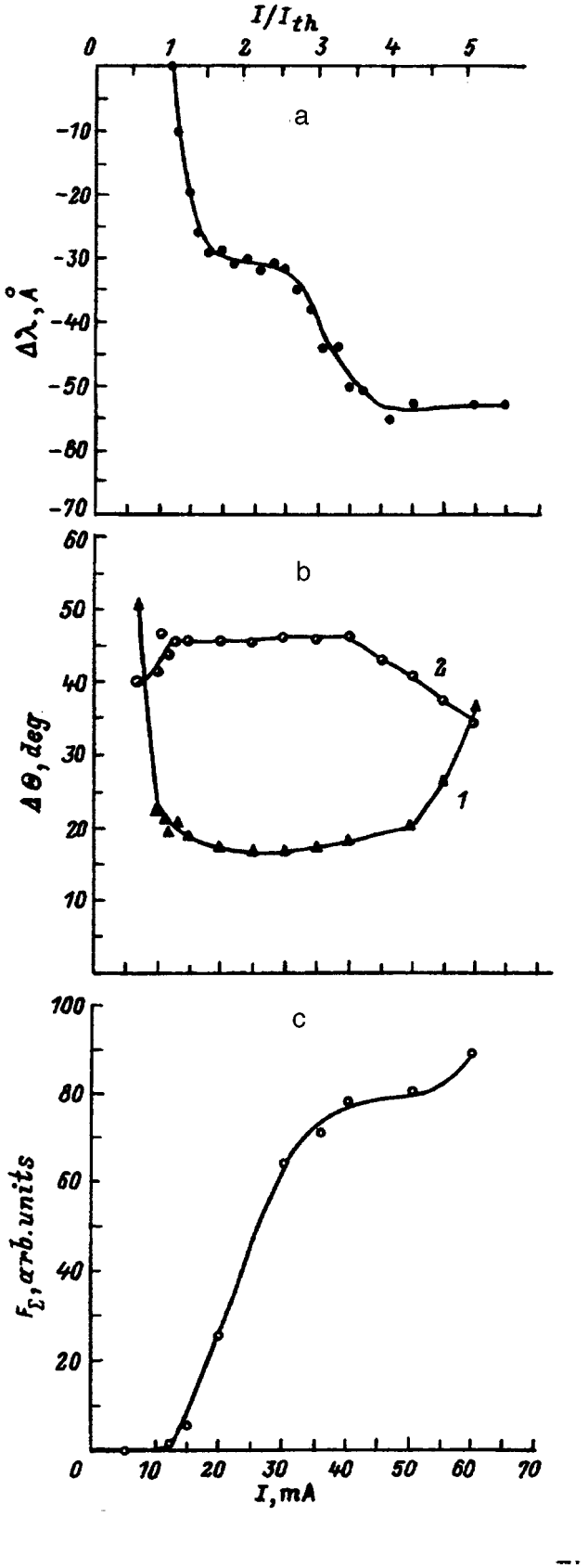

FIG. 3. Current (I) dependence of: a) the shift of the mode position $\Delta\lambda$ versus current I; b) the full width at half maximum (intensity) of the radiation pattern in the plane of the p–n junction (graph 1) and in the plane perpendicular to the p–n junction (graph 2); c) the total emission intensity F_Σ. All the graphs are for laser V1219 No. 1.

slower rate than for $I<I_{\text{th}}$. In the plane perpendicular to the p–n junction (curve *2*) the radiation pattern does not change with the current. The emission intensity increases superlinearly with the current (Fig. 3c).

In the current interval from $1.5I_{\text{th}}$ to $2.8I_{\text{th}}$, i.e., in the single-mode regime, $F_{\max}/\Sigma F_i$ has values from 0.8 to 1 (Fig. 2), the slope of the $\Delta\lambda(I/I_{\text{th}})$ curve is very slight, and the shift of λ toward shorter wavelengths is $\sim$2.5 Å. In this current interval the radiation pattern in the plane of the p–n junction attains its minimum value $\Delta\Theta\approx 17°$ (Fig. 3b, curve *1*), and in the plane perpendicular to the p–n junction $\Delta\Theta$ remains unchanged (Fig. 3b, curve *2*). The intensity F_Σ depends linearly on the current (Fig. 3c).

In the current interval from $2.5I_{\text{th}}$ to $3.5I_{\text{th}}$ the ratio $F_{\max}/\Sigma F_i$ decreases from $\sim$1 to 0.5, and the mode shifts toward shorter wavelengths by $\sim$20 Å (Fig. 3a). In this interval the radiation pattern (Fig. 3b) in the plane of the p–n junction (curve *1*) and in the plane perpendicular to the p–n junction (curve *2*) does not change. The current dependence of the emission intensity (Fig. 3c) is sublinear.

At currents from $3.5I_{\text{th}}$ to $5.5I_{\text{th}}$ the mode whose position we are tracking loses its dominance and shifts 2–3 Å toward longer wavelengths. A mode of the same intensity emerges at a distance of four mode spacings on the short-wavelength side and gradually becomes dominant as the current is increased. The radiation pattern (Fig. 3b) in the plane of the p–n junction broadens considerably (curve *1*) and in the plane perpendicular to the p–n junction it narrows considerably (curve *2*), and in both cases the FWHM attains approximately the same value $\sim 36°$. The intensity-current curve is observed to have a shelf at first, but then the intensity rises as the current is increased.

3. We now discuss the results. An examination of the experimental results reveals that as the current is increased from I_{th} to $4I_{\text{th}}$ in the investigated lasers, the modes shift toward the short-wavelength end by an amount almost equal to the mode spacing. This behavior rules out the self-focusing, which would produce a long-wavelength shift,[4] in the investigated lasers with a stripe of width $\sim 10\ \mu$m in the given current range. The shift of the mode position in the spectrum toward shorter wavelengths could be the result of a decrease in the refractive index as the current is increased if the injection of free carriers into the semiconductor tends to raise the density of nonequilibrium carriers (N) at currents above I_{th}. An increase in N produces a change in the interband absorption coefficient by an amount $\Delta\alpha(\hbar\omega)$, which is related to the increment of the refractive index Δn by the Kramers–Kronig relation

$$\Delta n=\frac{\hbar c}{\pi}\int_0^\infty \frac{\Delta\alpha(\hbar\omega)}{(\hbar\omega)^2-(\hbar\omega_0)^2}d(\hbar\omega)$$

$$\approx\frac{\hbar c}{2\pi E_g}\int_0^\infty =20\frac{\Delta\alpha(\hbar\omega)}{\hbar\omega-\hbar\omega_0}d(\hbar\omega),$$

where E_g is the width of the band gap in the active zone of the laser, c is the speed of light, $\hbar$ is the Planck constant, ω is the lasing angular frequency, and if $\hbar\omega_0$ is interpreted as the photon energy of the emitted laser radiation. Therefore, Δn is related to this radiation.

The variations of the refractive index n for $x=0.05$, which corresponds to the composition of the active zone of the investigated lasers, can be estimated from the calculations of Paskov.[7] For a carrier density of $5\times 10^{17}\text{cm}^{-3}$, which is 1.5 orders of magnitude higher than the equilibrium carrier density in the active zone, the increment of n is equal to 0.1–0.15 at the photon energy corresponding to the edge of the intrinsic absorption edge. Paskov's calculations were carried out at room temperature. However, since $\sigma=dn/dN\sim -1/T$ for III–V semiconductors,[6,8] our increment would have to be at least the stated amount at 77 K.

However, it is evident from Fig. 3 that within the current range from I_{th} to $\sim 4I_{\text{th}}$, where the mode shifts toward shorter wavelengths with increasing current, there is an interval from $1.5I/I_{\text{th}}$ to $2.8I/I_{\text{th}}$ where this shift is very slight ($\sim$2.5 Å). On the other hand, single-mode operation of the laser is observed in this current interval, where $F_{\max}/\Sigma F_i$ attains values of 0.8–1, i.e., a self-stabilizing effect is observed.[6] The strong mode suppresses amplification in a spectral interval extending from the long-wavelength side to the short-wavelength side. Maximum narrowing of the radiation patterns in the plane of the p–n junction is observed in this same interval. The slowing of the mode shift toward shorter wavelengths in single-mode lasing as the current is increased is an experimental consequence of a slight increase in the density of nonequilibrium carriers with $E>E_F$ (E_F is the Fermi energy at the lasing threshold) when the current is increased. This carrier density depends on the ratio of the characteristic times τ/τ_r, where τ is the energy relaxation time, and τ_r is the carrier recombination time. This ratio probably becomes significantly smaller in the single-mode regime of the investigated lasers than in the regime $F_{\max}/\Sigma F_i<0.8$.

At higher currents, above $4I_{\text{th}}$, the refractive index probably becomes so small in the active zone as to significantly reduce the optical confinement, and the light wave enters the wide-gap region. This event broadens the light beam in the plane perpendicular to the p–n junction and causes the radiation pattern to become narrower in this plane as a result of the diminished influence of slit diffraction. The penetration of light into passive zones increases the free-carrier absorption losses and can account for the shelf of the light intensity-current curve. The broadening of the radiation pattern in the plane of the p–n junction can be attributed to the transition from single-mode to multimode operation, rather than to the variation of the refractive index. The short-wavelength shift ceases in this interval, and the mode position is observed to shift slightly toward the long-wavelength end in the spectrum. This behavior indicates compensation of the short-wavelength shift by the long-wavelength shift, a phenomenon that can be linked to a decrease in the width of the band gap as a result of an increase in the density of nonequilibrium carriers[9] or as a result of heating.

In summary, an investigation of double-heterostructure InAsSb/InAsSbP with a narrow mesa stripe and a low threshold current has enabled us to trace the shifting of the coher-

ent emission modes within a broad current range (up to $5I_{\text{th}}$). We have discovered that the modes shift toward the short-wavelength end of the spectrum as the current is increased in such lasers, indicating an increase in the density of nonequilibrium carriers with energies $E>E_F$. The spectral mode positions shift with increasing current by an amount approximately equal to the total mode spacing, but the rate at which the modes shift with the current differs in different current intervals and depends on the degree of single-mode dominance of the laser emission spectrum. At currents above $4I_{\text{th}}$ the nonequilibrium carrier density increases to such an extent as to substantially lower the refractive index in the active zone, thereby reducing the optical confinement and the transfer of radiation into passive zones.

This work has received support in part from the U.S. Air Force European Office of Aerospace Research and Development (EOARD), Contract F6170894 C0011, in part from a grant of the Ministry of Science of the Russian Federation Program ''Optics and Laser Physics,'' and in part from Copernicus Contract No. CIPA-CP 94-0158.

[1] A. N. Baranov, T. N. Danilova, O. G. Ershov, A. N. Imenkov, V. V. Sherstnev, and Yu. P. Yakovlev, Pis'ma Zh. Tekh. Fiz. **18**(22), 6 (1992) [Sov. Tech. Phys. Lett. **18**, 725 (1992)].
[2] Yu. P. Yakovlev, A. N. Baranov, A. N. Imenkov, V. V. Sherstnev, M. V. Stepanov, and A. Ya. Ponurovskiĭ, Kvantovaya Élektron. **20**, 839 (1993) [Quantum Electron. **23**, 726 (1993)].
[3] A. N. Baranov, A. N. Imenkov, V. V. Sherstnev, and Yu. P. Yakovlev, Appl. Phys. Lett. **64**, 2480 (1994).
[4] T. N. Danilova, O. I. Evseenko, A. N. Imenkov, N. M. Kolchanova, M. V. Stepanov, V. V. Sherstnev, and Yu. P. Yakovlev, Pis'ma Zh. Tekh. Fiz. **22**(16), 7 (1996) [Tech. Phys. Lett. **22**, 645 (1996)].
[5] T. N. Danilova, O. G. Ershov, A. N. Imenkov, M. V. Stepanov, V. V. Sherstnev, and Yu. P. Yakovlev, Fiz. Tekh. Poluprovodn. **30**, 1265 (1996) [Semiconductors **30**, 667 (1996)].
[6] P. G. Eliseev and A. P. Bogatov, Tr. Fiz. Inst. Akad. Nauk SSSR **166**, 15 (1986).
[7] P. P. Paskov, Solid State Commun. **82**, 739 (1992).
[8] D. A. B. Miller, C. T. Seaton, M. E. Prise, and S. D. Smith, Phys. Rev. Lett. **47**, 197 (1981).
[9] V. M. Asnin and A. A. Rogachev, Fiz. Tverd. Tela (Leningrad) **5**, 1730 (1963) [Sov. Phys. Solid State **5**, 1257 (1963)].

Translated by James S. Wood

Influence of valence band absorption on the threshold characteristics of long-wavelength InAs lasers

N. A. Gun'ko, G. G. Zegrya, N. V. Zotova, Z. N. Sokolova, N. M. Stus', and V. B. Khalfin

A. F. Ioffe Physicotechnical Institute, Russian Academy of Sciences, 194021 St. Petersburg, Russia
(Submitted April 2, 1997; accepted for publication April 10, 1997)
Fiz. Tekh. Poluprovodn. **31**, 1396–1403 (November 1997)

The mechanism of intraband absorption of radiation with hole transition into the spin-orbit split-off band, or so-called intervalence-band absorption (IVA), is subjected to microscopic analysis. It is shown that this IVA mechanism significantly influences the threshold characteristics and quantum efficiency of InAs-based heterolasers. The dependences of the laser threshold characteristics on the temperature and the parameters of the laser heterostructure are analyzed in detail, taking into account the new (IVA) channel of intraband absorption by holes.
© *1997 American Institute of Physics.* [S1063-7826(97)03011-1]

1. INTRODUCTION

Superior long-wavelength InAs-based lasers have been constructed recently,[1] but the working temperatures and quantum efficiency are far below those of short-wavelength ($\leqslant 1.5\ \mu$m) lasers.[2] It has been shown[3] that the low working temperature of long-wavelength lasers is attributable to strong band-to-band Auger recombination, which does not, however, account for the quantum efficiency of these lasers at 77 K.

The maximum working temperature of long-wavelength lasers is known to depend on the rate factor of nonradiative channels for the recombination of nonequilibrium carriers, but it also depends on the intraband radiation absorption coefficient.[4] An analysis has shown that the intraband absorption mechanism depends significantly on the actual band structure of the semiconductor. A unique attribute of the band structure of InAs and solid solutions of similar composition is the fact that the width of the band gap E_g is close to the spin-orbit splitting Δ. Consequently, radiation generated in a laser with $\hbar\omega \sim E_g$ would be highly prone to strong absorption by holes in the valence band, which are excited into the spin-orbit split-off band in this case. We refer to the absorption of light by holes with transition of the latter into the split-off band as intervalence-(sub)band absorption (IVA). Such absorption will necessarily be much stronger at the lasing frequency in InAs than in lasers utilizing quaternary InGaAsP/InP solid solutions, in which the indicated loss mechanism is substantial, despite the large difference between E_g and Δ (Ref. 5).

The objective of the present study is to investigate IVA in InAs and the influence of this loss mechanism on the characteristics of long-wavelength InAs lasers. We propose to show that IVA is one cause of the low quantum efficiency of lasers made from InAs and solid solutions of similar composition. We look at the recombination processes in InAs and calculate the IVA coefficients associated with transitions of heavy and light holes into the split-off band. The analogous coefficients for nondegenerate holes have been calculated previously.[6] Intraband absorption within the valence band, on the other hand, has never been investigated in application to long-wavelength lasers.

It has been found that IVA in InAs lasers and similarly constituted solid solutions can be comparable with the level of light amplification in band-to-band transitions from the conduction to the valence band and can have a powerful influence on the threshold current of long-wavelength lasers emitting at wavelengths of $3-3.5\ \mu$m and on the maximum working temperature. This assertion is corroborated by the experimental investigations reported below in regard to the characteristics of InAs heterolasers.

The paper is divided into four sections, including the introduction, two main sections, and conclusions. In Sec. 2 we calculate the heavy-hole and light-hole IVA coefficients and the optical gain. The calculations are carried out in the first approximation with respect to the ratio of the intraband hole energy to the width of the band gap. We derive analytical expressions for the IVA coefficients and the optical gain. We also take into account intraband relaxation with respect to the momentum for the absorption and amplification of radiation. We then repeat the calculations of the IVA coefficients using the exact Kane model.

In Sec. 3 we investigate the influence of IVA on the characteristics of long-wavelength heterolasers with an InAs active zone. We compare the theoretical relations with our experimental results.

In Sec. 4 we discuss the results of the study and submit recommendations for improving the characteristics of long-wavelength lasers.

2. CALCULATION OF THE INTERVALENCE-BAND ABSORPTION COEFFICIENTS AND THE OPTICAL GAIN

a) The IVA coefficients and the optical gain are calculated in the 4-band Kane model, which is fully applicable to InAs, where the wave vectors of all particles involved in absorption are small by virtue of the closeness of E_g to Δ.

The absorption coefficient α and the optical gain g are expressed in terms of the imaginary part of the dielectric permittivity ε'':

$$\alpha = -g = \frac{\omega}{c\sqrt{\varepsilon_\infty}}\varepsilon''(\omega), \tag{1}$$

where ε_∞ is the rf dielectric permittivity, and c is the speed of light.

According to Ref. 7,

$$\varepsilon''(\omega)=\lim_{q\to 0}\frac{4\pi^2e^2}{q^2}\int\frac{d^3k}{(2\pi)^3}|M(\mathbf{k},\mathbf{q})|^2(f_1-f_2)\,\delta(E_1-E_2-\hbar\omega), \tag{2}$$

where $\mathbf{q}$ is the photon wave vector, $\mathbf{k}$ is the particle wave vector, e is the electron charge, E_1, E_2, f_1, and f_2 are the energies and Fermi distribution functions of the charge carriers, and $M(\mathbf{k},\mathbf{q})$ is the matrix element of transition between the Bloch wave functions of the initial and final states. For band-to-band transitions from the conduction band (c) to the valence band the indicated matrix element is given by the equation

$$M(\mathbf{k},\mathbf{q})=\sum_{i=h,l}\int\Psi_i^*(\mathbf{k}+\mathbf{q},\mathbf{r})e^{iqr}\Psi_c(\mathbf{k},\mathbf{r})d\mathbf{r}, \tag{3}$$

where $i=h$ for heavy holes, and $i=l$ for light holes.

In the Kane model the square of the modulus of the matrix element is conveniently expressed in terms of the projection operators onto electron states Λ^c, onto heavy-hole states Λ^h, onto light-hole states Λ^l, and onto the state of the split-off band Λ^{so}. For band-to-band transitions

$$|M(\mathbf{k},\mathbf{q})|^2=\sum_{i=h,l}\mathrm{Tr}\Lambda^i(\mathbf{k}_i+\mathbf{q})\Lambda^c(\mathbf{k}_i)=\sum_{i=h,l}B^{ic}(\mathbf{k}_i,\mathbf{q}), \tag{4}$$

where B^{hc} and B^{lc} are the overlap integrals of the periodic parts of the Bloch wave functions of the conduction band with the heavy-hole and light-hole subbands.

For intraband transitions involving the split-off band the matrix element has a form analogous to (3) with $\Psi_c(\mathbf{k},\mathbf{r})$ replaced by $\Psi_{so}(\mathbf{k},\mathbf{r})$. The square of the modulus of the matrix element for intraband transitions is

$$|M(\mathbf{k},\mathbf{q})|^2=\sum_{i=h,l}\mathrm{Tr}\Lambda^i(\mathbf{k}_i+\mathbf{q})\Lambda^{so}(\mathbf{k}_i)=\sum_{i=h,l}B^{iso}(\mathbf{k}_i,\mathbf{q}), \tag{5}$$

where B^{hso} and B^{lso} are the overlap integrals of the split-off band with the heavy-hole and light-hole subbands.

The projection operators have already been calculated in the 3-band Kane model[8] and in the 4-band model.[9] In Ref. 9 the overlap integral of the heavy-hole band and the split-off band is obtained in the form

$$B^{hso}(\mathbf{k}_{so},\mathbf{q})=\frac{3}{4}\frac{\hbar^4}{m_{so}^2\Delta^2}[\mathbf{k}_{so}\cdot\mathbf{q}]^2, \tag{6}$$

where $[\mathbf{k}_{so},\mathbf{q}]$ denotes the vector product of the hole wave vector in the split-off band and the photon wave vector, $\mathbf{q}=|\mathbf{k}_h-\mathbf{k}_{so}|$, $\mathbf{k}_h$ is the heavy-hole wave vector, and m_{so} is the effective mass of a hole in the split-off band. The overlap integral of the conduction and heavy-hole bands has also been calculated in Ref. 9:

$$B^{hc}(\mathbf{k}_c,\mathbf{q})=\frac{3}{2}\frac{\hbar^2(E_g+\Delta)}{m_cE_g(3E_g+2\Delta)}\frac{[\mathbf{k}_c\cdot\mathbf{q}]^2}{k_c^2}, \tag{7}$$

where $\mathbf{k}_c$ and m_c are the wave vector and the effective mass of an electron in the conduction band.

In InAs the characteristic wave vectors $\mathbf{k}_c$ and $\mathbf{k}_{so}$ are small in comparison with $k_g=\sqrt{E_gm_c}/\hbar$. It then follows from Eqs. (6) and (7) that B^{hso} has an additional smallness proportional to $(k_{so}/k_g)^2$ over and above B^{hc}. This attribute is a consequence of the fact that transitions between the conduction and valence bands are allowed, but transitions between subbands of the valence band are forbidden for $\mathbf{k}=0$.

The overlap integral of the conduction and light-hole bands has been obtained previously[7] and has the form

$$B^{lc}(\mathbf{k}_l,\mathbf{q})=\frac{\hbar^2(E_g+\Delta)}{2m_cE_g(3E_g+2\Delta)}\frac{k_l^2q^2+3(\mathbf{k}_l\cdot\mathbf{q})^2}{k_l^2} \tag{8}$$

where $\mathbf{k}_l\cdot\mathbf{q}$ denotes the scalar product of the light-hole and photon wave vectors.

An equation for the overlap integrals of the light-hole and split-off bands is obtained for the first time in the present paper:

$$B^{lso}(\mathbf{k}_l,\mathbf{q})=\frac{\hbar^4}{4m_{so}^2\Delta^2E_g}\left[(7E_g+4\Delta)(\mathbf{k}_l\cdot\mathbf{q})^2+\frac{(3E_g+2\Delta)^2}{E_g}k_l^2q^2\right]. \tag{9}$$

The overlap integrals (6)–(9) are evaluated on the assumption that the photon wave vector is much smaller than the electron and hole wave vectors and also that the particle energies in the corresponding bands are small in comparison with E_g and Δ.

To calculate the IVA coefficient we substitute the quantity $|M(\mathbf{k},\mathbf{q})|^2$ from (5) into Eq. (2), assume that the degree of degeneracy of heavy and light holes is arbitrary, and disregard the population of the split-off band. Therefore,

$$f_1-f_2=\left[1+\exp\left(\frac{\hbar^2k_i^2}{2m_iT}-\frac{\zeta_h}{T}\right)\right]^{-1},$$

where $i=h$ or l, m_i is the effective mass of holes in the valence band, and ζ_h is the hole Fermi level measured downward from the edge of the valence band.

Integrating Eq. (2) over the angles and over $\mathbf{k}$ with allowance for the delta function, we obtain equations for the IVA coefficients for transitions into the split-off band both from the heavy-hole band α_h^{so} and from the light-hole band α_l^{so}:

$$\alpha_h^{so}=A\frac{M_{so,h}^{5/2}(\hbar\omega-\Delta)^{3/2}}{1+\exp\left[\dfrac{M_{so,h}}{m_h}\dfrac{\hbar\omega-\Delta}{T}-\dfrac{\zeta_h}{T}\right]}, \tag{10}$$

$$\alpha_l^{so}=A\frac{17E_g^2+20E_g\Delta+6\Delta^2}{3E_g^2}\frac{M_{so,l}^{5/2}(\Delta-\hbar\omega)^{3/2}}{1+\exp\left[\dfrac{M_{so,l}}{m_l}\dfrac{\Delta-\hbar\omega}{T}-\dfrac{\zeta_h}{T}\right]},$$

where

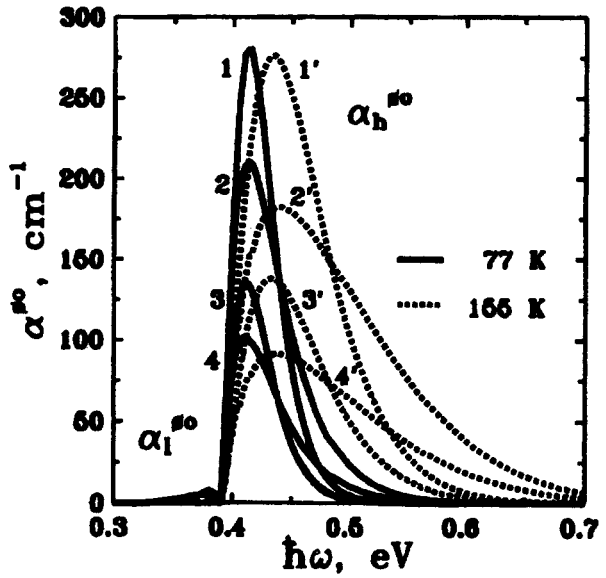

FIG. 1. Frequency dependence of intervalence-band absorption for InAs with the participation of heavy holes (α_h^{so}, $\hbar\omega>\Delta$) and light holes (α_l^{so}, $\hbar\omega<\Delta$) at $T=77$ K (*1–4*) and at $T=155$ K (*1′–4′*). *1, 1′*) Calculated from Eq., (10) at a carrier concentration of 6×10^{17}cm^{-3}; *2, 2′*) Eq., (17), 6×10^{17}cm^{-3}; *3, 3′*) Eq., (10), 3×10^{17}cm^{-3}; *4, 4′*) Eq., (17), 3×10^{17}cm^{-3}.

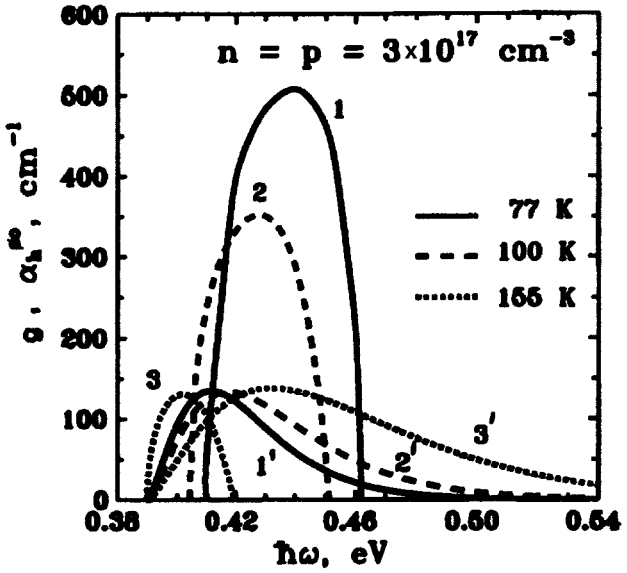

FIG. 2. Frequency curves of the gain (*1–3*) and the IVA coefficient (*1′–3′*) for InAs. *1 1′*) $T=77$ K; *2 2′*) 100 K; *3 3′*) 155 K. The carrier concentration for all curves is 3×10^{17}cm^{-3}.

$$A=\frac{2\sqrt{2}e^2}{c\sqrt{\varepsilon_\infty}\hbar^2}\,\frac{E_g}{\Delta^2 m_{so}^2},\quad M_{so,i}=\frac{m_{so},m_i}{\pm(m_i-m_{so})}.$$

Here $i=h$or l, and the plus sign goes with the subscript h.

It follows from Eq., (10) that absorption by heavy holes with excitation of the latter into the split-off band occurs only in the range $\hbar\omega>\Delta$, and absorption by light holes only occurs in the range $\hbar\omega<\Delta$.

It is evident from a comparison of α_h^{so} and α_l^{so} that the absorption of light by heavy holes is tens of times stronger than absorption by light holes, owing to the high density of states for heavy holes. This contrast is illustrated in Fig. 1, which shows the frequency dependence of the IVA coefficient in InAs at temperatures of 77 K and 155 K. The frequency dependence of α_h^{so} is also shown in Fig. 2 (curves *1′–3′*). It is evident from the figures that the maximum values of α_h^{so} are virtually independent of the temperature at a constant hole density. On the other hand, as the temperature rises, the frequency interval broadens, and the frequency of the maximum of α_h^{so} increases.

It is particularly important to note that in the Kane model hole transitions from the heavy-hole to the light-hole band do not take place when a photon of energy of the order of E_g is absorbed in InAs, because only in direct-band semiconductors with $\Delta\geqslant1.5E_g$ can the laws of conservation of energy and momentum be satisfied simultaneously for such transitions.

To assess the influence of IVA on the characteristics of long-wavelength lasers, we compare the absorption coefficients (10) with the optical gain g calculated in Ref. 7. To find the gain, we substitute the quantity $|M(\mathbf{k},\mathbf{q})|^2$ from (4) into Eq. (2). We assume that electrons in the conduction band and holes in the valence band are degenerate, in general, so that

$$f_1-f_i=\frac{1-\exp\left[\dfrac{\hbar\omega-E_g}{T}-\dfrac{\zeta_c+\zeta_h}{T}\right]}{\left\{1+\exp\left[\dfrac{\hbar\omega-E_g}{T}-\dfrac{\zeta_c}{T}\right]\right\}\left\{1+\exp\left[\dfrac{m_c}{m_i}\,\dfrac{\hbar\omega-E_g}{T}-\dfrac{\zeta_h}{T}\right]\right\}},\tag{11}$$

where $i=h,l$, and ζ_c is the electron Fermi level measured upward from the edge of the conduction band.

Integrating Eq. (2) over the angles and $\mathbf{k}$ with allowance for the energy delta function, we obtain an equation for the optical gain for the transition of electrons into the heavy-hole and light-hole bands:

$$g=g^{ch}+g^{cl}=A\,\frac{m_{so}^2(E_g+\Delta)\Delta^2}{m_cE_g(3E_g+2\Delta)}\times\sqrt{\hbar\omega-E_g}\sum_{i=l,h}\mu_{ci}^{3/2}(f_1-f_i),\tag{12}$$

where $\mu_{ci}=m_cm_i/(m_c+m_i)$, and A is defined in Eq. (10).

Frequency curves of the gains and IVA coefficient in InAs at temperatures of 77 K, 100 K, and 155 K are shown in Fig. 2. It is evident from the figure that as the temperature increases, the coefficient g decreases as usual, and the position of the maximum shifts into the long-wavelength range as a result of the temperature dependence of E_g. We assume that in InAs E_g depends linearly on the temperature, is equal to 0.41 eV at 77 K, and is equal to 0.354 eV at 300 K, whereas Δ does not depend on the temperature[10]; at 155 K we have $E_g=\Delta=0.39$ eV. It should be noted that as the carrier concentration increases, g increases as well, and the maximum of the curve shifts toward shorter wavelengths. It is evident from Fig. 2 that max(g) is several times the value

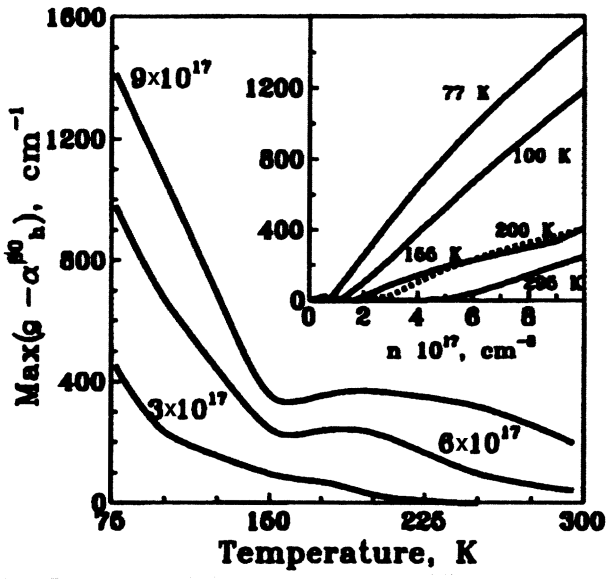

FIG. 3. Temperature dependence of the effective gain at the frequency of the maximum of $(g-\alpha_h^{so})$ in InAs at three carrier concentrations: $3\times10^{17}\mathrm{cm}^{-3}$, $6\times10^{17}\mathrm{cm}^{-3}$, and $9\times10^{17}\mathrm{cm}^{-3}$. Inset: Concentration dependence of the same quantity at temperatures of 77 K, 100 K, 155 K, 200 K, and 295 K.

of $\max(\alpha_h^{so})$ at 77 K. Moreover, the maxima shift far along the frequency scale, and IVA is small in the vicinity of $\max(g)$. At 100 K the values of $\max(g)$ decrease, and the positions of the maxima fall within a common frequency interval. Consequently, IVA is already appreciable at the frequency of $\max(g)$.

At 155 K the maxima of g and α_h^{so} are close together, but amplification prevails over IVA in the vicinity of $\max(g)$ because of the shift of $\max(\alpha_h^{so})$ into the short-wavelength range, whereas $\max(g)$ shifts into the long-wavelength region. It is essential to note that E_g becomes smaller than δ at $T>155$ K, and the absorption of light by heavy holes disappears.

It is therefore evident from Fig. 2 that the coefficient α_h^{so} becomes comparable with g in a certain range of frequencies and charge densities at given temperatures. Assuming identical Fermi factors in both cases, we obtain the following equation from (10) and (12):

$$\frac{g}{\alpha_h^{so}}=\frac{2}{5}\frac{E_g}{\hbar\omega-\Delta}\frac{\sqrt{m_c}m_{so}^2}{M_{so,h}^{5/2}}. \tag{13}$$

In InAs at frequencies $\hbar\omega\sim E_g$ and a temperature of 77 K we have $g/\alpha_h^{so}\approx1.1$.

The large IVA is a consequence of the much higher normalized density of states for transitions between the heavy-hole band and the split-off band in comparison with transitions between the valence band and the conduction band. This large ratio of the normalized densities of states compensates for the low value of $(\hbar\omega-\Delta)/E_g$ due to the prohibition of IVA at the Γ point of the Brillouin zone.

Figure 3 shows the temperature dependence of the effective gain at the frequency of the maximum of $(g-\alpha_h^{so})$ for InAs. It is evident from the figure that the curves for carrier concentrations of $6\times10^{17}\mathrm{cm}^{-3}$ and $9\times10^{17}\mathrm{cm}^{-3}$ have a minimum at 155 K, when IVA is a maximum. At high temperatures the IVA falls off sharply and practically disappears when the photon energy becomes smaller than Δ as a result of the decrease in the width of the band gap. This behavior causes the curves to rise in the temperature interval 155–200 K. The indicated minimum is also manifested in the concurrence of the curves for 155 K and 200 K in the inset to Fig. 3, which shows the dependence of the effective gain on the carrier concentration at various temperatures.

b) All the results of the optical-gain and absorption spectrum calculations in Figs. 1–3 have been obtained without regard for intraband carrier relaxation. As a first approximation, this effect can be taken into account in the first approximation by convoluting the frequency dependence obtained without the effect with a suitable relaxation function. In regard to the latter, it is known to be almost Lorentzian for a small frequency deviation, with a characteristic half-width ΔE determined by the intraband relaxation time τ $(\Delta E\approx\hbar/\tau)$, and for large frequency deviations it decays exponentially according to a Gaussian law.[11] A similar procedure with a Lorentz relaxation function is used extensively for the calculation of gain spectra and yields correct results in the vicinity of the absorption maximum (see, e.g., Ref. 11 and the references cited there). It is readily apparent that, in principle, a Lorentz function cannot be used to calculate intraband absorption, because the corresponding integrals diverge. On the other hand, the results are not too sensitive to the actual form of the relaxation function in the case of small frequency deviations.

Consequently, to take approximate account of intraband relaxation, we form the convolution of the IVA and gain spectra with a Gaussian function, using the intraband relaxation time determined from mobility data.[12] We assume that the carrier mobilities depend on the temperature but not on the concentration. The calculations show that the inclusion of intraband relaxation merely produces slight numerical changes, but no real qualitative differences in the IVA and gain spectra.

c) The calculations in subsection a) have been carried out in the first approximation with respect to the parameter $\gamma=(\hbar\omega-\Delta)/\Delta\ll1$. To test the admissibility of this approximation, we calculate the next higher-order corrections in this small parameter. For the overlap integral of the heavy-hole band with the split-off band (B^{hso}) we obtain the expression (for $E_g\approx\Delta$)

$$B_K^{hso}(\mathbf{k}_{so},\mathbf{q})=B^{hso}\left[1+\frac{x}{2\Delta}\right],\quad x=\frac{\hbar^2k_{so}^2}{2m_{so}}, \tag{14}$$

where B^{hso} is described by Eq. (6). It is evident from Eq. (14) that the corrections to B^{hso} are small with respect to γ, since $x\sim\hbar\omega-\Delta$.

Integrating Eq. (2) over the angles and over $\mathbf{k}$ with allowance for the analogous γ correction in the energy delta function, we obtain the following equation for the IVA coefficient:

$$(\alpha_h^{so})_1=\alpha_h^{so}\left[1+\left(1-\frac{21}{2}M\right)\frac{M}{2}\gamma\right], \tag{15}$$

where

$$M=\frac{m_h}{m_h-m_{so}},$$

and α_h^{so} is given by Eq. (10).

For InAs we have $M=1.52$ and

$$(\alpha_h^{so})_1=\alpha_h^{so}(1+\beta), \tag{16}$$

where $\beta=-11\gamma$. It is evident from Eq., (16) that the small parameter in the correction to α_h^{so} for InAs is preceded by a numerical coefficient of the order of 10, and the corresponding correction (β) is significant. It is evident from Eq., (10) and Fig. 1 that $\hbar\omega-\Delta=(3/2)kT$. We have $\beta=-0.28$ at 77 K and $\beta=-0.56$ at 155 K, and the validity of the given expansion is no longer justified at 155 K. We therefore calculate the IVA coefficient for heavy holes using the exact Kane model in the overlap integral and also in the energy conservation law. In this case the IVA coefficient can be written in the form

$$(\alpha_h^{so})^K=\frac{-Am_{so}^{5/2}x^{3/2}}{\left[1+\exp\left(M_1\frac{x}{T}-\frac{\zeta_h}{T}\right)\right]\left[M_1+\frac{(E_g+\Delta)(3E_{so}+2\Delta)}{3E_{so}^2+2E_{so}(\Delta-E_g)-E_g\Delta-3x(E_g+\Delta)}\right]}, \tag{17}$$

where $M_1=m_{so}/m_h$, $E_{so}=-\Delta-\varepsilon_{so}$, ε_{so} is the Kane energy of a hole in the split-off band, A is defined in (10), and x is defined in (14). The relation between x and E_{so} is specified by the energy conservation law

$$E_{so}+M_1x+\hbar\omega=0 \tag{18}$$

and by the following relation deduced from the Kane equation:

$$x=\frac{E_{so}[E_{so}^2+(\Delta-E_g)E_{so}-E_g\Delta]}{(E_g+\Delta)(3E_{so}+2\Delta)}. \tag{19}$$

The spectral curves of $(\alpha_h^{so})^K$ for InAs are represented by curves *2*, *2′*, *4*, and *4′* in Fig. 1. It is evident from the figure that the quantitative differences between the exact equation (17) and the approximation expression (10) are significant. Calculations using the exact and approximate equations give the same energy position of the IVA maximum. However, when the exact equation (17) is used, the absorption level at the maximum is roughly 30% lower. Also, the absorption spectra extend into the short-wavelength range, especially at 155 K.

3. INFLUENCE OF INTERVALENCE-BAND ABSORPTION ON THE CHARACTERISTICS OF HETEROLASERS

a) We have investigated the influence of IVA on the characteristics of heterolasers. The investigated objects were long-wavelength, double-heterostructure, injection lasers with an *n*-InAs active zone.

Double heterostructures of composition *n*-$InAs_{1-x-y}Sb_xP_y$/*n*-InAs/*p*-$InAs_{1-x-y}Sb_xP_y$ ($0.05<x<0.09$; $0.09<y<0.18$) were grown on an *n*-InAs(111) substrate by liquid-phase epitaxy under conditions creating high substrate plasticity so as to reduce the misfit voltages induced by mismatch of the lattice constants through the preponderant formation of dislocations in the substrate. The end products were structurally perfect epitaxial layers with an all-time low dislocation density $\leqslant 10^{+3}\text{cm}^{-2}$. The *p*-type emitter was doped with zinc. The energy differential across the band gap and the refractive index at the heterointerfaces were equal to 100 meV and 0.03, respectively. The confining layers had a thickness of 4–6 μm, and the thickness of the active zone (d) varies from 0.8 μm to 6 μm. The refractive index of the active zone was equal to 3.52. Four-chip lasers were investigated together with wide-contact lasers, whose lateral surfaces were sufficiently rough to suppress internal closed mode configurations. The width of the contact was varied in the interval 35–200 μm, and the cavity had a length $L=100$–1500 μm. The wavelength of the laser mode was 3.05 μm (at 77 K), corresponding to the maximum of the photoluminescence peak of undoped *n*-InAs in the active zone. Lasing was observed in the temperature range 2–150 K in pulsed and continuous-wave operation with minimum threshold current densities of 60 A/cm^2 and 100 A/cm^2, respectively (at 77 K).

We now discuss the influence of IVA on the characteristics of the above-described heterolasers. We note that the influence of the heterointerfaces on absorption is weak, owing to the considerable width of the active zone, and we ignore it. We use the exact Kane model for all the calculations in this section. We analyze the laser characteristics in the following order. We first determine the threshold carrier concentration n_{th} in the active zone of the heterolaser for various values of d, L, and T. According to Ref. 13,

$$\Gamma[\max(g-\alpha_h^{so})]=\alpha^*, \tag{20}$$

where only two types of optical losses are taken into account: IVA (α_h^{so}) and output losses $\alpha^*=(1/L)\ln(1/R)$, where $R=0.3$ is the reflection coefficient of the laser mirrors, and Γ is the optical confinement factor in the investigated heterostructure. It is evident from the calculations that the greatest increase in the threshold density should be observed in lasers having thinner active zones ($d\leqslant 1$ μm) and short cavities ($L=0.03$ cm), for which the output losses are highest.

Next we calculate the external differential quantum efficiency (η_i), defined as the ratio of the output losses (α^*) to the total losses:

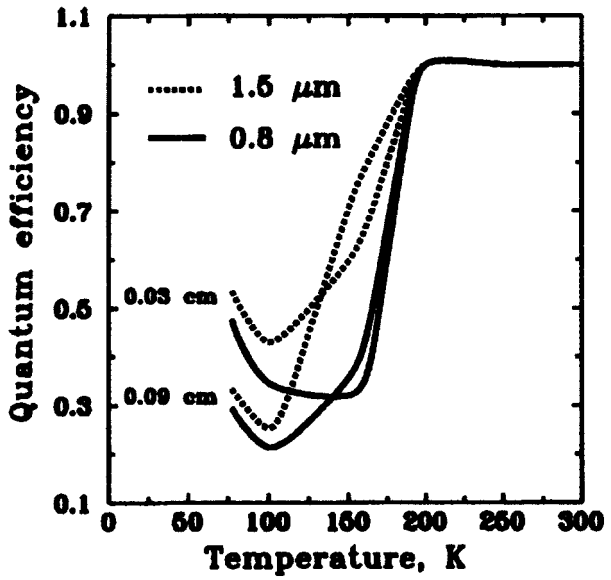

FIG. 4. Temperature curves of the external differential quantum efficiency of a heterolasers with InAs active zones of thickness 0.8 μm and 1.5 μm and with a cavities of length 0.03 cm and 0.09 cm.

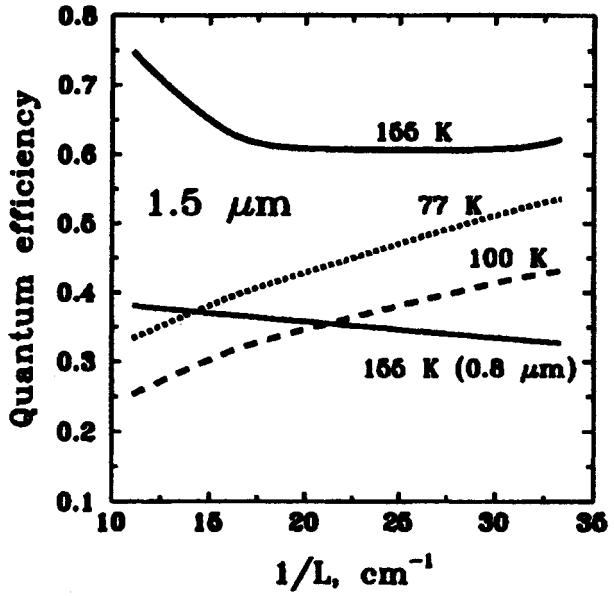

FIG. 5. External differential quantum efficiency versus normalized output losses for heterolasers with InAs active zones of thickness 0.8 μ at 155 K and of thickness 1.5 μm at three temperatures: 77 K, 100 K, and 155 K.

$$\eta_i = \frac{\alpha^*}{\alpha^* + \alpha_h^{so}}. \tag{21}$$

Figure 4 shows temperature curves of the quantum efficiency for two thicknesses of the active zone of the heterolaser, $d = 0.8$ μm and 1.5 μm, and for two lengths of the active zone, $L = 0.03$ cm and 0.09 cm. It is important to note that as the temperature increases in the interval 100–155 K, IVA increases not only as a result of the increased carrier concentration, but also in connection with the shift of the optical-gain maximum into the range of maximum absorption (Fig. 2). At temperatures above 155 K, where E_g becomes smaller than Δ, the IVA level at the frequency $\max(g - \alpha_h^{so})$ falls off sharply, dropping to zero. Consequently, all the curves exhibit a minimum at $T = 100$–155 K due to the frequency alignment of the gain and absorption maxima.

Figure 5 shows the dependence of the quantum efficiency on the normalized output losses $1/L$ at temperatures of 77 K, 100 K, and 155 K. The parameter is the thickness of the active zone. At 77 K and 100 K, as usual, the quantum efficiency increases with $1/L$, although in fact a sublinear dependence associated with enhanced IVA is observed for high output losses. The dependence $\eta_i = f(1/L)$ exhibits anomalous behavior at 155 K, η_i decreasing as $1/L$ increases, because IVA increases more rapidly than the output losses.

We also calculate the temperature dependence of the threshold current density J_{th} in the investigated lasers with an InAs active zone (Fig. 6), using the calculated values of n_{th}. In determining the threshold current density, we take into account radiative recombination and band-to-band Auger recombination. The threshold current density is then described by the equation

$$J_{th} = 1.6 \times 10^{-23} n_{th}^2 [B_r + (R_1 + R_2) n_{th}], \tag{22}$$

where B_r is the radiative recombination coefficient, R_1 is the coefficient of the subband-to-subband CHHS Auger process with hole transition into the split-off band, and R_2 is the coefficient of the band-to-band CHCC Auger process associated with the excitation of an electron in the conduction band. Relying on Ref. 14, for the CHHS process in InAs we obtain $R_1 = 4 \times 10^{-27}$ cm^6/s, which is essentially independent of the temperature. Also, on the basis of InAs data in Ref. 14, taking the degeneracy of electrons into account, we

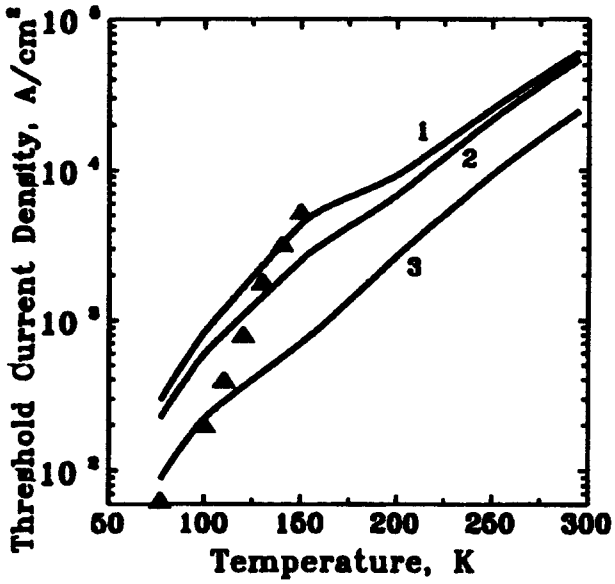

FIG. 6. Experimental and theoretical temperature dependence of the threshold current density for a heterolaser with an InAs active zone. The solid curves are calculated for various heterostructures: *1*) thickness of the active zone $d = 0.8$ μm, cavity length $L = 0.03$ cm; *2*) $d = 1.5$ μm, cavity length $L = 0.03$ cm; *3*) four-chip heterostructure with $d = 1.8$ μm. The triangles represent experimental data for a four-chip heterostructure with $d = 1.8$ μm.

calculate the CHCC recombination coefficient, which decreases by two orders of magnitude as the temperature drops from room to liquid-nitrogen temperature: $R_2 = 3.3 \times 10^{-27}$ cm^6/s at 300 K, and $R_2 = 2.2 \times 10^{-29}$ cm^6/s at 77 K.

In calculating the radiative recombination component of the threshold current, we take into account the degeneracy of electrons and holes, i.e., not only the dependence of the radiative recombination coefficient B_r on the temperature, but also its dependence on the carrier concentration.

Calculations have shown that the radiative current component is comparable with the nonradiative (Auger) component at 77 K (Ref. 3). As the temperature increases, the nonradiative component begins to prevail, and at 155 K it is already an order of magnitude greater than the radiative component.

It follows from the calculations that in long lasers ($L = 0.09$ cm) the threshold current is essentially independent of the thickness of the active zone. In short lasers ($L = 0.03$ cm), on the other hand, the threshold current density depends on the thickness of the active zone in the temperature interval 100–200 K. For $d = 0.8$ μm we observe a slight ''shelf'' associated with the ''shutdown'' of IVA at $T > 155$ K.

b) Figure 6 also shows the experimental temperature dependence of the threshold current density for a four-chip laser with an InAs active zone of thickness 1.8 μm. This thickness corresponds to the minimum measured threshold current density. Satisfactory agreement between theory and experiment can only be obtained in the temperature interval 77–100 K. At higher temperatures the experimental values of the threshold current density are much higher than the theoretical values. The discrepancy between theory and experiment at higher temperatures is attributable to the fact that our model ignores carrier heating effects and leakage currents. Three carrier heating mechanisms are possible in the investigated structures: 1) heating by carrier injection through the heterointerfaces; 2) heating due to Auger excitation; 3) heating by the intraband absorption of radiation. The analysis of the influence of various heating mechanisms on the threshold characteristics of such lasers and on their working temperature limit is the object of a separate investigation. The existence of neglected, highly temperature-dependent, internal absorption mechanisms is also possible, for example, owing to the presence of the heterointerfaces.[15] Further evidence of the existence of internal absorption mechanisms is the experimentally observed continuous decline of the differential quantum efficiency of such lasers as the temperature increases.[16]

Figure 7 shows the theoretical and experimental values of the threshold current density plotted as a function of the normalized output losses at 77 K in a laser having the same basic heterostructure as in Fig. 6. Good agreement is observed between the experimental and theoretical data, except that the theory gives somewhat excessive values of the threshold current density in the case of low losses.

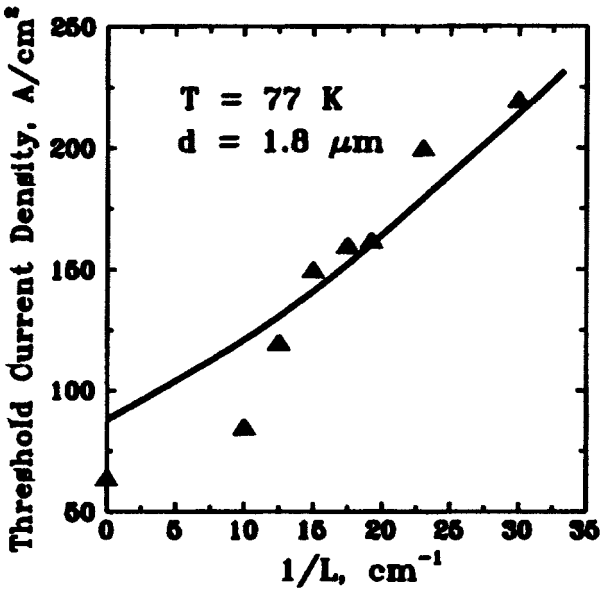

FIG. 7. Experimental (triangles) and theoretical (solid curve) plots of the threshold current density versus normalized output losses at 77 K for a heterolaser with an InAs active zone of thickness $d = 1.8$ μm.

4. DISCUSSION OF THE RESULTS AND CONCLUSIONS

The present investigation has shown that the mechanism of intervalence-band absorption significantly influences the characteristics of heterolasers emitting at a wavelength of 3–3.5 μm and incorporating an active zone of InAs or similarly constituted solid solutions. When IVA is taken into account, the differential quantum efficiency is found to have an anomalous dependence on the temperature and on the normalized output losses (at certain temperatures). Intervalence-band absorption raises the threshold current density. Lasers with long cavities and wider active zones are preferable for diminishing the influence of IVA on the threshold current density and for raising the working temperature of such lasers.

We have shown that in III–V semiconductors, as in Ge (Ref. 6), the heavy-hole IVA coefficient is tens of times higher than the long-wavelength IVA coefficient. However, the absorption of light by heavy and light holes takes place in different frequency ranges: heavy holes at $\hbar\omega > \Delta$ and light holes at $\hbar\omega < \Delta$. Semiconductors with $E_g < \Delta$ must be used to suppress the mechanism of strong absorption by heavy holes. This condition can be achieved either by varying the temperature or by using solid solutions of the appropriate composition. In InAs E_g becomes smaller than Δ at $T > 155$ K. In $In_yGa_{1-y}As_{1-x}Sb_x$ solid solutions, which closely resemble InAs, we have $E_g < \Delta$ at any temperature, and in $InAs_{1-x}Sb_x$ we have $E_g > \Delta$ for $x < 0.1$ at temperatures close to 77 K. One final note of importance; Not only is IVA suppressed in semiconductors with $E_g < \Delta$, but Auger recombination involving the split-off band (the CHHS process) also diminishes, as does heating associated with Auger recombination.

In closing, we express our gratitude to E. L. Ivchenko for a discussion of the results and for valuable consultations, and to Yu. P. Yakovlev for attention and interest in the work.

The experimental part of the study has been supported by the Scientific Fund on Category No. 4.14: ''Optics and Laser Physics.''

[1] M. Aidaraliev, N. V. Zotova, S. A. Karandashev, B. A. Matveev, N. M. Stus', and G. N. Talalakin, Infrared Phys. Technol. **37**, 83 (1996).
[2] P. J. A. Thijs, L. F. Tiemeijer, J. J. M. Binsma, and T. van Dongen, IEEE J. Quantum Electron. **QE-30**, 477 (1994).
[3] M. Sh. Aĭdaraliev, G. G. Zegrya, N. V. Zotova, S. A. Karandashev, B. A. Matveev, N. M. Stus', and G. N. Talalakin, Fiz. Tekh. Poluprovodn. **26**, 246 (1992) [Sov. Phys. Semicond. **26**, 138 (1992)].
[4] G. G. Zegrya, in *Antimonide-Related Strained-Layer Heterostructures*, Edited by M. O. Manasreh (Gordon and Breach, New York, 1997).
[5] A. R. Adams, K. C. Heasman, and J. Hilton, Semicond. Sci. Technol. **2**, 761 (1987).
[6] B. L. Al'tshuler, E. L. Ivchenko, A. N. Moskalev, G. E. Pikus, and R. M. Ryndin, Zh. Éksp. Teor. Fiz. **85**, 349 (1983) [Sov. Phys. JETP **58**, 203 (1983)].
[7] B. L. Gel'mont and G. G. Zegrya, Fiz. Tekh. Poluprovodn. **25**, 2019 (1991) [Sov. Phys. Semicond. **25**, 1216 (1991)].
[8] B. L. Gel'mont, Zh. Éksp. Teor. Fiz. **75**, 536 (1978) [Sov. Phys. JETP **48**, 258 (1978)].
[9] B. L. Gel'mont, Z. N. Sokolova, and I. N. Yassievich, Fiz. Tekh. Poluprovodn. **16**, 592 (1982) [Sov. Phys. Semicond. **16**, 382 (1982)].
[10] *Numerical Data and Functional Relationships in Science and Technology*, Vol. 17: *Semiconductors*, Edited by O. Madelung (Springer-Verlag, Berlin-New York, 1982).
[11] *Quantum Well Lasers*, Edited by P. Zory (Academic Press, New York, 1993).
[12] N. V. Zotova, Author's Abstract of Candidate's Dissertation [in Russian] (FTI im. A. F. Ioffe, Leningrad, 1964).
[13] H. C. Casey Jr. and M. B. Panish, *Heterostructure Lasers* (Academic Press, New York, 1978) [Russ. trans., Mir, Moscow (1981)].
[14] N. V. Zotova, Author's Abstract of Candidate's Dissertation [in Russian] (FTI im. A. F. Ioffe, Leningrad, 1982).
[15] G. G. Zegrya, Author's Abstract of Doctoral Dissertation [in Russian] (FTI im. A. F. Ioffe, St. Petersburg, 1995).
[16] M. Sh. Aĭdaraliev, N. V. Zotova, S. A. Karandashev, B. A. Matveev, N. M. Stus', and G. N. Talalakin, Fiz. Tekh. Poluprovodn. **27**, 21 (1993) [Semiconductors **27**, 10 (1993)].

Translated by James S. Wood

Influence of plasma treatment of the surface of silicon carbide on the characteristics of buried-gate junction field-effect transistors

P. A. Ivanov, O. I. Kon'kov, V. N. Panteleev, and T. P. Samsonova

A. F. Ioffe Physicotechnical Institute, Russian Academy of Sciences, 194021 St. Petersburg, Russia
(Submitted April 11, 1997; accepted for publication April 16, 1997)
Fiz. Tekh. Poluprovodn. **31**, 1404–1407 (November 1997)

For SiC buried-gate junction field-effect transistors it is demonstrated that the charge state of the channel surface, which functions as a secondary, ''floating'' gate in such transistors, can be stabilized by treating it in a hydrogen plasma at room temperature. It is shown that the need for such stabilization is especially crucial for transistors having a relatively low donor density in the channel (high-voltage type), in which the surface charge can strongly modulate the drain voltage under the influence of short-channel effects. © *1997 American Institute of Physics.* [S1063-7826(97)03111-6]

1. INTRODUCTION

It is a well-known fact that the surface properties of semiconductors have a strong influence on the operation of many electronic devices utilizing them. For this reason, special techniques are employed in device technology with a view toward modifying the surface in such a way as to obtain a particular combination of surface properties. At present, a crucial aspect of the development of devices based on silicon carbide is the reliable passivation (or stabilization) of the SiC surface at sites where it connects with the active zones of devices (especially the high-voltage kind).

As a rule, no special measures are implemented to stabilize the channel surface in SiC buried-gate junction field-effect transistors fabricated by various groups worldwide.[1] On the other hand, one needs to be aware that the channel of this type of transistor is cut off by the space-charge region of the p–n gate on the surface (Fig. 1), whose charge state can vary, in principle. This means that the surface emerges as a kind of ''floating'' gate, so that steps must be taken to stabilize the surface charge. Ideally the density of this charge should be either much smaller or, conversely, much greater than the surface density of donors in the channel, Na (N is the bulk density of donors, and a is the thickness of the channel). In the first case ''flat-band'' conditions are established on the surface (so that a surface space-charge region is simply nonexistent), and in the second case the thickness of the subsurface space-charge region is stabilized by the high surface charge (Fermi level pinning on the surface). It is important to note the practice exercised in several studies of SiC buried-gate junction transistors, of protecting the channel surface with a heat-resistant oxide (mainly to safeguard the transistors against environmental effects). For surface charge stabilization, however, oxidation cannot really be deemed an effective method, because the total density of states at the SiO_2–SiC interface (of the order of 10^{12} cm^{-2}, Ref. 2) is commensurate with the surface density of donors in the transistor channel. Surface-charge stabilization is especially crucial for transistors having a low channel donor density (high-voltage type). Since the channel length-to-thickness ratio in such transistors is usually smaller than in transistors having a high donor density (low-voltage type), short-channel effects can be more pronounced in the former and have a definite influence on the surface charge.

In previous work we have shown that the surface properties of crystalline silicon carbide can be modified considerably by treatment in hydrogen and helium gas-discharge plasmas. In particular, this technique has resulted in the formation of high-resistivity surface layers through the generation of a high density of electrically active point defects.[3] We now propose to demonstrate how the characteristics of high-voltage buried-gate transistors are influenced by: 1) reactive ion etching of the channel in a SF_6 gas-discharge plasma; 2) subsequent treatment of the surface in a hydrogen plasma.

2. OBJECT AND PROCEDURE OF THE INVESTIGATIONS

The transistors were prepared on the basis of 6*H*-SiC epitaxial p^+(substrate)–n_0–n^+ structures grown by chemical deposition from the gaseous phase. The technology used to fabricate discrete mesa-insulated transistors involved standard procedures for the formation of nickel-based ohmic contacts to the source, the drain, and the gate and selective reactive ion etching of SiC in a SF_6 plasma. The donor density in the channel was $3\times10^{16}cm^{-3}$ (we note that this value is set approximately an order of magnitude higher for low-voltage transistors), and the channel length was 5 μm.

After the transistor characteristics (the current-voltage and capacitance-voltage curves of the control p–n junction) had been measured, the samples were treated in a hydrogen plasma to modify the surface properties of the channel. The parameters of this process included: the hydrogen pressure in the dc-discharge reaction chamber 2×10^{-3} torr; the accelerating voltage between the anode and the cathode 600 V (the discharge power density did not exceed 1 W/cm^2); room temperature; treatment time 1 h. Following this procedure, the transistor characteristics were again measured for comparison with the characteristics before hydrogen-plasma treatment.

In addition, for comparative analysis the capacitance-voltage curves were measured for reference Au–SiC surface-barrier structures (using n-type 6*H*-SiC films grown by sublimation epitaxy), which were formed on each crystal before

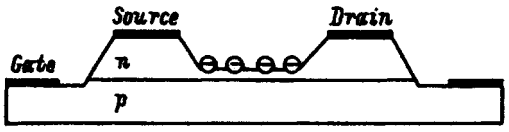

FIG. 1. Schematic vertical cross section of the buried-gate junction field-effect transistor, showing the surface charge in the role of a secondary, floating gate.

the plasma treatments, then after etching in SF_6, and finally after subsequent hydrogen-plasma treatment.

3. EXPERIMENTAL RESULTS AND DISCUSSION

Typical output characteristic curves of the fabricated transistors are shown in Fig. 2 (for measurements performed at room temperature by means of an L2-56 cathode-ray curve tracer).

The curves measured before hydrogen-plasma treatment have features that distinguish them from low-voltage transistors. First, they do not exhibit well-marked saturation of the drain current as a function of the drain voltage (Fig. 2a). The form of the curves depends on the specified parameters of the measurements, in particular, on the amplitude and sweep time of the drain voltage. For example, when the voltage amplitude is increased, the differential slope of the curves in the initial interval drops considerably, further diminishing their saturation. Second, the drain current depends superlinearly on the drain voltage near the opening threshold (Fig. 2b), i.e., the channel is opened from the closed state by the drain voltage (in low-voltage 6*H*-SiC transistors the subthreshold drain current does not depend on the drain voltage[4]).

We assume that this behavior is attributable to the influence of the drain potential on the surface charge induced by the short-channel effect (see the Appendix): An increase in the drain potential induces a positive charge on the surface (due to ejections of electrons from surface-state levels), and this charge partially blocks the gate, producing the observed superlinear behavior of the curves near the threshold.

Subsequent hydrogen-plasma treatment leads to a radical change in the output *I-V* curves of the transistors. First of all, we see an improvement in the saturation of the drain current as a function of the drain voltage (Fig. 2c; moreover, the form of the curves is essentially no longer dependent on the amplitude and the sweep time). Second, the curves become sublinear near the opening threshold, tending to saturation (Fig. 2d). Third, the channel cutoff voltage is higher.

We attribute this modification of the *I-V* curves to the generation of a high density of electrically active (donor) point defects near the surface. According to our estimates, the bulk density of generated defects is at the level of 10^{18}–10^{19} cm^{-3}, and the thickness of the generation zone is of the order of a tenth of a micrometer.[3] As a result, the Fermi level in the surface layer is pinned to deep defects, creating between this layer and the interior of the channel an antigate barrier totally devoid of a depletion zone. This situation accounts for the increase in the channel cutoff voltage as a result of treatment. On the other hand, since the surface density of generated defects is greater than 10^{13}–10^{14} cm^{-2} (which itself is one or two orders of magnitude higher than the surface donor density in the channel, $Na=10^{12}$ cm^{-2}), the antigate barrier leads to Fermi level pinning at the surface (i.e., stabilizes the surface as a ''floating'' gate) and to improvement of the transistor characteristics.

Further evidence in support of the postulated surface sta-

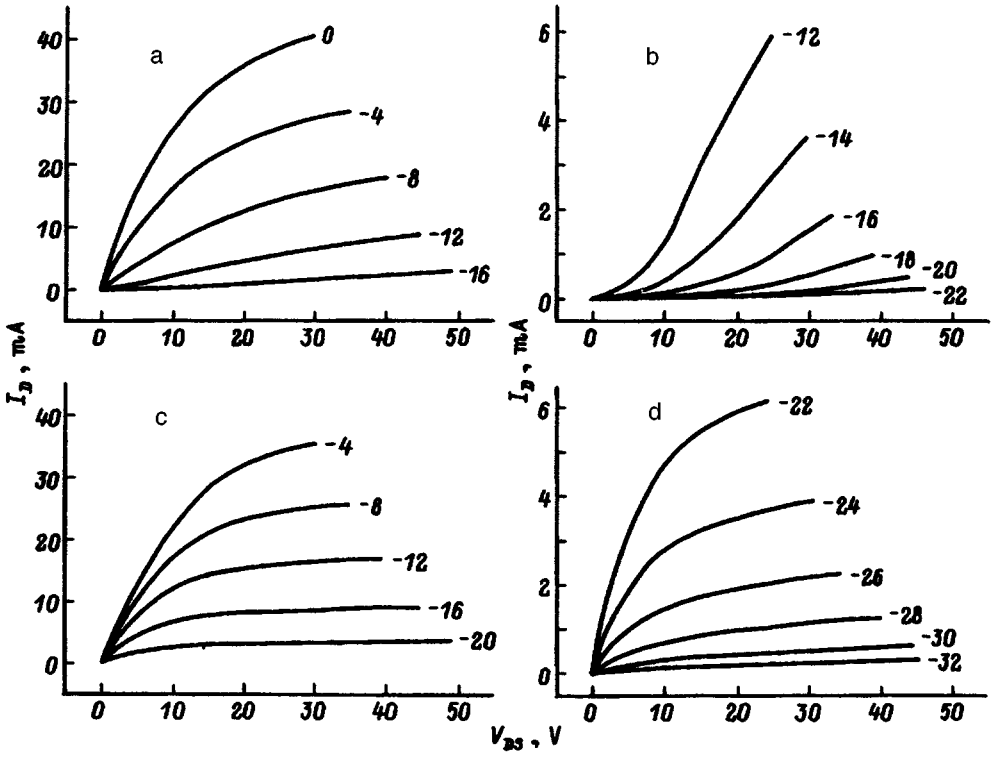

FIG. 2. Typical transistor output current-voltage curves. a, b) Measured after etching of the channel in SF_6; c, d) after subsequent hydrogen-plasma treatment. The numbers alongside the curves are the values of V_{GS} [V].

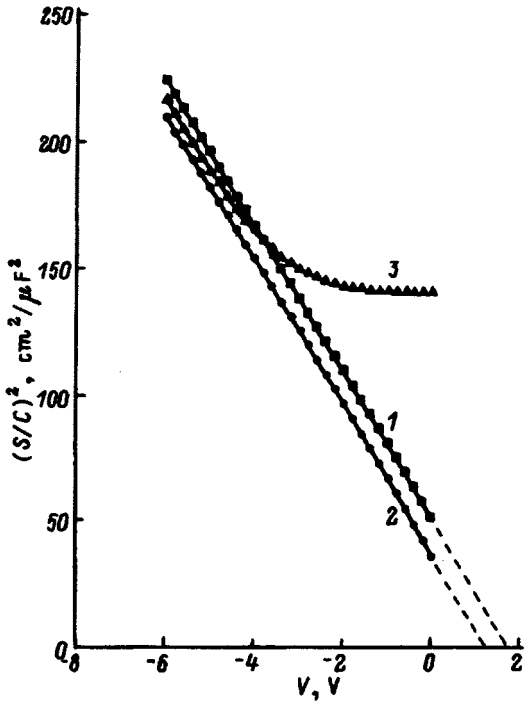

FIG. 3. Capacitance-voltage curves of reference Au–6*H*-SiC structures. *1*) Before plasma treatments; *2*) after surface etching in SF_6; *3*) after hydrogen-plasma treatment of the surface.

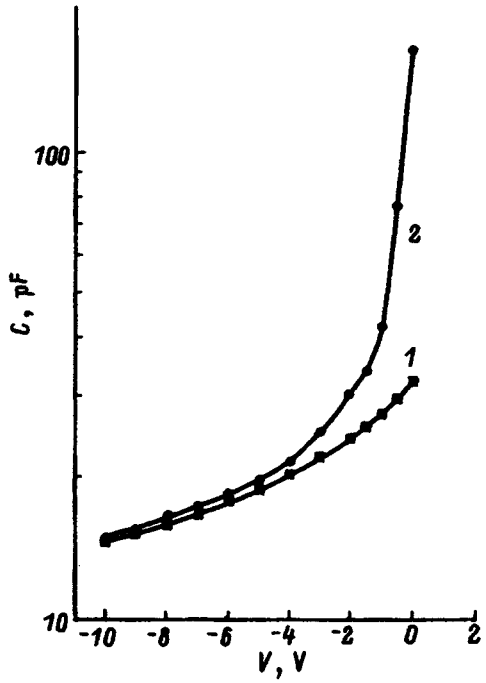

FIG. 4. Capacitance-voltage curves of the *p–n* gate. *1*) before hydrogen-plasma treatment (after etching of the channel in SF_6); *2*) after hydrogen-plasma treatment.

bilization mechanism is found in measurements of the *C–V* curves of the reference Au–SiC structure and the *C–V* curves of the control *p–n* junction. Measurements of the *C–V* curves of Schottky barriers indicate that the SF_6 etching of SiC merely lowers the height of the Au barrier to some extent, and subsequent hydrogen-plasma treatment leads to the formation of a high-resistivity layer of thickness $\sim 0.1\ \mu$m near the surface (Fig. 3). On the other hand, indicative results are obtained from measurements of the *C–V* curves of the control *p–n* junction. After hydrogen-plasma treatment the zero-bias capacitance of the junction becomes much higher, but the application of a bias voltage restores it to its values measured prior to treatment (Fig. 4). This result might seem unexpected at first glance, but there is an explanation. As a matter of fact, because of the structural characteristics of the fabricated transistors, not only the surface of the channel, but also the *p*-type material beyond the limits of the mesa structure is exposed to the influence of the plasma (Fig. 5). Our previous investigations[5] have shown that hydrogen-plasma treatment of the *p*-type material can change the type of conductivity in a thin layer near the surface, and indeed this is most likely what happens here. As a result, the capacitance of the control *p–n* junction increases because, on the one hand, its area increases and, on the other, a high (in comparison with n_0) donor density occurs at the edges of the *p–n* junction. But when a bias voltage is applied, the space-charge region of the *p–n* junction overlaps the thin n^+ layer at the edges, ''closing off'' this zone from the measurements, and the capacitance is again determined entirely by the parameters of the *p–n* junction within the limits of the mesa structure.

Consequently, hydrogen-plasma treatment of the transistor channel surface substantially improves their characteristics, at least at room temperature. Of course, before a final conclusion can be drawn as to the efficacy of the method, the thermal stability of defects will need to be studied further, because one of the principal areas of application of silicon carbide is in high-temperature devices.

The authors are grateful to A. Konstantinov, N. Nordell, S. Karlsson, and K. Harris of the Industrial Microelectronics Center in Stockholm for furnishing the epitaxial SiC structures used in the study.

APPENDIX

The influence of short-channel effects on the subthreshold conductivity is well known in the case of silicon insulated-gate transistors and is explained by the influence of the drain bias voltage as well as the gate bias voltage on the potential distribution in the short channel. An empirical criterion for the minimum channel length $L_{\min}$ [μm], at which short-channel effects begin to appear, has been developed for silicon inversion-layer metal-insulator-semiconductor (MIS) transistors:[6]

$$L_{\min} = 0.4[r_j d(w_s + w_d)^2]^{1/3},$$

FIG. 5. See explanations in the text.

where r_j [μm] is the depth of the drain and source p–n junctions, d [Å] is the thickness of the insulator, and w_s+w_d [μm] is the sum of the thicknesses of the source and drain depletion layers. For an MIS transistor the thickness of the insulator d characterizes the degree of ''short-range action'' of the gate on the channel. In the case of a transistor utilizing a buried p–n junction as the gate the channel thickness a functions in the same role. By analogy with the above equation, an analogous criterion $L_{\min}$ for our transistors can be introduced by replacing d [and, for rough estimates, (w_s+w_d) and r_j] by the channel thickness a. Then, taking into account the relation $V_p=qNa^2/2\varepsilon$, we can determine $L_{\min}$ as a function of the degree of doping N of the channel and the specified cutoff voltage V_p. It becomes clear that $L_{\min}$ will be significantly higher for a high-voltage transistor, which requires a low donor density in the channel, than for a low-voltage transistor. In our case specifically (with a doping level $3\times10^{16}\text{cm}^{-3}$), the calculated value of $L_{\min}$ is approximately 9 μm, as opposed to $L=5$ μm.

[1] P. A. Ivanov and V. E. Chelnokov, Fiz. Tekh. Poluprovodn. **29**, 1921 (1995) [Semiconductors **29**, 1003 (1995)].
[2] P. A. Ivanov, V. N. Panteleev, R. P. Samsonova, and V. E. Chelnokov, Fiz. Tekh. Poluprovodn. **29**, 271 (1995) [Semiconductors **29**, 135 (1995)].
[3] A. O. Konstantinov, N. S. Konstantinova, O. I. Kon'kov, E. I. Terukov, and P. A. Ivanov, Fiz. Tekh. Poluprovodn. **28**, 342 (1994) [Semiconductors **28**, 209 (1994)].
[4] P. A. Ivanov, N. S. Savkina, V. N. Panteleev, T. P. Samsonova, and A. A. Maltsev, in *Transactions of the Third International High Temperature Electronics Conferences (HiTEC)* (Albuquerque, N.M., 1996), p. P-213.
[5] A. O. Konstantinov, P. A. Ivanov, O. I. Konkov, and E. I. Terukov, in *Institute of Physics Conference Series, No. 137, Silicon Carbide and Related Materials*, edited by M. G. Spencer, R. P. Devaty, J. A. Edmond, M. Asif Khan, R. Karlan, and M. Rahman (IOP Publ., Bristol-Philadelphia, 1993), p. 275.
[6] J. R. Brews, W. Fitchner, E. H. Nicolian, and S. M. Sze, IEEE Trans. Electron Devices **EDL-1**, 2 (1980).

Translated by James S. Wood

SIMC-X 1998

10th Conference on
Semiconducting and Insulating Materials
June 1–5, 1998
Berkeley, California

Scope of the Conference

This conference has traditionally been the leading meeting for fundamental materials problems of compound semiconductors of relevance for electronic and optoelectronic devices. In its early years, the conference focused on defect problems in semi-insulating substrates used for device fabrication. Later, following the decision of the International Advisory Committee, the scope of the conference was extended to include other device-relevant issues in compound semiconductor materials. The conference brings together specialists from various fields, including materials science, solid state physics, and device and process engineering. The purpose of the meeting is to discuss growth, characterization, theory, device applications, and materials problems related to semiconducting and insulating compounds such as GaAs, InP, III-nitrides, II–VI compounds, and SiGe. Participants in the conference will have an opportunity to exchange ideas and to discuss future directions in the development of this expanding field. The conference program will include invited, oral, and poster presentations.

Novel Materials Systems of Special Interest for this Conference:

III-nitrides
III-oxides
Non-stoichiometric III-Vs

Topics

Growth: Bulk and epitaxial growth (molecular-beam epitaxy and metal-organic chemical vapor deposition), control of stoichiometry, and defect control.

Characterization: Electrical and optical evaluation, deep level analysis, structure of point and extended defects and interface studies.

Theory: Heat and mass transport in technological processes, surface and interface states, identification of defects and impurities, and compensation processes.

Applications: Electronic and optoelectronic devices, the role of point and extended defect, reliability and processing issues, application of wide-gap materials, aluminum based oxides, and nonstoichiometric III-Vs. The program and other details will be posted on the conference web site: http://www.lbl.gov/×sinc

You are encouraged to joint the mailing list by using e-mail: simc@ux5.lbl.gov. Please include your e-mail address and your postal address.

Abstract deadline: December 15, 1997. Additional information will be given in the second announcement.

Abstracts and questions can be sent to the conference chair:

Dr. Zuzanna Liliental-Weber
Lawrence Berkeley National Laboratory
MS 62-203
1 Cyclotron Road
Berkeley, CA 95720, USA
simc@ux5.lbl.gov

International Advisory Committee

A. Claverie (Chair)	(France)
I. Akasaki	(Japan)
M. Brozel	(UK)
J. Baranowski	(Poland)
F. Dubecki	(Slovakia)
R. Fornari	(Italy)
C. Jagadish	(Australia)
W. Jantz	(Germany)
D. Look	(USA)
C. Miner	(Canada)
B. Monemar	(Sweden)
E. Weber	(USA)
W. Zanguo	(China)

Program Committee*

Wladek Walukiewicz, Chairman
Jon Abrokwah
Kent Choquette
Robert Davis
Richard Depuis
Tim Drummond
Lester Eastman
Diana Huffaker
Robert Hull
Chris Kocot
David Look
Umesh Mishra
William Mitchel
Fernando Ponce
Don Shaw
Chris Van de Walle
Gerald Witt
Jerry Woodall

**All from USA*

1216